

Annual Report 2012

Annual Report 2012

Heinz Maier-Leibnitz Zentrum (MLZ)

SPONSORED BY THE



Federal Ministry
of Education
and Research

Bayerisches Staatsministerium für
Wissenschaft, Forschung und Kunst



Content

Directors' Report	4
Directors' Report: Growing Cooperation	7
The year in pictures	8
Instruments & Methods	12
New instruments, user facilities & opportunities	14
Towards the European Spallation Source ESS	24
Improving service, infrastructure and components	26
Scientific Highlights	34
Quantum Phenomena	
Higgs transition in quantum spin ice $\text{Yb}_2\text{Ti}_2\text{O}_7$	36
Long-wavelength helimagnetic order and skyrmion lattice phase in Cu_2OSeO_3	38
Fluctuation-induced first-order phase transition in Dzyaloshinskii-Moriya helimagnets	40
Simultaneous uniform and non-uniform reversal of magnetization in exchange coupled systems	42
Instability of the magnetic order in the distorted triangular lattice antiferromagnet $\alpha\text{-CaCr}_2\text{O}_4$	44
Roton-Phonon interactions in superfluid ^4He	46
Bond randomness induced magnon decoherence in a spin-1/2 ladder compound	48
Depth profiles of LSMO/SRO films	50
Competition between crystal electrical field shift and Kondo screening in $\text{CeNi}_9\text{Ge}_{4-x}\text{Si}_x$	52
Direct manipulation of the uncompensated spins in an exchange coupled system	54
Soft Matter	
Proteins need it wet. Don't they ?	56
Structure and dynamics of the iron-binding protein Lactoferrin studied using neutron scattering	58
Thermal fluctuations of haemoglobin from different species	60
Changes in structure and dynamics of beta-casein protein during micellization process	62
Effect of confinement on the dynamics of polymer melts: interfaces and interphases	64
SANS study of the morphology of a novel polymer electrolyte membrane	66
Time-resolved SANS studies on the crystalline complexes of syndiotactic-polystyrene	68
Small angle neutron scattering studies on self-healing model polymers	70
Lipase-induced changes in fundamental surfactant monolayer properties	72
Depth-dependent morphology investigation of diblock copolymer films using TOF-GISANS	74
The influence of processing additives on the morphology of bulk heterojunction films	76
Polyelectrolyte brushes: Swelling in water and incorporation of nanoparticles	78
Influence of diffusion and dipping time on the inner structure of polyelectrolyte multilayers	80
Neutron reflectometry reveals an asymmetric distribution of anionic phospholipids on SiO_2	82

Structure Research

The neutron crystal structure of a perdeuterated enzyme inhibitor complex	84
Crystal and magnetic structure of multiferroic $\text{Ba}_2\text{CoGe}_2\text{O}_7$	86
A single-crystal neutron diffraction study of pezzottaite, $\text{Cs}(\text{Be}_2\text{Li})\text{Al}_2\text{Si}_6\text{O}_{18}$	88
Investigation of oxygen mobility in $\text{Ca}_{12}\text{Al}_{14}\text{O}_{33+\delta}$	90
The fundamental biomolecule guanidine through the eyes of single-crystal neutron diffraction	92
Antiferromagnetic domains in $\text{YBa}_2\text{Cu}_3\text{O}_{6.0}$ detected by neutron Larmor diffraction	94

Materials Science

Growth and characterization of large high quality brownmillerite $\text{CaFeO}_{2.5}$ single crystals	96
Spatial resolved phase analysis in sodium-metal chloride batteries	98
Channel ion distribution in $\text{A}_2\text{Ti}_6\text{O}_{13}$ determines effectiveness as anode for Li-ion batteries	100
Residual stresses in steel specimens induced by laser cladding and their effect on fatigue strength	102
Inducing compressive residual stresses in multi-pass welds using transformation plasticity	104
In-situ investigation of the phase transformation kinetics of Austempered Ductile Iron (ADI)	106
BH_4^- hindered rotations in $\beta\text{-Mg}(\text{BH}_4)_2$	108
In-situ studies of mass transport in liquid alloys by means of neutron radiography	110
PGAA analysis of the younger dryas impact event	112
Non-destructive elemental determination of kidney stones using PGAA	114

Neutron Methods

An experimental determination of the relative biological effectiveness of thermal neutrons	116
The antineutrino spectrum of the fission products of ^{238}U	118
Using PGAA in development of the Transmutation Detector method	120
Determination of the thermal neutron capture cross section of trans-uranium actinides	122

Reactor & Industry

124

Safe reactor operation in 2012 with 207 days of beam time for research and industrial applications	126
Progress in reactor conversion and fuel development	128
Manufacturing of cylindrical LEU Mo-99 targets by sputtering	130

Facts & Figures

132

Events 2012: Workshops, meetings, courses and open day	134
User Office: Growing together	140
Visitors' service and public relations: Between science and safety	142
Committees	144
Staff	150
Partner institutions	156
Imprint	158
Publications	159

Directors' Report

1





Directors' Report: Growing Cooperation

Research using neutrons makes essential and unique contributions to the major challenges facing our society. Yet again in 2012, there had been a large number of impressive scientific publications resulting from research conducted at our Forschungs-Neutronenquelle Heinz Maier-Leibnitz (FRM II). The highlights are presented in this Annual Report.

The cooperation between the Technische Universität München (TUM), Forschungszentrum Jülich (FZJ), Helmholtz-Zentrum Berlin (HZB) and Helmholtz-Zentrum Geesthacht (HZG), which began in 2011, was extended successfully in 2012. To merge the know-how and to further exploit synergies, joint scientific groups have been founded covering five important fields of neutron research: Materials Science, Soft Matter, Quantum Phenomena, Structure Research as well as Neutron Methods. However, due to financial constraints, HZB has withdrawn active support for the moment, but is still a silent partner. Therefore, the three axes spectrometer PANDA has been taken over by FZJ.

The competence and experience of the cooperation is reflected in particular in the development of new and innovative neutron instruments and techniques: The small angle neutron scattering instrument SANS-1 had neutrons on the detector for the first time in 2012. Being a joint venture between TUM and HZG, SANS-1 will complement the already operating set of small angle cameras KWS-1 to -3 and aims to be one of the most intense and versatile instruments worldwide in its field. It is optimized for investigations on materials science and magnetism covering basic research and industrial applications.

The newly inaugurated polarized reflectometer MARIA (FZJ) focuses on magnetism and is dedicated to the investigation of thin layers, interfaces and nano-structured samples. The latter case is particularly interesting because here the spin diffusion length of electrons in metals and oxides is on the same length scale, to be probed with

a reflectometer for the first time. We expect to observe new effects such as non-collinear magnetism at the surface, different orderings at the surface and perhaps even some new physics. Major progress can also be reported from the new neutron guide hall east: The new multi anvil press SAPHiR of the Bayerisches Geoinstitut, University of Bayreuth, was delivered and put into operation. SAPHiR is expected to realize pressures up to 25 GPa with sample temperatures of 2000 °C. Thus, it allows the study of matter under the extreme condition of the transition zone between the upper and lower earth mantle.

Furthermore, great steps towards the implementation of high precision experiments with ultra-cold neutrons have been made: An ambient magnetic field compensation coil system and a passive metal shield were built and commissioned at the beam position, achieving the world's lowest residual magnetic field. Gratifyingly, in the Excellence Initiative's 2nd Round in 2012, the excellence cluster "Structure and Origin of the Universe" is to be continued until 2017.

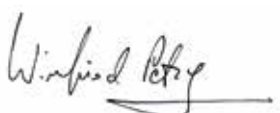
We shall not disguise the fact that, due to the ¹⁴C-issue, we were not able to provide our users with a full schedule of four reactor cycles in 2012. Also, there was a longer maintenance break at neutron guides 5 and 6. Therefore, some users were not able to perform experiments at the instruments SPHERES, RESEDA, MARIA, MIRA and DNS.

In 2013, the scientific cooperation will enter a new era: It is going to operate under the new name Heinz Maier-Leibnitz Zentrum (MLZ), emphasizing that the scientific use of the FRM II constitutes a national cooperative research centre financed by the Federal Ministry of Education and Research and the Bavarian State.

We look forward to a full schedule of four reactor cycles and to exciting new scientific findings in 2013.



Klaus Seebach



Winfried Petry



Dieter Richter



Anton Kastenmüller

The year in pictures



January 11th

Colleagues from the reactor division of the high-flux neutron source Institute Laue-Langevin in Grenoble visit their sister institute in Garching.



March 21st

Christopher Berkel's „journeyman's piece“, a testing machine for a laboratory in Canada, being prepared for shipping overseas.



March 23rd

More than 100 users get together at the 4th User Meeting, jointly organized by FRM II and JCNS.



April 18th

The Garching city council and the office manager of mayoress Hannelore Gabor, Hans-Martin Weichbrodt, are informed about changes and new plans at the FRM II by Prof. Dr. Winfried Petry, Dr. Anton Kastenmüller and Dr. Klaus Seebach.

May 4th

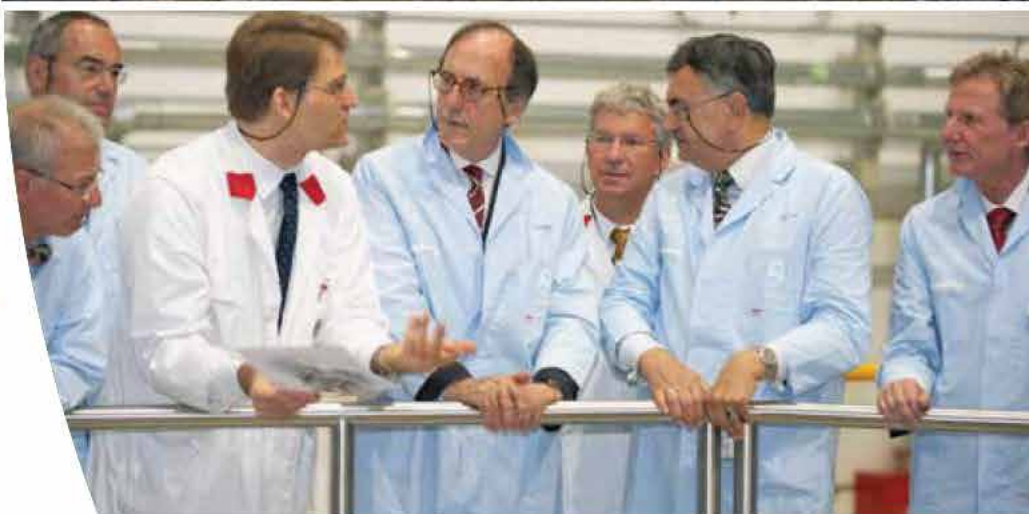
The Scientific Advisory Board chaired by Prof. Dr. Peter Fratzl, Director of the Max-Planck-Institute for Colloids and Interfaces, gets together for its first meeting.

**June 27th**

Work begins on the foundations for the connecting building between the experimental hall and the future neutron guide hall east.

**July 7th**

At the invitation of Dr. Adalbert Weiß of the Bavarian State Ministry of Sciences, Research and the Arts, Dr. Karl Eugen Huthmacher of the Federal Ministry of Education and Research (BMBF) pays an informative visit to the FRM II.

**July 18th**

70 kilograms of roast, quite a quantity of beer and a lot of sunshine play a crucial role at this year's summer party for the staff.



The year in pictures



July 31st

On the last day of the school year, Friederike Rust from the Otto von Taube-Gymnasium in Gauting is busy at TOFTOF preparing her research for the W-seminar.



September 15th-16th

The FRM II attracts a lot of people at the trade show „Garchinger Herbsttage“. The new throwing game for children also found favor with a lot of grown-ups, including the mayoress of Garching, Hannelore Gabor (left).



September 12th

Students at the 16th JCNS Laboratory Course on Neutron Scattering concentrate hard during their training at the MLZ.



October 23rd

Very early in the morning, an escorted heavy vehicle delivers the long-awaited passive shield for the new instrument to measure the electric dipole moment of the neutron, a new experiment being set up in the neutron guide hall east.

October 27th

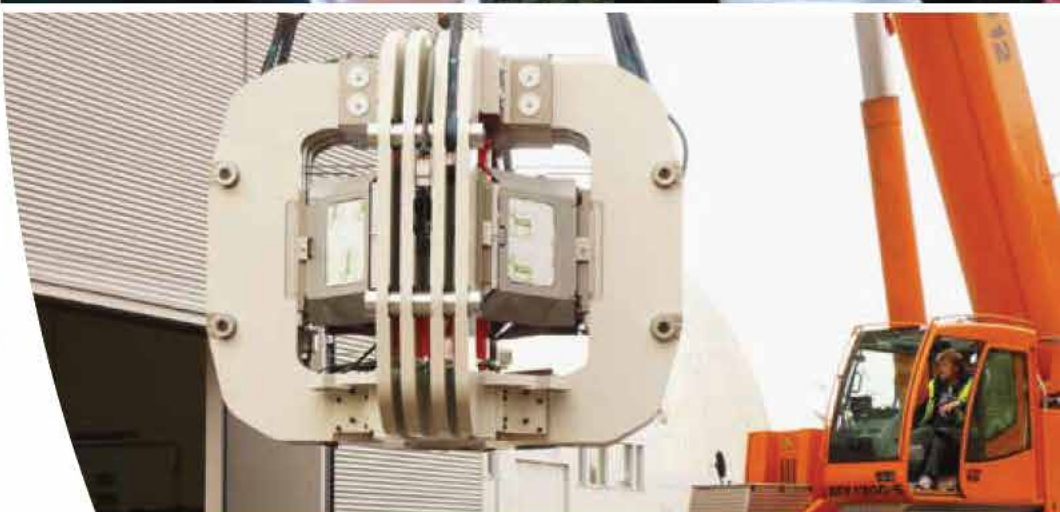
On the open day of the Technische Universität München in Garching, almost 500 people queue at the registration desk for guided tours to take the opportunity to have a look at the interior of the Forschungs-Neutronenquelle Heinz Maier-Leibnitz and to learn more about the research of the scientists.

**November 8th**

At the „Hochschulkontaktmesse (HOKO)“ at the Munich University of Applied Sciences, many students show great interest in the numerous offers for traineeships, Bachelor, Master or PhD degrees at the FRM II.

**November 13th**

The new multi anvil press of the Bayerisches Geoinstitut, University of Bayreuth, at 50 tons a device as heavy as a truck, is delivered and put into operation in the neutron guide hall east.

**November 27th**

Members of the CSU state parliamentary group visit the reactor: Dr. Guido Klinger, Dr. Thomas Zimmermann and Oliver Jörg (from left) as well as the former Bavarian Minister of Sciences, Research and the Arts, Dr. Thomas Goppel (2nd from right).



Instruments & Methods

The large analyser bank of the SPHERES backscattering spectrometer.

2



New instruments, user facilities & opportunities

M.-S. Appavou¹, P. Fierlinger², A. Feoktystov¹, W. Gan³, R. Georgii⁴, W. Häußler⁴, A. Heinemann³, O. Holderer¹, Ch. Hugenschmidt⁴, V. Hutani^{1,5}, P. Link⁴, W. Lohstroh⁴, A. Ostermann⁴, S. Pütter¹, A. Radulescu¹, B. Schillinger⁴, A. Schneidewind¹, G. Simeoni⁴, N. Walte⁶

¹Forschungszentrum Jülich GmbH, Jülich Centre for Neutron Science at MLZ, Garching, Germany

²Technische Universität München, Exzellenzcluster „Origin and Structure of the Universe“, Garching, Germany

³Helmholtz-Zentrum Geesthacht GmbH, GEMS at MLZ, Garching, Germany

⁴Technische Universität München, Forschungs-Neutronenquelle Heinz Maier-Leibnitz (FRM II), Garching, Germany

⁵RWTH Aachen, Institut für Kristallographie, Aachen, Germany

⁶Universität Bayreuth, Bayerisches Geoinstitut, Bayreuth, Germany

The first instruments arrived at the new Neutron Guide Hall East. This initial step towards extending the capacity of the MLZ is accompanied by the rebuilding of instruments and sources, the upgrading of existing instruments and the commissioning of completely new ones. Be it a boost in the performance or the provision of smaller improvements, the user will profit from a large number of excellent new opportunities. Furthermore, complementary techniques, including the transmission electron microscope (TEM) or the molecular beam epitaxy (MPE) thin film deposition system, are made available to the user in order to support neutron research.

The new ANTARES station

To provide a cold neutron beam, the beam position for the future guide hall east, the radiography station ANTARES was moved from SR4b to SR4a. A lot of effort was invested in order to provide the excellent measurement conditions at the completely rebuilt ANTARES station once more. Furthermore, ANTARES benefits from the new location since more space along the neutron flight path allows for the installation of a number of new beam devices.

The new ANTARES consists of three separate chambers, shown in figure 1. The first chamber provides space for beam forming devices such as a fast shutter, the previously installed double crystal monochromator and crystal filters (Sapphire, Beryllium), as well as for the new velocity selector and two neutron optical periscopes. Both periscopes reflect the beam via 2 supermirrors in order to break the direct line of sight, stopping fast neutrons and gamma radiation

at the sample position. One of the periscopes consists of polarizing mirrors with a combined polarization efficiency of more than 99 %. Both periscopes can be rotated by 90 degrees, providing either a narrow, but high beam for samples in cryostats, or a wide, but lower beam for tomography.

The consecutive space is divided into two separate experimental chambers. Chamber 3, further away from the neutron source, provides almost identical conditions to the original ANTARES. Chamber 2 is closer to the reactor and provides a smaller beam with higher intensity and even lower background, since the main source of background, the beam catcher, is situated in chamber 3.

The new location at SR4a also allowed for the installation of a rotary drum selector for six collimators (instead of the former two), ranging from $L/D = 200$ to $L/D = 7100$ in chamber 3, and about half the values in chamber 2. Here, with $L/D = 100$ in the first experimental chamber, the expected maximum flux will be of the order of $1.6 \cdot 10^9 \text{ n/cm}^2\text{s}$, i.e. 16 times the flux of the old ANTARES at $L/D = 400$. This high intensity will make it possible to observe fast transient processes using high-speed radiography. ANTARES will restart operation in 2013.

Renewal of the positron source NEPOMUC

Until 2010, NEPOMUC was operated successfully with an intensity of about 10^9 moderated positrons per second. The lifetime of this first positron source, which used a converter of natural Cd with a thickness of 3 mm, was limited by the burn-up of ^{113}Cd after 1250 days of reactor operation at the nominal power of 20 MW. For

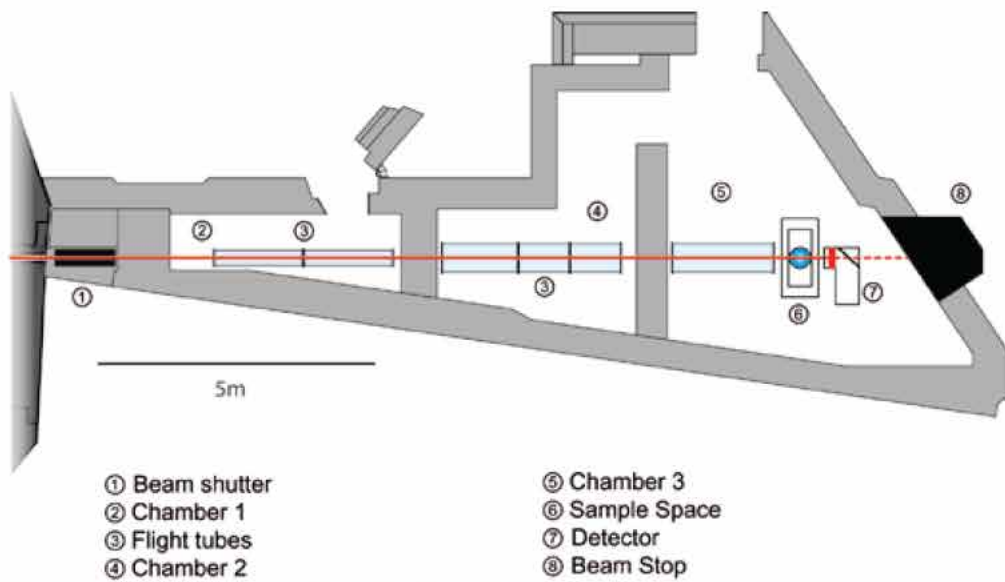


Figure 1: Outline of ANTARES. The new location allows for additional experimental space along the beam.

this reason, the inclined beam tube SR11 has been replaced. At the FRM II, the SR11 was the first beam tube to be completely dismantled, including all inner parts of the in-pile positron source (fig. 2). The main task for the new positron source NEPOMUC upgrade was a considerable extension in the operating time to 25 years. In order to enhance the intensity and the beam brightness, additional improvements have been made to the design of the source components.

To extend the operating time, Cd enriched with 80 % ^{113}Cd , i.e. 6.5 times greater amount of ^{113}Cd than in natural Cd, has now been used. The absorption of high energy -quanta in the Pt front section through additional small vanes and in the electrical lenses contribute to the positron production. For the formation of a beam with high brightness, only moderated positrons from the Pt front plate with low transverse momentum are collected. A higher total moderation efficiency is expected due to the improved geometry and (inelastic) scattering of positrons from the Pt lenses onto the front moderation foil.

In 2012, the operational reliability of SR11 was confirmed and the primary positron beam was successfully guided to the outside of the reactor pool. In a first test, the shape and the intensity of the positron beam were determined at a beam energy of 540 eV in a magnetic guide field

of 5 mT. The beam diameter amounts to about 10 mm and the intensity was determined to $> 10^9$ moderated positrons per second (preliminary). Hence, NEPOMUC delivers the world highest intensity of monoenergetic positrons.

The rebuilt NEPOMUC enables the continuation of a large variety of positron beam experiments and the development of new experimental setups. The experiments range from fundamental studies in atomic and plasma physics, through highly sensitive and elemental selective investigations in surface and solid state physics to applications in materials science.

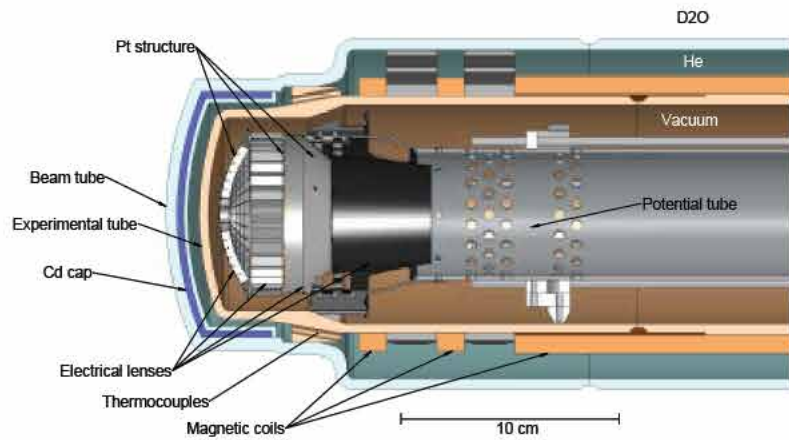


Figure 2: Cross sectional view of the new in-pile positron source.



Figure 3: Biological shielding of POLI installed at beam tube SR9a.

POLI grows up

An important milestone on the way to an independent operation of the diffractometers HEiDi (single crystal) and POLI (polarized) at beam tube SR9 (hot source) has been achieved. The new monochromator shielding for POLI was installed. Figure 3 shows the biological shielding mounted in the experimental hall at SR9a (blue-orange) between instruments HEiDi at SR9b (green-orange) and RESI (rose-red). At the new beam line using optimised Cu 220 and Si 311 monochromators, POLI will offer thermal neutrons $2\Theta_M = 41^\circ$ with wavelengths 0.89 Å and 1.15 Å; and hot neutrons $2\Theta_M = 25^\circ$ with wavelengths 0.55 Å and 0.7 Å.

A new digital NMR spectrometer has been built for independent in-situ monitoring of the ^3He polarisation of the polariser and analyser spin filter cells. The setup decreases the errors of the time dependent polarisation corrections and thus improves the quality of the polarimetry data.

In cooperation with the Sample Environment Group, an optimised setup for the investigation of the magnetoelectric domains in multiferroic materials has been realised and successfully tested in two user experiments. Using a new high voltage sample stick in combination with precise pressure control in the sample tube of a CCR cryostat, it is now possible to apply electric fields up to 10 kV with full temperature control at the sample down to 4 K inside the CRYOPAD.

Three axes option of MIRA

MIRA has recently been upgraded for three axes

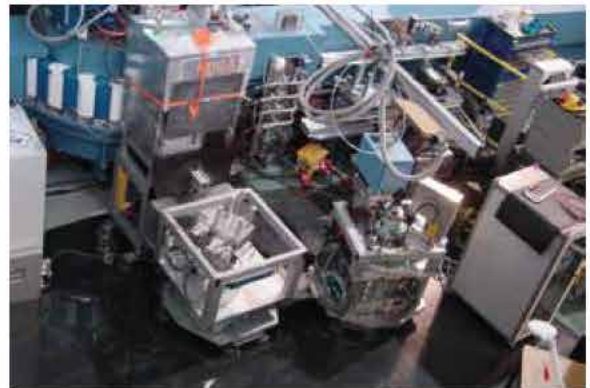


Figure 4: First measurement with the MIRA three axes mode.

measurements using cold neutrons (fig. 4). This opens the possibility of studying the dynamics of large scale structures with excellent \mathbf{q} resolution. The main emphasis was placed on the use of small samples, for instance in pressure cells. Therefore, the existing elliptical focussing guides were included in this development. Furthermore, an Eulerian cradle can be operated in three axes mode, which makes inelastic measurements in arbitrary scattering planes possible.

The instrument control software was adopted from the existing three axis machines PANDA and PUMA and is now consistent between all three instruments. This makes it easy for users to switch between several instruments at the MLZ. Additional software visualizing the accessible reciprocal space and plotting the instrument resolution function at different instrument setups

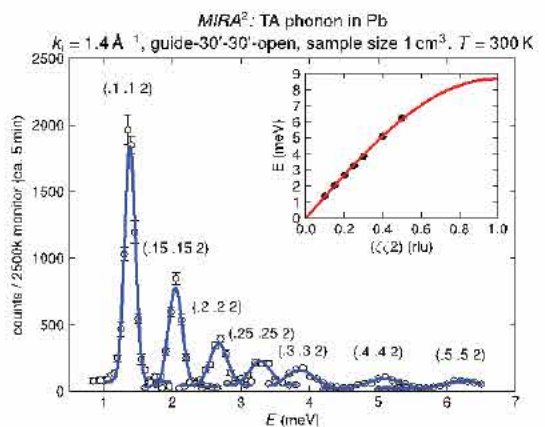


Figure 5: Phonons in lead measured with the MIRA three axes option. Two 30-minute collimators were used before and after the sample. The inset shows the acoustic phonon branch in lead extracted from the constant k_i scans.

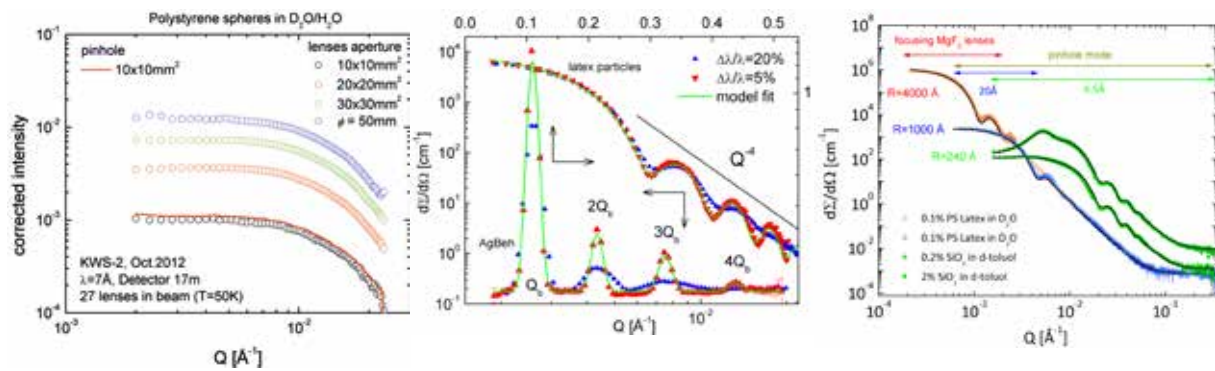


Figure 6: a) An intensity gain up to 11 times on the sample compared to the conventional pinhole mode when focusing lenses are used, keeping the resolution. b) Measurements at KWS-2 with variable resolution on polystyrene latex particles (samples – courtesy of M.Hellsing and A.Rennie, Uppsala University) and silver behenate; the green lines indicate the fit, including instrumental resolution. c) Scattering patterns from silica and polystyrene particles in solution measured in the pinhole and high-resolution (focusing lenses) modes. The fits include the form factor and the structure factor of the particles and the instrumental resolution.

for better measurement planning has also been developed and can be used in parallel with the instrument control software.

A first test, and simultaneously a benchmark, for the MIRA three axes option was performed with a 1 cm³ lead sample. The result is shown in figure 5 and demonstrates the excellent performance of the three axes option of MIRA. Using the focusing guides on a small sample will further improve the peak to background ratio, thereby allowing for inelastic measurements with high intensity in pressure cells or on small samples.

Lenses, chopper and a new detector: boosting performance at KWS-2

KWS-2 was the subject of a major upgrade aimed at boosting its performance with respect to the three most important parameters of a small angle scattering instrument: intensity on the sample, Q-range and resolution. Thus, the instrument was equipped with focusing elements (MgF₂ parabolic lenses), a double-disc chopper with variable slit opening and a high-resolution position-sensitive detector (0.45 mm). Besides the conventional pinhole measurement mode, the following setups were tested and optimized throughout the year 2012 in order to have the instrument up and running in 2013 and increase their flexibility and versatility:

- the high-intensity mode with lenses – an intensity gain of up to 11 times (fig. 6a) as

compared to the conventional pinhole mode for the same resolution can be achieved by increasing the sample size (up to 5 cm in diameter);

- the tuning of the resolution $\Delta\lambda/\lambda$ between 2 % and 20 % will allow for an improved characterization of the scattering features within different Q ranges (fig. 6b) using the chopper and the time-of-flight method;
- the high-resolution/extended Q-range mode down to $1 \cdot 10^{-4}$ Å⁻¹ by means of the lenses (fig. 6c), used in combination with the chopper to narrow the $\Delta\lambda/\lambda$ and minimize the chromatic aberrations and gravity effects and the high resolution detector, will enable exploration of sizes over a continuous length scale from 1 nm to 1 micron.

Extended scientific opportunities at RESEDA

A pilot neutron Larmor diffraction experiment



Figure 7: Exterior view of a new radiofrequency spin flipper at RESEDA.

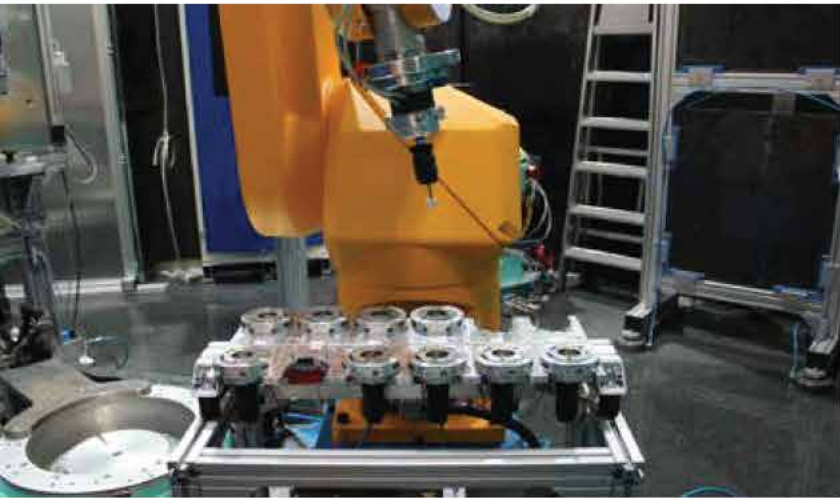


Figure 8: STRESS-SPEC robot taking a sample from the sample changer magazine.

has been conducted at the resonant spin echo spectrometer RESEDA. A prerequisite was the installation of a pair of newly designed B_0 coils providing large beam windows, which are rotatable with respect to the beam optical axis up to an angle of 60° (fig. 7). A complementary addition, a small-angle option has been developed which involves evacuated flight tubes and exploits in an optimal way the large sample-to-detector distance of about 4 meters. This opens up a new avenue in respect of polarized SANS measurements at RESEDA.

In order to achieve shorter neutron wavelengths down to 3 Å and/or narrower incoming spectrum bandwidths, the neutron velocity selector has been mounted on a tilt stage inside a new lead shielding. This extends the capabilities of the instrument towards new applications, such as high-resolution Lamor diffraction.

Robot changes samples at STRESS-SPEC

Since the installation of the robot system at STRESS-SPEC (see annual report 2010), all texture analysis and some strain measurements on complex sample shapes have been performed exclusively with this new equipment. In order to improve the efficient usage of beam time, the robot has been extended to be used also as an automatic sample changer (fig. 8). This development now allows serial measurements with up to 12 different samples in one setup and is mainly

intended to be used for texture analysis. Besides having the advantage of making it possible to perform a series of measurements, the sample changer will also save about 30 minutes when compared to changing the samples manually, as no additional alignment procedures are necessary.

New cryostream system at BIODIFF

During the last reactor cycle in 2012, a new Oxford CryoSystem cryostream 700+ system was commissioned and successfully integrated into the infrastructure of the instrument BIODIFF (fig. 9). This open flow gaseous nitrogen cooler system for crystallography is widely used in the protein crystallography community and makes it possible to cool the sample crystal down to 90 K (full temperature range: 90 – 500 K). In addition to the conventional cryostream set-up, it was necessary to add a moveable thin cylindrical aluminium foil shielding around the sample position.



Figure 9: The new cryostream system of the single crystal diffractometer BIODIFF.

This shields the cold nitrogen gas stream from turbulences originated by the detector drum rotation during the readout process of the image plate detector. This shielding efficiently avoids ice formation on the sample. A complete dataset



Figure 10: The passive shield with a very small magnetic field inside.

of a β -lactamase crystal was already successfully measured at 100 K within 10 days without any ice formation.

A cage for neutrons - the new measurement of the electric dipole moment

The discovery of a neutron electric dipole moment (nEDM) would provide an unambiguous indication of time reversal violation in a fundamental system, a necessary ingredient for the explanation of the matter anti-matter asymmetry in the Universe. Current experimental limitations on the nEDM are roughly six orders of magnitude above the Standard Model (SM) prediction and, therefore, searches for the nEDM provide powerful tests of physics beyond the SM, most of them expected to show a non-zero result within the next two orders of magnitude improvement.

As part of the laboratory for ultra-cold neutron physics, we are currently implementing a new experimental installation at the neutron guide hall east at the MLZ with the aim of improving this limit up to two orders of magnitude. The project is realized within the framework of an international collaboration based at the FRM II. Conceptually, the experiment is based on a clock-comparison of neutrons and various magnetometers. The main improvements are expected from (i) an increased density of ultra-cold neutrons in the apparatus and (ii) improved control of systematic effects. Systematic effects mainly stem from distortions and fluctuations in magnetic fields from the surroundings, any components of the apparatus, the magnetic field measurement methods



Figure 11: EDM field cage and non-magnetic beam position in the Neutron Guide Hall East.

and from electric field issues that effectively contribute to magnetic fields.

Major steps towards the implementation of the apparatus were achieved in 2012: (i) a beam position with non-magnetic concrete was realized to decouple the performance of the instrument from neighbouring installations in the same building; (ii) an ambient magnetic field compensation coil system with 180 magnetometers and 24 correction coils for static and active distortions of the magnetic field was built and commissioned (fig. 10); (iii) a passive μ -metal shield with a 2×2 m access door was built and commissioned. Here, the lowest residual magnetic field in the world over 1 m^3 has been achieved, with a fraction of 1 nT absolute (fig. 11); (iv) a glass-fiber based vacuum chamber has been built with residual magnetism of $< 20 \text{ pT}$ in 2.5 cm distance from the surfaces; (v) a fully optical Cs vapor magnetometer with 40 fT sensitivity has been commissioned as the prototype for an array of magnetometer cells in the experiment, which operates in addition to polarized ^{199}Hg magnetometer cells inside the EDM apparatus. Integration of all major hardware components at the beam position is scheduled for 2013.

SAPHiR – the new multi-anvil press installed in the neutron guide hall east

A milestone for the instrumentation of the neutron guide hall east was achieved in November. The centrepiece of the instrument SAPHiR (Six Anvil Press for High pressure Radiography) had been delivered and installed inside the prepared



Figure 12: The multi-anvil press of the instrument SAPHiR in the Neutron Guide Hall East.

pit (fig. 12). This press is dedicated to time-of-flight neutron diffraction studies and high resolution neutron radiography at extreme pressure and temperature comparable to conditions at the earth's mantle. The multianvil press has six independently controlled rams that have a combined pressing force of up to 23.5 MN (2400 tons). The force is transferred and focussed through a set of smaller secondary anvils to a cubic assembly that includes the sample and an internal heating furnace. With this 6-6 anvil geometry, it is possible to subject a large volume of crystalline solid material or melt to pressure conditions of at least 15 GPa (150 kbar) and temperatures above 2000 K to carry out neutron scattering and ra-



Figure 13: The team of PANDA in front of the instrument.

digraphy measurements. Ultimately, the press will reach 25 GPa. In addition to maintaining extreme conditions hydrostatically for extended periods of time, arbitrary anvil pairs can be pushed into or retracted from the sample assembly to achieve controlled deformation with varying strain rates of 10^{-2} to 10^{-6} s^{-1} .

Upgrading PANDA

As part of the upgrade, the monochromator unit was refurbished and improved, the reliability of the focusing in particular was increased and the monochromator table was exchanged to allow the use of a Si-monochromator. It is now possible to exchange the monochromators automatically. In addition, several hardware components were standardized. The instrument control software (the upcoming standard at MLZ – NICOS 2 – see also <http://trac.frm2.tum.de/projects/NICOS>) was upgraded to match the needs of the instrument control and those users performing experiments. Resolution calculation, electronic logbook and special requests of the users are also catered for.

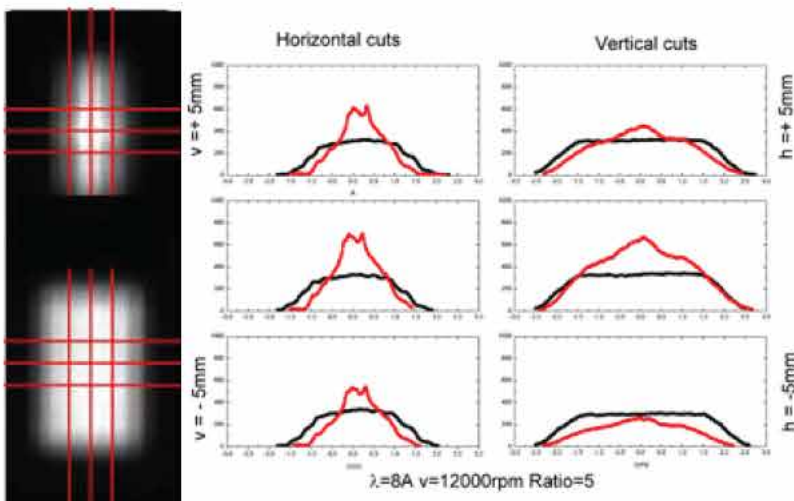


Figure 14: Left: Beam cross section, at $\lambda = 8 \text{ \AA}$, measured with a detector at the sample position - focusing guide (top) vs. linear guide (bottom); Right: Horizontal and vertical beam profile. Horizontal and vertical cuts taken at the centre of the beam and around 1 cm^2 area centred around it - focusing guide (red) vs. linear guide (black).

Within the TUM – HGF cooperation, Helmholtz-Zentrum Berlin pauses its contribution

and PANDA has been operated by JCNS since 1st January 2012. We acknowledge the hospitality and support of HZB during the last years of PANDA operation, especially the Joint Research Group TU Dresden - HZB, the Department Quantum Phenomena in Novel Materials and the Sample Environment Group.

TOFTOF – Neutron spectroscopy under extreme conditions

The direct geometry cold time of flight spectrometer TOFTOF had a general overhaul of its data acquisition systems. The instrument control software was upgraded to the new NICOS and TACO device drivers are used to connect to standard sample environments. The standard CCR cryostat was upgraded, resulting in considerably reduced cooling times down to base temperature.

Great effort has been invested in the technological development for the investigation of small samples under extreme conditions.

The prototype of a focusing neutron guide, developed and produced completely in-house at the FRM II, has recently been installed at the instrument and is already routinely in operation.

It represents the first device in the world to combine cutting-edge supermirror technology with Adaptive Neutron Optics, suitable for Neutron Spectroscopy with a thermal-cold white neutron beam. It is able to squeeze the beam cross section down to less than a squared centimeter (see figure 14). This determines a considerable intensity gain factor for cold neutrons, whereas it significantly reduces the background from the surrounding sample environment for thermal neutrons. This translates into a more than doubling of the signal-to-background ratio. Moreover, the reduced sample size improves the scattering efficiency at high scattering angles.

A lot of progress has also been made in the development of the high-pressure equipment. The TOFTOF sample environment now includes: 1) hydraulic cells for liquid samples up to 3.3 kbar (operated in collaboration with JCNS partners);

2) gas cells for gaseous samples up to 1.5 kbar and compatible with standard cryostats, 3) gas and hydraulic cells for large-volume samples (4 cm³) up to 4 kbar, compatible with standard cryostats.

Larger correction coils at J-NSE

The limiting factors for the use of longer Fourier times are the count rate on the detector and the ability to correct for field inhomogeneities. Both have been improved with the continuation of the development of correction elements. Larger correction coils, which increase the detected solid angle of the scattered neutrons and hence the detector count rate, have been installed (fig. 15). Now, Fourier times up to 200 ns are provided for user experiments to address scientific questions ranging from classical polymer dynamics, polymers with new architecture such as ring polymers, the effects of soft and hard confinement through to microemulsions and microgels and biology (dynamics of proteins and protein aggregates). The spin glass dynamics of small clusters was an example of hard matter experiments at the J-NSE.

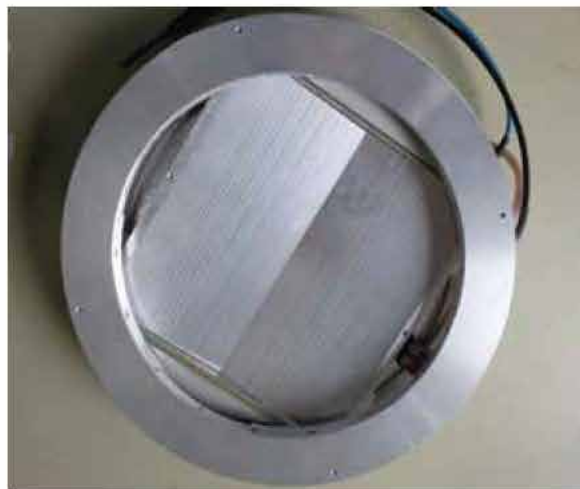


Figure 15: One of the new larger correction coils for the J-NSE spectrometer.

The demand of the users for the new interface sensitive technique of grazing incidence NSE is continuously increasing. Several experiments on the interface dynamics of microemulsions, microgels, polyelectrolytes and phospholipid layers have been carried out.



Figure 16: The compensated, vertical 5 Tesla cryomagnet with the new hexapod at KWS-1.

New Hexapod for heavy weights at KWS-1

Samples under investigation at the small angle scattering instrument KWS-1 are usually very light in weight. However, these samples often need to be measured under special conditions using additional sample environment equipment. More specifically, every time high magnetic fields

come into play, the weight around the sample increases considerably. To use the new 350 kg 5 Tesla cryomagnet at the KWS-1, a new hexapod was installed (fig. 16). A special adapter was constructed to hold the magnet and to make use of the full adjustment options in the neutron beam. Now, it is possible to control the setup in different directions with a precision of reproducibility as high as 10 µm. Installation and commissioning included fitting it into the instrument control software and controlling it remotely. A user friendly graphical interface provides easy to use access to all options.

SANS-1 commissioned and in operation

The SANS-1 instrument, a joint project between HZG and FRM II, is now fully operational and available for user experiments. The very flexible collimation systems allow experimental setups optimized for both high flux and high resolution experiments. The lateral movable detector combined with interchangeable beam-stops allows the full Q-range to be covered with only two sample-detector distances. This significantly shortens the necessary measuring time for a large number of sample types and increases the throughput of experiments at the instrument. A wide range of additional experimental equipment including a compensated, horizontal 5 Tesla dry magnet is already available. Together with a polarization option based on two optimized polarizers and an adiabatic spin flipper, a wide range of magnetic SANS experiments can be performed. Many other sample environments such as cryostats and furnaces were successfully commissioned. The next step in providing state-of-the-art SANS options is the installation of the TISANE mode in 2014. Additionally, and together with this option, we will install a second velocity selector for very high resolution experiments. This will be accompanied by the installation of a second high resolution detector in the detector vessel.

New user facility: MBE system

Within the framework of a thin film laboratory, a state-of-the-art Molecular Beam Epitaxy (MBE)



Figure 17: Top view into the sample chamber at SANS-1.

system is operated to prepare tailored samples for investigation using neutron reflectometry such as MARIA or other neutron scattering instruments. MBE is a fascinating method for depositing high quality epitaxial thin films (fig. 18). Epitaxy means the deposition of a crystalline layer on a crystalline substrate in which the crystal structure of the substrate is reproduced onto the film. In this way, new materials can be fabricated which might reveal unexpected properties, such as ferromagnetism at the interface between two antiferromagnetic layers or conductivity between two insulating layers.

Within the MBE system, a molecular beam is established either by thermal heating of the material in a crucible (effusion cell) or by heating the material by electron bombardment (e-gun). Currently, there are two e-guns, each with four crucibles and six effusion cells, i.e. up to eight different materials can be evaporated simultaneously. Oxides can be grown by using the oxygen plasma source. Typically available elements include Ag, Al, Au, Co, Cr, Cu, Fe, La, Mn, Nb, Sr, and Ti. Film analysis by RHEED, LEED and

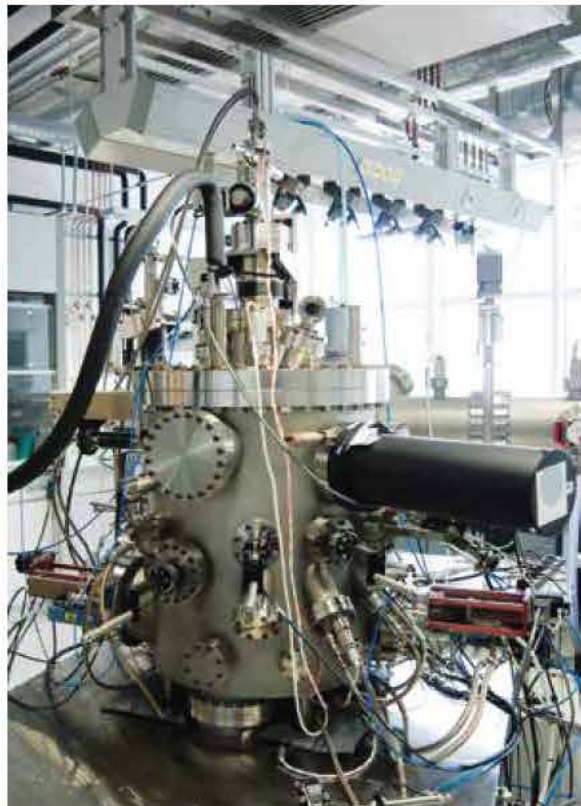


Figure 18: JCNS operates a state-of-the-art oxide Molecular Beam Epitaxy (MBE) system.

AES is integrated into the system. An additional sample characterization method in the laboratory, Atomic Force Microscopy (AFM), is available. MLZ users are invited to make use of this well-equipped laboratory.



Figure 19: Transmission electron microscopy available to users of the MLZ.

New user facility: TEM

A new 200 kV Energy Filter Cryo-transmission electron microscope (Cryo-EFTEM) has been installed at the MLZ (fig. 19). TEM is a complementary technique to neutron scattering in the frame of soft matter studies. With the TEM, real space investigations are performed to access information regarding the shape, size and size distribution of particles, self-assembly and aggregation in nanometer scale. Cryo-specimen investigation at low temperature around -180 °C and under vacuum is offered to meet the requirements of the soft matter community. Users will be supported by on-site scientists to make suitable preparations and conduct TEM investigations.

Towards the European Spallation Source ESS

W. Lohstroh¹, G. Brandl¹, R. Georgii¹, W. Häußler¹, B. Schillinger¹, M. Schulz¹, L. Silvi¹, G.G. Simeoni¹, I. Stefanescu¹, K. Zeitelhack¹

¹Technische Universität München, Forschungs-Neutronenquelle Heinz Maier-Leibnitz (FRM II), Garching, Germany

The first neutrons from the European Spallation Source (ESS) to be built in Lund, Sweden, are foreseen for the year 2019. The Design Update Phase of the project is almost complete and with the finalization of the Technical Design Report (TDR) in February 2013, ESS is ready to enter its next stage in preparation for construction. As part of the German contribution to the Design Update Phase of the ESS, the Helmholtz centres in Jülich (FZJ), Berlin (HZB) and Geesthacht (HZG) and FRM II are developing novel instrumentation concepts that make optimum use of the high brilliance and the long pulse structure of the future ESS.

At FRM II, concepts for a cold direct geometry time-of-flight spectrometer, an imaging beam-line and a neutron resonant spin-echo (NRSE/MIEZE) spectrometer are being pursued. Moreover, two projects are dedicated to the critical development of fast rotating chopper disks and new gaseous detectors with solid ¹⁰Boron converters.

The high brilliance of the neutron beams at the ESS together with its unique long pulse structure is well suited to a versatile, direct time-of-flight spectrometer with medium to high energy resolution, such as is currently available at the FRM II. With a broad base of scientific applications ranging from magnetism to soft condensed matter and biology, such an instrument will be especially beneficial for small sample volumes or time resolved measurements. With a sample position at 115 m from the source, the natural wavelength band will be 2.4 Å and operation of the chopper system in Rate Repetition Mode (RRM) allows simultaneous monitoring of a wide area of the $S(q,\omega)$ space.

Innovative techniques for more contrast

Materials characterization via neutron imaging reached a new level of application with the development of innovative techniques using more advanced contrast mechanisms than simply the attenuation of the beam. At the ESS, these advanced techniques can be realized in a flexible instrument with adjustable wavelength resolution, as designed by a team at the FRM II together with partners from HZB, Paul Scherrer Institute (PSI) and ESS. The chopper concept relies on optical blind choppers for the adjustment of the wavelength resolution while the implementation of the Wavelength Frame Multiplication (WFM) makes full use of the unique time structure of the neutron beam.

Based on previous work on the resolution function of a MISANS (MIEZE for a SANS instrument), an instrument concept combining MISANS, MIEZE II and NRSE is being proposed for the ESS. The advantages are more equal path lengths for extended samples and usage of the complete direct



Figure 1: Vision of the future ESS in Lund, Sweden.

beam, thus obtaining higher usable fluxes. Such an instrument would allow for measurements in a magnetic field with the high-energy resolution of a NSE instrument, or on depolarizing samples, which is not easily achieved in a NSE instrument. A workshop in connection with the international conference on Polarised Neutrons in Condensed Matter Investigation (PNCMI) in Paris was organized to promote the instrument in the user community (fig. 2).

In all likelihood, ^3He gas detectors will be unavailable to cover large areas of detection at instruments of the ESS and therefore suitable alternatives are urgently needed. Detectors with solid ^{10}B -converters are one promising alternative for such large area devices. One major obstacle is the low efficiency of the single boron layer and typically 20 to 30 converter layers will be needed for a working device.



Figure 2: Participants of the “MIEZE” satellite meeting in July 2012 in Paris.

More efficient detectors

At the detector group of the FRM II, microstructured $^{10}\text{B}_4\text{C}$ layers are being investigated. Various pitch angles and depth profiles of grooved substrates have been investigated experimentally and in GEANT4 simulation. In this way, it has been possible to increase the efficiency of the single layer significantly, as compared to a flat film in comparable detectors (fig. 3).

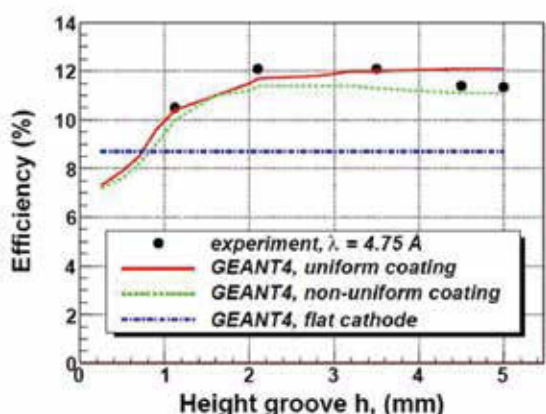
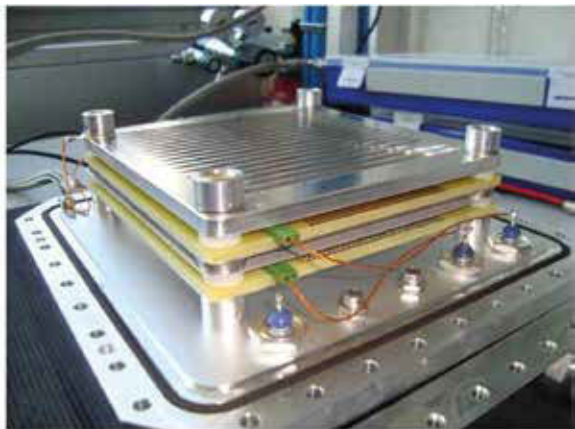


Figure 3: Upper panel: prototype detector using grooved ^{10}B -converter layers, lower panel: efficiency increase of the grooved single layers compared to a flat coating.

With the ESS being a pulsed source, all instruments will rely on a series of choppers with various functionalities. Together with the Institute of Light Weight Structures at the TUM, the FRM II investigates the possibilities of carbon fibre reinforced plastic chopper disks to operate at very high rotation speeds. Today's direct time-of-flight chopper spectrometers operate with max 22 000 rpm rotation speed at the instrument TOFTOF at the MLZ. Bi-spectral chopper spectrometers in particular will benefit from faster rotation due to the better energy resolution in the thermal neutron energy range. Based on finite element calculations, prototype discs are being designed and built and will eventually be tested up to failure to verify the ultimate performance.

To summarize, things are progressing fast and we are looking forward to the future ESS.

Improving service, infrastructure and components

P. Link¹, S. Masalovich¹, K. Zeitelhack¹, J. Peters¹, J. Pulz¹, H. Wenninger¹, J. Krüger¹, J. Wuttke², H. Reithmeier¹

¹Technische Universität München, Forschungs-Neutronenquelle Heinz Maier-Leibnitz (FRM II), Garching, Germany

²Forschungszentrum Jülich GmbH, Jülich Centre for Neutron Science at MLZ, Garching, Germany

Reorganization and extending support for the instrument groups was one of the major challenges of 2012. A new group for technical infrastructure has been established. Their work deals with large projects in civil engineering, from the connection of the new neutron guide hall east and its technical infrastructure up to the engineering of neutron shielding for guide systems and instrument components. The IT-software group has been split into three separate groups to better focus on their objectives. Besides these organisational issues, a wide range of technical developments and building of new components has been achieved by the service groups for neutron optics, sample environment, detectors, and scientific computing.

Neutron guide elements exchanged

During 2012, the instruments in the neutron guide hall west had to overcome a number of drawbacks related to the neutron guide system. In total, four different neutron guide elements, namely at NL1, NL6 and 2 times at NL5 imploded due to mechanical failure. A combined effort on the part of the neutron optics group, personnel from the instruments and the radio protection service ensured that, within a short space of time, the affected guide sections were cleaned and the damaged guide elements replaced. Clearly our capability to produce neutron guide elements in-house helped to keep the shutdown times as short as possible. Including the replacement elements at NL1, NL5 and NL6, during 2012 ten different guide elements, with a total length of 16 m, were built. Finally, with the start of the reactor cycle 31 in January 2013, all guides and

their connected instruments in the neutron guide hall west were back to routine operation.

While the failure of the elements at NL1 and NL5 may be attributable to mechanical reasons, the element No. 14 of NL6-S may have imploded due to substrate damage by neutron irradiation. As the guide elements themselves maintain the internal vacuum, the side walls have to withstand the permanent load from the atmospheric pressure. Although the thickness of the substrate is chosen so as to be far beyond the bending strength limit of glass, one must be aware that a tiny scratch may be sufficient to limit the life time of a glass plate exposed to a permanent force. The neighboring elements of NL6-S-14, surprisingly, just showed the same typical scratches arising from the irradiation damage of the Borofloat substrate as the guide elements, which had been replaced in 2011. These were placed at a distance of only 8 m from the cold source, while NL6-S-14 is much further away at a distance of 27 m. Therefore, we investigated the origin of the substrate irradiation in detail. Numerical simulations using the McStas package clearly demonstrated that, due to a change in the supermirror coating, the fluence into the substrate of the broken element was of the same order of magnitude as the fluence at distances of about 10 m from the cold source. On the basis of the detailed simulations performed of the whole neutron guide system of FRM II, guidelines for the substrate selection for future neutron guides can be given.

HELIOS – ^3He for neutron polarization analysis
In 2012 the optical scheme of the HELIOS was redesigned and rebuilt with the aim of allowing four lasers to polarize ^3He gas simultaneously.

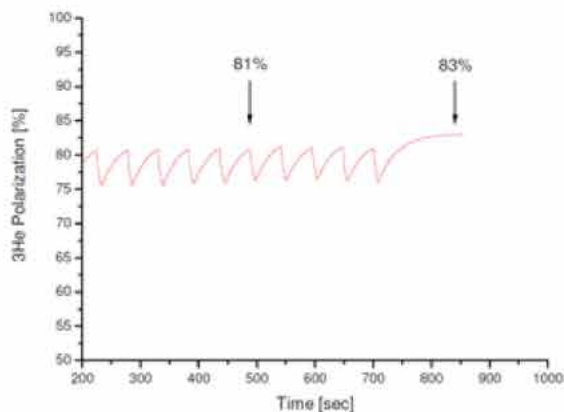


Figure 1: Dynamics of the ${}^3\text{He}$ gas polarization in the optical pumping volume at the HELIOS during the production cycle. After the completion of the production cycle the polarization reaches its maximum at equilibrium.

So, at the moment two new and two old lasers are in use and ensure the high production rate of the polarized ${}^3\text{He}$ gas with a polarization of about 80 % (fig.1) which should be compared with 72 % attainable previously.

The application of cells with polarized ${}^3\text{He}$ gas for the precise polarization analysis of the white neutron beam under conditions where the incident beam intensity experiences a variation during a long-lasting experiment was studied. This method is an extension of the method developed at the FRM II utilizing the 2×1 neutron spin filter. The distinctive feature of the new approach is that it only requires a knowledge of the ratio of the count rates measured for any two groups of neutrons with the wavelengths ratio 2:1. It was shown that the polarization of the transmitted neutrons of any wavelength within the incident spectrum can be estimated to high accuracy.

In 2012 ${}^3\text{He}$ cells were used for user experiments at the instruments REFSANS, POLI and MIRA. At SANS-1 a ${}^3\text{He}$ cell was used for the very first test of the polarization hardware integrated into the instrument. The first measurements with the polarization analysis are in the pipe-line.

Improving neutron detection

Since the beginning, a main function of the Detector & Electronics group has been to ensure that all detectors and the corresponding readout

electronics installed at the scientific instruments are continually improved to achieve a state-of-the-art instrument performance. These improvements are mainly aimed at increased efficiency, detection areas or enlarged count rate capability. As an example, the detector of the NREX reflectometer was replaced in 2012 by a new 2D-position sensitive Multiwire-Proportional Chamber with $20 \times 20 \text{ cm}^2$ active area to significantly improve detection efficiency and homogeneity. The required amount of expensive ${}^3\text{He}$ was recycled from the old detector using the purification and fill station built in the detector lab. The new detector was equipped with highly integrated commercial readout electronics, which provides event-based 2D-position, energy and time information.

Often, however, improvements aim for greater robustness against background, electronic noise and all sources of interference. In autumn 2011 the complete detector electronics installation at the PGAA instrument was renewed. When PGAA resumed operation in 2012, the measures undertaken were shown to significantly reduce the influence of sources of interference and enabled the Germanium detector to be used for an all-time energy resolution.

New detection technologies:

Gaseous Scintillation Proportional Counters

The application of Gaseous Scintillation Proportional Counters (GSPC) with light readout in



Figure 2: The GSPC19 detector mounted at CT2 beam line at ILL for a first integration test.

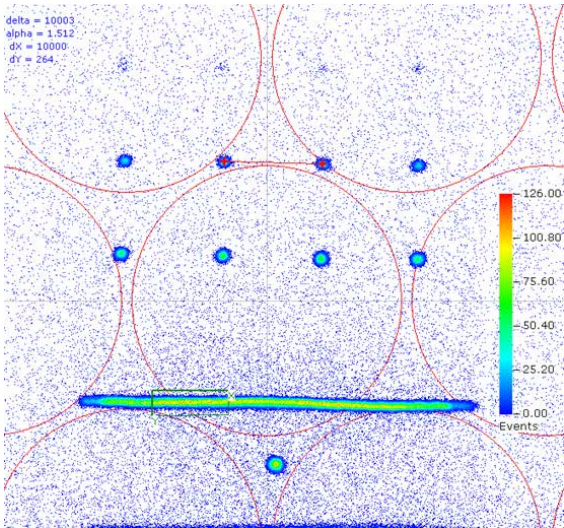


Figure 3: 2D-position spectrum of 2.5A neutrons recorded with the GSPC19 with a multihole / slit BN-mask in front.

neutron detection made possible the design of neutron counting detectors with superior performance that exhibit high count rate capability of up to MHz, sub-millimeter spatial resolution and low gamma sensitivity on a par with gaseous detectors. Within a Joint Research Activity of the NMI3 collaboration in the Seventh European Framework Programme (FP7), the FRM II detector group has been actively involved in the development of a demonstrator detector based on GSPC-technology with the Anger camera readout shown in figure 2. In November 2012, the GSPC19 was installed for a first integration test with the fast readout electronics system developed at FZ Jülich and FRM II at the CT2 beam line at the Institute Laue-Langevin. Figure 3 shows the result when the detector is irradiated with 2.5 A neutrons with a multihole / slit BN-mask mounted in front. The hole diameter is 8 x 0.5 mm on 10 mm pitch and the slit width is 0.2 mm. From a preliminary analysis, a position resolution of $\Delta x = 0.6$ mm (FWHM) close to the physical limit is deduced.

Detectors using solid ^{10}B neutron converters

The investigation of techniques alternative to ^3He based neutron detectors is still an important task in the field of detector development. FRM II is actively participating in three international programmes which evaluate the potential use of

solid Boron converters in gaseous detectors. Figure 4 shows a design study of a fully modular Boron-10 based detector developed at FRM II. The device with $40 \times 40 \text{ cm}^2$ active area with resistive wire readout is aiming for $5 \times 5 \text{ mm}$ spatial resolution. A demonstrator presently under construction in collaboration with the ESS detector group will be equipped with up to 20 layers of Boron converters with macro-structured topology to increase the efficiency of the individual layers.

New specialized sample environments

Research on rechargeable energy storage systems such as lithium-ion batteries is of increasing interest for a wide range of industrial applications. Using the potential of neutron scattering techniques helps to get a closer insight into the underlying physical and chemical processes. This results in improved performance and helps to trigger the development of new types of batteries. To achieve this, the batteries have to be probed at their adequate environmental operating conditions. On the other hand, more extreme conditions such as high or low temperatures can be of interest.

At the MLZ dedicated heater elements are available providing temperatures up to 700°C and optional electrical contacts (fig. 5). Depending on experimental parameters, battery size and temperature specification, the furnaces have to be designed and manufactured individually. Heating is achieved via an appropriate set of high performance cartridge heaters allowing for tempera-

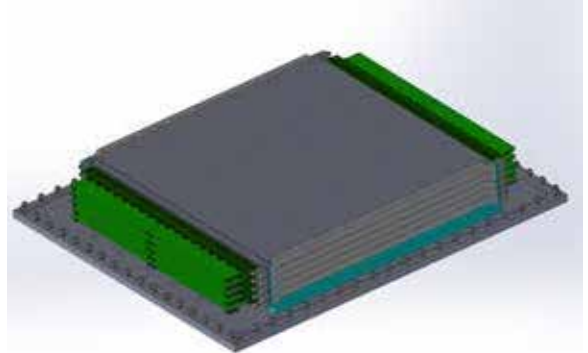


Figure 4: Design study of a $40 \times 40 \text{ cm}^2$ detector with solid Boron converter with macro-structured topology developed at FRM II.



Figure 5: Battery furnace setup.

tures up to 700 °C. Optional temperatures below room temperature (RT) are also possible.

A remote controlled power supply fitting into the TACO software concept provides the heater current.

A new type of sample sticks used in the FRM II top loading cryostat (CCR) is now available. A high voltage sample stick allows for electric fields up to 10 kV in arbitrary orientation. The temperature range goes from 3 K up to RT.

Furthermore, a sample stick suitable for high pressure gas cells up to 4 MPa is in operation.

Another setup which allows for higher pressures is in preparation.

For gas adsorption experiments, e.g. experiments on hydrogen storage materials, a sample stick is available that tolerates pressure up to 50 bars. Regarding hydrogen absorption experiments, a furnace has been designed and built allowing for temperatures up to 500 °C and pressures up to 100 bar.

Restructuring of the IT Infrastructure

In summer 2012 the former IT Infrastructure de-

partment was restructured and split into three new groups, namely IT services, Software Solutions and Instrument control.

IT Services

Besides the maintenance of the entire network service at the MLZ, the main activities of the group in 2012 helped to improve the services regarding internet access, speed and telephone connection as well as data storage.

Better internet availability for mobile devices during meetings is achieved by the installation of W-LAN access points in three further seminar rooms. Also, the network infrastructure in the new office container-building on the premises of FRM II was put into operation, providing wired and wireless access to the FRM II network.

Furthermore, the speed of the connection between the FRM II network and the internet has been increased from 100 Mbit/s to 1 Gbit/s. Concomitantly, the firewall system has been exchanged by a new redundant system to meet current demands for more flexibility and better performance.

In 2012 Voice over IP (VoIP) telephony was introduced, giving more flexibility and more options to provide telephone extensions on the premises of FRM II. In the new office-container building in particular, this greatly increased the number of telephone extensions possible.

Another activity concerns centralised data storage. The storage system for archiving measured data at the FRM II instruments was renewed, resulting in a dramatic rise in storage capacity to keep up with demand for the coming years.

Software Solutions

Though it is formally new, as a part of IT Infrastructure, it has been providing applications for many years for staff and users of the FRM II.

One important project of the group is the DoRIS (Dokumentations-, Rückverfolgungs- und Informationssystem) application. This comprehensive

software solution provides services for the operational division of the FRM II, which include the tracking of recurring checks and the life cycle of the technical equipment.

Beginning with DoRIS-1 in 2003, a FoxPro application and the first attempt to manage the business processes, the system was later modernized with DoRIS-2 to an object-oriented architecture and the use of a database management system. The development of DoRIS-3 is currently underway. The new system is better adapted to the current workflow used at the FRM II. It avoids the shortcomings of the old systems and uses a more advanced database system. In 2012 data migration from the old system began and DoRIS-3 entered its test phase.

The AdminTool, an external program created in 2012, provides search and scheduling facilities using both DoRIS-2 and DoRIS-3 systems. It assists the reactor enhancement and reactor operation department in optimizing their workflow and the fast creation of reports.

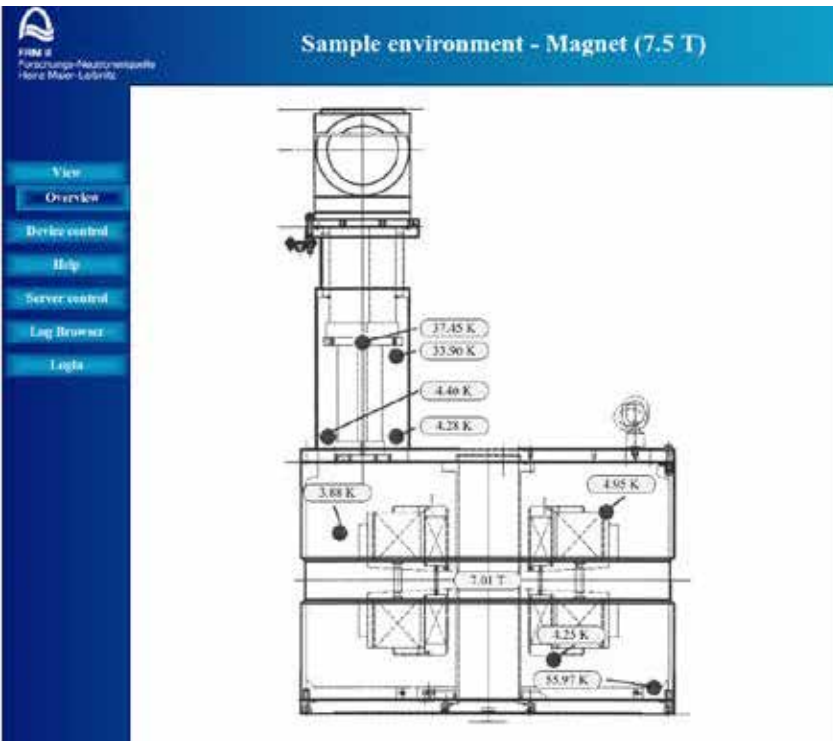


Figure 6: The web-based interface of ICSE for the control of sample environments, e.g. magnets, showing the schematic view of the magnet, the current magnetic field and temperatures.

Another major project is the digital user office (DUO) system which manages the application of scientific users for beamtime, the review process and the scheduling of allocated beamtime. The current user office web application software is difficult to adapt to changes in the workflow, so a new digital user office web application will be developed. The specifications for this software are now in the final stages of development. In the current system, a new proposal categorization was introduced and the review process was changed to reflect the new upcoming requirements due to the transition to MLZ.

The archive database of the quality assurance group and the staff database of the reactor monitoring and radiation protection department were totally revamped and moved to a more advanced database system to better suite the respective workflows. In the future, it will eventually become possible to link the databases to other more general databases such as DoRIS.

Instrument Control

The main activities of the recently founded group Instrument control include the continuation of the work of the software development group with respect to the instrument control software. The goal of the group is to provide a better integration of selected hardware and instrument control software as well as ongoing support for the latter, which is based on a combination of TACO/TANGO hardware servers and NICOS control software as a user interface.

With this combination, our aim is to provide a better and more individual support for the instruments.

The main activities of the last year include:

- Stabilisation of hardware servers
- Improvements to NICOS, based on the needs of some instruments, in close co-operation with G. Brandl, B. Pedersen, A. Schneidewind, and E. Faulhaber
- Development of the QMesyDAQ software for the detector electronics of MesyTec GmbH

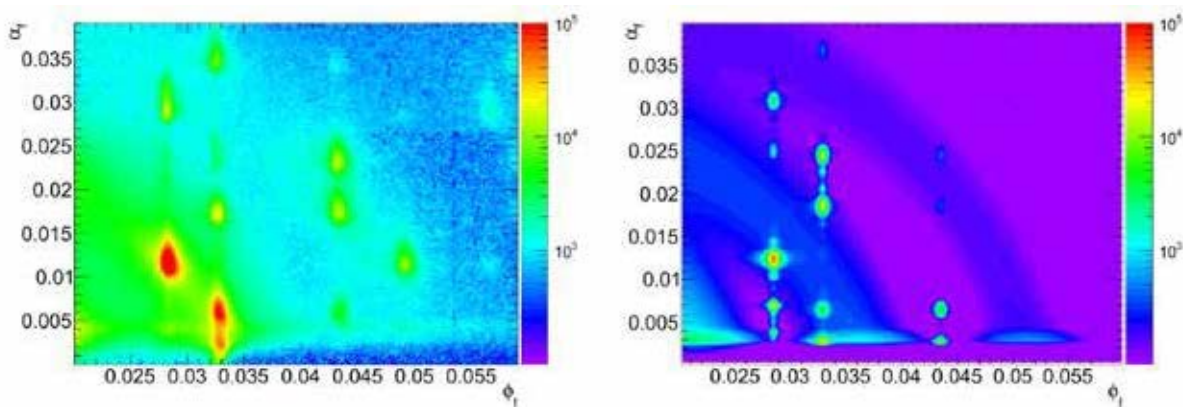


Figure 7: Grazing-incidence small-angle X-ray scattering from a mesocrystalline system (left, courtesy Elisabeth Josten et al.), compared to a BornAgain simulation (right). The mesocrystals have cylindrical shape and a size of about 1000 nm; they are vertically oriented, and randomly distributed on a silicon substrate. Each of these mesocrystals consists of an FCC lattice composed of 5 nm spherical particles.

- in close cooperation with the HZB
- Enhancements of the TACO/TANGO boxes (for the sample environments)
- Definition of standard device classes for TANGO
- Realization and continuous support of the Integrated Control System Environment (ICSE)

ICSE is an in-house developed web framework. It is used by the instrument control group to create consistent, web-based interfaces for sample environments and similar systems (fig. 6).

The standard ICSE interface provides the following possibilities:

- Monitoring of devices, provided by the TACO system
- Controlling of devices, provided by the TACO system
- Monitoring and Controlling of TACO servers and other important processes

Besides these standard functionalities, the ICSE provides the possibility of customizing the system for each sample environment. These customizations consist of custom pictures, new designs, sample environment specific help for the user etc. Even completely new functionality can be implemented for individual sample environments. There is one more great advantage to

the ICSE, which mainly affects the instrument control group: The ICSE has one single code-base for each sample environment. This makes the maintenance of existing SEs and the integration of new SEs very time-saving.

In close cooperation with the ZEA-2 (former ZEL) group of the Forschungszentrum Jülich, we defined the standard device classes for the TANGO servers. These classes form the base and interface for the development of the TANGO servers, which are the interface to the hardware in the instrument control system. The latter were enhanced based on the experiences of the use of the TACO base device classes. The unification of the device classes simplifies the development of the instrument control software, which is based on re-useable components.

BornAgain: software for grazing-incidence scattering by the Scientific Computing Group
Currently, the Scientific Computing (SC) group is concentrating on the development of a new software for simulating and fitting grazing-incidence small-angle scattering (GISAS). This project is embedded in workpackage 3 of the High Data Rate Processing and Analysis Initiative (HDRI) of the Helmholtz Association, and the final product will serve the synchrotron (GISAXS) as well as the neutron (GISANS) instruments.

The working title of the software, BornAgain, indicates the central role of the distorted-wave Born approximation (DWBA) in the physical description of the scattering process. The software provides a generic frame for modelling multi-layer samples with smooth or rough interfaces and with various types of embedded nanoparticles. In this way, it reproduces and enhances the functionality of the present reference software, IsGisaxs by Rémi Lazzari, and lays a solid base for future extensions in response to specific user needs. The first public release will be presented in April 2013 at the workshop on GISAS data analysis organized by the SC group. The first major extension, planned for 2013/14, will provide coverage of polarized GISANS for the investigation of magnetic domains.



Figure 8: Floor deepening in the neutron guide hall east for the instrument SAPHiR; top: during structural work, middle: finished, bottom: with instrument installed.

In collaboration with Elisabeth Josten and Artur Glavic of Jülich, the framework was applied to the simulation and fitting of a system of self-assembled nanoparticles (mesocrystals). This required the implementation of new simulation algorithms and more flexible approaches for the sample description. As shown in figure 7, good agreement between experimental data and fit results has been found.

Open-source components for image processing, cataloguing and fitting

Among the smaller projects of the SC group, image processing for the instrument BIODIFF deserves mention: A preprocessor for the data treatment software DENZO was written, in order to allow an automatized work flow from the detector to the physical analysis of protein diffraction data.

While preparing for a web catalogue of experimental data, the SC group contributed a web service client module, PyICAT, to the catalogue software ICAT. Using the client module, metadata retrieved from experimental data sets can be inserted into the catalogue data base.

Another open-source contribution of the SC group is the library libkww for efficient and precise computation of the Laplace-Fourier transform of the stretched exponential function. Also known as the Kohlrausch-Williams-Watts (KWW) function, it is routinely used to fit relaxation spectra of disordered systems. The library also allows for direct computation of the primitive of the KWW cosine spectrum, for use in an improved convolution procedure that prevents numeric artifacts when the fit function is sharper than the instrumental resolution. All this has been documented in the new open-access journal Algorithms (J. Wuttke, Algorithms 5, 604 (2012)).

Integrating the neutron guide hall east

The newly formed group Infrastructure supports the staff and instrument scientists of the MLZ in engineering and inter-divisional projects, including project planning and coordination.

A major task of the group is the structural connection and the system integration of the new neutron guide hall east. This includes, e.g. structural works within the hall to deepen the floor to meet the requirements for structural foundation and level matching of the instruments SAPHiR (fig. 8) and EDM.

After successful completion of the cavities, the first parts of the instruments were put in place, namely the multi-anvil press of SAPHiR (fig. 8, bottom) and the low magnetic field cage of the EDM experiment.

Another milestone was achieved with the completion of the baseplate for the containment bridging the reactor building and the guide hall east. It is foreseen that this will be finished in 2013.

A small building erected inside the hall provides access to the controlled area of the new guide hall. It comprises the radiation protection control



Figure 9: 3D visualisation of experimental areas in the neutron guide hall east.

area, rest rooms and, at the top, a viewing balcony for visitors.

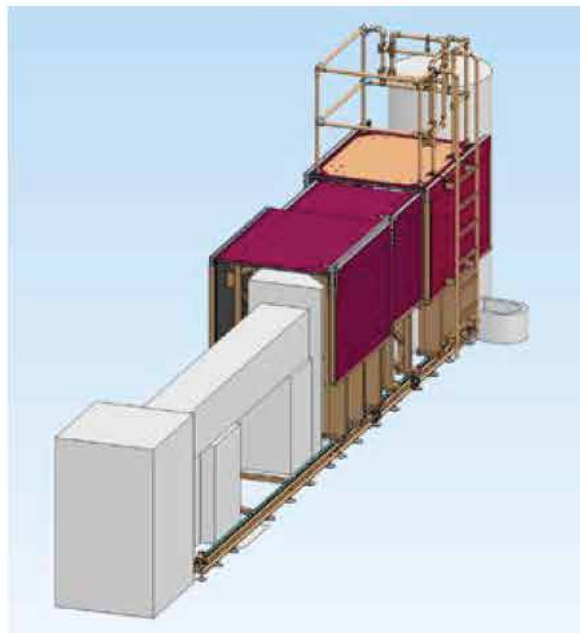


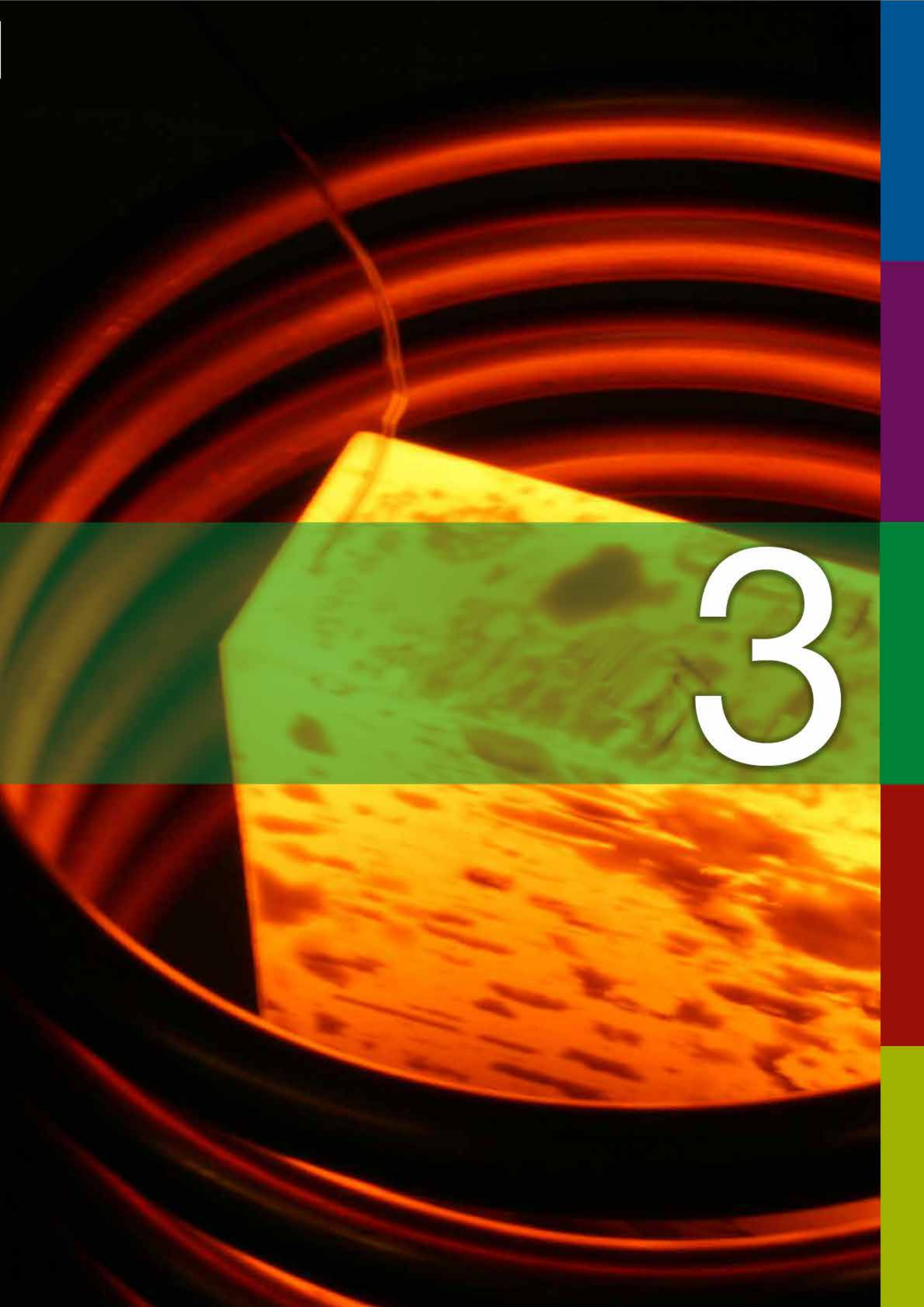
Figure 10: New shielding design implemented at RESEDA.

The system integration of the neutron guide hall east requires effective planning and seamless cooperation in order to supply the start-up instrumentation commensurate with the special needs of the experiments (e.g. concerning media supply or accessibility); for this purpose, a 3D planning guide is in development (fig. 9).

The Infrastructure group also provides technical consulting services as well as planning and the realization of mechanical engineering tasks in order to support scientific utilization. This includes, e.g. the custom-tailored design for instrument-specific fitments (e.g. neutron collimator) or for shielding measures for the experimental field (e.g. instrument RESEDA, see figure 10).

Other advanced projects include the shared neutron guides between the experimental hall and the neutron guide hall east for the instruments MEPHISTO, POWTEX, TOPAS, TRISP and SAPHiR.

Scientific Highlights



3

Higgs transition in quantum spin ice $\text{Yb}_2\text{Ti}_2\text{O}_7$

L.-J. Chang¹, S. Onoda², Y. Su³, Y.-J. Kao⁴, Y. Yasui⁵, K. Kakurai⁶, M. R. Lees⁷

¹Department of Physics, National Cheng Kung University, Tainan, Taiwan

²RIKEN, Condensed Matter Theory Laboratory, Wako, Japan

³Forschungszentrum Jülich GmbH, Jülich Centre for Neutron Science at MLZ, Garching, Germany

⁴National Taiwan University, Department of Physics, Taipei, Taiwan

⁵Nagoya University, Department of Physics, Furo-cho, Chikusa-ku, Japan

⁶Japan Atomic Energy Agency, Quantum Beam Science Directorate, Tokai, Japan

⁷University of Warwick, Department of Physics, Coventry, United Kingdom

Researchers at CERN in Geneva have probably proved the existence of the Higgs boson as predicated by the British physicist Peter Higgs in the 1960s. The Higgs mechanism, which explains how elementary particles obtain their mass, can also play a role beyond elementary particle physics. Via polarized neutron scattering experiments carried out at DNS on quantum spin ice $\text{Yb}_2\text{Ti}_2\text{O}_7$, we have revealed that this mechanism can explain a first-order phase transition at 210 mK as if from a magnetic Coulomb liquid state where the fractionalized magnetic monopole quasi-particles are deconfined, to a ferromagnet where a Higgs condensate is formed via the Bose-Einstein condensation of monopole quasi-particles.

Spin ice: from classical to quantum

Magnetic monopoles can be regarded as the magnetic version of a charged particle such as electrons and protons. They carry an isolated magnetic pole, either the North or South pole.

Normally, magnets come in the form of dipoles, with both North and South poles appearing in pairs. In a class of magnetic materials called *spin ice*, four electron spins residing at the four corners of a tetrahedron will be compromised to a spin configuration of 2-in and 2-out towards the center of the tetrahedron, i.e. obeying the ice rule as in *water ice*. When a spin is excited and its direction reversed, emergent magnetic monopoles can be created as a classic defect that interact with each other via the magnetic Coulomb law. However, in the quantum version of spin ice, where spins can rotate away from the “in” and “out” spin configuration imposed by local single-ion anisotropy, magnetic monopoles may appear as fractionalized bosonic quasi-particles. Neutron scattering can play an important role in the experimental quests for fractionalized quasi-particles in quantum spin liquids in many strongly frustrated spin systems.

Polarized experiments at DNS: results and new perspectives

Polarized neutron scattering experiments on single crystal $\text{Yb}_2\text{Ti}_2\text{O}_7$ were performed at the high-flux polarized diffuse neutron scattering spectrometer DNS. A $^3\text{He}/^4\text{He}$ dilution refrigerator was used for the measurements in the temperature range 0.02–1 K. A neutron wavelength of 4.74 Å was chosen in the experiments. The [1–10] direction of the crystals was aligned perpendicular to the horizontal scattering plane so that the (h,h,l) reciprocal plane can be mapped out by rotating the sample step by step. The neutron polarization at the sample position was aligned along the [1–10] direction of the sample, that is, the z-direction of the chosen experimental coordinate system (z-direction polarized neutron scattering). The magnetic diffuse scattering

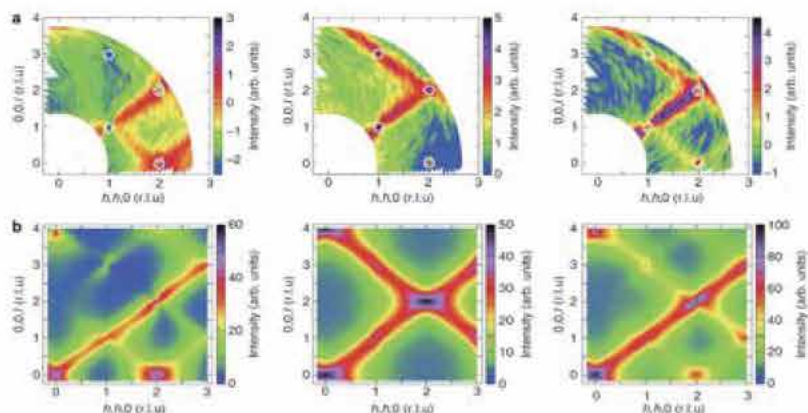


Figure 1: (a) Experimentally observed profiles for the spin-flip (SF) (left), non spin-flip (NSF) (middle) and total (right) magnetic diffuse neutron scattering cross-sections in the (h,h,l) plane above T_c at $T = 0.3$ K. (b) Theoretically calculated magnetic profiles via RPA for the SF (left), NSF (middle) and total (right) magnetic diffuse neutron scattering cross-sections.

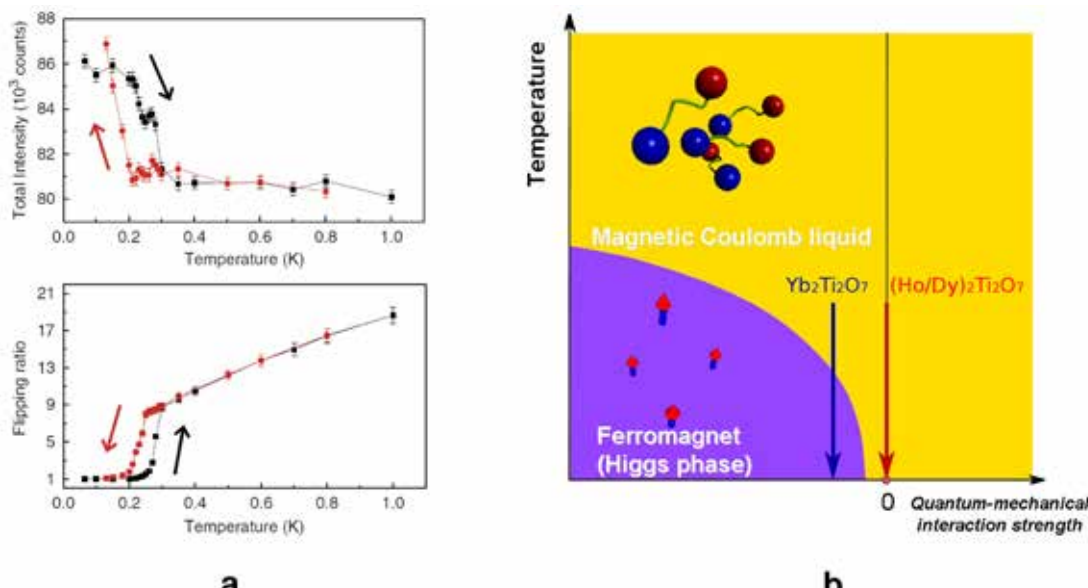


Figure 2 (a) Top: the sum of the SF and the NSF (111) Bragg peak intensities versus temperature showing a hysteresis with temperature. The sum increases by almost 6 % below T_c in agreement with the previous measurements. Bottom: the flipping ratio of the scattered (111) Bragg peak as a function of temperature. This ratio falls off steeply to unity below T_c with a clear hysteresis. The data were collected by first warming and then cooling. This sequence is indicated by the arrows. (b) A schematic phase diagram as a function of temperature and the quantum-mechanical interaction strength of $\text{Yb}_2\text{Ti}_2\text{O}_7$.

profiles measured at 0.3 K is shown in fig. 1 (a), which agrees well with our theoretical calculation based on a quantum spin ice model (as shown in fig. 1 (b)). In particular, the appearance of the so-called pinch-point singularity at (111) strongly supports the existence of fractionized magnetic monopole quasi-particles that are deconfined and governed by the magnetic Coulomb law in this temperature regime. Below $T_c \sim 0.21$ K, the rod-like diffuse scattering along the [111] directions and the pinch-point features are suddenly suppressed, where magnetic Bragg peaks and a full depolarization of the neutron spins are observed with thermal hysteresis, thus indicating a first-order transition (as shown in fig. 2 (a)). In spin ice, the spins remain unordered even at low temperatures, and the monopoles behave as if they are fractionalized. On the other hand, a quantum spin ice that can exhibit a magnetic order realized by a Bose-Einstein condensation of monopoles was predicted theoretically. In this case, a coupling to fictitious electromagnetic fields, called gauge fields, endows a mass for otherwise gapless spin excitations in the ordered state, forming an analogous superconducting state of monopoles via the Higgs mechanism. The first

order transition at 0.21 K is thus a transition from a state with fractionalized unstable monopoles to a ferromagnetic state with condensed stable monopoles, as schematically shown in fig. 2 (b). The discovery of the Higgs phase of magnetic monopoles in quantum spin ice will not only motivate scientists to investigate many fascinating physical properties of this exotic state of matter, but may also open up a new direction in spintronics that aims at the efficient control of spins for technological applications.

Long-wavelength helimagnetic order and skyrmion lattice phase in Cu₂OSeO₃

T. Adams¹, A. Chacon¹, M. Wagner¹, A. Bauer¹, G. Brandl^{1,2}, B. Pedersen², H. Berger³, P. Lemmens⁴ and C. Pfleiderer¹

¹Technische Universität München, Physik-Department E21, Garching, Germany

²Technische Universität München, Forschungs-Neutronenquelle Heinz Maier-Leibnitz (FRM II), Garching, Germany

³École Polytechnique Fédérale de Lausanne, Lausanne, Switzerland

⁴Technische Universität Braunschweig, Institut für Physik der Kondensierten Materie, Braunschweig, Germany

We report a long-wavelength helimagnetic superstructure in a bulk sample of the ferrimagnetic insulator Cu₂OSeO₃ [1]. The magnetic phase diagram associated with the helimagnetic modulation includes a skyrmion lattice phase and is strongly reminiscent of MnSi, FeGe and Fe_{1-x}Co_xSi, i.e., binary isostructural siblings of Cu₂OSeO₃ that order helimagnetically.

The helimagnetic order in Cu₂OSeO₃ relates to binary transition metal compounds such as MnSi and FeGe, which share the space group P2₁3 with Cu₂OSeO₃, supporting a hierarchy of three energy scales in their B20 crystal structure [2]. These are ferromagnetic exchange and Dzyaloshinsky-Moriya interactions on the strongest and second strongest scale, respectively, generating a longwavelength helimagnetic modulation. The propagation direction of the helix is finally the result of very weak magnetic anisotropies on the weakest scale. Most spectacularly, a skyrmion lattice phase was recently discovered in binary P2₁3 transition metal compounds [3 - 6], giving rise to an emergent electrodynamics [7, 8].

Excellent sample quality

For our study a large Cu₂OSeO₃ single crystal (~0.2 g) was grown by chemical vapour transport. An excellent sample quality was established by means of neutron diffraction at RESI at MLZ, notably an absence of impurity phases well below 1 % and a lattice mosaic spread smaller than the resolution limit of 0.02°. Laue X-ray diffraction was used to orient the sample. The Small Angle Neutron Scattering (SANS) measurements were performed at the diffractometer MIRA 2 at MLZ

using a neutron wavelength $\lambda_n = 5 \text{ \AA} \pm 5 \%$. The rotation axis coincided with a crystallographic 110 axis.

Helimagnetic order

Typical integrated rocking scans are shown in figure 1. For B = 0, the intensity pattern consists of well-defined spots at $k \approx (0.0102 \pm 0.0008) \text{ \AA}^{-1}$ along all three <100> axes, characteristic of a modulation with a long wavelength $\lambda = 616 \pm 45 \text{ \AA}$. This is shown in figures 1(a) and 1(b), which display the intensity patterns for neutrons parallel <100> and <110> respectively. Preliminary tests with polarized neutrons suggest a homochiral helical modulation. The weak additional spots along the <110> axes (fig. 1(a)) are characteristic of double scattering. By analogy with the binary P2₁3 systems, the scattering pattern at B = 0 is characteristic of a multidomain single-k helimagnetic state, where spots along each <100> axes correspond to different domain populations.

In contrast, in MnSi, the helical modulation is along <111>. This implies a change of sign of the leading order magnetic anisotropy in Cu₂OSeO₃ [3, 4, 9, 10] but contrasts distinctly the <110> propagation direction in thin samples. In the range $B_{c1} < B < B_{c2}$, the zero-field pattern (fig. 1(a) and 1(b)) collapses into two spots parallel to the field, as shown for B = 58 mT and T = 5 K in figure 1(c). Accordingly, the modulation is parallel to B and, in analogy with the binary P2₁3 compounds, characteristic of a spin-flop phase also known as conical phase.

Skyrmion lattice in the A-phase

In the A-phase, finally, the intensity pattern consists essentially of a ring of six spots perpendicular to the field, regardless of the orientation of the

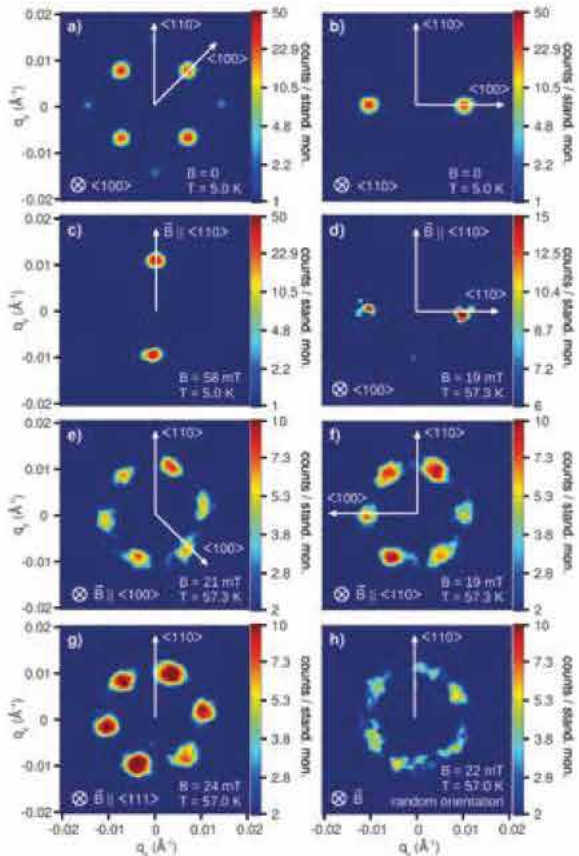


Figure 1: Typical integrated small-angle neutron scattering rocking scans in Cu_2OSeO_3 . Data are shown as counts per standard monitor (stand. mon.). (a) Zero-field scattering pattern along $<100>$, characteristic of helimagnetic order along $<100>$. (b) Zero-field scattering pattern along $<110>$, characteristic of helimagnetic order along $<100>$. (c) Typical scattering pattern in the field range $B_{c1} < B < B_{c2}$ for $T < T_c$. (d) Scattering pattern in the A phase for magnetic field perpendicular to the neutron beam. Panels (e) to (h): Typical scattering pattern in the A phase for magnetic field parallel to the neutron beam for various orientations.

sample with respect to the field (figs. 1(d) to 1(h)). We begin with panel (d) which demonstrates that the pattern for field perpendicular to the neutron beam is also perpendicular to the field. Further, figures 1(e) to 1(h) show the six-fold pattern for field parallel to the neutron beam. The six-fold pattern in the plane perpendicular to the field is thereby roughly aligned along $<100>$, consistent with very weak magnetic anisotropy terms that are sixth order in spin-orbit coupling and small demagnetizing fields (see, e.g., [3, 4]). As demonstrated for the binary $\text{P}2_1\text{3}$ compounds, the six-fold pattern arises from a triple-k state, with $\sum_i k_i = 0$, coupled to the uniform magnetiza-

tion and stabilized by thermal Gaussian fluctuations. The topology of the triple-k state is that of a skyrmion lattice, i.e., the winding number is 1 per magnetic unit cell. This has been confirmed experimentally in MnSi by means of Renninger scans in SANS [11] and the topological Hall signal [12]. We therefore interpret the A-phase in Cu_2OSeO_3 as a skyrmion lattice.

Search for emergent electrodynamics

Thus, bulk samples of Cu_2OSeO_3 represent the first example of helimagnetic order in a structural sibling of the B20 compounds that is nonbinary, an oxide, a compound with a nonferromagnetic leading-order exchange interaction, and an insulator. Being an insulator, the skyrmion lattice in Cu_2OSeO_3 thereby promises an emergent electrodynamics akin to that observed in its binary siblings [7, 8], where electric fields may now be used to manipulate the skyrmions.

- [1] T. Adams et al., Phys. Rev. Lett., 108, 237204 (2012).
- [2] L. D. Landau and E. M. Lifshitz, Course of Theoretical Physics, 8 (1980).
- [3] S. Mühlbauer et al., Science, 323, 915 (2009).
- [4] W. Münzer et al., Phys. Rev. Lett., B 81, 041203 (R) (2010).
- [5] X. Z. Yu et al., Nature, 465, 901 (2010).
- [6] X. Z. Yu et al., Nature Mater., 10, 106 (2011).
- [7] T. Schulz et al., Nature Phys., 8, 301 (2012).
- [8] F. Jonietz et al., Science, 330, 1648 (2010).
- [9] P. Bak and M. H. Jensen, J. Phys.: Condens. Matter, 13, L881 (1980).
- [10] O. Nakanishi et al., Solid State Commun., 35, 995 (1980).
- [11] T. Adams et al., Phys. Rev. Lett., 107, 217206 (2011).
- [12] A. Neubauer et al., Phys. Rev. Lett., 102, 186602 (2009).

Fluctuation-induced first-order phase transition in Dzyaloshinskii-Moriya helimagnets

M. Janoschek^{1,2,3}, M. Garst⁴, A. Bauer¹, P. Krautscheid⁴, R. Georgii^{1,5}, P. Böni¹, C. Pfleiderer¹

¹Technische Universität München, Physik-Department E21, Garching, Germany

²University of California, Department of Physics, San Diego, USA

³Los Alamos National Laboratory, Los Alamos, USA

⁴Universität zu Köln, Institut für Theoretische Physik, Köln, Germany

⁵Technische Universität München, Forschungs-Neutronenquelle Heinz Maier-Leibnitz (FRM II), Garching, Germany

Two centuries of research on phase transitions have repeatedly highlighted the importance of critical fluctuations that abound in the vicinity of a critical point. Strikingly, should such soft fluctuations be too abundant, they may alter the nature of the phase transition profoundly; the system might evade the critical state altogether by undergoing a discontinuous first-order transition into the ordered phase. Fluctuation-induced first-order transitions have been the subject of broad theoretical discussion, but clear experimental confirmation remains scarce. Our results from neutron scattering and thermodynamics on the model Dzyaloshinskii-Moriya helimagnet MnSi show that such a fluctuation-induced first-order transition is realized between its paramagnetic and helimagnetic state with remarkable agreement between experiment and theory.

The theory of phase transitions

Critical phenomena were observed for the first time in 1822 in the form of critical opalescence of water vapour when Cagniard de la Tour discovered the critical point of the gas-liquid phase transition [1], and have attracted continuous scientific interest ever since. At the critical point the corresponding phase transition is continuous (or second-order), implying that the order parameter characterizing the onset of order changes smoothly. A prime example is the transition from the disordered paramagnetic state to the ordered ferromagnetic (FM) state that occurs spontaneously in the absence of a magnetic field when a FM material is cooled below its critical temperature T_c : at T_c the magnetization - the order parameter of the FM state - changes continuously from zero and assumes a finite value in the ordered state [2]. As recognized by Cagniard de la Tour, a critical point represents a "special

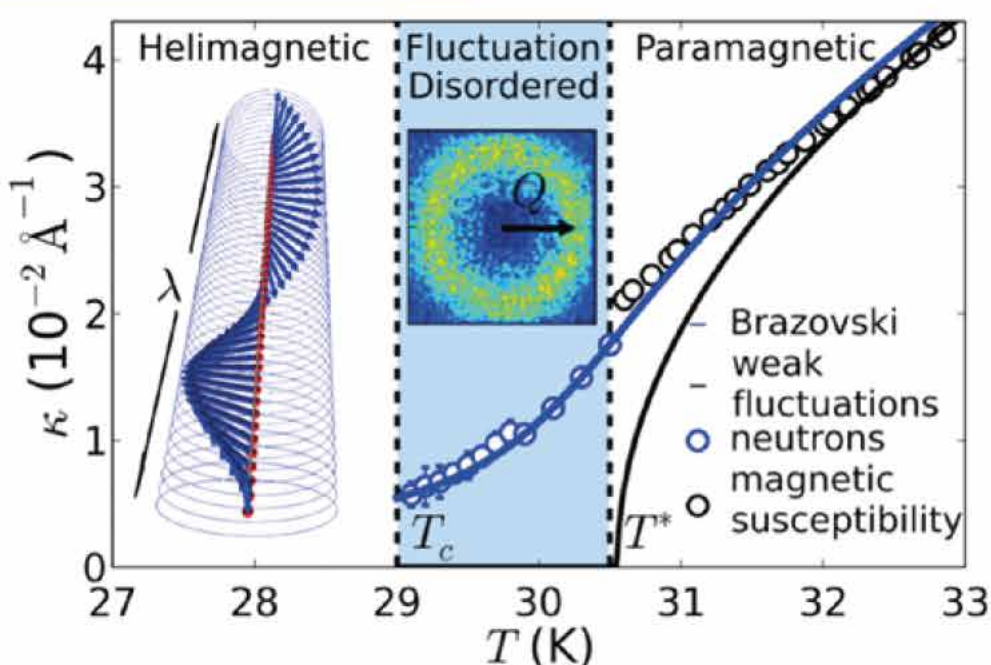


Figure 1: Brazovskii-type phase transition between the paramagnetic and helimagnetic phase of MnSi

state” (état particulier) [3], because at a continuous phase transition the disordered and the ordered phase are indistinguishable, resulting in unusual physical properties generally referred to as critical phenomena. At their origin are the critical low-energy fluctuations of the order parameter that extend over increasing length scales as T_c is approached. The divergence of their so-called correlation length ξ results in universal scaling laws for observables that only depend on the symmetries of the critical system while being independent of its specific microscopic details. This led to the notion of universality classes — a cornerstone of modern physics — explaining that a wide range of systems exhibit the same critical behaviour in spite of differing microscopic compositions [4].

Remarkably, an excess of soft fluctuations close to criticality can change the nature of the phase transition entirely. If the phase space available for the critical degrees of freedom is sufficiently large, the system may evade the critical state to avoid the large entropy associated with the fluctuations by realizing a discontinuous first-order transition into the ordered phase. As a result, the correlation length does not diverge and the order parameter varies discontinuously at the transition, which is also accompanied by the release of latent heat. Such fluctuation-induced first-order transitions have been discussed broadly, and transitions are of interest for a wide range of topics such as liquid crystals, superconductors, cold atom systems or even phase transitions in the early universe, but clear experimental confirmation remains scarce.

SANS experiments at MIRA

Our results from small angle neutron scattering (SANS) measurements at the instrument MIRA and thermodynamics on the model Dzyaloshinskii-Moriya (DM) helimagnet MnSi show that such a fluctuation-induced first-order transition is realized between its paramagnetic and helimagnetic state with remarkable agreement between experiment and a theory put forward by Brazovskii in the 1970’ies [5].

Brazovskii-type phase transition in MnSi

Below $T_c = 29$ K, MnSi forms a magnetic helix with a period λ as shown in the left inset of the figure. Above T_c , MnSi is paramagnetic and shows magnetic fluctuations as expected for a second-order phase transition. However, below T_{MF} the fluctuations form on a sphere in momentum space with a radius $Q = 2\pi/\lambda$ prototypical for a Brazovskii transition (the centre inset shows a cut through the sphere). For a second-order phase transition with weak fluctuations, the inverse correlation length $\kappa = 2\pi/\xi$ should go to zero at the phase transition (black curve). However, the strong and abundant fluctuations on the sphere lead to a fluctuation-disordered regime (blue shaded region) and renormalize the observed κ (circles) near the phase transition, leading to fluctuation-induced first-order transition. The blue line is a fit to the Brazovskii theory, indicating the excellent agreement between theory and experiment.

While our study clarifies the nature of the helimagnetic phase transition in MnSi that has puzzled scientists for several decades, more importantly, our conclusions based entirely on symmetry arguments are also relevant for other DM helimagnets with only weak cubic and magnetic anisotropies. This is in particular noteworthy in the light of a wide range of recent discoveries that show that DM helimagnetism is at the heart of problems such as topological magnetic order, multiferroicity, and spintronics.

- [1] C. Cagniard de la Tour, Ann. Chim. Phys., 21, 127 (1822).
- [2] P. Curie, Ann. Chim. Phys., 5, 289 (1895).
- [3] C. Cagniard de la Tour, Ann. Chim. Phys. 22, 410 (1823).
- [4] K. G. Wilson, Rev. Mod. Phys., 55, 583 (1983).
- [5] S. A. Brazovski, Sov. Phys. JETP, 41, 85 (1975).

Simultaneous uniform and non-uniform reversal of magnetization in exchange coupled systems

A. Paul¹, C. Schmidt², A. Ehresmann², N. Paul³, S. Mattauch⁴, P. Böni¹

¹Technische Universität München, Physik-Department E21, Garching, Germany

²Universität Kassel, Institut für Physik and Centre for Interdisciplinary Nanostructure Science and Technology (CINSaT), Experimentalphysik IV, Kassel, Germany

³Helmholtz-Zentrum Berlin für Materialien und Energie GmbH, Berlin, Germany

⁴Forschungszentrum Jülich GmbH, Jülich Centre for Neutron Science at MLZ, Garching, Germany

The non-equilibrium arrangement of antiferromagnetic spins at the antiferromagnetic-ferromagnetic interface, related to the AF uniaxial anisotropy, plays a crucial role during the initial training process. We apply different methods to initialize or modify the unidirectional anisotropy using moderate energy ion irradiations. Magnetization reversal mechanisms were investigated during the first two field cycles to identify the role played by each of the methods in training. A detailed analysis of polarized neutron scattering reveals a simultaneous process of domain nucleation (non-uniform) and coherent rotation (uniform) for magnetization reversal.

Role of unidirectional and uniaxial anisotropy on exchange bias

It has previously been shown that training, particularly that between the first and second field cycles, can be primarily related to magnetocrystalline anisotropy in the antiferromagnet and its frustration. [1,2] It was also conjectured that an antiferromagnet with strong uniaxial anisotropy (CoO) may be more susceptible to training than an antiferromagnet with no or insignificant uniaxial anisotropy (IrMn). The aim of this study is to investigate the magnetization reversal mechanism in the untrained as well as the trained specimens to identify the role of unidirectional anisotropy and field-induced extrinsic uniaxial anisotropy by complying different conditions de-

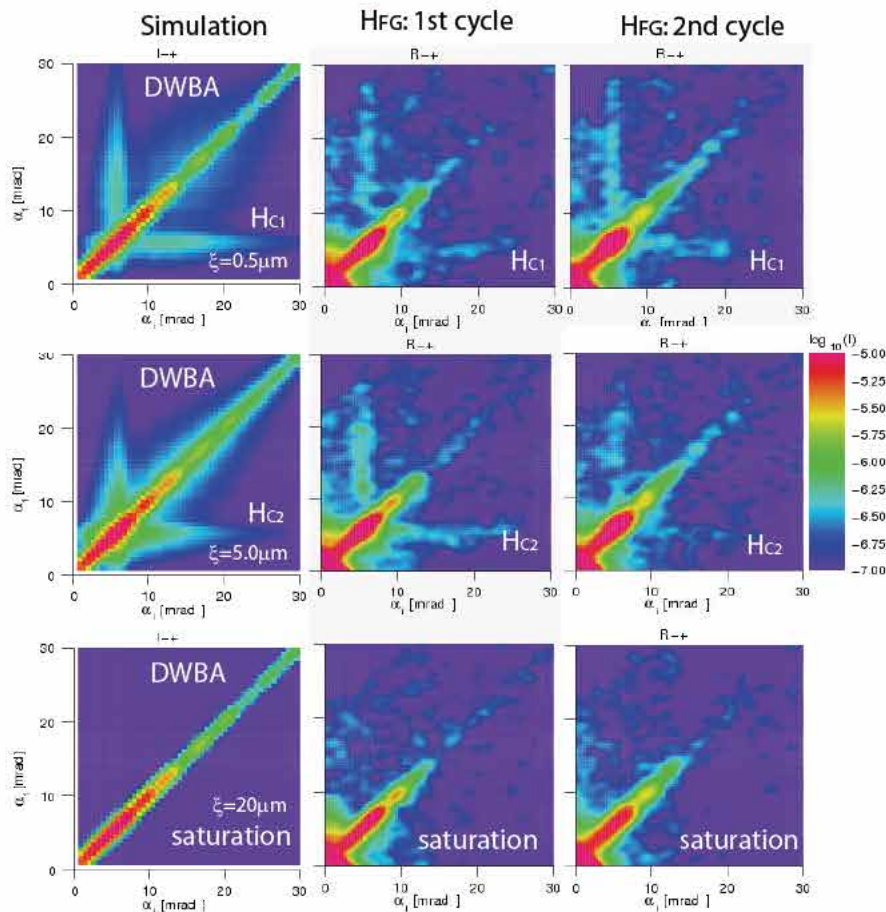


Figure 1: SF intensity maps from representative IrMn/CoFe samples for the field growth condition and measured at the coercive fields HC1 (along the first half of the first field cycle -untrained), HC2 (along the second half of the first field cycle) and that at saturation. The measurements for the second field cycle (trained) are also shown alongside along with DWBA simulated patterns. Here $\alpha_{i,e}$ are the incident and exit angles.

fining the unidirectional anisotropy on exchange coupling.

Using neutrons as a vector magnetometric probe
 IrMn(10nm)/CoFe(5nm)/Ta(8nm) films were deposited onto naturally oxidized Si(100) substrates with a buffer layer of 50 nm Cu. By applying a field during growth or during moderate energy (keV) ion irradiation on our specimens, we have redefined the unidirectional anisotropy apart from the usual field cooling. We used an ion source at the University of Kassel for the irradiation with 10 keV He⁺ ions. Depth sensitive vector magnetometry was carried out using polarized neutron scattering at the TREFF reflectometer at the MLZ. In our experiment four different cross sections can be distinguished, namely, non spin-flip (NSF) (R++ and R--) and spin-flip (SF) channels (R+- and R-) measuring the respective longitudinal and transverse component of magnetization with respect to the guiding field.

Simultaneous coherent rotation and domain process in reversal

The fitted values from the neutron scattering data show that there are no signatures of asymmetric reversal of magnetization in any of the specimens. Magnetization reversal takes place similarly along both branches of the hysteresis loop, irrespective of the biasing conditions. The measured SF intensity maps along with DWBA simulated patterns at around the coercive fields is shown in figure 1 for a field grown sample by way of an example. All specimens at their respective coercive fields exhibit a significant decrease in the magnetic scattering part of their scattering length. Such a decrease indicates a loss of net magnetization due to multiple-domain formation (nonuniform). At the same time, all specimens exhibit a significant increase in their SF signal, indicating coherent rotation (uniform). It is also evident that all specimens have undergone training after the first half of the first field cycle. [3]

The anisotropy energy creates barriers against the free rotation of the magnetization within a magnetic specimen, which lead to energeti-

cally preferred directions for the magnetization within individual single-domain grains. Here, we observe that the minimum energy path changes from coherent rotation to nucleation followed by domain wall motion until the whole magnetization is reversed. One can see that the energy for coherent rotation is almost similar in magnitude to that of the domain wall energy. This explains the simultaneous observation of a uniform and a nonuniform reversal mechanism in our samples as well as the symmetric loop shape.

Symmetry and asymmetry in reversal depends on the uniaxial anisotropy

Magnetization reversal for the specimen with or without the influence of any external field (either during the cooling process or during ion irradiation) indicates the coexistence of small scale and large scale domains. Whereas the smaller domains reverse via nucleation and wall motion, the larger domains reverse via coherent rotation along both branches of the hysteresis loop. Thus, a symmetric reversal mechanism is evident for a low anisotropic AF layered system. The training observed here is therefore due to a rearrangement of local anisotropic directions with respect to the applied field direction during growth and/or during the field cooling or ion-irradiation process upon field cycling. Training can be associated with the degree of variation of the mean magnetization direction as well as the variation in the domain configuration. The mechanism of reversal remains similar even during the first-loop training. Training observed by magnetometric methods can often be misleading and obscure. PNR and off-specular scattering measurements can together estimate the degree of training more precisely even when the reversal process is comprised of coherent rotation and domain nucleation and wall movement simultaneously.

[1] A. Paul et al, Appl. Phys. Lett., 95, 092502 (2009).

[2] A. Paul et al., New J. Phys., 13, 063008 (2011).

[3] A. Paul et al., Phys. Rev. B., 86, 094420 (2012).

Instability of the magnetic order in the distorted triangular lattice antiferromagnet $\alpha\text{-CaCr}_2\text{O}_4$

S. Tóth¹, B. Lake^{2,3}, K. Hradil⁴, A. T. M. N. Islam²

¹Paul Scherrer Institute, Villigen, Switzerland

²Helmholtz-Zentrum Berlin für Materialien und Energie GmbH, Berlin, Germany

³Technische Universität Berlin, Berlin, Germany

⁴Technische Universität Wien, Wien, Austria

We explored the excitation spectra of a distorted triangular lattice antiferromagnet $\alpha\text{-CaCr}_2\text{O}_4$. It has a unique distortion that is different from the extensively investigated isosceles triangular lattice. It develops long-range magnetic order with 120° angle between neighboring spins. Inelastic neutron scattering reveals unusual roton-like minima of the magnon dispersion at reciprocal space points different from those corresponding to the magnetic order. We show that these minima are due to the instability of the magnetic order against small perturbations of the Hamiltonian.

One of the simplest frustrated quantum magnetic model systems is the triangular lattice antiferromagnet, yet its properties are not fully understood. In contrast to the simple geometry, triangular lattice supports spin liquid states [1] and novel excitations such as Z_2 vortices [2] as a combined result of frustration, quantum and thermal fluctuations. Real materials typically have more complex magnetic interactions, such

as spatially anisotropic exchange or additional terms in the Hamiltonian such as the Dzyaloshinskii-Moriya interaction. These additional “complications” can introduce new and interesting physics, as is the case for $\alpha\text{-CaCr}_2\text{O}_4$. $\alpha\text{-CaCr}_2\text{O}_4$ has a distorted triangular lattice with spin-3/2 magnetic Cr^{3+} ions.

It has four inequivalent 1st neighbour direct exchange interactions that build up two zigzag and two straight chains running along the b -axis, see figure 1(a). In contrast to the low symmetry of the interactions, the magnetic ground state is identical to the isotropic triangular lattice, where the angle between neighboring spins is 120° [3]. Inelastic neutron scattering reveals the low symmetry of the magnetic exchange interactions.

Inelastic neutron scattering at PUMA

The magnon spectra of $\alpha\text{-CaCr}_2\text{O}_4$ was measured at the PUMA thermal triple axis spectrometer. The sample was a single crystal weighing 340 mg. It consists of three crystallographic twins rotated around the shared a -axis by 60° . To measure the magnetically ordered state, the sample was

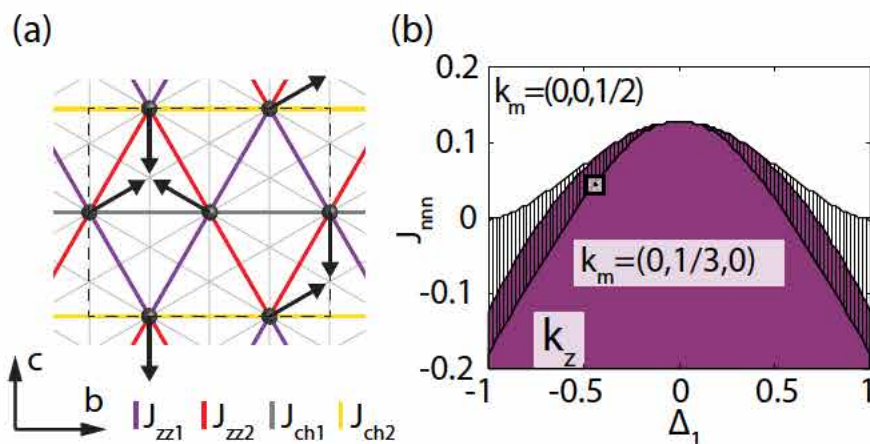


Figure 1: (a) Ordered magnetic structure of a Cr^{3+} triangular layer. Black arrows denote the 120° spin order. (b) Slice of the magnetic phase diagram as a function of the difference between the two zigzag exchanges ($\Delta_1 \sim J_{zz1} - J_{zz2}$) and the average of the 2nd neighbour interactions. Plain purple region denotes the 120° ordered phase. From Ref. [4].

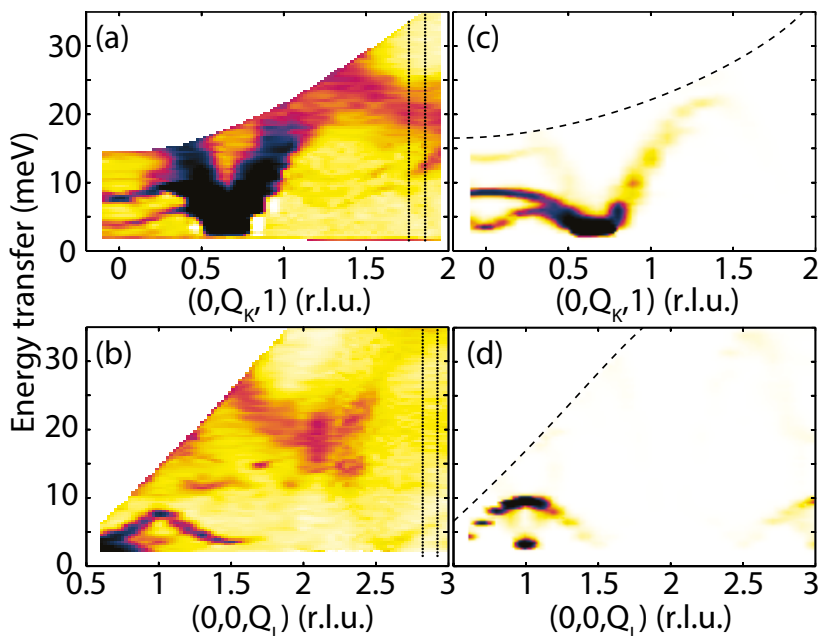


Figure 2: (a-b) Inelastic neutron spectra measured at PUMA along two perpendicular directions in reciprocal space. Note that the weaker broad intensity at high Q is due to phonon scattering. (c-d) Calculated LSWT spectra. From Ref. [4].

cooled to the base temperature of 3.5 K. The final neutron wavelength was fixed at $k_F=2.662 \text{ \AA}^{-1}$ and the energy resolution was 0.75 meV. Constant Q scans were performed in the $(0, 0, Q_L)$ and $(0, Q_K, 1)$ planes, see figure 2(a - b). To separate the magnon and phonon signals, several scans were repeated above the magnetic ordering temperature at 200 K.

Magnon modes with local minima

$\text{-CaCr}_2\text{O}_4$ has a complex low temperature spectrum. It contains several overlapping magnon modes due to the large magnetic unit cell and the three crystallographic twins. The strong cone shaped dispersion centered at $(0, 2/3, 1)$ is the legacy of the isotropic triangular lattice; see fig. 2(a). The small 4 meV gap at $(0, 2/3, 1)$ is due to the antiferromagnetic inter-plane coupling. The striking feature of the spectrum is the two sharp modes with local minima at $(0, 0, 1)$ in the Q_K plane; see figure 2(b). In the $(0, 0, Q_L)$ plane, the upper one has a maximum while the lower has a minimum.

Evidence of distortion

These modes provide evidence of the distortion. The measured inelastic data were fitted using linear spin wave theory (LSWT) that well describes the two low energy modes; see figure 2(c - d).

The values of the 1st and 2nd neighbour interactions could be extracted from the fit. The results confirm that the 1st neighbour interactions are a direct exchange, as they depend strongly on the distance between interacting ions (the Cr^{3+} - Cr^{3+} distances range between 2.889 and 2.939 Å). The fit also places $\text{-CaCr}_2\text{O}_4$ on the magnetic phase diagram to the edge of the 120° magnetic phase as a function of the 1st and 2nd neighbour interactions, see Figure 1(b) – white square.

Possibility to observe quantum phase transition
A small increase in the 2nd neighbour interaction or the distortion parameter Δ , would drive the system into a new ordered state with multi- k magnetic structure (shaded region). This opens up the possibility of investigating the quantum phase transition by applying pressure or doping the non-magnetic Ca site.

[1] L. Balents, Nature, 464, 199 (2010).

[2] H. Kawamura et al., J. Phys. Soc. Jpn., 79, 023701 (2010).

[3] S. Toth et al., Phys. Rev. B, 84, 054452 (2011).

[4] S. Toth et al., Phys. Rev. Lett., 109, 127203 (2012).

Roton-phonon interactions in superfluid ^4He

B. Fåk¹, T. Keller^{2,3}, M. E. Zhitomirsky¹, A. L. Chernyshev⁴

¹CEA Institut Nanosciences et Cryogénie, Statistical Physics, Magnetism and Superconductivity, Grenoble, France

²Max-Planck-Institut für Festkörperforschung, Stuttgart, Germany

³Technische Universität München, Forschungs-Neutronenquelle Heinz Maier-Leibnitz (FRM II), Garching, Germany

⁴University of California, Department of Physics and Astronomy, Irvine, USA

We have used the high-resolution neutron resonance spin-echo spectrometer TRISP to study the energy and lifetime of rotons in superfluid ^4He , the archetype of a Bose-condensed system. We find that the roton energy does not have the same temperature dependence as the roton line width. This effect can be understood quantitatively in terms of roton-phonon interactions involving both four- and three-particle processes. The latter process is characteristic of the Bose condensate, and our results are expected to have wide-ranging implications for other Bose-condensed systems.

One of the most important concepts in condensed matter physics is that of quasiparticles, which allows strongly correlated systems to be described in terms of weakly interacting quasiparticles. Well-known examples of quasiparticles are phonons in crystalline solids, magnons in magnetically ordered solids, heavy fermions in correlated metals, and spinons in spin-1/2

chains. The quasiparticle concept makes sense only if the quasiparticles are stable and long-lived. For fermionic systems, such as electrons in metals, the quasiparticles are only well-defined close to the Fermi surface. In this work we investigate the stability of the bosonic quasiparticles in superfluid ^4He , the prototype Bose-condensed system.

The quasiparticles in superfluid ^4He are called phonons and rotons, and their energy versus momentum relation (dispersion curve) measured by neutron scattering [1] is shown in figure 1. Phonons and rotons are essentially the same type of bosonic excitations, and belong to the same single continuous dispersion curve shown in the figure. However, they behave differently, since the phonons are long wavelength excitations analogous to massless phonons in solids while the rotons are heavy, almost localized atom-like excitations.

Unexpected temperature dependence

The most important process limiting the lifetime of the roton at temperatures of the order of 1 K is the scattering of a roton against a thermally excited roton. Such a four-particle process was predicted theoretically by Landau and Khalatnikov (LK) to introduce a finite line width of the excitation, simply proportional to the number of thermally excited rotons, which is given by an exponential law in temperature [2]. This effect was confirmed experimentally using the high-resolution neutron spin-echo technique [3]. It was also found that the energy of the roton shifted downwards, following a similar relation to the lifetime. The development of high-resolution neutron backscattering techniques for inelastic scattering confirmed the result for the roton lifetime [4].

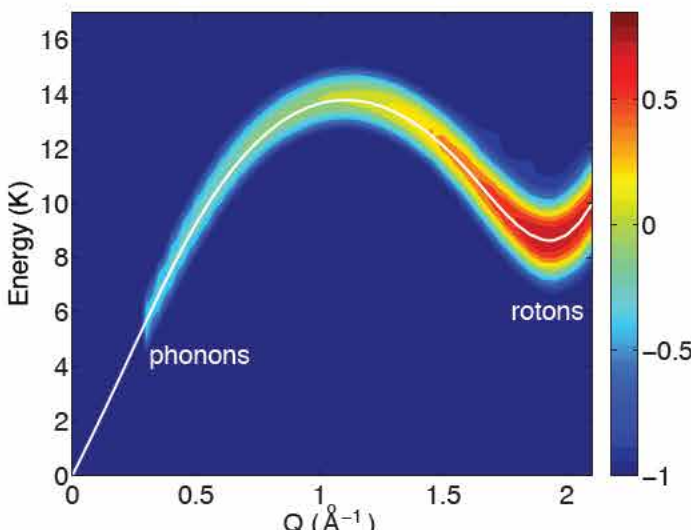


Figure 1: Phonon-roton dispersion in superfluid ^4He . The color coding corresponds to the logarithm of the intensity of neutrons scattered from the quasiparticles.

However, the roton energy had a different temperature dependence, in disagreement with both experimental and theoretical work.

To solve this longstanding enigma, we have performed high-resolution neutron resonance spin-echo measurements of superfluid ^4He using the thermal polarized neutron triple-axis spectrometer TRISP. Due to a specific design of the radio-frequency coils, TRISP offers unprecedented precision in determining small energy shifts, at the same time as the lifetime of an excitation. The measurements were performed on bulk superfluid ^4He at temperatures between 0.5 and 1.6 K using a bespoke sample cell and gas-handling system. A final neutron energy of 6 meV was used in combination with a supermirror bender to analyze the neutron polarization. Radio frequencies between 60 and 300 kHz in both boot-strap and non-boot-strap mode covered spin-echo times between 15 and 190 ps, resulting in a precision of the roton energy shift and line broadening of 0.0002 meV.

Repulsive roton-phonon interaction

The measurements show that the roton energy initially increases with increasing temperature, before it decreases at higher temperatures according to the LK expression, while the roton line width increases continuously (fig. 2) [5]. These results are consistent with those of [4]. A non-monotonous energy shift implies that more than one mechanism is involved, and the most likely candidate is the interaction of rotons with thermally excited phonons. To explain our experimental findings, we analyzed systematically all low-order self-energy contributions using modern diagrammatic methods [5]. We find that while the roton-roton scattering process considered by LK dominates at temperatures above 1 K, roton-phonon processes become increasingly important at lower temperatures. Our calculations show that the roton-phonon interaction gives a leading T^4 power law to the energy shift, in agreement with experiment, while the same processes only give rise to an insignificant T^7 contribution to the line width (fig. 2).

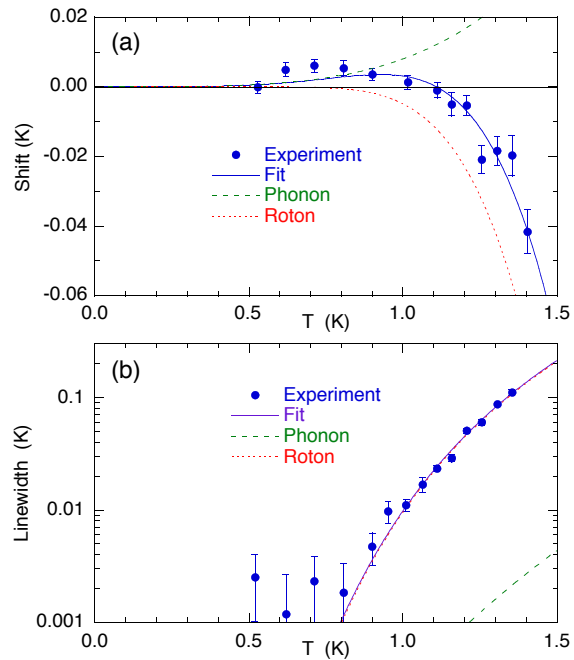


Figure 2: Temperature dependence of (a) the roton energy shift and (b) the roton line width. Symbols are experimental data and lines a fit to the theory, with red dotted line being the roton-roton contribution, green dashed line the roton-phonon contributions, and blue solid line the sum of the two.

The initial increase of the roton energy with increasing temperature implies that the net roton-phonon interaction is repulsive, rather than attractive as has been thought until now, and also in contrast to the roton-roton interaction, which is attractive. Our quantitative analysis also highlights the importance of three-particle processes, which are characteristic of the broken gauge symmetry of the Bose condensate. This is expected to have a wide-ranging impact on Bose-condensed systems in general, such as excitons in semiconductors, magnon decay, nonlinear effects in spintronics, and strongly interacting ultracold Bose gases.

[1] K. H. Andersen et al., J. Phys.: Condens. Matter, 6, 821 (1994).

[2] L. D. Landau and I. M. Khalatnikov, Zh. Eksp. Teor. Fiz., 19, 637 (1949).

[3] F. Mezei, Phys. Rev. Lett., 44, 1601 (1980).

[4] K. H. Andersen et al., Phys. Rev. Lett., 77, 4043 (1996).

[5] B. Fåk et al., Phys. Rev. Lett., 109, 155305 (2012).

Bond randomness induced magnon decoherence in a spin-1/2 ladder compound

B. Náfrádi¹, T. Keller¹, H. Manaka², U. Stuhr³, A. Zheludev⁴, B. Keimer¹

¹Max-Planck-Institut für Festkörperforschung, Stuttgart, Germany

²Kagoshima University, Graduate School of Science and Engineering, Kagoshima, Japan

³Paul Scherrer Institute, Laboratory for Neutron Scattering, Villigen, Switzerland

⁴ETH Zürich, Laboratorium für Festkörperphysik, Neutron Scattering and Magnetism Group, Zürich, Switzerland

Quantum systems with long-living coherent states are proposed for use in quantum computing. However, finite coherence lengths and thus decoherence limit the time frame for information storage and manipulation. We have used a combination of neutron resonant spin-echo (NRSE-TAS) and triple-axis spectroscopies (TAS) to determine the magnon decoherence in IPA-Cu(Cl_{0.95}Br_{0.05})₃, a model spin-1/2 ladder antiferromagnet where Br substitution induces bond randomness. We find that the bond defects induce a blueshift, $\delta\Delta$, and broadening, $\delta\Gamma$, of the magnon gap excitation compared to the pure compound. At temperatures exceeding the energy scale of the inter-ladder exchange interactions, $\delta\Delta$ and $\delta\Gamma$ are temperature independent. Upon cooling, $\delta\Delta$ and $\delta\Gamma$ become temperature dependent and saturate at values lower than those observed at higher temperature, consistent with the crossover from one-dimensional to two-dimensional spin correlations with decreasing temperature previously observed in pure IPA-CuCl₃.

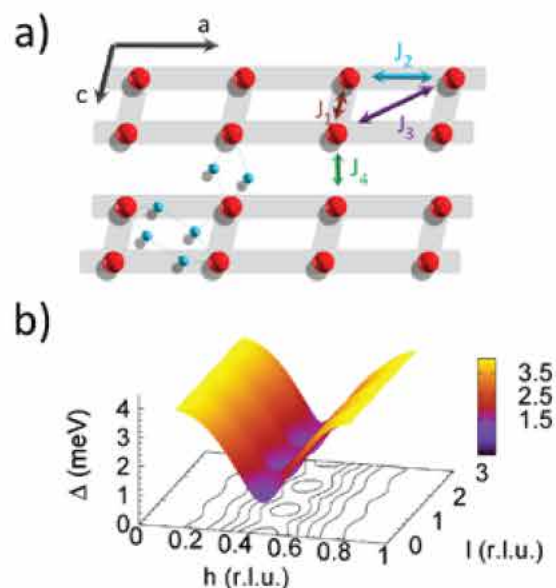


Figure 1: (a) Schematic view of the a-c plane of IPA-Cu(Cl:Br)₃. The ladder structure is highlighted in gray. Cu atoms are represented by red. Cl and Br positions represented by blue. The arrows show the exchange interactions: $J_1 = -2.3$ meV, $J_2 = 1.2$ meV, $J_3 = 2.9$ meV and $J_4 = -0.3$ meV. (b) Color plot of the magnon dispersion.

thus observables such as the energies, Δ , and linewidths, Γ , of the magnons depend solely on T/Δ_0 [1,2,3].

A simple yet effective picture is that magnons are confined into finite 1D potential “boxes”, defined by both static and dynamic defects. The goal of our experiments is to test the applicability of this simple rule for the energy, Δ , and width, Γ , of the magnon resonance in a disordered $S = 1/2$ ladder system.

NRSE spectroscopy

IPA-Cu(Cl_{0.95}Br_{0.05})₃ is an excellent model system to experimentally study the effect of bond disorder on the Δ and Γ of the magnon resonance in gapped quantum spin liquids. The structure is

Magnon in a potential box

One-dimensional (1D) spin liquids, such as $S = 1$ chains or $S = 1/2$ ladders with antiferromagnetic interactions, have emerged as important model systems for the study of long-range quantum coherence. These systems have collective spin-singlet ground states. Their magnetic excitations are mobile “magnon” quasiparticles, with a gap Δ_0 even for temperature $T \rightarrow 0$. In an ideally clean system, the magnon mean free path is infinitely long at $T = 0$. At $T > 0$, theoretical work based on the non-linear sigma model (NLoM) predicts that the T -dependent coherence length, and

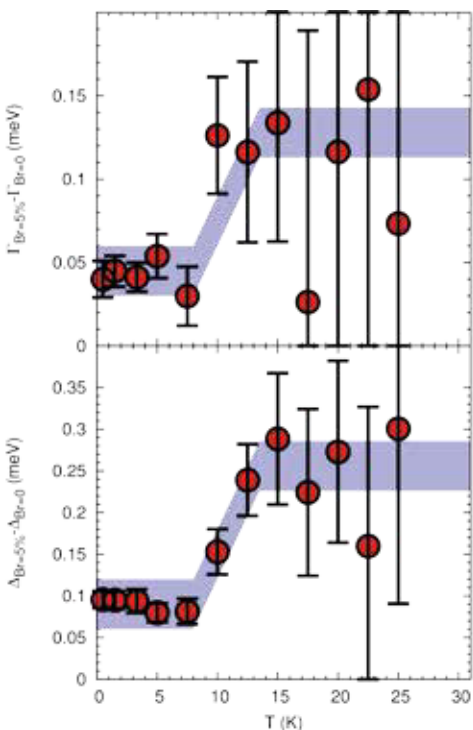


Figure 2: (a) Temperature dependence of the bond randomness induced magnon blueshift of IPA-Cu($\text{Cl}_{0.95}\text{Br}_{0.05}$)₃. (b) Temperature dependence of the magnon decoherence induced by bond randomness of IPA-Cu($\text{Cl}_{0.95}\text{Br}_{0.05}$)₃. The broad shaded lines are a guide for the eyes. Line used in panel-b is the same as in panel-a but divided by a factor 2.

depicted in figure 1a [4]. The Cu²⁺ ions carry a spin S = 1/2 and form ladders along the a axis. Exchange interactions within these Cu²⁺ ions are mediated by Cl di-bridges. Substituting Cl with Br results in a substantial change in the interaction strength [4], but IPA-Cu($\text{Cl}_{0.95}\text{Br}_{0.05}$)₃ remains in a gapped quantum spin liquid state (fig. 1b).

NRSE-TAS experiments at TRISP

The NRSE-TAS experiments were performed on the TRISP spectrometer at MLZ in Garching, Germany. The energy resolution of these measurements was about 1 μeV [3]. The TAS measurements were carried out at the TASP spectrometer at PSI in Villigen, Switzerland. The energy resolution of this setup was about 0.16 meV.

Magnon decoherence and dimensional crossover

In IPA-Cu($\text{Cl}_{0.95}\text{Br}_{0.05}$)₃, Δ and Γ is always larger, but its temperature evolution is similar to that of the pure compound (fig. 2a and fig. 2b respectively). Furthermore, $\delta\Delta$ and $\delta\Gamma$ show very similar

behavior in the entire T-range. For T > 13 K, $\delta\Delta$ and $\delta\Gamma$ is T-independent within our experimental precision. Upon lowering T, both $\delta\Delta$ and $\delta\Gamma$ drop in a narrow T-range of 8 < T < 13 K. For T < 8 K, $\delta\Delta$ and also $\delta\Gamma$ saturate at ~ 0.1 meV and ~ 0.05 meV respectively.

The observation of approximately T-independent values of $\delta\Delta$ and $\delta\Gamma$ in IPA-Cu($\text{Cl}_{0.95}\text{Br}_{0.05}$)₃ at high-T is qualitatively consistent with the NLoM, and with Matthiessen's rule[5]. Written in terms of the magnon mean free path, L, this rule stipulates that $L^{-1} = L_d^{-1} + L_s^{-1}$, where L_d and L_s arise from magnon-magnon and magnon-defect collisions, respectively. At high temperatures, the T-dependence of L arises solely from L_d , which is well described by the NLoM. We can thus compare our experimental data to the results of Monte Carlo calculations for finite S = 1 chains, which yield a chain length of $L_s \sim 10a$. A similar estimate can be made on the basis of the broadening, which translates into $L_s \sim 22a$ [5].

In the low-T limit, L is expected to be dominated by L_s . The observation of T-independent values of $\delta\Delta$ and $\delta\Gamma$ for T ≤ 8 K is consistent with this expectation. The reduced values of $\delta\Delta$ and $\delta\Gamma$ at low, compared to those observed in the high-T regime, are in qualitative agreement with the dimensional crossover picture developed for IPA-CuCl₃[3].

At temperatures 8 K < T < 13 K, $\delta\Delta$ and $\delta\Gamma$ are strongly T-dependent, which indicates that the simple Matthiessen's rule no longer applies in this regime, where dimensional crossover phenomena occur. We hope that our data will stimulate further experimental and theoretical work on dimensional crossover phenomena and their influence on the magnon spectrum and magnon-mediated thermal transport in IPA-CuCl₃ and other quasi-1D quantum magnets.

[1] D. Senechal, Phys. Rev. B 48, 15880 (1993).

[2] G. Y. Xu et al., Science, 317, 1049 (2007).

[3] B. Náfrádi et al., Phys. Rev. Lett., 106, 177202 (2011).

[4] H. Manaka et al., Phys. Rev. B, 73, 104407 (2006).

[5] B. Náfrádi et al., Phys. Rev. B, 87, 020408(R) (2013).

Depth profiles of LSMO/SRO films

J.-H. Kim¹, I. Vrejoiu², Y. Khaydukov^{1,5}, T. Keller^{1,5}, J. Stahn³, A. Rühm^{4,5}, D.K. Satapathy⁶, V. Hinkov^{1,7}, B. Keimer¹

¹Max-Planck-Institut für Festkörperforschung, Stuttgart, Germany

²Max-Planck-Institut für Mikrostrukturphysik, Halle, Germany

³Paul Scherrer Institut, Laboratory for Neutron Scattering, Villigen, Switzerland

⁴Max-Planck-Institut für Intelligente Systeme, Stuttgart, Germany

⁵Technische Universität München, Forschungs-Neutronenquelle Heinz Maier-Leibnitz (FRM II), Garching, Germany

⁶University of Fribourg, Department of Physics and Fribourg Centre for Nanomaterials, Fribourg, Switzerland

⁷University of British Columbia, Quantum Matter Institute, Vancouver, Canada

The magnetic depth profiles on superlattices composed of the two ferromagnets $\text{La}_{0.7}\text{Sr}_{0.3}\text{MnO}_3$ (LSMO) and SrRuO_3 (SRO) were investigated using spin polarized neutron reflectivity. In combination with magnetometry, the neutron data indicates that there is antiferromagnetic coupling between LSMO and SRO and that each SRO layer has a modulated magnetic structure with enhanced magnetization at the interfaces. We suggest that the combined effects of antiferromagnetic exchange interactions of the Mn and Ru moments across the interface, and the magnetocrystalline anisotropy of the Ru moments, determine the spin structure.

Superlattices composed of two ferromagnets
Transition-metal-oxides are used when looking for new quantum states at the interfaces between different material layers, since these materials exhibit a broad spectrum of appealing electronic and magnetic properties. For example, $\text{La}_{0.7}\text{Sr}_{0.3}\text{MnO}_3$ (LSMO) and SrRuO_3 (SRO) are both perovskites with bulk ferromagnetic Curie temperatures of 364 K and 163 K, respectively [1,2]. However, in LSMO/SRO heterostructures, there is a strong anti-ferromagnetic interlayer coupling below the Curie temperatures of the SRO layer ~ 150 K (fig. 1) [3]. Motivated by these

results, we have carried out a specular polarized neutron reflectivity (PNR) study of the magnetization profiles in LSMO/SRO superlattices.

Experiments at NREX

The high-quality $[\text{LSMO} (2 \text{ nm}) / \text{SRO} (5 \text{ or } 8 \text{ nm})]_{15}$ superlattices (SL2/5 and SL2/8) on vicinal TiO_2 -terminated SrTiO_3 (100) substrates were used for the PNR measurements. The experiments were performed at NREX at MLZ and at AMOR at SINQ. For the NREX measurements, the neutron wavelength was set to $\lambda = 4.32 \text{ \AA}$ and both polarizer and analyzer were used to observe non-spin-flip channels (R^{++} and R^- , which originate from the nuclear structure and the in-plane magnetic components parallel to the applied field). The external magnetic field, $H = 0.1 \text{ T}$, was applied perpendicular to the scattering plane and parallel to the film surface.

Non collinear magnetic structures in LSMO/SRO

Our PNR spectra of SL2/5 taken at 3 K (fig. 2) show a clear difference between the intensities of the R^{++} and R^- reflections. To understand this result, we tested several models for the fit of the data. The solid lines in figure 2 (a)-(d) are the results of the fit and the corresponding magnetic depth profiles are illustrated in the bottom row. As a starting point, we constrained the magnetic profiles of SRO to be homogeneous. As shown in figure 2 (a), the model provides a poor fit. To improve the fit, we allowed the magnetization of the SRO to vary. The enhanced magnetization at the LSMO/SRO interface provides a well matched fit (fig. 2(b)), while a magnetic model with a suppressed magnetization near the interfaces (fig. 2(c)) failed to yield satisfactory agreement with the data. To further refine our fit, we used a model with a variation of the magnetiza-

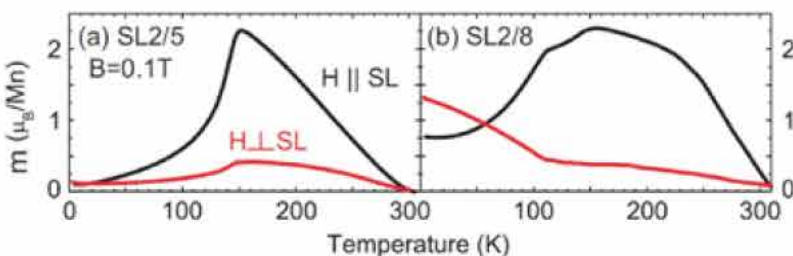


Figure 1: Magnetization curves of superlattices (a) SL2/5 and (b) SL2/8 with 0.1 T.

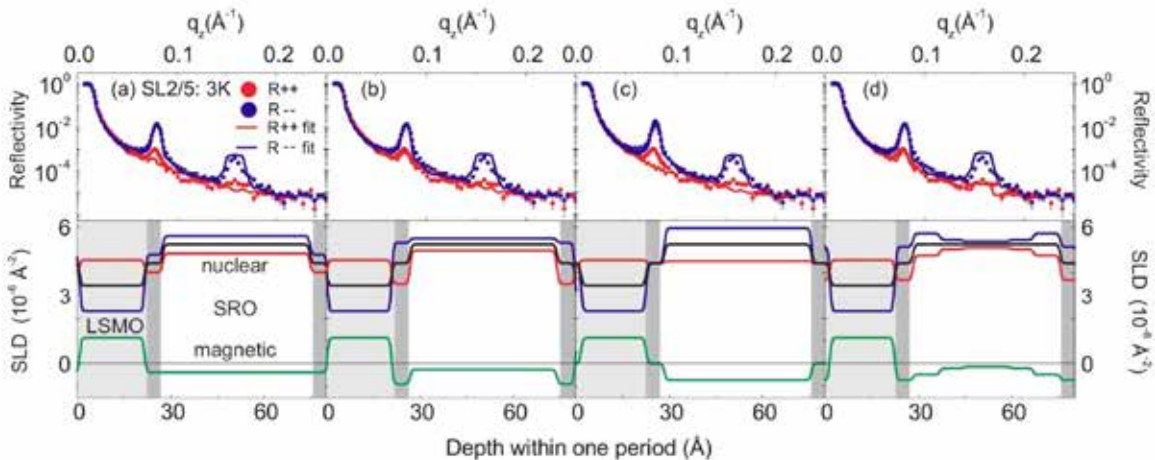


Figure 2: PNR spectra of SL2/5 at 3 K.

tion within the SRO layer. Figure 2(d) shows that the magnitude of the in-plane magnetization is reduced to almost zero around the center of the SRO layer. Compared to figure 2(b), this model provides an improved fit.

magnetization of single SRO films. Mn moments orient more easily in plane, and when approaching the interfaces, the Ru moments are forced into an in-plane configuration by the Mn-Ru coupling which dominates over the magnetocrystal-

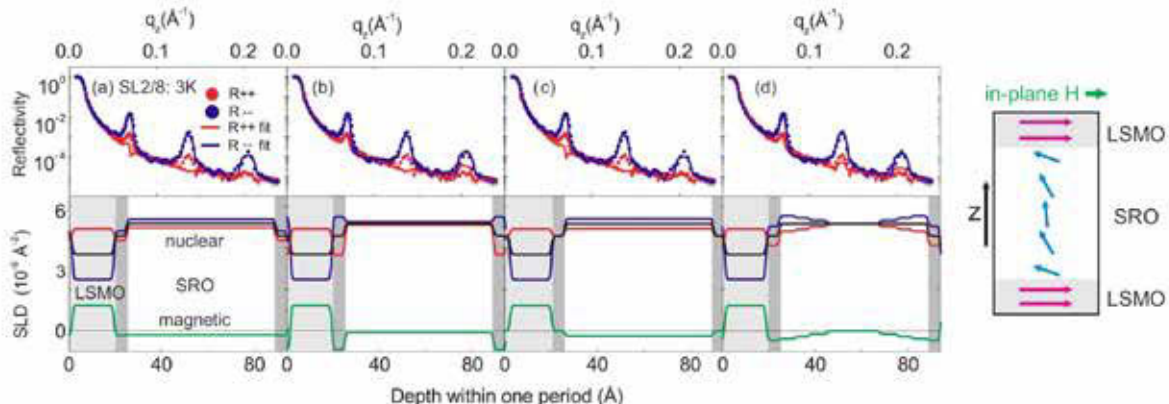


Figure 3: PNR spectra of SL2/8 at 3 K. The sketch shows a schematic of the spin configuration below the Curie temperature of SRO.

Analogous data analysis was performed on SL2/8 (fig. 3). The three models with homogeneous SRO magnetization produce equally poor fits (fig. 3(a)-(c)). In contrast, the second-order superlattice peak is significantly better fitted by a magnetization profile of figure 3(d).

While PNR is only sensitive to the in-plane component of magnetic moments, the combination of PNR and magnetometry data indicates that the magnetization profile is determined by the interplay of the Mn-Ru antiferromagnetic exchange coupling at the interfaces and the magnetocrystalline anisotropy of the SRO layers. The latter effect is known to result in an out-of-plane

line anisotropy. It yields a non-collinear magnetization profile as shown in the sketch of figure 3.

Conclusion

Our data indicate the formation of a non-collinear magnetic structure in the SRO layers of a LSMO/SRO superlattice. It is closely related to the “exchange spring” structures previously observed in multilayers composed of ferromagnetic elements and alloys [4].

[1] Y. Moritomo, et. al., Phys. Rev. B, 51, 16491 (1995).

[2] A. Kanbayasi, J. Phys. Soc. Jpn, 41, 1876 (1976).

[3] M. Ziese, et. al., Phys. Rev. Lett., 104, 167203 (2010).

[4] J-H. Kim, et. al, Phys. Rev. B, 86, 180402(R) (2012).

Competition between crystal electrical field shift and Kondo screening in $\text{CeNi}_9\text{Ge}_{4-x}\text{Si}_x$

C. Gold¹, G. G. Simeoni², W. Scherer¹, E.-W. Scheidt¹

¹Universität Augsburg, Institut für Physik, Chemische Physik und Materialwissenschaften, Augsburg, Germany

²Technische Universität München, Forschungs-Neutronenquelle Heinz Maier-Leibnitz (FRM II), Garching, Germany

The pseudo-ternary solid solution $\text{CeNi}_9\text{Ge}_4\text{Si}_x$ ($0 \leq x \leq 4$) has been investigated by means of X-ray diffraction, magnetic susceptibility, specific heat, electrical resistivity, thermopower and inelastic neutron scattering studies. The isoelectric substitution of Germanium by Silicon atoms causes a dramatic change in the relative strength of competing Kondo, RKKY and crystal field (CF) energy scales, as underlined by quasi-elastic and inelastic neutron scattering investigations carried out at the time-of-flight spectrometer TOFTOF.

CeNi_9Ge_4 is an outstanding Fermi liquid compound which is positioned at the borderline to a non Fermi-liquid state. So far, it exhibits the largest ever recorded Sommerfeld coefficient

$\gamma = 5.5 \text{ J/mol/K}^2$ at 0.08 K among paramagnetic Ce compounds [1]. This behavior is mainly driven by local magnetic fluctuations. The $J=5/2$ ground state of the Ce^{3+} ion splits in a tetragonal crystal field, generated by the squareantiprismatic environment, into three Kramer's doublets. The two lowest doublets reveal a minute energetic separation of $\Delta_1 \approx 6 \text{ K}$ and are energetically well separated from the higher one ($\Delta_2 \approx 128 \text{ K}$) [2]. Due to the fact that the Kondo energy $T_K = 3.5 \text{ K}$ is of the same order of magnitude as Δ_1 , the first excited doublet contributes significantly to the Kondo ground state. As the splitting of the two Kondo broadened low lying doublets is neither resolved in specific heat nor by cold neutron inelastic scattering, we denote the crystal field ground state as a quasi-quartet (effectively four-fold degenerate N) [3]. Recently, we reported for

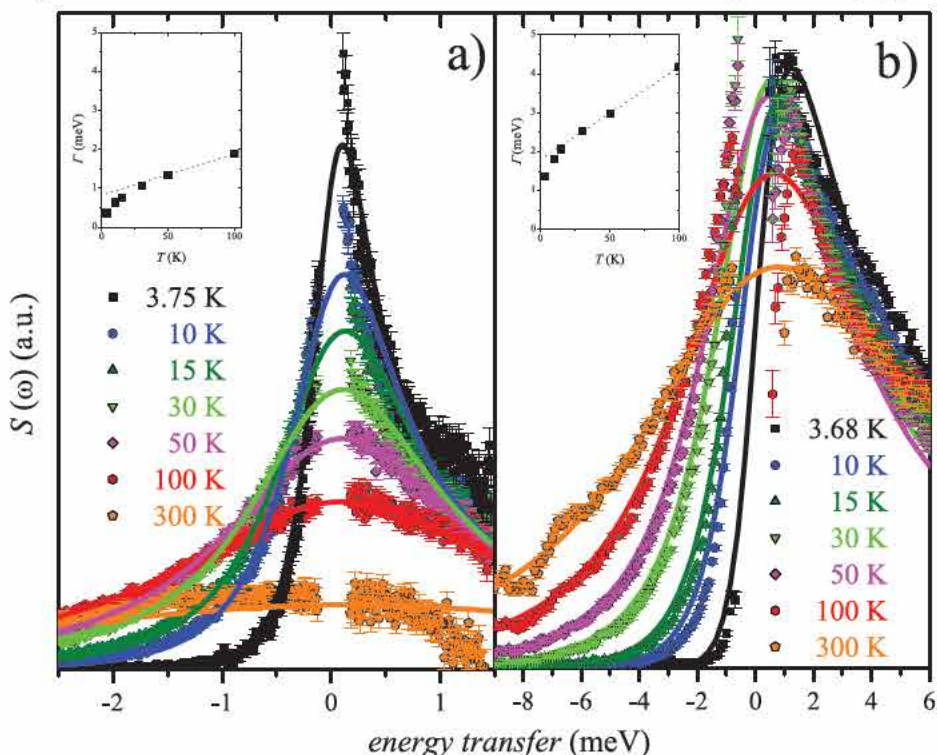


Figure 1: The magnetic correlation function $S(\omega)$ at selected temperatures as labelled for a) $\text{CeNi}_9\text{Ge}_{3.9}\text{Si}_{0.1}$ and b) $\text{CeNi}_9\text{Ge}_3\text{Si}$ (the lines represent Lorentzian fits). The inserts show the T dependence of the line widths, $\Gamma(T)$ obtained from the Lorentzian fits [5].

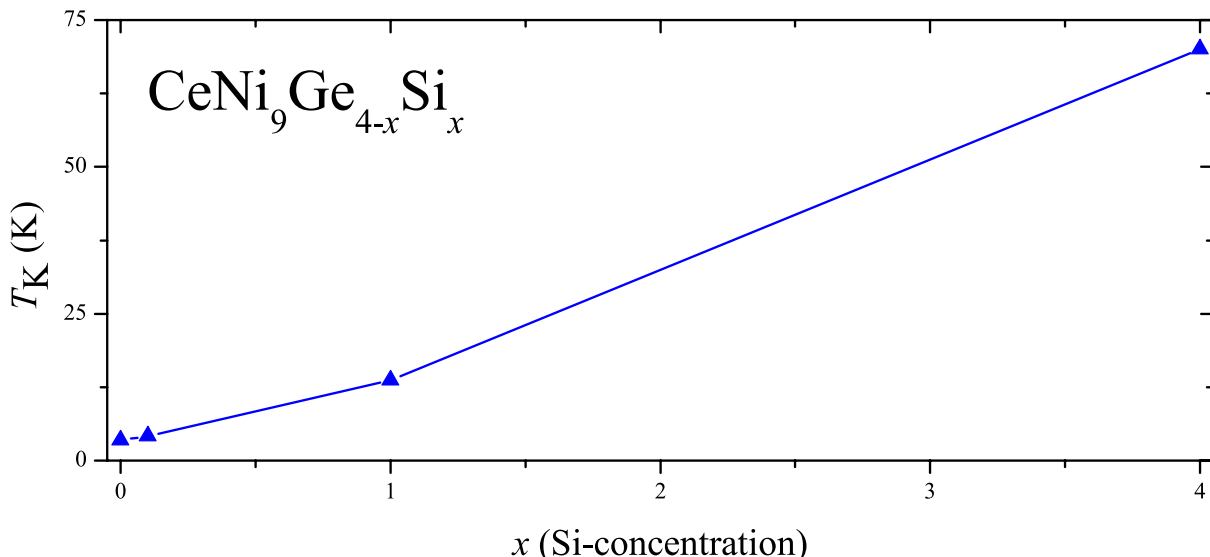


Figure 2: The Si-concentration x dependent Kondo temperature.

$\text{CeNi}_{9-x}\text{Cu}_x\text{Ge}_4$ that the change of N by shifting the first excited doublet to higher energies enforces the system towards a quantum critical point [2, 4]. To gain more insight into the fluctuation spin dynamics of the CeNi_9Ge_4 ground state, we studied the $\text{CeNi}_9\text{Ge}_{4-x}\text{Si}_x$ substitution series [5]. The quasi-elastic (QENS) and inelastic neutron scattering experiments were performed at the time-of-flight spectrometer TOFTOF at the MLZ. Specifically, the magnetic contribution to the QENS broadening provides information about the Kondo temperature, whereas the crystal field levels can be observed as gapped dispersionless inelastic excitations. CeNi_9Si_4 is a model-type Kondo lattice system ($\gamma = 155 \text{ mJ/mol/K}^2$) which can be well described by a six-fold degenerate Coqblin-Schrieffer model [6]. A strong volume decrease of about 5.6 % by the substitution of Ge for Si indicates an increasing $T_K(x)$ in the Doniach picture. In contrast to this, specific heat $C(T)$ and resistivity $\rho(T)$ studies indicate that, below the Si-concentration $x = 0.5$, T_K decreases with increasing x , while this trend is reversed for $x > 0.5$. To clarify this unusual scenario, inelastic neutron scattering measurements were performed. From the quasielastic correlation function $S(\omega)$ (fig. 1) and the resulting temperature dependent line widths $\Gamma(T)$ (inserts in fig. 1), the Kondo temperatures are determined for $\text{CeNi}_9\text{Ge}_{3.9}\text{Si}_{0.1}$ $T_K = 4.2 \text{ K}$ and $\text{CeNi}_9\text{Ge}_3\text{Si}$

$T_K = 13.7 \text{ K}$. As plotted in figure 2, these temperatures are in agreement with those Kondo temperatures determined from single crystal susceptibility data ($x = 0$) and specific heat investigations using the Coqblin-Schrieffer model [6]. These results support a continuous increase of $T_K(x)$. Therefore, we conclude that the observed discontinuity of $T_K(x)$ is due to the interplay between the Kondo screening and the change of the CF scheme, which initially leads to an incipient reduction of the quasi-fourfold ground state degeneracy towards a lower ($N < 4$) interstitial state on the Ge-rich side, finally followed by an ensuing sixfold increase [5].

- [1] U. Killer et al., Phys. Rev. Lett., 92, 27003 (2004).
- [2] L. Peyker et al., Europhys. Lett., 93, 37006 (2011).
- [3] E.W. Scheidt et al., Physica B, 154, 378 (2006).
- [4] L. Peyker et al., J. Phys.: Condens. Matter, 21, 235604 (2009).
- [5] C. Gold et al., J. Phys.: Condens. Matter, 24, 355601 (2012).
- [6] H. Michor et al. Phys. Rev. B, 67, 224428 (2003).

Direct manipulation of the uncompensated spins in an exchange coupled system

A. Paul¹, N. Paul², S. Mattauch³, C. Trautmann⁴, P. Böni¹

¹Technische Universität München, Physik-Department E21, Garching, Germany

²Helmholtz-Zentrum Berlin für Materialien und Energie GmbH, Berlin, Germany

³Forschungszentrum Jülich GmbH, Jülich Centre for Neutron Science at MLZ, Garching, Germany

⁴GSI Helmholtzzentrum für Schwerionenforschung GmbH, Darmstadt, Germany

Incident ion energy to matrix electrons of a material is dissipated within a narrow cylinder surrounding a swift heavy ion path. The temperature of the lattice exceeds the melting point and, upon quenching, causes nanometric modifications. We present here a unique ex situ approach in manipulating the uncompensated spins in antiferromagnetic layers of ferro-/antiferromagnetic (CoO-Co) exchange coupled systems on a nanometric scale. We use the impact of relativistic heavy ion (GeV) irradiation on such systems. This study demonstrates the possibility of nanoscale tailoring of exchange coupled systems that survive even in the trained state.

High energy ions on exchange bias

It has previously been shown that the coercive field and magnetic anisotropy of magnetic multilayers (MLs) can be accurately controlled by low energy irradiation in the elastic, or by high energy ions, in the inelastic regime. [1] In particular, local manipulations of magnetization in the

inelastic regime are (a) confined to a few nanometers only (b) without significant modification of the interface structure, and (c) applicable for ex situ changes. Thus, irradiation techniques offer a means of magnetic-tailoring devices in information technology such as in an exchange biased system. [2] In this work, we demonstrate a unique way of affecting the uncompensated AF spins of an archetypical exchange coupled system as we irradiate it with GeV energy ions.

Using neutrons as a depth resolved probe

We have investigated a multilayer of the composition $\text{SiO}_2/\text{[Co}(11\text{nm})/\text{CoO}(5\text{nm})/\text{Au}]x16$. Irradiations were performed at GSI Helmholtzzentrum für Schwerionenforschung. The ion fluences used were $1 \cdot 10^{12}$, and $1 \cdot 10^{13}$ ions/ cm^2 for 8.4 MeV/amu of ^{197}Au (1.6 GeV) and ^{238}U (2 GeV) ions. Depth sensitive vector magnetometry was carried out using polarized neutron scattering at the TREFF reflectometer at the MLZ. In our experiment four different cross sections can be distinguished, namely, non spin-flip

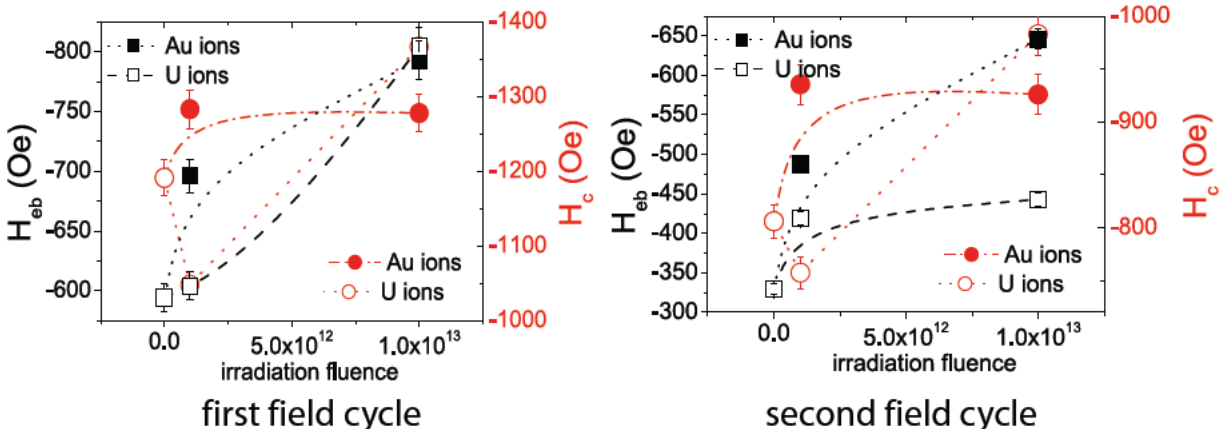


Figure 1: Plots of H_θ (squares) and H_c (circles) as a function of irradiation fluence of Au and U ions respectively during the first and second hysteresis field cycles after field cooling to 10 K.

(NSF) (R_{++} and R_{--}) and spin-flip (SF) channels (R_{+-} and R_{-+}), measuring the respective longitudinal and transverse component of magnetization with respect to the guiding field. We used a cooling field 4 kOe down to 10 K directed along an in-plane direction for all specimens.

Variation in the layer magnetic profile

For the irradiated specimens, one can see an increase in the bias field H_{eb} and coercive field H_c as shown in figure 1.

Figure 2 shows the specular reflectivity data (NSF and SF) and the off-specular SF intensities corresponding to two different applied fields (H_a) for the $U 1 \cdot 10^{13}$ ions irradiated ML. We also plot the spin asymmetry (SA) signals (difference in R_{++} and R_{--} divided by the sum of the two) as we compare these with the as-deposited specimen at saturation. Relative variation of the multilayer Bragg peak intensities is quite evident here. Fits to the reflectivity data revealed a small increase in the AF layer (~2 nm) at the Co-CoO interface. The NSF intensity map shows vertically correlated multilayer interfaces added up in phase and forming the Bragg sheets in reciprocal space at the first Bragg peak position of 15 mrad. A small increase in the SF intensity at $Q = 0.02 \text{ \AA}^{-1}$, measured during the first field cycle close to the coercive field (as compared to that in saturation), is only due to an increased instability induced in the system as the layers are on the verge of flipping and cannot be attributed to coherent rotation of the layers (similar behavior is also observed during the second field cycle). This is further corroborated by an increase in the off-specular SF intensities near the critical edge around the coercive field, a signature typical of the random non-collinear arrangement of small scale (<1 μm) domains just before flipping. [3] Distorted wave Born approximation (DWBA) has been applied in simulating the corresponding SF intensity map.

Ex-situ magnetic tailoring

Ion-induced magnetic manipulation allows us to increase H_{eb} and recover untrained magnetization states in an otherwise trained exchange

coupled system. The method demonstrated here is limited to nanometric scale with little influence on their interface structure. Such local manipulation holds promise for post production extrinsic treatment of integrated magnetic memory devices or sensors by choosing “specific” (energy/nucleon) ion energies.

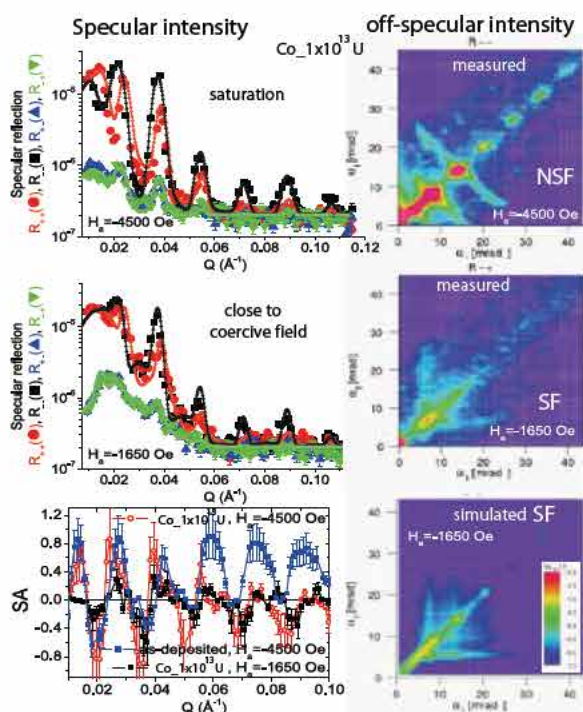


Figure 2: Specular reflectivity patterns (solid symbols) along with their fits (dashed lines) at two different applied fields, for the ML irradiated with $U 1 \cdot 10^{13}$ ions. The measurements were done during the first field cycle at field indicated after cooling the sample in field down to 10 K. $Q = 2\pi/\lambda(\sin\alpha_i + \sin\alpha_f)$, where α_{if} are the incident and exit angles. The SA signal is also plotted in the bottom panel for comparison with the as-deposited specimen. The right hand panels show the measured NSF and SF intensity maps along with DWBA simulated patterns at around the coercive field for the SF channel.

Proteins need it wet. Don't they ?

F.-X. Gallat¹, J. Wuttke², A. W. Perriman³, M. Weik¹

¹Institut de Biologie Structurale, Grenoble, France

²Forschungszentrum Jülich GmbH, Jülich Centre for Neutron Science at MLZ, Garching, Germany

³University of Bristol, Center for Organized Matter Chemistry, Bristol, UK

The water layer covering protein surfaces has long been thought of as being crucial for biological activity. But is water really necessary for macromolecular function? We investigated novel nano-materials that are hybrids of proteins surrounded by a 'corona' of polymer surfactant molecules. These nano-hybrids are devoid of any water, and yet, the protein moiety shows biological activity. By combining incoherent neutron scattering and specific deuteration, we found that the protein moiety undergoes motions similar to a hydrated protein, thus offering a rationale for the observed biological activity in the nano-hybrids.

As molecular workhorses, proteins fulfill a multitude of tasks that keep the complex machinery in biological cells alive. The cellular environment is highly hydrated and accordingly, the majority of proteins are bathed in water. A layer of hydration water molecules is connected to the protein surface via a fluctuating hydrogen-bonding network that allows the protein to undergo the conformational changes it requires for biological activity [1]. Hydration water is thus not merely a passive bystander, but rather an integral part of the biologically active protein. It is this delicately balanced give-and-take between a biological macromolecule's structural dynamics and those of its hydration water that governs macromolecular function in a cellular context [2]. But do proteins necessarily need it wet in order to be biologically active? The discovery of novel solvent-free protein-polymer nano-hybrids suggests they don't [3]. Despite the absence of water, indeed, myoglobin surrounded by a 'corona' of polymer surfactant molecules is still biologically active, i.e. remains capable of reversibly binding oxygen [4]. Yet, the molecular mechanism of biological activity in solvent-free protein-polymer nano-hybrids remained elusive and has now been addressed by combining incoherent neutron scattering and specific deuteration.

Incoherent neutron scattering reveals dynamics in a protein-polymer nano-hybrid

Elastic incoherent neutron scattering (EINS) on the backscattering spectrometers SPHERES (Jülich Centre for Neutron Science at MLZ) and IN16 (ILL) was employed to probe the ns-ps dynamics of a solvent-free myoglobin-polymer nano-hybrid (fig. 1; [5]). The EINS results revealed that the atomic mean square displacements (MSD) of a fully hydrogenated hybrid resemble

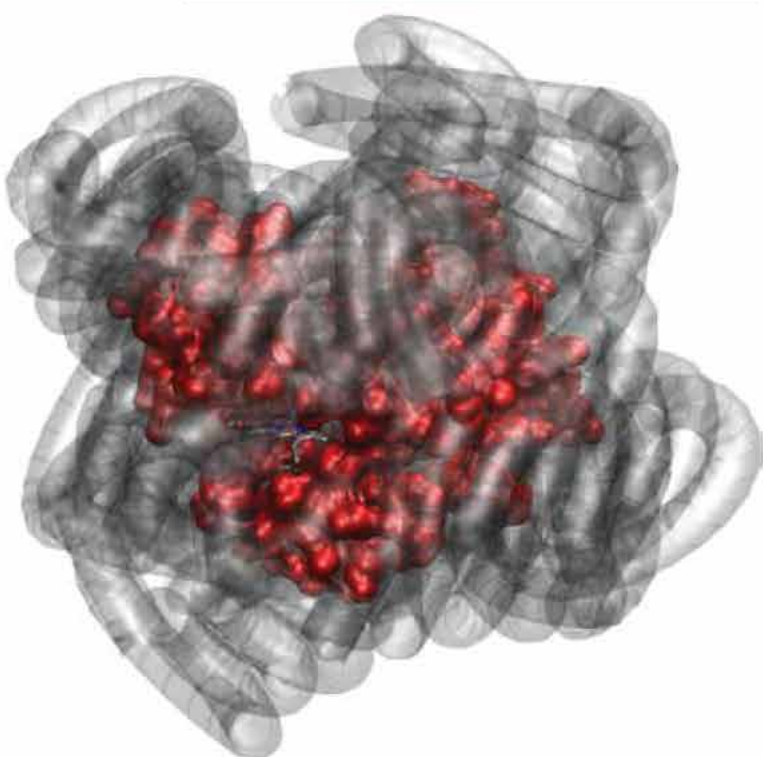


Figure 1 : Myoglobin (red) exhibits biologically relevant dynamics, even when its hydration sphere is replaced by a polymer surfactant corona (grey).

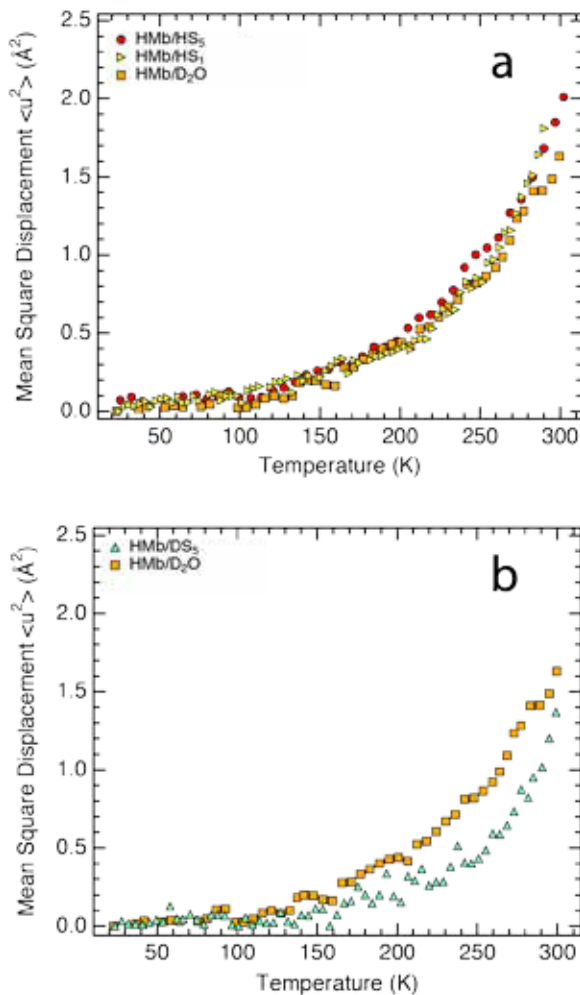


Figure 2 : Atomic mean square displacements (MSD) as a function of temperature of solvent-free myoglobin-polymer surfactant hybrids and of their components [5]. (a) Cationized, hydrogenated horse myoglobin (Mb) complexed with the hydrogenated polymer HS₁ (HMB/HS₁; yellow triangles), cationized, hydrogenated horse Mb complexed with the hydrogenated polymer HS₅ (HMB/HS₅; red circles), hydrogenated horse Mb in a powder hydrated at 0.43 g D₂O / g Mb (HMB/D₂O, orange squares). (b) Cationized, hydrogenated horse myoglobin complexed with the deuterated polymer DS₅ (HMB/DS₅, green triangles) and HMB/D₂O (orange squares). All data presented in the figure were collected on SPHERES and IN16 and were processed in exactly the same way.

those of hydrogenated myoglobin (Mb) hydrated at 0.43 g D₂O / g protein (fig. 2a), irrespective of the polymer employed (S1 or S5; see [5] for a detailed description of the polymers). Further EINS experiments then focused on the dynamics of either the protein or the polymer moiety.

This separation has been made possible through specific labelling, by which either polymer or protein motions are masked by replacing hydrogen with its heavier isotope, deuterium. The resulting MSD of the protein within the polymer surfactant corona qualitatively resemble those of a protein covered with a shell of hydration water (fig. 2b). In particular, the temperature-dependence of MSDs revealed a *dynamical transition* [6] at around 220-240 K that is characteristic of functional proteins and suppressed in a dry protein without polymer-coating. Furthermore, it was found that the polymer surfactant coating exhibited similar MSD to hydration water (not shown). The biological activity in solvent-free protein-polymer nano-hybrids has thus a dynamical origin, in that polymer surfactant motions efficiently substitute for hydration-water motions [5]. Details at the atomic level on the coupling between polymer and protein motions are currently under investigation by using quasi-elastic neutron scattering on SPHERES and by molecular dynamics simulations.

Proteins don't necessarily need it wet. In fact, polymer surfactants can replace protein hydration water, resulting in biologically active nano-hybrids. These solvent-free nano-hybrids could be used in the development of new industrial enzymes, with applications ranging from biosensor development to electrochemical reduction of CO₂ to produce liquid fuels.

- [1] P. Ball, Chem. Rev., 108, 74 (2008).
- [2] F.X. Gallat et al., Biophys J., 103, 129 (2012).
- [3] A.W. Perriman and S. Mann, ACS Nano, 5, 6085 (2011).
- [4] A.W. Perriman et al., Nat. Chem., 2, 622 (2010).
- [5] F.X. Gallat et al., J. Am. Chem. Soc., 134, 13168 (2012).
- [6] W. Doster et al., Nature, 337, 754 (1989).

Structure and dynamics of the iron-binding protein Lactoferrin studied using neutron scattering

C. Sill¹, R. Biehl¹, B. Hoffmann², A. Radulescu³, M. S. Appavou³, A. Feoktystov³, B. Farago⁴, D. Richter¹

¹Forschungszentrum Jülich GmbH, Jülich Centre for Neutron Science: Neutron Scattering & ICS-1: Neutron Scattering, Jülich, Germany

²Forschungszentrum Jülich GmbH, ICS-7: Biomechanics, Jülich, Germany

³Forschungszentrum Jülich GmbH, Jülich Centre for Neutron Science at MLZ, Garching, Germany

⁴Institut Laue-Langevin, Grenoble, France

The shape and internal motions of the human iron-binding protein Lactoferrin were investigated in solution using neutron scattering methods and interpreted by means of elastic normal modes. The goal was to elucidate the link between iron-binding, conformational change and domain dynamics. Comparison of the small angle scattering data with calculations of 3D crystal structures confirmed the existence of three conformations. Repulsive and attractive inter-protein interactions were found, presumably dependent on the presence of Fe^{3+} -ions in the solution. The neutron spin echo spectroscopy results showed relative motions of the two main domains, independent of the protein conformation and the pH-value.

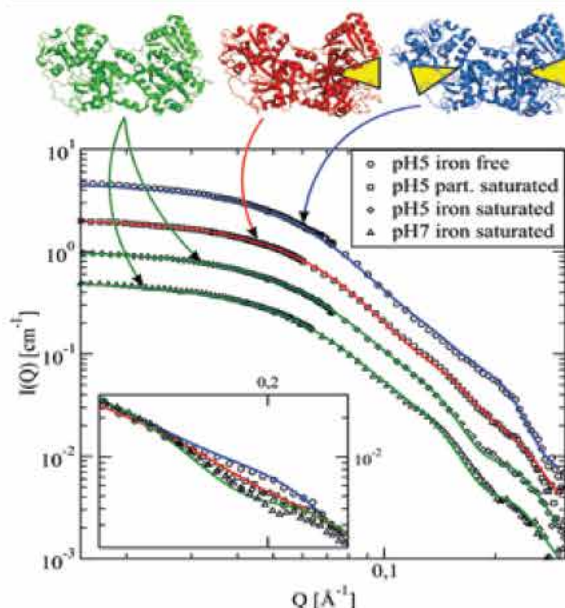


Figure 1: Top: Three conformations of Lf, both domains closed (left), one closed and one open (middle), both domains open (right). Open domains are indicated by yellow triangles. Bottom: Measured form factors (symbols) and calculations (lines) from the conformation models, displaced for better visibility. The inset shows the relevant Q-range without displacement.

Conformation and domain motions of Lactoferrin
Lactoferrin (Lf) is an iron-binding protein with antimicrobial activity as a part of the innate immune system. It consists of two domains with one binding site each located in a cleft. Each domain is capable of binding and releasing one iron ion, which is connected with a conformational change between open and closed [1]. The aim of our study was to clarify the link between iron-binding, conformational change and thermodynamically driven domain motions.

Combined approach to probe structure and dynamics of Lactoferrin

Human Lf was purchased commercially and prepared in aqueous solution in different iron binding states (< 5 %, ~ 30 %, > 90 % iron content) and with different pH-values. A combined approach of small angle neutron scattering (SANS at KWS-1 and KWS-2, MLZ, Garching) for structural characterization and neutron spin echo spectroscopy (NSE at IN15, ILL, France) to elucidate the dynamic properties of different binding states was undertaken to throw light on the influence of iron binding on large scale protein dynamics. The evaluation of the experimental data was based on the crystallographic structures of fully and half iron-saturated Lf (PDB codes 1b0l and 1lfh) and a homology structure of iron-free Lf (based on PDB code 1dtz). The normal modes of deformation of these structures were used to model the shape and domain motions.

Three different conformations are determined by the iron-binding state

A comparison of the SANS data with the 3D crystal structures proved that the binding sites are closed when occupied by iron and open otherwise (fig. 1). In general, good agreement between

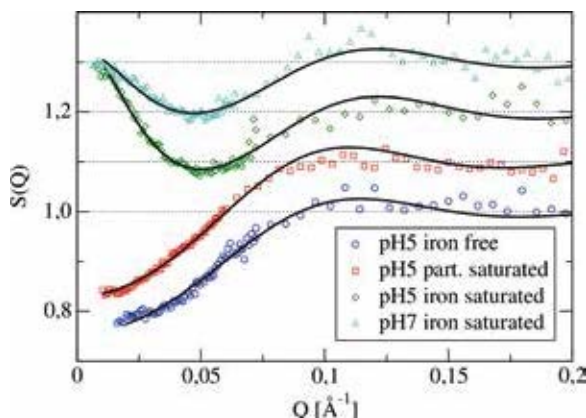


Figure 2: Structure factors of Lf (displaced for better visibility): hard-sphere interaction for iron free and partially iron saturated Lf (fit: Percus-Yevick), attractive interaction for iron saturated Lf at pH = 5 and 7 (fit: Hayter-Penfold MSA).

the experiment and the models was found, only slight deviations in the opening degree of the clefts (10-20 %) being observed.

The SANS experiments also revealed an attractive interaction between the Lf molecules for the iron saturated samples (fig. 2). An analysis of the conditions showed that neither the pH-value, nor the iron binding can be responsible. The attraction is probably due to Fe^{3+} -ions in the solvent, and similar behavior is reported for Y^{3+} -ions [2].

Dynamic is dominated by overdamped inter-domain motions

The evaluation of the NSE data was based on the SANS results, calculated diffusion from HY-

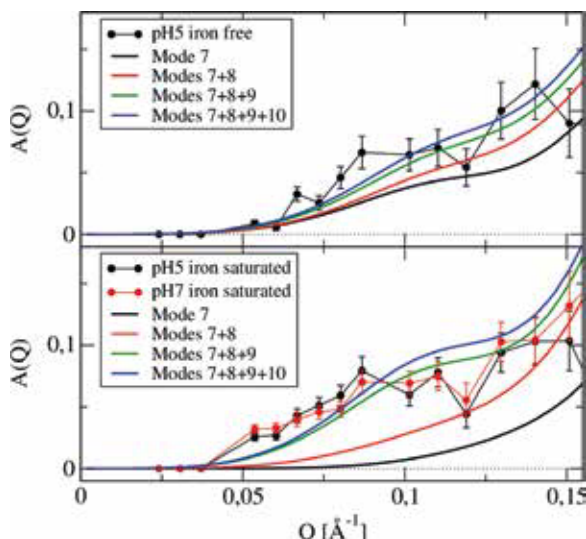


Figure 3: Relative contribution of the internal dynamics to normalized intermediate scattering function. Experimental data (symbols) and modelling (lines) with normal modes of the respective protein conformation.

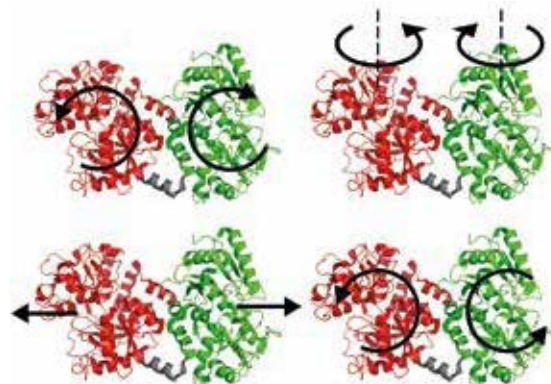


Figure 4: Motion patterns of the dominant normal modes 7-10.

DROPRO [3] and the methodology by Biehl et al. [4] involving the normal modes of deformation of the protein. It was found that the dominant internal dynamics are independent of the iron-binding state, i.e. whether the domains are open or closed (fig. 3) with relaxation times on the 50 ns scale (30 ns for pH 7) with root mean square displacements of 5–7 Å. The prevalent motions that describe the dynamics found are overdamped relative movements of the main domains such as stretching and twisting motion patterns (fig. 4).

Conclusion

In summary, we have been able to prove the existence of three different conformations of Lf in solution. For one of them (both domains open) no published crystallographic structure is available for human Lf. We found attractive interaction, presumably dependent on the presence of trivalent iron ions in the solution.

The internal dynamics of Lf is dominated by overdamped relative motions of the two main domains. These movements are independent of the conformation, i.e. the iron-binding state, and could be identified as stretching and twisting motion patterns.

[1] B.F. Anderson et al., Nature, 344, 784 (1990).

[2] F. Zhang et al., Phys. Rev. Lett., 101, 148101 (2008).

[3] J. García de la Torre et al., J. Phys. Chem. B, 111, 955 (2007).

[4] R. Biehl et al., Soft Matter, 7(4), 1299 (2011).

Thermal fluctuations of haemoglobin from different species

A. M. Stadler¹, C. J. Garvey², A. Bocahut³, S. Sacquin-Mora³, I. Digel⁴, G. J. Schneider⁵, F. Natali⁶, G. M. Artmann⁴, G. Zaccai⁶

¹Forschungszentrum Jülich GmbH, Jülich Centre for Neutron Science/ICS-1, Jülich, Germany

²Australian Nuclear Science and Technology Organisation, New South Wales, Australia

³Laboratoire de Biochimie Théorique, Paris, France

⁴FH Aachen, Jülich, Germany

⁵Forschungszentrum Jülich GmbH, Jülich Centre for Neutron Science at MLZ, Garching, Germany

⁶Institut Laue-Langevin, Grenoble, France

Motions and internal forces of haemoglobin of different species were investigated using elastic incoherent neutron scattering and coarse-grained Brownian dynamics simulations. Although significant differences were found in the internal dynamics of haemoglobin in solution, the mean square displacements of hydrated powder samples showed no differences, demonstrating that not all biologically relevant motions of haemoglobin are activated with only one hydration layer. Coarse-grained Brownian dynamics simulations on the other hand are a complementary and very informative tool as they provide residue-resolved information on protein flexibility.

Haemoglobin dynamics and body temperature

Haemoglobin (Hb) is the major macromolecular component of red blood cells. The structures of

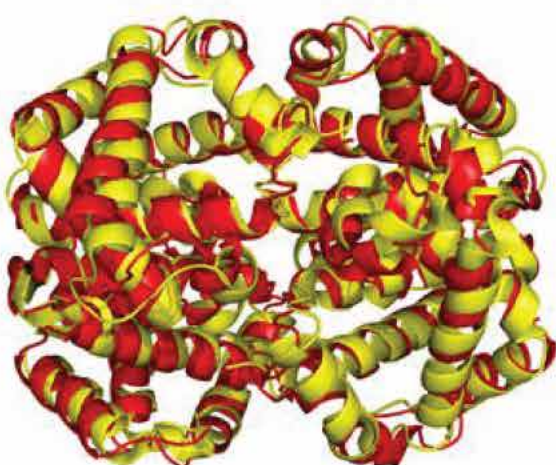


Figure 1: Crystal structures of human (yellow) and chicken Hb (red).

human and chicken Hb are shown in figure 1. Previous studies reported a partial loss of secondary structure of Hb close to body temperature [1]. The partial unfolding temperature of Hb from a large variety of species was directly correlated with the body temperature of the animal, ranging from 34 °C for the duckbilled platypus, which was the animal with the lowest body temperature in that study, to 42 °C for a bird, the spotted nutcracker, which had the highest body temperature in the study [1]. The aim of our study was to investigate whether the internal dynamics and thermodynamic parameters of Hb from different species are adapted to body temperature, and to identify the thermo-sensitive amino acids on a residue-specific level [2].

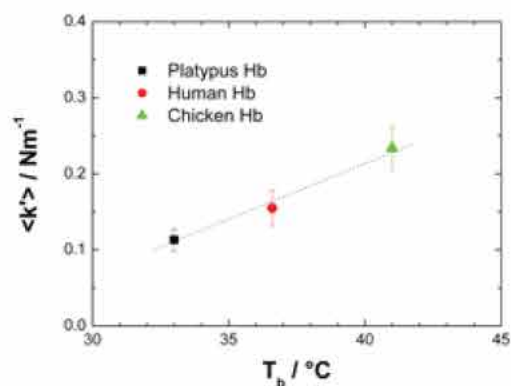


Figure 2: Correlation between effective force constants and body temperature of the investigated species.

Incoherent neutron scattering and simulation

Highly concentrated Hb solutions were measured on the thermal neutron backscattering spectrometer IN13 at the ILL in Grenoble. Hydrated powder samples were investigated using the high resolution cold neutron backscattering spectrometer SPHERES at the MLZ. The experimental studies were complemented by

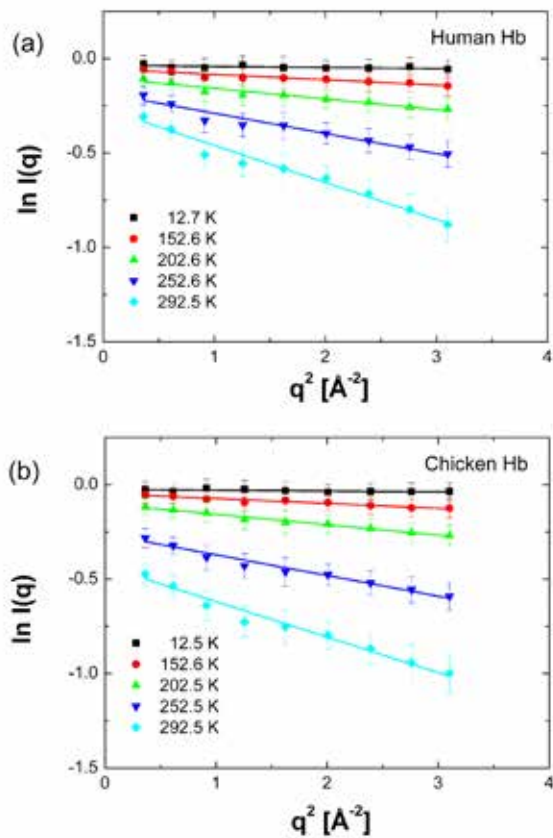


Figure 3: Measured elastic intensities of hydrated Hb powder using the SPHERES spectrometer.

coarse-grained Brownian dynamics simulations of human and chicken Hb structures [2].

Dynamics of Hb in solution and powders

The experimental results from Hb solutions revealed a direct correlation between internal forces and average body temperature of the different species on the 0.1 ns time scale, see figure 2.

Measured elastic intensities from hydrated powder samples of human and chicken haemoglobin using the high resolution backscattering spectrometer SPHERES are shown in figure 3. The mean displacements obtained on the 1 ns time scale are given in figure 4. The results of the hydrated powder samples showed no differences over the whole temperature range from 10 to 300 K, in contrast to the solution case. A result of the study, therefore, is that one hydration layer is not sufficient to activate all conformational fluctuations of Hb in the pico- to nanosecond

time scale, which might be relevant for biological function.

Coarse-grained Brownian dynamics simulations made it possible to explore residue specific effects. They indicated that temperature sensing occurs mainly at amino acid residues lining internal cavities in haemoglobin [2].

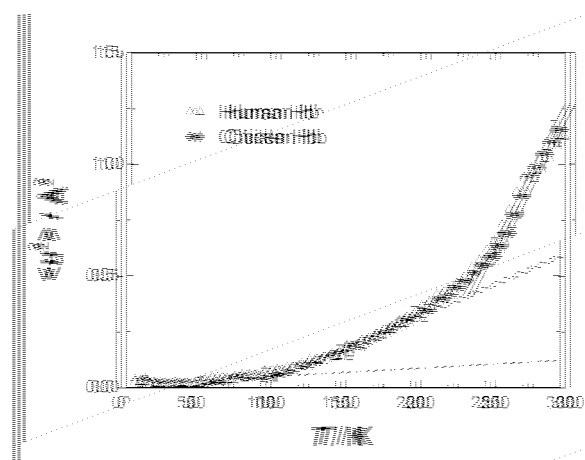


Figure 4: Mean square displacements of the hydrated power samples measured using SPHERES.

Thermal adaptation through mutational effects

Our results indicate that thermal adaption of Hb internal dynamics might result from a long-range mutational effect, similar to that previously observed in the bacterial photosynthetic reaction centre [3], where point mutations would affect the mechanical properties of residues located more than 15 Å away.

[1] K.F. Zerlin et al., Eur. Biophys. J., 37, 1 (2007).

[2] A.M. Stadler et al., J. R. Soc. Interface, 9, 2845 (2012).

[3] S. Sacquin-Mora et al., Biochemistry, 46, 14960 (2007).

Changes in structure and dynamics of beta-casein protein during micellization process

H. Nakagawa^{1,2}, M.-S. Appavou¹, J. Wuttke¹, M. Zamponi¹, O. Holderer¹, T. E. Schrader¹, D. Richter¹, W. Doster³

¹Forschungszentrum Jülich GmbH, Jülich Centre for Neutron Science at MLZ, Garching, Germany

²Japan Atomic Energy Agency, Quantum Beam Science Directorate, Tokai, Japan

³Technische Universität München, Physik-Department E13, Garching, Germany

The structure and dynamics of beta-casein were studied using small angle neutron scattering (SANS), neutron spin echo (NSE) and backscattering spectroscopy (BS). Beta-casein is an intrinsically disordered polypeptide chain, and forms micelles above a critical temperature. Inter-chain fluctuations in a confined space within micelles were observed upon micellization. This suggests a relatively mobile conformation of the beta-casein segments inside the micelle, which seems to be better described as a rheomorphic structure rather than a tightly packed one.

Casein micelle

Beta casein is a protein constituting casein micelles in milk. The protein is like a block copolymer with negatively charged hydrophilic and uncharged hydrophobic segments. Consequently, the monomers form micelles depending on the temperature. The protein is natively disordered, therefore the micelle structure is dif-

ficult to determine. Two structural models have been proposed: the Rheomorphic model and the Tensegrity-based model [1]. The structural flexibility plays a central role in these models. The fluctuations occur on a pico- to nano-second time scale, which can be ideally studied using quasi-elastic neutron scattering [2].

To elucidate the architecture of the casein micelles, we measured their structure and chain dynamics. These studies on protein solutions will allow us to determine how the dynamics are affected by increasing the confinement from monomers at low temperatures (at about 5 °C) to micelle at higher temperatures (at about 60 °C).

Experiments at KWS-1, J-NSE and SPHERES

SANS experiments have been performed at the KWS-1 instrument at a wavelength of $\lambda = 7.0 \text{ \AA}$ covering a Q range from 0.0022 to 0.1 \AA^{-1} . NSE experiments have been performed at the J-NSE spectrometer with four different wavelengths of 8, 10, 12 and 17 \AA . BS experiments have been performed at the SPHERES spectrometer with an energy resolution of $0.67 \mu\text{eV}$. The beta-casein sample condition was the same for all experiments; 0.1 M deuterated phosphate buffer $\text{pD} = 6.9$ with 1 mM EDTA and 0.1 M NaCl. Neutron measurements were performed at five temperatures; 5 °C (10 °C for SANS), 20 °C, 40 °C, 60 °C and 75 °C. The protein concentrations were 80 mg/ml for BS and NSE, and 5, 40 and 80 mg/ml for SANS.

Structural change on micellization

Figure 1 shows the SANS scattering profiles of beta-casein at 80 mg/ml. The inter-molecular structure factor peak is observed at every temperature. The peak is attenuated at 40 mg/ml and disappears at 5 mg/ml, showing the exist-

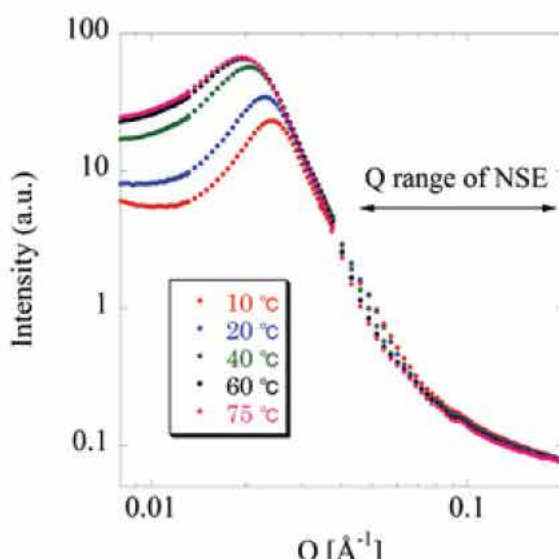


Figure 1: SANS profiles for Beta-casein protein solution at 80 mg/ml and various temperatures.

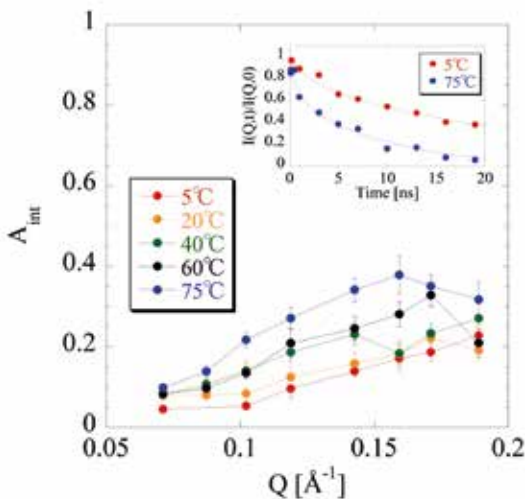


Figure 2: Amplitude of the internal motion of beta-casein in solution obtained by NSE. Inset shows intermediate scattering function for two temperatures.

ence of the inter-particle interaction at high concentration. The peak position is shifted to lower \$Q\$ value as the temperature increases, indicating the micellization. The data also indicate that NSE experiments at \$Q\$ value higher than \$0.05 \text{ \AA}^{-1}\$ can report on the internal motion of the beta-casein molecules or the micelles.

Dynamical change on micellization

The intermediate scattering functions of beta-casein in solution can be modeled by coupling the segmental dynamics and global diffusion of monomer or micelle (inset of fig. 2) [3], according to:

$$\frac{S(Q,t)}{S(Q,0)} = [(1 - A_{int}) + A_{int} \cdot \exp(-\Gamma_{int}t)] \cdot \exp(-\Gamma_{diff}t)$$

where \$A_{int}\$ is the amplitude of the decay rate \$\Gamma_{int}\$ due to the internal dynamics, and the diffusion rate \$\Gamma_{diff}\$. At low \$Q\$, \$A_{int}\$ is almost zero, indicating that the internal dynamics is invisible and only the whole diffusion contributes to the NSE signal. The internal dynamics is observed in the higher \$Q\$ region. In the micelle state (at higher temperature), an additional \$A_{int}\$ appears as compared to the monomer data. This result indicates the relative motions among the amino acid chains of beta-caseins within the micelle.

BS is sensitive to both the global and internal motion of protein in solution [4]. The inset of figure 3 shows a quasi-elastic spectrum at

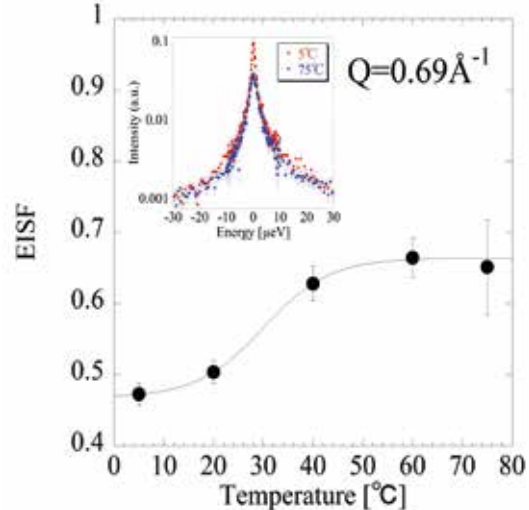


Figure 3: EISF at \$Q = 0.69 \text{ \AA}^{-1}\$. Inset shows the scattering profiles of BS and the fitting lines at 5 and 75 °C.

\$Q = 0.69 \text{ \AA}^{-1}\$ obtained for the beta-casein solution at two temperatures. Because of the finite spatial range, the internal motions give rise to an Elastic Incoherent Structural Factor (EISF). The neutron spectra were fitted with two Lorentzians, weighted by the EISF, representing the internal and the total motions of the beta casein respectively. Figure 3 shows that EISF in the micelle state is larger than that in the monomer state, indicating a spatial restriction of the internal motions upon micellization.

Conclusion

Upon micellization, each beta-casein monomer is spatially confined within the micelle, but the polypeptide chains are still mobile within the micelle despite the confinement effect. These results suggest that the beta-casein micelle structure can be described as rheomorphic rather than tightly packed. This study also suggests that these combined neutron scattering measurements should be a promising method to observe biological events on a mesoscopic scale, such as aggregation and fibrillization, which is highly relevant to non-conformational protein involved in some neurodegenerative diseases.

- [1] P.X. Qi et al., Trends Food Sci. Technol., 12, 339 (2001).
- [2] A.M. Gaspar et al., Eur. Biophys. J., 37, 573 (2008).
- [3] J. Adelsberger et al., Macromolecules, 43, 2490 (2010).
- [4] S. Busch et al., In Proc. QENS2006, 116 (2006).

Effect of confinement on the dynamics of polymer melts: interfaces and interphases

M. Krutyeva¹, A. Wischnewski¹, M. Monkenbusch¹, L. Willner¹, J. Maiz², C. Mijangos², A. Arbe³, J. Colmenero^{3,4}, D. Richter¹

¹Forschungszentrum Jülich GmbH, Jülich Centre for Neutron Science & Institute for Complex Systems, Jülich, Germany

²Consejo Superior de Investigaciones Científicas, Instituto de Ciencia y Tecnología de Polímeros, Madrid, Spain

³Centro de Física de Materiales, San Sebastián, Spain

⁴Materials Physics Center and Donostia International Physics Center, San Sebastián, Spain

The aim of this work is to study the influence of surface interaction and confinement on the dynamics of a polymer melt using neutron spin-echo (NSE) spectroscopy. We investigated the dynamics of polydimethylsiloxane (PDMS) confined in nanopores of anodic aluminium oxide (AAO). PDMS dynamics in confinement is rather determined by two phases, one fully equal to the bulk polymer and another that is partly anchored at the surface (interface). Through strong topological interaction, this phase confines further chains with no direct contact to the surface. These form the frequently invoked interphase where the full chain relaxation is impeded through the interaction with the anchored chains. The confined phase is internally highly mobile and not glassy as has so far often been claimed in the literature.

The presence of a solid surface reduces the number of possible conformations of a polymer chain, in particular for those macromolecules which are close to the surface. Understanding the underlying mechanisms at and close to the surfaces is important for applications in nanotechnology. In this work we demonstrate that the attractive polymer-surface interaction leads to the formation of the frequently discussed interphase in a confined linear polymer melt [1].

Polydimethylsiloxane (PDMS) with a molecular weight a factor 1.5 larger than the entanglement molecular weight M_e was infiltrated into AAO templates (pore radius 13 nm). Calculations using density functional theory showed an adsorption interaction between the AAO surface and PDMS. Small Angle Neutron Scattering (SANS) experi-

ments were carried out at the JCNS instrument KWS-2 at the MLZ. The dynamics were investigated using the Neutron Spin Echo (NSE) spectrometer SNS-NSE at the JCNS outstation at the spallation neutron source in Oak Ridge (ORNL), USA, and at the J-NSE spectrometer of the JCNS in Garching.

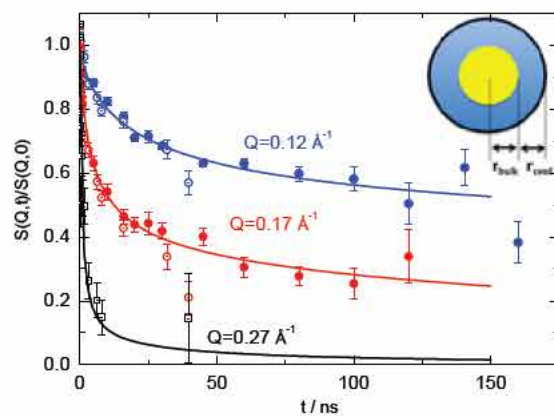


Figure 1: J-NSE (filled symbols) and SNS-NSE (open symbols) results for confined PDMS. Solid lines present the fitting with the Eq. (1). The sketch of the two-phase model is shown in the inset.

SANS experiments

The main purpose of the SANS experiment was to assess the residual scattering caused by inhomogeneities in the pore filling and/or nonideal matching. From this experiment we concluded that, if the sample is tilted by 25° relative to the incident beam, in the NSE Q-window the total scattering is strongly dominated by the scattering from the polymer.

NSE experiment

The NSE data show a significantly slowed-down chain dynamics compared to bulk. Proper inspection of the plateaus at long times made it

possible to exclude the existence of an immobilized (glassy) layer, since the plateaus are Q-dependent. Furthermore, the observed Q-dependence cannot be described in terms of a simple confined polymer, because fitting such a model to the data yields a Q-dependent confinement length.

Modified Rouse model

Therefore, a new model was derived containing (i) a fraction of free Rouse-like chains, since many chains far away from the surface are not affected in any way and (ii) a second fraction of chains which is close to the surface and assumed to be effectively confined. The respective dynamic structure factor reads:

$$S(Q, t) = A_{\text{bulk}} S_{\text{bulk}}(Q, t) + A_{\text{conf}} S_{\text{conf}}(Q, t) \quad (1)$$

where A_{bulk} and $A_{\text{conf}} = 1 - A_{\text{bulk}}$ are the fractions of the bulk and confined phases respectively; $S_{\text{bulk}}(Q, t)$ is the dynamic structure factor of the bulk chain defined by the Rouse model [2] and $S_{\text{conf}}(Q, t)$ is the dynamical structure factor of the confined chain. This model contains three variable parameters: fraction A_{bulk} (or $A_{\text{conf}} = 1 - A_{\text{bulk}}$), the number of suppressed Rouse modes p_{supp} reflecting the effective confinement in $S_{\text{conf}}(Q, t)$ and an additional parameter Δp , the width of a cut off function describing the transition from active to suppressed modes. Δp accounts for a variety of anchoring and confinement conditions. By fitting all Q simultaneously, A_{bulk} was found to be 25 % of the total amount of polymer in the pores, $p_{\text{supp}} = 5$ and $\Delta p = 1$ (fig. 1). From the longest active mode in the confined phase, one can calculate the effective confinement length $d = 3.4$ nm.

Polymer interphase

The fractions A_{bulk} and A_{conf} obtained can be transferred to a corresponding layer thickness which was found to be $r_{\text{conf}} = r_{\text{bulk}} = 6.5$ nm (see inset in fig. 1). The fact that the size of the PDMS polymer chain considered here in the bulk is 3.4 nm and should even be reduced for a multiple adsorbed chain, clearly indicates that the

layer with a thickness of 6.5 nm is not only made up of chains adsorbed at the surface. The polymer chains anchored to the surface may form loops; neighbouring chains can then interpenetrate these loops (fig. 2). These penetrating chains can be considered as the interphase between the polymer adsorbed on the surface and the bulk polymer phase.

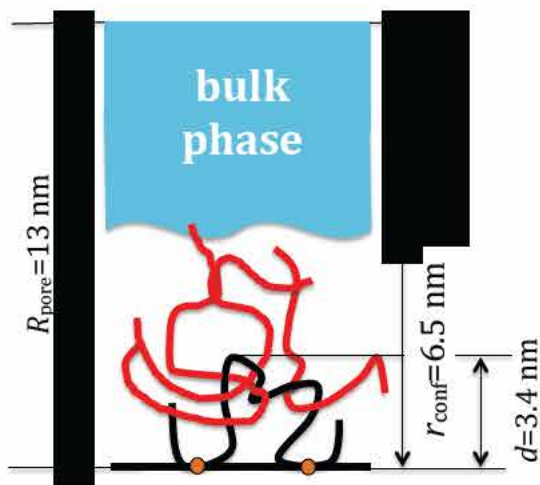


Figure 2: Schematic representation of the artificial surface-induced entanglements in the confined polymer melt. Black line represents the chain adsorbed on the surface of AAO nanopore, red lines show entangled chains in confined phase.

Conclusions

The dynamics of PDMS confined in cylindrical AAO nanopores is strongly affected by the confinement and characterized by two phases, one fully equal to the bulk polymer and another that is partly anchored at the surface. By topological interaction, the anchored part confines further chains with no direct contact to the surface. They form the frequently invoked interphase. The confined phase is internally highly mobile and not glassy as has so far been claimed frequently in the literature. These results are inferred from the space-time dependent chain dynamics that is observed in terms of the single chain dynamic structure factor and represent the first direct and quantitative observation of the interphase.

[1] M. Krutyeva et al., Phys. Rev. Lett., 110, 108303 (2013).

[2] P.J. Rouse, J. Chem. Phys., 21, 1272 (1953).

SANS study of the morphology of a novel polymer electrolyte membrane

Y. Zhao¹, S. Koizumi¹, M. Rikukawa², M. Yoshida², A. Radulescu³, D. Richter³

¹Japan Atomic Energy Agency, Quantum Beam Science Directorate, Ibaraki, Japan

²Sophia University, Department of Materials & Life Sciences, Chiyoda, Japan

³Forschungszentrum Jülich GmbH, Jülich Centre for Neutron Science at MLZ, Garching, Germany

Contrast variation small-angle neutron scattering experiments have been performed at KWS-2 at the MLZ to investigate the morphologies of newly synthesized hydrocarbon polymer electrolyte membranes, made of amphiphilic multiblock-copolymer poly(sulphonate phenylene)-*b*-poly(arylene ether ketone). Two scattering maxima were clearly observed for the wet membranes at low angle and high angle regions due to the formation of microdomains and ionic clusters, respectively. The model analysis suggests that: i) the microdomains are spherical and percolated; ii) the matrix of the membranes is inverted from hydrophobic to hydrophilic if the hydrophilic block is long.

Introduction to polymer electrolyte membrane

Proton exchange membrane fuel cells play an important role against today's oil shortage. As the key part of such fuel cells, the development of the polymer electrolyte membrane (PEM) has attracted a great deal of attention over recent decades, including both cutting down the cost and improving its performance [1]. So far, Nafion, a costly fluorinated membrane, has been the most

industrially accepted PEM. However, its proton conductivity decreases dramatically at high temperature and low humidity. In order to reduce the cost while maintaining good performance, a new PEM composed of hydrocarbon block copolymers (bcps) is being seriously considered.

Hydrocarbon bcp can be synthesized using general polymerization methods. When it is casting to a membrane, it may self-assemble into multiple-phase structures including micro- (or nano-) scale structures composed of segments and primary bcp chains and higher-order structures composed of bcp chains and aggregates, which is believed to be important to improve the electric property of the membrane. Generally, the higher-order structures depend on the microphase separation process, hence considering both the chemical structure of the bcp itself and the morphology of its self-assembly is a practical way to design a new PEM. In view of this, a combined study of the polymer synthesis and structural analysis is crucial.

In this study, we aimed to investigate the multiple-phase structures of a newly synthesized hydrocarbon PEM, made of multiblock poly(sulphonate phenylene)-*b*-poly(arylene ether ketone) $[(\text{PSP})_x - \text{b} - (\text{PAEK})_y]_n$ bcps and looked at: (i) the morphologies of microdomains; (ii) how the structure varies with the chemical structure of the bcp chains, i.e., the block ratios.

SANS experiment at KWS-2 at MLZ

The molecular structure of $(\text{PSP})_x - \text{b} - (\text{PAEK})_y$ bcps, designated as $\text{S}_{14}\text{-AEK}_{14}$ ($M_n \sim 69,200$ g/mole) and $\text{S}_{28}\text{-AEK}_{14}$ ($M_n \sim 124,000$ g/mole), are shown in figure 1. The subscript 14 or 28 refer to the repeating unit number of the PSP or PAEK segments. Obviously, the hydrophilic PSP blocks in $\text{S}_{28}\text{-AEK}_{14}$ are twice as long as those in $\text{S}_{14}\text{-AEK}_{14}$.

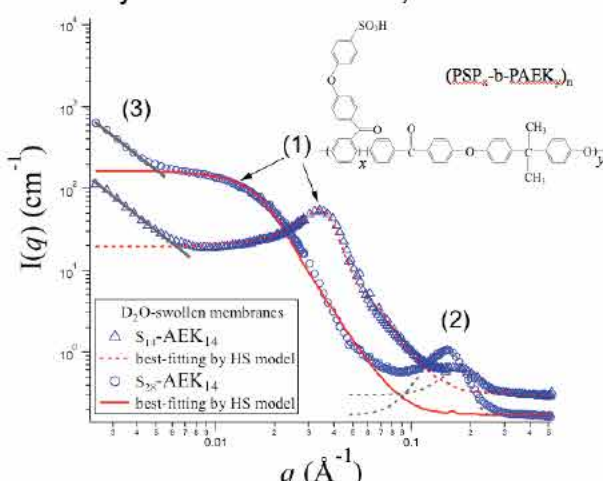


Figure 1: Molecular structure of $(\text{PSP}_x - \text{b} - \text{PAEK}_y)_n$ and SANS profiles for D_2O -swollen membranes.

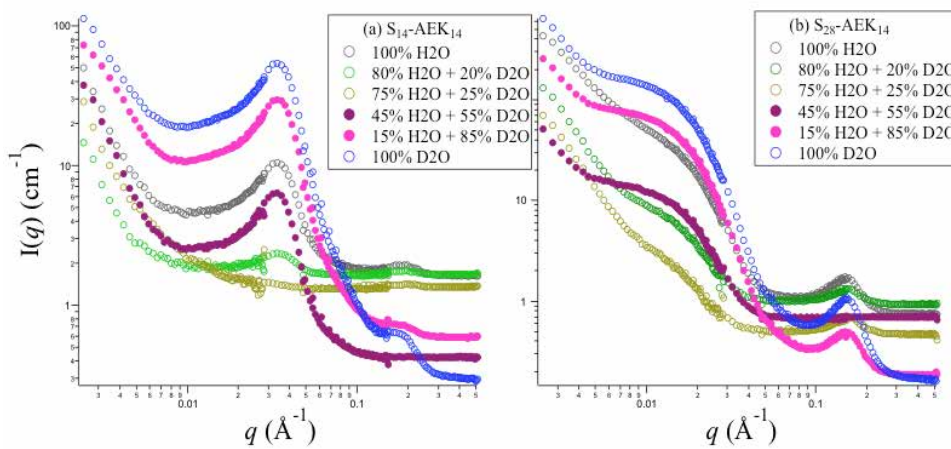


Figure 2: Contrast variation SANS profiles for (a) S_{14} -AEK₁₄; (b) S_{28} -AEK₁₄.

AEK₁₄. Membranes with a thickness of $\sim 50 \mu\text{m}$ were obtained using the solvent-casting method from a DMSO solution. The water-uptake (the volume ratio of water to dried membrane) value for each water-swollen membrane was determined by weight measurements to be ~ 0.27 for S_{14} -AEK₁₄, and ~ 0.7 for S_{28} -AEK₁₄, respectively. Contrast variation small-angle neutron scattering (SANS) experiments were performed at KWS-2 at the MLZ [2], where the membranes were fully swollen in water mixtures (H_2O and D_2O) with various ratios before conducting SANS. The incident neutron beam was monochromatized by a velocity selector to obtain the average wavelength (λ) of 4.5 \AA , with a wavelength distribution of about $\Delta\lambda/\lambda = 20 \%$.

SANS elucidation on the morphology of PEM

SANS profiles for the two D_2O -swollen membranes are also shown in figure 1. The scattering intensity, $I(q)$, is plotted as a function of the magnitude of the scattering vector q , where $q = (4\pi/\lambda)\sin(\theta/2)$, with λ and θ being the wavelength and scattering angle, respectively. $I(q)$ increases greatly upon swelling, and three contributions are clearly observed: (1) a strong maximum at $0.01 < q_1 < 0.04 \text{ \AA}^{-1}$, due to the formation of microdomains, (2) a weak maximum at $0.1 < q_2 < 0.2 \text{ \AA}^{-1}$, due to the formation of ionic clusters, and (3) an upturn in the low q region, due to the smooth interface between domains.

To understand the morphology of the microdomains, the Hard-Sphere (HS) model with the Percus-Yervick approximation is applied to analyze

the scattering data (the fitting curves are shown by red lines). From this model, the size (R_{sphere}) and volume fraction (Φ_{sphere}) of the microdomains are determined to be $\sim 85 \text{ \AA}$ and ~ 0.31 for S_{14} -AEK₁₄ and $\sim 155 \text{ \AA}$ and ~ 0.07 for S_{28} -AEK₁₄. Φ_{sphere} for S_{28} -AEK₁₄ is surprisingly small, which forces us to consider the composition of the microdomains. For this purpose, contrast variation SANS was performed (see fig. 2), where the averaged scattering length density of the hydrated regions is variable. The consistence between the theoretically calculated front factor in the HS model and the experimentally extrapolated intensity at $q = 0$ for all contrasts provides a means of judging the amphiphilicity of the microdomains. Our analysis shows that the microdomains in S_{14} -AEK₁₄ are hydrophilic and percolated spheres, while S_{28} -AEK₁₄ is characterized by an inverse network of hydrophobic polymer

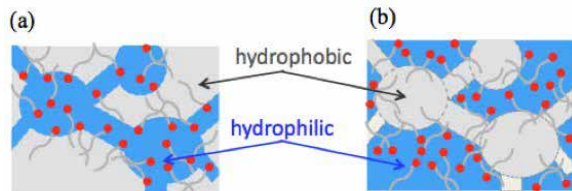


Figure 3: Illustration of morphologies of (a) S_{14} -AEK₁₄; (b) S_{28} -AEK₁₄.

spheres dispersed in the hydrated matrix, as shown in figure 3. This conclusion is reasonable if one takes the water uptake value of each sample into account.

[1] W. Vielstich et al., Wiley (2003).

[2] A. Radulescu et al., J. Phys., 351, 012026 (2012).

Time-resolved SANS studies on the crystalline complexes of syndiotactic-polystyrene

F. Kaneko¹, A. Radulescu², K. Sasaki¹, N. Seto¹, K. Ute³

¹Osaka University, Graduate School of Science, Osaka, Japan

²Forschungszentrum Jülich GmbH, Jülich Centre for Neutron Science at MLZ, Garching, Germany

³University of Tokushima, Department of Chemical Science and Technology, Tokushima, Japan

The ability of crystalline polymers to hold various kinds of molecules as guests in the cavities between polymer helices and form crystalline complexes – clathrates and intercalates – presents applied potential for chemical separations, sensing elements, nanoporous and composite materials doped with functional molecules. The mechanism of the guest-induced crystallization and guest-exchange phenomena in syndiotactic-polystyrene (sPS) were investigated for the first time using time-resolved SANS.

sPS exhibits a diversity of crystalline states, depending on the crystallization conditions as well as subsequent treatment. One of the important properties of sPS is the formation of crystalline complexes – clathrates and intercalates, where organic compounds are stored as guests in the vacancies between sPS helices with TTGG conformation. A wide range of chemical species, including functional molecules, can be incorporated into sPS lattice – for example, crown ethers, paramagnetic molecules, photo-reactive, fluorescent and dye molecules, and even polymeric molecules. However, the detailed mechanism of crystallization and guest exchange processes has not yet been fully clarified. sPS forms a co-

crystal with only a few compounds directly from its glass or a solution state. As recently demonstrated [1-3], bulky molecules can be introduced into sPS lattices using a new approach, the guest exchange phenomenon.

The results of the first time-resolved SANS (TR-SANS) experiments on the guest exchange phenomenon in sPS have demonstrated the considerable potential of this method as a probe for structure evolution in polymer crystalline complexes.

SANS chasing guest-exchange

TR-SANS experiments carried out at the KWS-1 SANS diffractometer provided valuable information about the characteristics of the guest exchange process. Using oriented fully deuterated polymer films and a special experimental setup, enabling the exposure of films to selective vapours, and exploiting the difference in molecular scattering length between the fully protonated (h) and deuterated (d) isotopologues, employed as old and new guests, the characteristics and mechanism of the guest-induced crystallization and guest exchange were investigated by monitoring the time evolution of the reflections appearing distinctively in well-defined areas due to lamellar structures in the oriented samples. The experimental setup made it possible to change the gas environment in the sample cell immediately with remote controlled valves, and to trigger the TR-SANS measurements at the very moment when the vapor circulating into the cell was switched to that of the new guest.

Guest uptake by lamellae

The one dimensional intensity function $I(q)$ was obtained from the corrected 2D data by reading and merging them with a proper width along

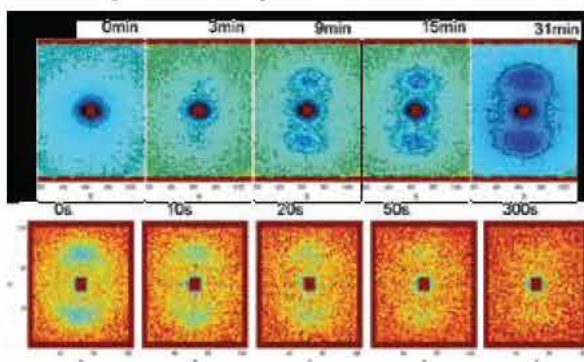


Figure 1: TR-SANS on crystallization due to exposure to h-chloroform (top) and guest exchange from h-toluene to d-toluene (bottom) in oriented sPS film.

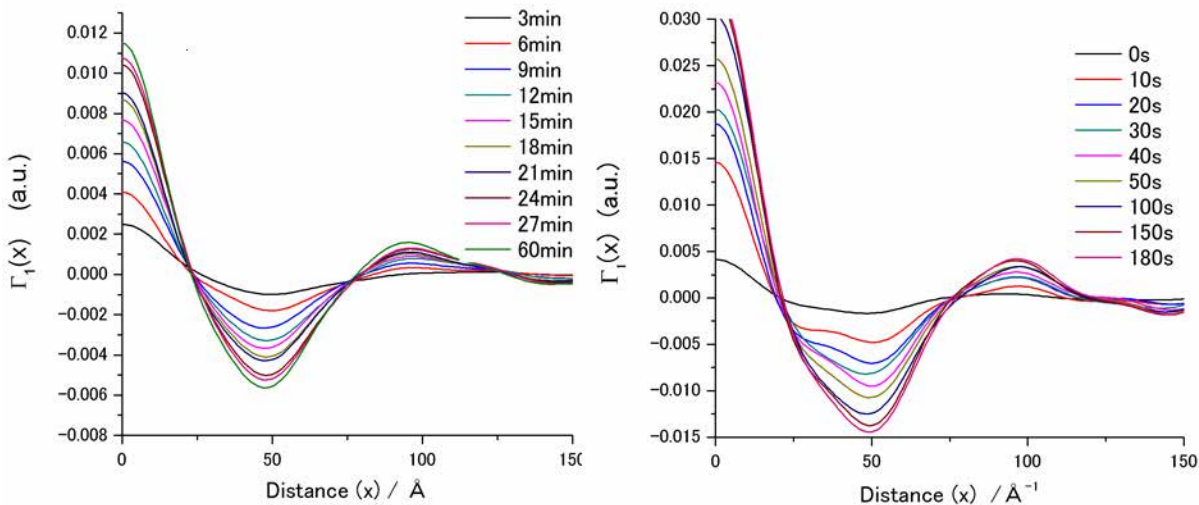


Figure 3: Time evolution of one-dimensional correlation functions $\Gamma_1(q)$ in CHCl_3 vapor induced crystallization (left) and guest exchange process from d-toluene to h-toluene (right).

the central meridian. Figure 1 reproduces the changes in SANS image caused by exposure to h-chloroform and the guest exchange from h-toluene to d-toluene. The initial d-sPS/h-chloroform complex showed two intense first-order reflections due to the formation and evolution of the periodic structure of crystalline lamellae in the meridian direction with low background scattering. The h-chloroform molecules stored in the crystalline lamellae enhanced the difference in the scattering length density, $|\Delta\rho(x)|$, between the crystalline and amorphous regions, which resulted in the intense lamellar reflections. When the subsequently loaded h-toluene was replaced by d-toluene, the $|\Delta\rho(x)|$ decreased and the reflections became obscure and almost disappeared in the final stage. The remarkable intensity changes are better followed in the time dependence of the one-dimensional scattering

intensity $I(q)$ (fig. 2).

The time dependence of the one-dimensional correlation function $\Gamma_1(x)$, obtained by carrying out Fourier transformation of $I(q)$, provides information about the lamellar parameters and the rate of exchange as well as the distribution of old and new guests in the crystalline region during the exchange process. The profile during the exchange process shows a non-monotonous time evolution, indicative of the occurrence and vanishing of inhomogeneity in the lamellae. The new guest molecules intrude into the crystalline lamellae from the lamellar surface, so that in the beginning new guest h-toluene molecules are concentrated around the lamellar surfaces, which results in the formation of narrow surface zones with low $\rho(x)$. The concentration of h-toluene in the lamellar interior increases with time and the inhomogeneity of $\rho(x)$ in the lamellae declines.

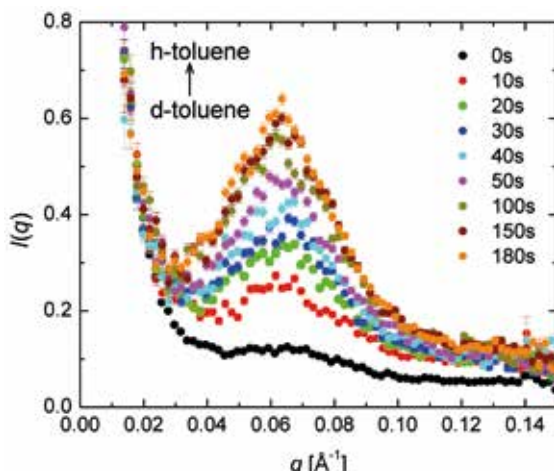


Figure 2: Time evolution of the one-dimensional $I(q)$ profile in guest exchange process from d-toluene to h-toluene.

Conclusions

Time-resolved SANS was first applied to the study of the guest exchange phenomenon of sPS. The preliminary results of the experiments concerning the vapor-induced guest exchange demonstrated the considerable potential of this method as a probe for structure evolution in polymer crystalline complexes.

[1] Y. Uda et al., Polymer, 45, 2221 (2004).

[2] F. Kaneko et al., Soft Materials, 9, 107 (2011).

[3] F. Kaneko et al., Polymer (submitted).

Small angle neutron scattering studies on self-healing model polymers

A. R. Brás¹, W. Antonius¹, C. Hövelmann¹, A. Radulescu², J. Allgaier¹, W. Pyckhout-Hintzen¹, A. Wischnewski¹, D. Richter¹

¹Forschungszentrum Jülich GmbH, Jülich Centre for Neutron Science, Jülich, Germany

²Forschungszentrum Jülich GmbH, Jülich Centre for Neutron Science at MLZ, Garching, Germany

We report on a Random Phase Approximation (RPA) approach to multiblock copolymers consisting of supramolecular building blocks and hydrogen-bonded complexes including interactions in solution which are model systems for the self-healing process.

Supramolecular polymers allow specific tailoring of polymer properties. A recent addition are self-healing polymers, displaying hydrogen-bonding interaction. Small Angle Neutron Scattering (SANS) measurements were performed on Polypropylene Glycol (PPG) systems at KWS-2, using the complementary end-groups THY and DAT (fig. 1), as a 50/50 mixture in toluene.

Recently [1], Small Angle X-Ray Scattering (SAXS) has been performed on these systems in the bulk from room temperature up to high temperatures and witnessed a low-intensity peak resulting from the correlation hole. The peak is indicative for high χN values and strong interactions between the segments (table 1)

Typical behaviour of a block copolymer

This behavior, typical of a block copolymer [1], is also expected in solution. Therefore, a Random Phase Approximation (RPA) approach to the SANS data is appropriate. The position of the maximum is almost independent of the number of associated blocks N_{agg} , and its amplitude rapidly reaches a limiting value. However, in dilute solution the chain length can be controlled by the concentration ϕ_p .

For the first time the assembly route is quantitatively accessed by a generalization of RPA to multiblocks including interactions in solution.

The general RPA result for a AB copolymer, neglecting interactions between the blocks ($\chi_{AB} = 0$) [3] is:

$$S_{RPA} = \frac{S_{AA}S_{BB} - S_{AB}^2}{S_{AA} + S_{BB} + 2S_{AB}} (\chi = 0)$$

Our system now contains three different scattering length densities and the multi-component RPA including all interactions χ_{ij} with $i,j = A, B, C$ (A is PPG, B is DAT --- THY and C is the solvent) and $S_{RPA} \rightarrow S_{RPA} = f(N_{agg}, \chi, \Delta\rho, \phi_p)$ can be applied. In polycondensation theory $N_{agg} = \text{sqrt}(K_{ass} \phi_p)$ [3, 4], K_{ass} being the equilibrium association constant in solution of the system studied. Since the RPA approach is strictly valid only in the θ -state

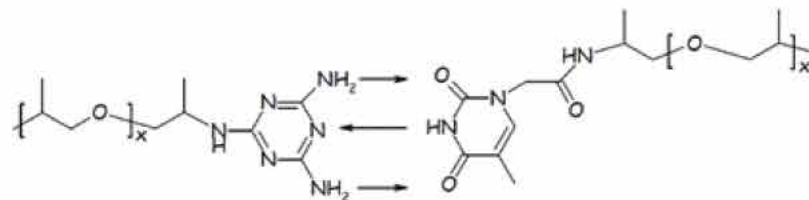


Figure 1: Complementarity between DAT and THY, leading to self-assembly.

χ	PPG	THY	DAT	Toluene
PPG	—	1.7-4.8	1.7-4.7	0.5-0.7
THY	1.7-4.8	—	0.01	3.8
DAT	1.7-4.7	0.01	—	4.1
Toluene	0.5-0.7	3.8	4.1	—

Table 1: Empirical estimations of χ [2].

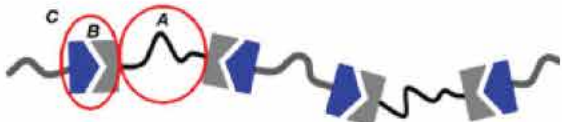


Figure 2: Sketch of the suggested block copolymer structure of the type $(AB)_{n-1}A$ in a solvent C.

and assumes Gaussian statistics, deviations are possible, especially at high Q.

Assuming monomolecularity as polydispersity in connection with RPA is not manageable, chain dimensions in toluene can be determined. A tentative Guinier representation with negligible χ parameters was used to qualitatively interpret the data. The intercept intensity $I_0 = (Q = 0) = \Delta\rho^2 \phi_p N_{\text{agg}} V_p$ is proportional to M_w . Association induces a dependence of $I_0 \approx (\phi_p)^{3/2}$. Similarly, the R_g obtained by the Guinier approach should depend on ϕ_p as $R_g \approx (\phi_p)^{1/4}$ (fig. 3 a) and b)).

The above proportionalities are observed only for $\phi_p < 6.0\%$. Therefore, the RPA model has been applied only for lower concentrations $\phi_p < 6.0\%$. The only model parameters are K_{ass} , χ_{AB} and χ_{BC} [2], obtained values being presented in table 2. A simultaneous fit to the data was made in order to obtain an accurate estimate of K_{ass} (fig. 4).

RPA approach describes SANS data

The RPA approach used describes the SANS data very reasonably. The intramolecular interac-

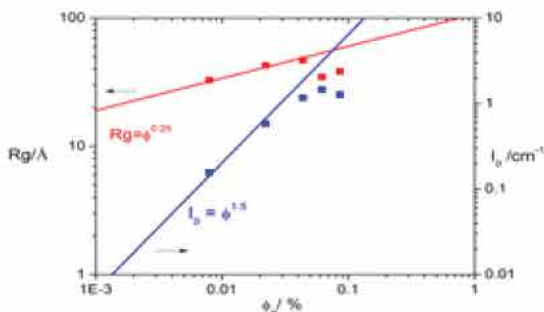


Figure 3 a) and b): I_0 and R_g vs. ϕ follow the predicted slopes of a linear association in a multiblock-like chain. Within experimental error the results are in agreement for $\phi_p < 6$.

Kass	χ_{AC}	χ_{AB}	χ_{BC}	
RPA	1400 ± 200	0.34	6.38 ± 0.06	4.0 ± 0.01

Table 2: Data parameters using the new generalized RPA.

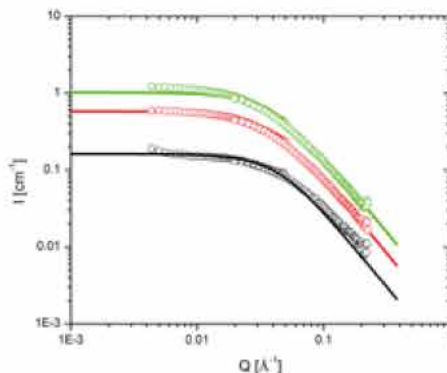


Figure 4: Coherent scattering intensities for the stoichiometric mixture at different concentrations below c^* in toluene at room temperature. The solid lines show a fit with the RPA approximation.

tion parameters are of the order typical for flexible polymers. Moreover, a linear conformation of these mixtures is abundantly present and ring-associated states can be neglected to a very good approximation.

Acknowledgements

Prof. Leibler for introducing these polymers to the FZJ group and SPP1568 for support.

[1] (a) J. Cortese et al., J. Am. Chem. Soc., 133, 49, 19672 (2011).

[1] (b) J. Cortese et al., J. Am. Chem. Soc., 134(8), 3671 (2012).

[2] (a) D.W. Van Krevelen, Properties of Polymers, Amsterdam (1990).

[2] (b) J.E. Mark, The Polymer Data Handbook, New York, (1999).

[2] (c) S.W. Kuo and H. T. Tsai, Macromolecules, 42, 4701 (2009).

[3] B. Hammouda, Probing nanoscale structures - The SANS Toolbox, http://www.ncnr.nist.gov/staff/hammouda/the_SANS_toolbox.pdf, downloaded 19.02.2013.

[4] L. Bouteiller, Adv. Polym. Sci., 207, 79 (2007).

Lipase-induced changes in fundamental surfactant monolayer properties

M. Subinya¹, S. Wellert², P. Busch³, O. Holderer³ and S. Engelskirchen^{1,4}

¹Universität Stuttgart, Institut für Physikalische Chemie, Stuttgart, Germany

²Technische Universität Berlin, Stranski-Laboratorium für Physikalische und Theoretische Chemie, Berlin, Germany

³Forschungszentrum Jülich GmbH, Jülich Centre for Neutron Science at MLZ, Garching, Germany

⁴Durham University, Department of Chemistry, Durham, UK

Usually, enzymatic substrates are lipophilic molecules that are not easily converted in an aqueous environment. Bicontinuous microemulsions provide a sponge-like connected separating surfactant monolayer structure capable of hosting amphiphilic enzymes such as the lipase B from *Candida Antarctica*. By using neutrons, we learned that introducing the lipase into microemulsions induces an unexpected development in the bending constants of the monolayer. Supported by complementary experiments, we conclude that the monolayer can only host a specific amount of lipase. Additional lipase is expelled into the water domain.

Pharmaceutical relevance

In pharmaceutical research and application the effectiveness of a treatment often strongly depends on the enantiomer applied, hence on high purity and selectivity. Enzymes typically show

high selectivity in racemic resolutions with the benefit of mild reaction conditions. Most synthetically interesting substrates, however, are bulky and very lipophilic molecules that can not readily be converted by an enzyme in an aqueous environment [1].

Bicontinuous microemulsions as a host

To date, solutions to this problem have involved water-soluble organic solvents or ionic liquids. A promising alternative avoiding inactivation of the enzymes are microemulsions. Recent literature presents droplet microemulsions as micro-heterogeneous reaction compartments. Bicontinuous microemulsions provide beneficial advantages over droplet microemulsions, such as maximal solubilization capacity and ultra-low interfacial tensions [2].

Small Angle Neutron Scattering (SANS) and Neutron Spin-Echo Spectroscopy (NSE) are predestined to study the effect of enzymes on bi-

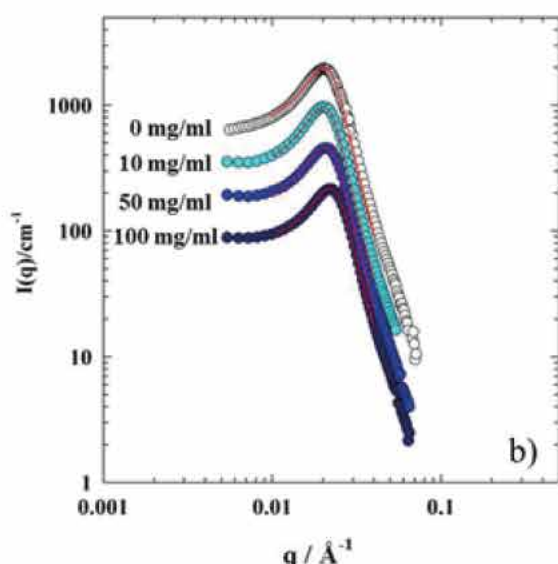
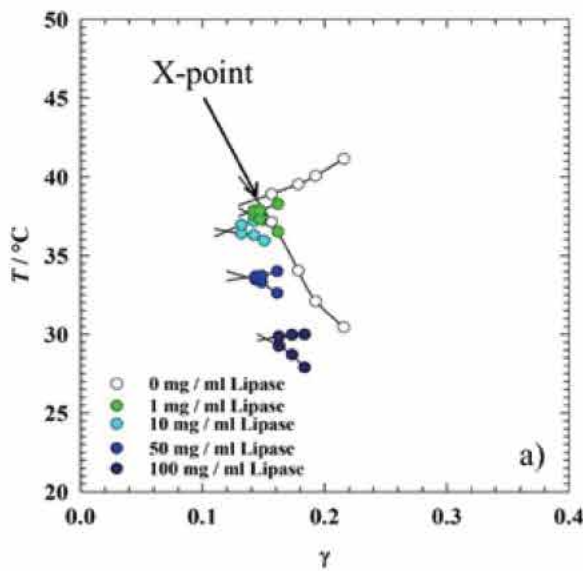


Figure 1a): Phase diagrams of microemulsions of type $\text{H}_2\text{O}/\text{NaCl}$ (4 wt%) – n-octane – C_{10}E_6 – CAL B. The X-points run through a maximum in efficiency, the phase boundaries continuously shift to lower temperatures. b) SANS curves of the base microemulsion and a CAL B concentration series. The characteristic structure peaks were fitted to the Teubner-Strey model.

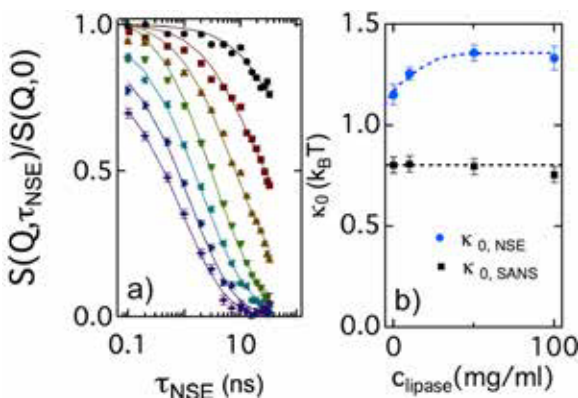


Figure 2a): Normalized intermediate scattering functions $S(Q, \tau_{\text{NSE}})/S(Q, 0)$ for the base microemulsion. b) Comparison of the lipase concentration dependence of the bending rigidities. SANS measurements indicate a constant κ_0 but NSE results suggest a stiffening of the interface.

continuous structures [3, 4]. We learned that the monolayer of a selected nonionic bicontinuous microemulsion possesses a limited loading capacity for the amphiphilic lipase B from *Candida Antarctica*. At increasing lipase B concentration, the monolayer bending constant first increases and then levels off into a plateau where additional lipase molecules no longer adsorb to the monolayer but are solubilized in the water phase of the microemulsion, as supported by complementary techniques.

In a temperature versus surfactant mass fraction (γ) diagram (fig. 1a) the key parameter is the X-point. In its vicinity, the microemulsion is bicontinuous, exhibiting the large connected surfactant monolayer structure separating randomly oriented interconnected water and oil subdomains. Into a well-defined microemulsion consisting of $\text{H}_2\text{O}/\text{NaCl}$ (4 wt.%) – n-octane – pentaethylene glycol monodecylether (C_{10}E_5) we introduced an aqueous solution of the lipase CAL B at different concentrations up to 100 mg/ml. The change in phase behavior was determined by visual inspection.

Neutron Scattering at KWS-1 and J-NSE

SANS measurements were carried out at the KWS-1 instrument on bulk contrast samples for different lipase concentrations (Fig. 1b). The scattering curves were fitted to the Teubner-Strey model and the mean domain size and correlation length was obtained. NSE directly measures the

bare bending elasticity constant. At the J-NSE instrument we studied film contrast samples comprising the previously discussed compositions (fig. 2a). The normalized intermediate scattering functions partially decay at low Q values and decay completely in the high Q range. The solid lines are fits to a numerical computation according to the Zilman-Granek [5, 6] description of the thermally induced membrane undulations. Sample specific start parameters were fixed, while bending rigidity and amplitude were used as free parameters.

Implications for the microemulsion

The neutron experiments performed allow us to present a final picture of the changes in the surfactant monolayer bending constants dependent on the concentration of the lipase CAL B in the aqueous phase of the bicontinuous microemulsion. Up to 10 mg/ml CAL B a shift of the X-point to lower temperatures was observed and increasingly less C_{10}E_5 was needed to reach it (increasing amphiphilic efficiency). The temperature trend continued at higher concentrations. The efficiency trend was reversed. SANS results (fig. 1b) contrasted these trends as the presence of lipase B in the surfactant monolayer had no influence on domain size and correlation length. In figure 2b the bending elastic constants obtained from the fits to the experimental NSE data are plotted as a function of enzyme concentration. The concentration dependence indicates a stiffening of the surfactant monolayer due to the adsorption of enzymes. Recent fluorescence and circular dichroism measurements support the picture that additional lipase molecules no longer adsorb to the surfactant monolayer, but are solubilized in the water phase.

- [1] M. Laupheimer et al., *Tens. Surf. Det.*, 48, 1 (2011).
- [2] S. Engelskirchen et al., *J. Colloid Interf. Sci.*, 312, 114 (2007).
- [3] S. Wellert et al., *Eur. Biophys. J.*, 33, 243 (2010).
- [4] M. Klostermann et al., *Soft Matter*, 8, 797 (2012).
- [5] A.G. Zilman and R. Granek, *Phys. Rev. Lett.*, 77, 4788 (1996).
- [6] M. Monkenbusch et al., *J. Phys.: Condens. Matter*, 17, 2903 (2005).

Depth-dependent morphology investigation of diblock copolymer films using TOF-GISANS

Y. Yao¹, E. Metwalli¹, J.-F. Moulin², M. Haese-Seiller², P. Müller-Buschbaum¹

¹Technische Universität München, Physik-Department E13, Garching, Germany

²Helmholtz-Zentrum Geesthacht GmbH, GEMS at MLZ, Garching, Germany

The depth-dependent morphology of the micro-phase separation structure in polystyrene(deuterated)-block-polybutyl methacrylate diblock copolymer films is investigated using time-of-flight grazing incidence small angle neutron scattering (TOF-GISANS) at the REFSANS instrument. Depending on the film thickness, a perpendicular or horizontal lamellar structure is observed for thin and thick films, respectively. This well-ordered polymer structure can be used as a matrix for producing hybrid films.

Hybrid nanocomposite films

Block copolymers with embedded nanoparticles mark one interesting class of hybrid nanocomposites. Control of the alignment and of the size of the nanoparticle array is achieved by using a templating polymer matrix. Thus, a well ordered polymer matrix is essential for producing well defined hybrid films [1]. We investigated P(Sd-b-BMA) diblock copolymer films which can

be used as a structure directing matrix, using TOF-GISANS. Structural information from different depths is achieved from the different neutron wavelengths λ in TOF mode, which have different scattering depths.

Sample preparation

P(Sd-b-BMA) films were prepared by spin coating on Si substrates. Two different film thicknesses were obtained by adjusting the spin coating parameters. To achieve an equilibrium morphology, all samples were annealed at 433 K for 3 days under N₂ atmosphere.

Morphology investigation using neutrons

The TOF-GISANS measurements were performed at the REFSANS instrument at MLZ, Garching, Germany. A fixed incident angle of 0.45°, a range of the mean wavelength of 0.23 nm to 1.22 nm and a sample-detector-distance of 10.6 m were used.

Lateral and vertical structures

In all two-dimensional (2D) GISANS data, the specular peak is observed almost at a fixed position. As seen in figure 1a to 1f, a second characteristic feature, the so-called Yoneda peak, is present in the 2D data. It is moves along the $(\alpha_i + \alpha_p)$ direction as the neutron wavelength increases. In addition, in the case of the thin P(Sd-b-BMA) film, two side peaks sit symmetrically at the same height along both sides of the Yoneda peak. These originate from the highly ordered structure perpendicular to the sample surface. In contrast, in the case of the thick P(Sd-b-BMA) film (fig. 1g to 1r), no obvious side peaks are visible, but the scattering patterns change significantly along the $(\alpha_i + \alpha_p)$ direction. Above the specular peak, additional strong peaks appear

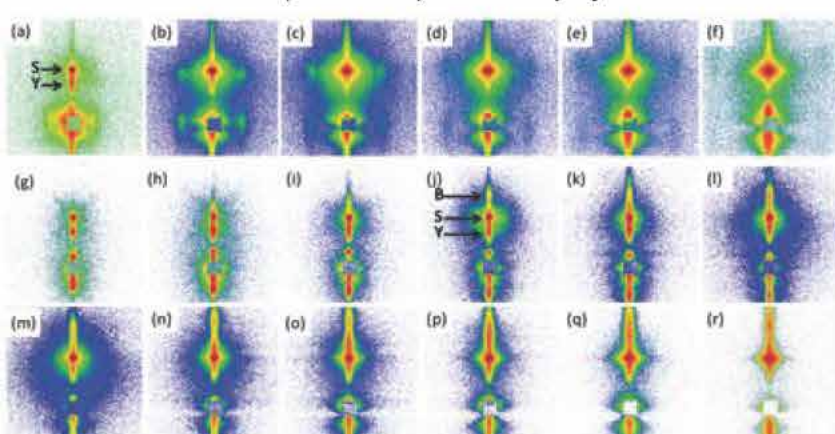


Figure 1: (a) to (f) and (g) to (r) 2D TOF-GISANS data measured simultaneously for the diblock copolymer with film thickness of 60 nm and 300 nm, respectively. The corresponding wavelengths increase along the image sequence with a mean wavelength of 0.23 nm up to 1.22 nm

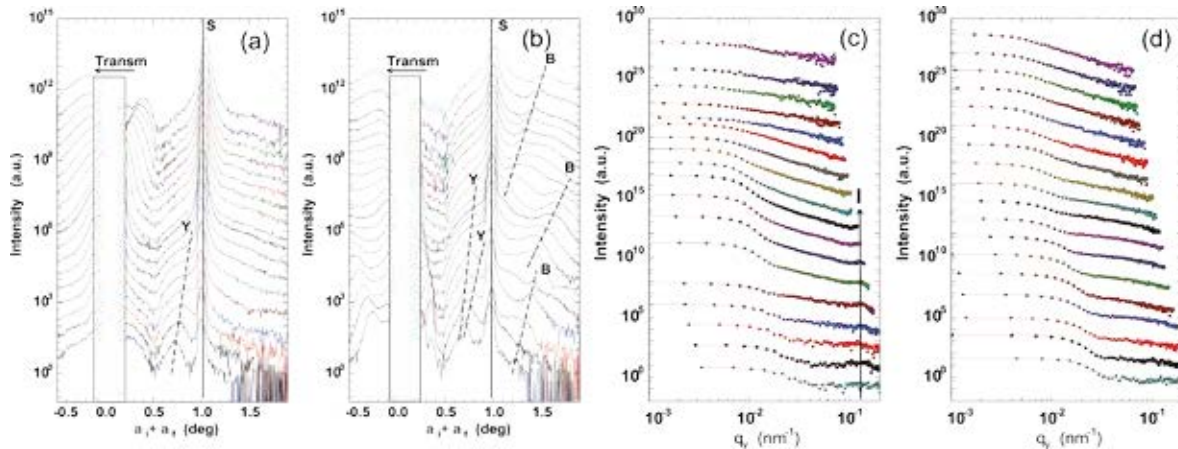


Figure 2: (a) and (b), vertical line cuts of the 2D data as a function of the detector angle ($\alpha_i + \alpha_f$) for 60 nm and 300 nm film thickness, respectively. The position of the specular peak (S) is indicated by the solid line. The position of the Yoneda peak (Y) and Bragg peak (B) are indicated by the dash line, respectively. (c) and (d), horizontal line cuts of the 2D data as a function of the q_y for 60 nm and 300 nm film thickness.

which are first and second order Bragg diffraction peaks. These higher order Bragg peaks indicate an ordered multilayer parallel to the film surface. For further quantitative analysis, the 2D data were cut in the vertical and horizontal direction (with respect to the sample surface) to address structures along the surface normal and in-plane structures.

As seen in the vertical cuts (fig. 2a and 2b), the Yoneda peaks approach the specular peaks with increasing wavelength. In the case of the thin block copolymer film, one mean Yoneda peak is observed (fig. 2a). In contrast, for the thick film (fig. 2b) two individual Yoneda peaks are found. One Yoneda peak originates from the substrate and one from the diblock copolymer. Moreover, Bragg diffraction peaks indicate the ordered parallel multilayer. The Bragg peaks are positioned at

$$\sin\alpha_f = \left\{ \sin^2 \alpha_{cp} + \left[\frac{m\lambda}{D} \pm (\sin^2 \alpha_i - \sin^2 \alpha_{cp})^{\frac{1}{2}} \right]^2 \right\}^{\frac{1}{2}}$$

D denotes the periodic distance of the micro-phase separation structure of the block copolymer film.

Horizontal line cuts (fig. 2c and 2d) show that the scattering intensity decayed first due to the presence of large and unresolved lateral structures.

In the case of the thin film sample, a pronounced peak appears in addition. This peak indicates the lateral orientation of the micro-phase separation structure with a characteristic distance of 53 nm. In contrast, in the thick film such a lateral structure is not present (fig. 2d) as the intensity shows only a broad shoulder.

Conclusion

In summary, the order of the micro-phase separation structure in the block copolymer film can be tuned from parallel to perpendicular orientation by changing the film thickness. For the P(Sd-b-BMA) films presented, no mixed morphologies of either the parallel or perpendicular lamellar, are found. Thus, promising templates for hybrid films are realized.

The influence of processing additives on the morphology of bulk heterojunction films

W. Wang¹, M. Philipp¹, D. Magerl¹, J.-F. Moulin², P. Müller-Buschbaum¹

¹Technische Universität München, Physik-Department E13, Garching, Germany

²Helmholtz-Zentrum Geesthacht GmbH, GEMS at MLZ, Garching, Germany

The blend system P3HT:PCBM is one of the most investigated systems in organic photovoltaics. The film morphology plays a critical role in solar cells. In the present investigation, a few volume percent of additive is added to P3HT:PCBM to modify the morphology. TOF-GISANS measurements are used to probe the internal structure to gain insights into the related efficiency increase from the structure-property relation.

Photoactive polymers used in bulk heterojunctions (BHJ) and their applications in organic photovoltaics have attracted tremendous attention. Compared to standard inorganic solar cells, plenty of promising advantages exist for these materials. Currently, the main drawback of organic photovoltaics is still the low efficiency. The morphology of the BHJ film plays an important role in the performance of organic solar cells [1]. Thermal annealing or solvent annealing can optimize the morphology of BHJ films. Recently, it was observed that by incorporating a few volume

percent of alkanedithiols in the solution of BHJs, the power conversion efficiency of photovoltaic cells can be increased a lot. Alkanedithiols selectively dissolve [6,6]-phenyl C₆₁-butyric acid methyl ester (PCBM), whereas the semi-conducting polymer poly(3-hexylthiophene) (P3HT) is not soluble [2]. Because of the different selectivity, the morphology of BHJ films can be tuned.

Investigation of the inner structure

In our investigation, the semi-conducting polymer P3HT is used as donor material and PCBM is chosen as acceptor material. P3HT and PCBM are dissolved in toluene with a ratio of 1:0.8. The 1,8-octanedithiol, which is used as the processing additive, is added in toluene with a volume fraction of 5 %. The P3HT:PCBM solution is deposited on a silicon substrate via spin coating. Then the films are heated at 140 °C for 20 min. The resulting surface structure is investigated by Optical Microscopy (OM) and Atomic Force Microscopy (AFM). The absorbance of the film is probed by ultraviolet-visible absorption spectroscopy. Time-of-Flight - Grazing Incidence Small Angle Neutron Scattering (TOF-GISANS) experiments are performed to investigate the inner structure of the film on a mesoscopic scale.

As seen in the OM images (fig. 1a and 1b), the P3HT:PCBM film with 1,8-octanedithiol shows better grown PCBM crystal clusters as compared to that without 1,8-octanedithiol. Furthermore, the P3HT:PCBM film with 1,8-octanedithiol shows prominent features of phase separation, which is critical for exciton dissociation in organic photovoltaic devices. AFM results (fig. 1c and 1d) give additional information about the surface morphology of the films on the nanometer scale. The P3HT:PCBM film with 1,8-oct-

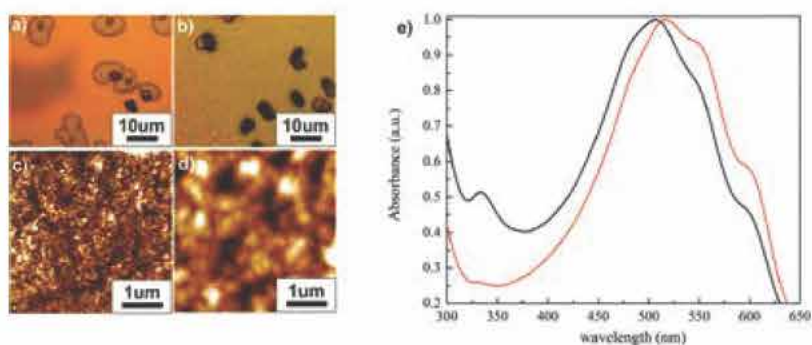


Figure 1: OM images of P3HT:PCBM films without (a) and with (b) 1,8-octanedithiol; AFM images of P3HT:PCBM films without (c) and with (d) 1,8-octanedithiol; absorbance data (e) of films without (black curve) and with (red curve) 1,8-octanedithiol.

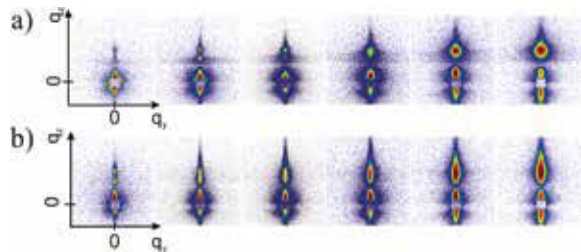


Figure 2: 2D TOF-GISANS data of the P3HT:PCBM films with (a) and without (b) 1,8-octanedithiol; the neutron wavelength increases from left to right: 0.324 nm, 0.475 nm, 0.624 nm, 0.664 nm, 0.924 nm and 1.074 nm.

tanedithiol shows more elongated structures and continuous networks as compared to that without 1,8-octanedithiol, which is beneficial to charge transport in organic photovoltaic devices. The P3HT:PCBM film with 1,8-octanedithiol also shows phase separation on larger length scales.

Figure 1e) presents normalized absorption spectroscopy images of the P3HT:PCBM films without and with 1,8-octanedithiol, respectively. The absorption band of P3HT in the film with 1,8-octanedithiol is red-shifted by 10 nm as compared to that without 1,8-octanedithiol, which indicates an increased conjugation length of P3HT. Thus, the P3HT crystallinity is improved by adding this processing additive to the solution.

Larger structures near the film surface

For the investigation of inner film morphology on mesoscopic scales, TOF-GISANS measurements were performed at the REFSANS instrument. Figure 2 shows these TOF-GISANS data for films with and without additive. The corresponding line cuts are shown in figure 3. As visible in the vertical line cuts (fig. 3a), with increasing wavelength, the Yoneda peak approaches the specular peak, which is due to the wavelength dependence of the critical angle. In addition, the curves of the P3HT:PCBM film without 1,8-octanedithiol show more prominent Yoneda scattering as compared to those with 1,8-octanedithiol, due to greater roughness. Figure 3b) shows horizontal line cuts together with model fits. As seen in the fitting results, the characteristic lateral structure size increases and gets

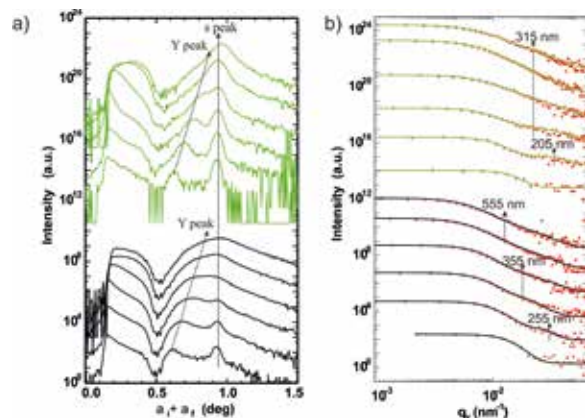


Figure 3: Vertical (a) and horizontal cuts (b) of the 2D TOF-GISANS data for P3HT:PCBM films with 1,8-octanedithiol (top, green curves) and without 1,8-octanedithiol (bottom, black curves); all curves are vertically shifted for presentation; the neutron wavelength increases from bottom to top 0.324 nm, 0.475 nm, 0.624 nm, 0.664 nm, 0.924 nm and 1.074 nm.

more broadly distributed with increasing neutron wavelength. When the incident angle is smaller than the critical angles of the polymer film, the neutron beam can no longer penetrate the full film. Thus, as the neutron wavelength increases, surface sensitivity is progressively gained. As a consequence, the fitting results show that, near the film surface, larger structures exist as compared to the film bulk. In general, in the absence of a processing additive the lateral structures are larger and increase more in size towards the film surface as compared to the film with the addition of 1,8-octanedithiol.

In summary, adding 1,8-octanedithiol to the solution of P3HT:PCBM gives rise to more ordered structures on the molecular level of the P3HT phase and more homogenous structures on the mesoscopic scale due to less strong demixing of P3HT and PCBM.

- [1] M.A. Ruderer et al., *Adv. Funct. Mater.*, 21, 3382 (2011).
- [2] J.K. Lee et al., *J. Am. Chem. Soc.*, 130, 3619 (2008).

Polyelectrolyte brushes: Swelling in water and incorporation of nanoparticles

Z. Yenice¹, O. Soltwedel², J. Genzer³, R. v. Klitzing¹, R. Köhler^{1,4}

¹Technische Universität Berlin, Stranski-Laboratorium, Institut für Chemie, Berlin, Germany

²Max-Planck-Institut für Festkörperforschung, Stuttgart, Germany

³North Carolina State University, Department of Chemical & Biomolecular Engineering, Raleigh, USA

⁴Helmholtz-Zentrum Berlin für Materialien und Energie GmbH, Institut für Weiche Materie und funktionelle Materialien, Berlin, Germany

Polyelectrolyte (PE) brushes represent a new class of thin film materials with tunable surface parameters and interactions, and stimuli responsive behavior. This allows for instance functionalization, or incorporation and exchange of solvents or particles. Neutron reflectivity (NR) was used to determine, first, the structure of these films, either in dry, collapsed state or fully extended, when swollen in buffer. Secondly, the penetration and the distribution of gold nanoparticles (Au-NP) in these brushes were investigated. Although still in its early stage, the study provides qualitatively interesting results. It shows a relatively homogeneous film thickness, i.e. distribution of the brush length, compared to other preparation techniques. It proved that nanoparticles can be incorporated into the PE-brushes irrespective of the size of the Au-NP and the length of the brush. In this case, the brush undergoes a thickness reduction.

PE-brushes – stimuli-responsive materials

Polymer brushes attract a lot of interest on account of their unique properties. They can be grown from different surfaces by the so-called

grafting from approach, using different polymerization techniques, as for instance Surface-Initiated Atom Transfer Radical Polymerization (SI-ATRP) [1]. The method used depends on the required chain length and grafting density (number of chains per unit area of grafted surface). By using the *grafting from* approach, densely packed brushes can be produced.

Surface grafted polymer brushes are good substrates for NP stabilization and are capable of responding to changes in temperature, solvent polarity, pH, and other stimuli, generally by reversible swelling and deswelling, which leads to changes in the physical behaviour, e.g. the optical properties of adsorbed NP, and opens a new pathway for nano-devices such as nanosensors and optical devices [2]. These studies are mostly based on Au-NP adsorbed on polymer brushes because of their nano-sensing abilities, which can be altered by changing the inter-particle distance between the NP and the swelling/deswelling properties of the brushes. These brushes also permit the formation of surface grafted molecular and macromolecular gradients for controlling the self-assembly of NP [3–4], but there is a lack of knowledge regarding the NP penetration and accumulation into the brushes, which would make a better understanding of the mechanism of the particle interpenetration and lateral assembly (Fig. 1). The effect of nanoparticle size, polymer brush chain length and grafting density might be key parameters of this process. In this work, [2-(Dimethylamino)ethyl Methacrylate] (PDMAEMA) brushes are used which are weak polyelectrolyte (PE) brushes having pH dependent properties and are positively charged due to protonation in solutions at pH ≤ 7 ; the positive charge increases as the pH value declines.

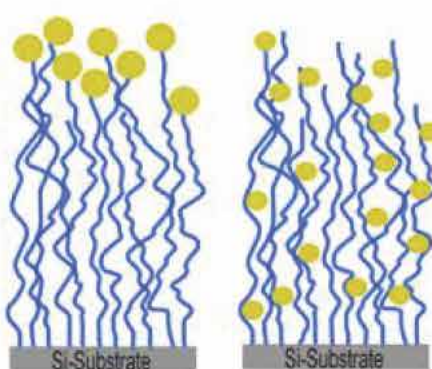


Figure 1: Illustrations of lateral and perpendicular distribution of Au-NP on surface initiated polymer brushes.

Experiments at the neutron reflectometer NREX

All PE brushes were synthesized using Si-ATRP. Brushes with different molecular weights were synthesized to see the effect of brush height / length for Au-NP assembly. Reflectivity measurements of PE brushes with different molecular weights were performed at NREX reflectometer at MLZ. The brushes were measured before and after Au-NP deposition in dry (collapsed) state and immersed in D₂O (i.e. swollen). The dry measurements were conducted using a vacuum chamber filled with He after vacuum. To observe the size effect of the Au-NP, 5 nm and 15 nm diameter particles were used for deposition. The deposition of the particles is done by immersion of the surface grafted PE brushes in Au-NP suspension for a specific time. All nanoparticle suspensions had the same pH for comparison purposes. A D₂O buffer solution at pH 5 was used for all reflectivity measurements in D₂O to obviate the pH dependent properties of the PE brushes.

Brush swelling with water and Au-NP

As seen in figure 2, the 25 nm thick dry (collapsed) brush shows a well-defined fringe pattern indicating a relatively flat surface. In D₂O at pH 5, the brushes swell dramatically by almost a factor of three, observed by the fringe spacing. The interfaces brush/water seem rough, with a low contrast between the swollen brush and the D₂O-subphase. The roughness traces back to the polydispersity of the brushes.

After Au-NP deposition, the curves show more pronounced Kiessig oscillations. Obviously, the NP modify the film, its contrast and/or the homogeneity of its surface. The effect is more distinct for 5-nm-particles than for 15-nm-particles. The film with 5 nm NP appears thicker than the film exposed to 15-nm-particles.

Confinement effects influenced by particle size

The unique properties of polyelectrolyte brushes promise a new approach for creating functional materials on a nano-scale. In addition, fundamental questions - as for our system - relating

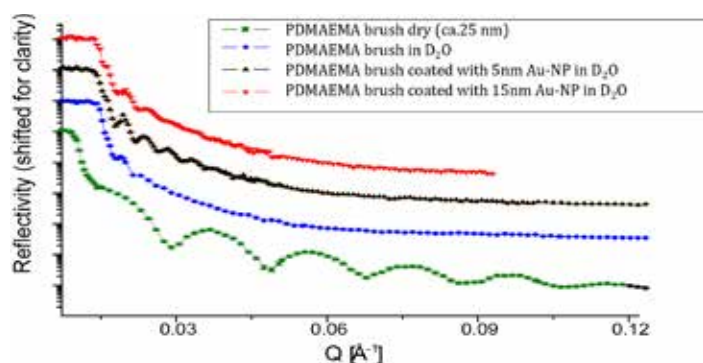


Figure 2: Neutron reflectivity curves of the PDMAEMA brush: dry (collapsed); fully swollen in D₂O and with immobilized Au-NP of either 5 or 15 nm diameter. Change in the curve of swollen brush indicates size-dependent incorporation of Au-NP.

to the complex crossover of steric interactions of incorporated particles and the internal forces as Coulomb forces, van-der-Waals-forces and hydrogen bonding interactions can be addressed.

Our NR study complements our former AFM results and shows that Au-NP can not only be adsorbed, but fully incorporated into the brush, irrespective of the size of the particle. The incorporated particles yield a better reflectivity of the film, possibly due to a homogenization of the film and an optimization of the contrast between sub- and super-phase and the gold-loaded film. The incorporation of Au-NP is attended by a reduction of the film thickness, which is slightly stronger for the bigger particles. This might originate from a different configuration and confinement of the polymer chains.

Due to the complexity of the system, the intended aim of determining a distribution profile or horizon for the gold particles has not been achieved to date. However, the unique option offered by neutron scattering of varying the solvent contrast by using H₂O/D₂O mixtures will help to overcome these difficulties in future experiments.

- [1] K. Matyjaszewski et al., Macromolecules, 32, 8716 (1999).
- [2] S. Gupta et al., Macromolecules, 41, 8152 (2008).
- [3] J. Genzer and R.R. Bhat, Langmuir, 24, 2294 (2008).
- [4] R.R. Bhat and J. Genzer, Appl. Surf. Sci., 252, 2549 (2006).

Influence of diffusion and dipping time on the inner structure of polyelectrolyte multilayers

M. Zerball¹, O. Soltwedel², R. v. Klitzing¹, R. Köhler^{1,3}

¹Technische Universität Berlin, Stranksi-Laboratorium, Institut für Chemie, Berlin, Germany

²Max-Planck-Institut für Festkörperforschung, Stuttgart, Germany

³Helmholtz-Zentrum Berlin für Materialien und Energie GmbH, Institut für Weiche Materie und funktionelle Materialien, Berlin, Germany

Neutron Reflectometry was used to investigate the influence of two fundamental preparation parameters -time and salt concentration- on the internal structure and swelling behavior of strong Polyelectrolyte Multilayers (PEM) exposed to water. A two-block structure of a deuterated and a protonated stack of PEM was built to reveal variations in the inner structure of PEM with respect to its vertical position relative to the solid substrate. Contrary to the common perception, no significant change in internal roughness was observed for different preparation time. The extent of swelling of PEM in water (D_2O) appears strongly influenced by the distance of the polyelectrolyte from the substrate.

Thin Films by Self-assembly of Polyelectrolytes

The subsequent adsorption of oppositely charged polyelectrolytes onto a solid surface (fig. 1) rendered it possible to modify surfaces by covering them with thin films of nanometer thickness [1]. The structure of PEMs in dependence of the preparation conditions, e.g. molecu-

lar weight [2], ionic strength [3] and the type of anion [4] was intensively investigated. It could be shown that the thickness and topography of the adsorbed layer are substantially dependent on the polymer chain conformation during the adsorption process and the topology of the preceding layer.

For the investigation of external properties (e.g. surface roughness and thickness) extensive knowledge was achieved using different techniques such as AFM, TEM, or XPS. More important seem the internal properties since these parameters describe the bulk-like properties in the final, rather equilibrated PEM. However, access to the internal, structural parameters is a challenging task.

Studying internal PEM-structure using NR

One option for studying buried interfaces is neutron reflectometry in combination with a specially prepared PEM block structure [5]. The initial layers of the PEM were deuterated, while the outermost layers were protonated. By this means, the physical quantity -scattering length density- of the inner part is changed without touching the chemical properties of the PEM. The new interface between the protonated and deuterated blocks created in this way, which is only visible for neutrons, reveals the inner structure of the PEM as interdigitation/roughness of adjacent blocks or layers. In our present study, we investigated the influence of two important preparation parameters: the diffusion time and salt concentration on the internal structure and the swelling behaviour of the film.

Experiments with block-structured PEM

The following polyelectrolytes were used to prepare multilayers: Poly(styrene sulfonate), PSS,

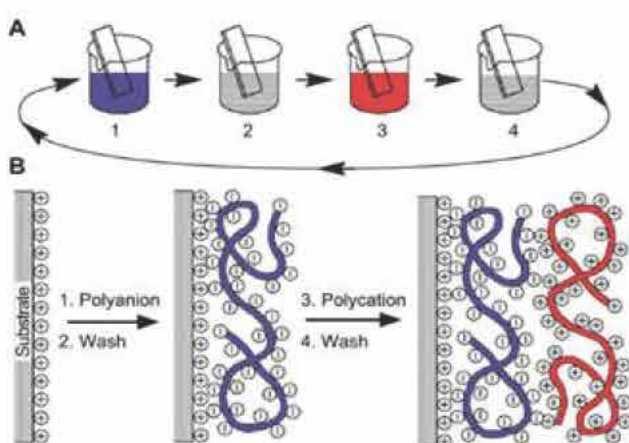


Figure 1: Assembly of Polyelectrolyte Multilayers by alternating adsorption of polyanion and polycation: Dipping Layer-by-Layer technique [1].

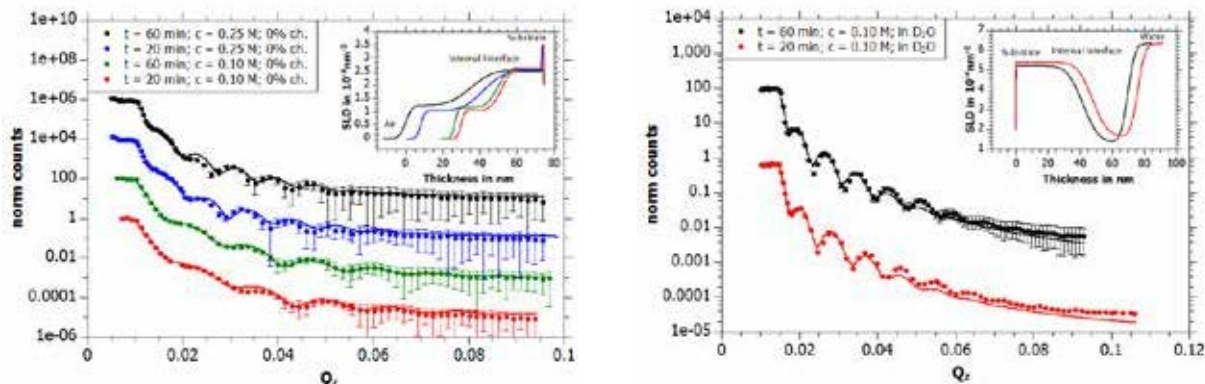
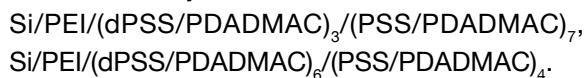


Figure 2 : Neutron Reflectivity curves and the corresponding SLD-Profiles of 2-Block PEMs prepared with dipping times of $t = 20$ min and $t = 60$ min and a NaCl concentration of 0.1 M and 0.25 M measured at 0 % r.h and fully swollen in D_2O .

Poly(diallyldimethylammonium chloride), PDADMAC and deuterated PSS (dPSS). PSS and dPSS are commercially available; linear PDADMAC was synthesized by the group of A. Laschewsky (University Potsdam, Germany). Two different combinations of deuterated and hydrogenated layers were used for one set of measurements, to probe the internal roughness close to the substrate and away from it:



To study the influence of the dipping time, a set of samples was made with dipping times of 20 min per polyelectrolyte layer, and another with 60 min dipping time. In addition, samples were prepared at a salt concentration of either 0.1 M NaCl or 0.25 M NaCl. We measured all 8 samples both in a dry condition and fully swollen in D_2O . The measurements were performed at the reflectometer NREX. For measurements in aqueous conditions, a self-constructed experimental cell was used, while for measurements in dry conditions the vacuum chamber of NREX was used.

Inhomogeneous Swelling of the Film

Figure 2 shows the Neutron Reflectivity curves and the corresponding SLD-Profiles of the investigated system. The fitted data for the reflectivity curves shows no significant change in internal roughness in dependence of the preparation time. This was unexpected since former results for PEM film formation predicted an increase in the internal roughness [6].

The D_2O -swollen PEM also show no significant

differences in internal roughness for different preparation times. The gain in thickness during the swelling is mainly caused by swelling of the internal block. This is contrary to other PEM systems e.g. the PSS/PAH system [7], where mainly the outermost layers contribute to the swelling. Apparently, the high internal roughness (compared to the external roughness) is caused by a less bound structure, which offers more space for D_2O molecules to incorporate inside the film.

New insights using block-structured PEM

2-Block structured PEMs were investigated using Neutron reflectometry to reveal information about the influence of dipping time and salt concentration on the inner structure and swelling behavior. It could be shown that, contrary to common perception, no significant change in internal roughness occurs in dependence of the preparation time. The swelling of PEM in water (D_2O) is mainly influenced by the distance between the polyelectrolyte layer and the substrate.

This study is planned to be continued with further swelling experiments of PEM with different internal block sizes. This will contribute to the lively debate on the crossover of internal interactions with new information about the non-homogeneously swelling of the PEM.

- [1] G. Decher, Science, 277, 1232 (1997).
- [2] P. Kujawa et al., J. Am. Chem. Soc., 127, 9224 (2005).
- [3] R. A. McAloney et al., Langmuir, 17, 6655 (2001).
- [4] J. E. Wong et al., Langmuir, 25, 14061 (2009).
- [5] O. Soltwedel et al., Macromolecules, 43, 7288 (2010).
- [6] C. Porcel et al., Langmuir, 22, 4376 (2006).
- [7] J. E. Wong et al., Macromolecules, 37, 7285 (2004).

Neutron reflectometry reveals an asymmetric distribution of anionic phospholipids on SiO_2

S. Stanglmaier¹, S. Hertrich¹, K. Fritz¹, J.-F. Moulin², M. Haese-Seiller², J. O. Rädler¹, B. Nickel¹

¹Ludwig-Maximilians-Universität, Department für Physik und Center for Nanoscience (CeNS), München, Germany

²Helmholtz-Zentrum Geesthacht, GEMS at MLZ, Garching, Germany

Anionic lipids play a prominent role in mediating the coupling of proteins to the cytoplasmic membrane. Therefore, the preparation and study of lipid bilayers with a controlled content of anionic lipids is a prerequisite for the understanding of hydrophobic-electrostatic interactions of proteins with lipid bilayers, which is a key element in many cellular signal pathways. We prepared POPC/d31-POPS (3:1) unilamellar vesicles and spread them onto a silicon oxide surface to study the distribution of anionic and neutral lipids in both halves of the bilayer. The neutron reflectivity measurement performed at REFSANS reveals the presence of anionic d31-POPS in the outer leaflet only [1].

Lipid membranes

The lipid compositions of the two leaflets of eukaryotic plasma membranes exhibit a high degree of asymmetry. For example, anionic lipids such as phosphatidylserine (PS) only occur in the cytoplasmic leaflet of eukaryotic plasma membranes under normal conditions. When a cell undergoes apoptosis, i.e. programmed cell death, the asymmetric lipid distribution is not sustained. Therefore, PS-binding proteins such as annexins2 are used as apoptosis markers. Here, we demonstrate that a negatively charged surface such as SiO_2 also induces such asymmetry in artificial membranes.

Neutron reflectometry experiments at REFSANS

Lipid vesicles (size 100 nm) were prepared by extrusion in buffer with high salt concentration and added onto a hydrophilic silicon oxide surface inside a fluidic chamber. We flushed the chamber with deionized water after the vesicles had adhered to the surface. In this hypotonic condition the vesicles rupture and spread into a bilayer. The chamber was subsequently filled with PBS buffer in D_2O first (green line) and with a mix of D_2O and H_2O buffer for second measurement (yellow line). The neutron reflectometry shown in figure 1 was performed at the REFSANS instrument at MLZ.

REFSANS is a time of flight instrument suited to reflectometry at the solid-liquid interface. To archive a wide q -range up to 0.18 \AA^{-1} the measurement was performed at four different angles: 0.3° , 0.6° , 1.4° and 2.8° . In figure 1, data from all measurements are plotted against q . The edge of total reflection is at $q \approx 0.015 \text{ \AA}^{-1}$ for the D_2O and at $q \approx 0.008 \text{ \AA}^{-1}$ for the contrast matched buffer. The reflectivity data in both measurements show

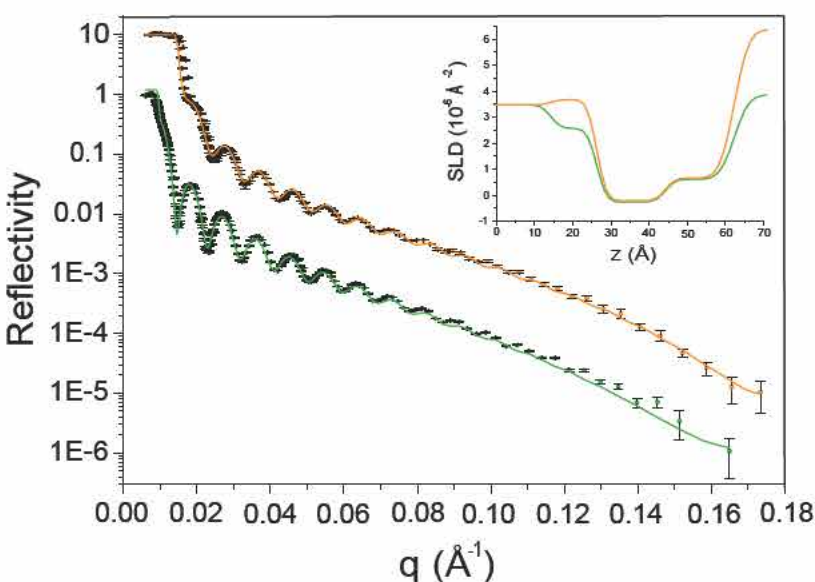


Figure 1: Neutron Reflectivity data from a POPC/d31-POPS (3:1) SLB. The corresponding modeling function is represented by colored lines: D_2O (yellow line), contrast matched buffer (green line). SLD profile as extracted from the modeling in the inset.

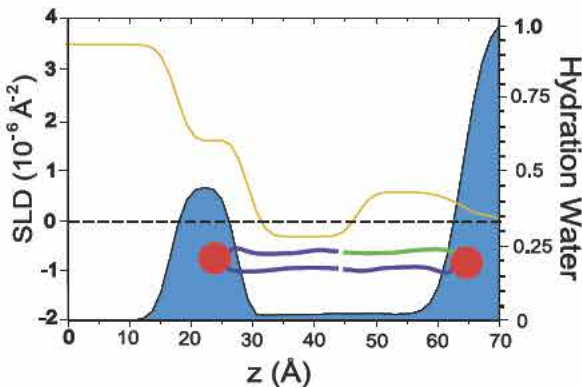


Figure 2: SLD profile without solvent (brown line) and hydration fraction (blue area).

rapid intensity oscillations originating from the thick SiO_2 layer and a broad shoulder originating from the lipid bilayer.

Membrane asymmetry

The analysis of the measurement of the bilayer, i.e. the SLD profile is shown in the inset of figure 1. In the region close to the silicon oxide, the fit to the D_2O data shows increased scattering length density (SLD) compared to the contrast matched data, indicating high hydration in the area of the head, as shown in figure 2. The region of the lipid chains exhibits two plateaus in the range between $z \approx 32 - 44 \text{ \AA}$ and $z \approx 48 - 60 \text{ \AA}$, i.e. there is clear asymmetry between the inner and outer leaflets. The SLD values show an enrichment of anionic deuterated (d31-POPS) lipids in the outer leaflet of the membrane. Using an areal density of $70 \text{ \AA}^2/\text{lipid}$ [1], the PS concentration in the outer bilayer leaflet is $27 \pm 8 \%$ (i.e., very close to the stoichiometric ratio of 25 %). We do not see contributions of PS at the substrate facing leaflet within the accuracy of the analysis ($0 \pm 3 \%$).

The observation that the stoichiometric ratio of the vesicles is conserved in the outer bilayer sheet but that PS is depleted in the leaflet adjacent to the substrate indicates that this asymmetric distribution is apparently not due to a redistribution of lipids between the inner and outer leaflets, but that some PS fraction in the vesicles is lost upon transfer to the supported bilayer.

Conclusion

We have shown that a mixture of anionic POPS and zwitterionic POPC lipids can be deposited on SiO_2 via vesicle fusion induced by osmotic shock. With this method, asymmetric lipid bilayers may be prepared and quantified using neutron reflectometry and deuterium-labeled lipids. Anionic POPS is depleted in the leaflet facing the substrate, and their fraction in the buffer-facing leaflet is in agreement with the initial stoichiometry of 3:1. The asymmetric distribution can be explained by electrostatic effects prior to the fusion of the vesicles. Apparently, electrostatic repulsion can be employed to suppress the transfer of PS in the layer proximal to the negatively charged substrate.

The neutron crystal structure of a perdeuterated enzyme inhibitor complex

S. Tomanicek¹, R. Standaert^{2,3,4}, K. Weiss², A. Ostermann⁵, T. Schrader⁶, J. Ng⁷, L. Coates²

¹Oak Ridge National Laboratory, Environmental Sciences, Oak Ridge, Tennessee

²Oak Ridge National Laboratory, Biology & Soft Matter, Oak Ridge, Tennessee

³Oak Ridge National Laboratory, Biosciences Divisions, Oak Ridge, Tennessee

⁴University of Tennessee, Department of Biochemistry and Molecular & Cellular Biology, Knoxville, Tennessee

⁵Technische Universität München, Forschungs-Neutronenquelle Heinz Maier-Leibnitz (FRM II), Garching, Germany

⁶Forschungszentrum Jülich GmbH, Jülich Centre for Neutron Science at MLZ, Garching, Germany

⁷University of Alabama in Huntsville, Department of Biological Sciences, Huntsville, USA.

The mechanism by which class A β -lactamases hydrolyze β -lactam antibiotics has been the subject of intensive investigations using many different experimental techniques. We used neutron protein crystallography to help elucidate the identity of the catalytic base in the acylation part of the catalytic cycle, where a β -lactam ring is opened and an acyl-enzyme intermediate forms. Using neutron diffraction data collected on the BIODIFF instrument from a perdeuterated enzyme-inhibitor complex, we were able to directly determine the positions of deuterium atoms in the active site.

Novel antibiotics and inhibitors are needed

The production of β -lactamases is the predominant cause of bacterial resistance to β -lactam antibiotics [1]. β -lactamases catalyze hydrolysis of the critical β -lactam ring, thereby rendering the antibiotic harmless to bacteria. To develop new and novel antibiotics and β -lactamase in-

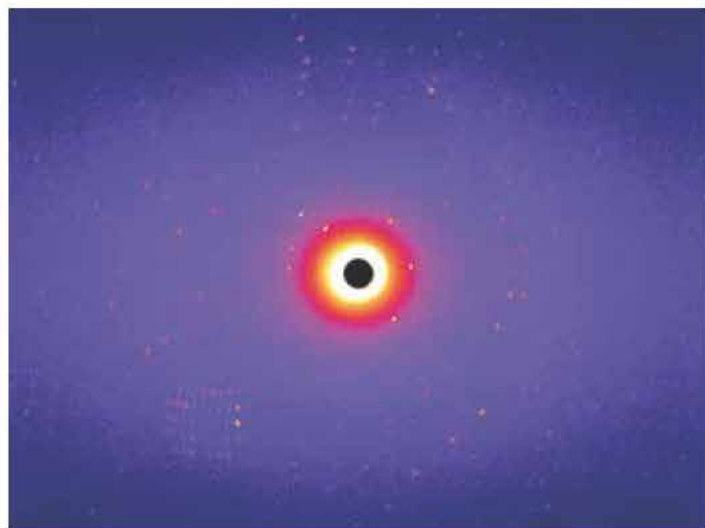


Figure 1: Diffraction pattern of the β -lactamase inhibitor complex crystal.

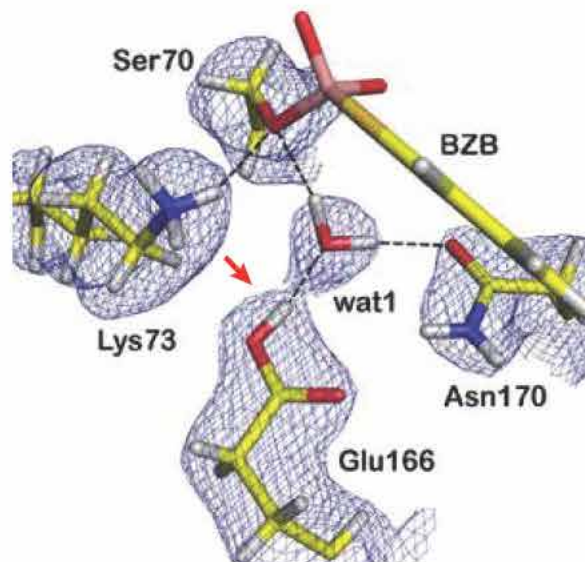


Figure 2: The neutron scattering length density at the active site of the enzyme inhibitor complex. The σ_A -weighted $2F_o - F_c$ positive nuclear density maps colored in blue is shown at 1 σ . The red arrow highlights the protonation site of Glu166. The neutron density for the BZB molecule has been omitted for clarity.

hibitors, a greater understanding of the catalytic mechanism by which these enzymes operate is required. All class A β -lactamases use an active site serine nucleophile to break the lactam bond of the substrate in a two-step acylation-deacylation reaction cycle that leads to overall hydrolysis. Several key aspects of the reaction mechanism remain unresolved and controversial. One of them is the identity of the residue that acts as the catalytic base in the acylation reaction. Two unique mechanisms, with different residues serving as the general base, have been proposed. A number of studies have suggested that the highly conserved residue Lys73 in its neutral form acts as the general base [2]. Another, opposing hypothesis proposes that the highly conserved Glu166, acting through the catalytic water, is the catalytic base during acylation [3].

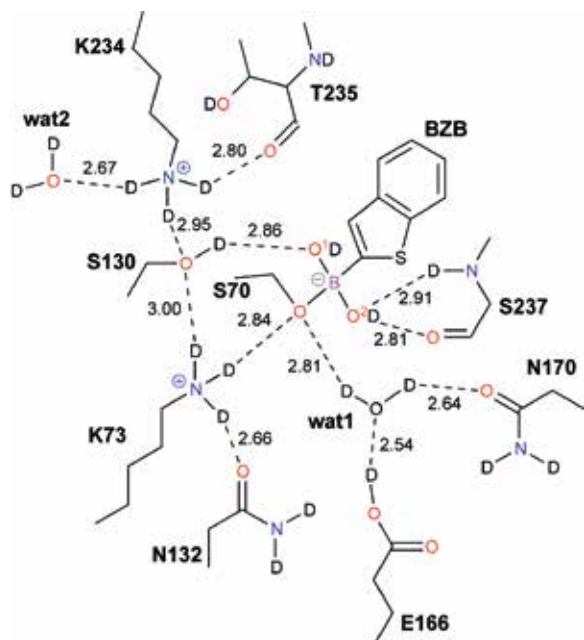


Figure 3: The complete hydrogen-bonding pathway throughout the active site region (dashed lines) and respective distances (in Å).

Experiments at BIODIFF

We synthesized a perdeuterated acylation transition state analog, benzothiophene-2-boronic acid (BZB), which was also isotopically enriched with ^{11}B , as ^{10}B is a known neutron absorber. The perdeuterated β -lactamase enzyme Toho-1 R274N/R276N was purified and crystallized as described previously [4]. Using an *E. coli* based protein expression system, the perdeuterated β -lactamase was expressed in a fully deuterated minimal medium according to a fed-batch fermentation protocol [5]. Large protein crystals suitable for neutron diffraction were grown at 20 °C using the batch crystallization method. For neutron diffraction experiments on BIODIFF a large single crystal ($\sim 1.5 \times 1.5 \times 1.2$ mm) was selected and soaked for 1 hour in a reservoir solution containing 5 % dimethyl sulfoxide-d6, 2.7 M ammonium sulfate, 0.1 M sodium citrate (pD 5.1), and 5.0 mM pd-BZB- ^{11}B (immediately prior to mounting the crystal in a round quartz capillary and initiating data collection). Monochromatic ($\lambda = 2.67$ Å) neutron diffraction data were collected at room temperature to a resolution of $d_{\min} = 2.0$ Å. A typical diffraction image is shown in figure 1. The final neutron model of the β -lactamase-BZB complex was obtained using

the PHENIX suite [6] after several rounds of maximum likelihood-based refinement of individual coordinates, individual atomic displacement parameters (ADP) and occupancies. The neutron density at the active site is shown in figure 2.

Glutamic acid 166 acts as the catalytic base

Of particular importance is the fact that the neutron structure showed that Glu166 is protonated in the complex (see figure 2, red arrow); Further, the Ser70 hydroxyl is deprotonated and has formed a tetrahedral boronate adduct with the BZB inhibitor, analogous to the tetrahedral intermediate (fig. 3). Finally, the Lys73 side chain is probably in the ammonium (protonated) form. These results imply that Glu166 acts as the catalytic base during acylation [7].

Conclusion

This neutron crystallographic study of a perdeuterated enzyme-inhibitor complex fills in considerable detail on the structure of the hydrogen bonding network in the active site of a class A β -lactamase during the acylation reaction. Although the deuteration of proteins and their ligands can be technically challenging, this work shows that there is considerable value in pursuing it.

- [1] A. Matagne et al., Nat. Prod. Rep., 16, 1 (1999).
- [2] D. Golemi-Kotra et al., J. Biol. Chem., 279, 34665 (2004).
- [3] R.M. Gibson et al., Biochem. J., 272, 613 (1990).
- [4] S. Tomanicek et al., FEBS Lett., 585, 364 (2011).
- [5] F. Meilleur et al., Biochemistry, 43, 8744 (2004).
- [6] P.D. Adams et al., Biol. Crystallogr., 65, 567 (2009).
- [7] S. Tomanicek et al., J. Biol. Chem., 288, 4715 (2013).

Crystal and magnetic structure of multiferroic $\text{Ba}_2\text{CoGe}_2\text{O}_7$

V. Hutu^{1,2}, A. Sazonov^{1,2}, M. Meven^{1,2}, H. Murakawa³, Y. Tokura³, I. Kézsmárki⁴, B. Náfrádi⁵

¹RWTH Aachen, Institut für Kristallographie, Aachen, Germany

²Forschungszentrum Jülich GmbH, Jülich Centre for Neutron Science at MLZ, Garching, Germany

³University of Tokyo, Department of Applied Physics, Tokyo, Japan

⁴Budapest University of Technology and Economics and Condensed Matter Research Group of the Hungarian Academy of Sciences, Department of Physics, Budapest, Hungary

⁵Ecole Polytechnique Fédérale de Lausanne, Laboratory of Nanostructures and Novel Electronic Materials, Lausanne, Switzerland

Detailed structural investigation of the novel multiferroic $\text{Ba}_2\text{CoGe}_2\text{O}_7$ was performed for the first time at low-temperature combining neutron diffraction with magnetization measurements and with the optical study of lattice vibrations on single crystals. The crystal structure above (10.4 K) and the crystal and magnetic structures below (2.2 K) the antiferromagnetic transition temperature of $T_N = 6.7$ K were determined using the single crystal diffractometer HEiDi. The orthorhombic polar Space Group (SG) $Cmm2$ is proposed as the true crystal structure. Below T_N the spins of the Co^{2+} ions form a square-lattice Néel order within the (a,b) plane, while their alignment is ferromagnetic along the c-axis. The magnitude of the ordered moment, lying fully within the (a,b) plane, is found to be $2.9(1) \mu_B/\text{Co}^{2+}$ and the easy-axis of the sublattice magnetizations corresponds to the [110] direction.

New multiferroic $\text{Ba}_2\text{CoGe}_2\text{O}_7$

The study of multiferroics, materials simultaneously having more than one primary ferroic order parameter, is a hot topic in material sciences. Recently, $\text{Ba}_2\text{CoGe}_2\text{O}_7$ (BCGO) has attracted significant scientific interest due to its peculiar magnetoelectric behavior [1,2] and its giant directional dichroism in resonance with both electrically and magnetically active spin excitations located in the terahertz region [3]. A number of different theoretical models have been proposed in order to explain these phenomena [2,4]. Very recently, a theoretical analysis based solely on symmetry arguments has shown that the main features of the magnetoelectric behavior of BCGO can be predicted and understood without appealing to any particular atomic mechanism [5]. It is clear

that precise structural information, both for the nuclei and relating to the spin order (crystal and magnetic structures), is essential if the complex physics behind the magnetoelectric behavior of the compound is to be unravelled. Nevertheless, detailed structural investigation of BCGO at low temperatures has not yet been carried out. In order to determine the structural parameters of BCGO and to fully characterize its magnetic order in the multiferroic state, we performed a detailed crystallographic study at temperatures above and below the magnetic phase transition using neutron diffraction on a single crystal diffractometer HEiDi [6]. These results provide a solid basis for an understanding of the microscopic origin of the magnetoelectricity in BCGO.

Crystal structure refinement

Prior to studies of the BCGO magnetic structure, the crystal structure was measured at 10.4 K. Recently, a detailed crystal structure determination of BCGO was performed at room temperature (RT) and at 90 K using synchrotron radiation [7]. The characteristic SG for melilite-type compounds, $P-42,m$, was confirmed to describe well the average structure at the studied temperatures. Moreover, as follows from the observation of a set of superstructure reflections violating the $2,$ symmetry, the real structure of BCGO is more distorted and has a lower symmetry. Symmetry analysis showed two possible SG candidates for the true structure: tetragonal $P-4$ (No. 81) and orthorhombic $Cmm2$ (No. 35). However, the distortions which lead to the symmetry lowering are found to be extremely small. Correspondingly, the refinements of the structural parameters within either of the two subgroups do not change the quality of the fit in any direction, which allowed us to exclude one of the

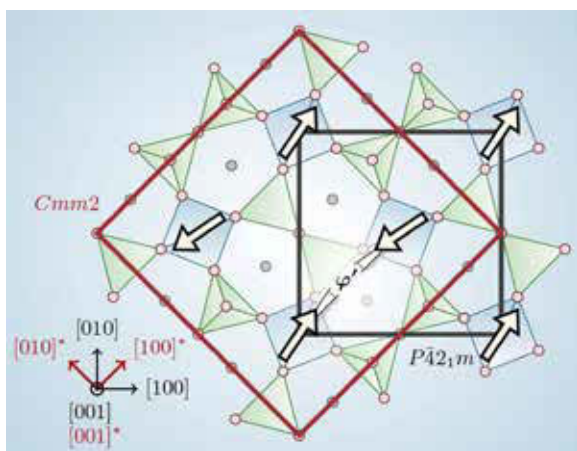


Figure 1: Magnetic structure of BCGO at 2.2 K: View along the [001] direction. Both $P-42,m$ and $Cmm2$ crystallographic unit cells are shown.

two proposed SG candidates. Under these circumstances one may conclude that, within the error of the experiment, tetragonal $P-42,m$ SG (No. 113) is a very good approximation of the average nuclear structure of BCGO at 10.4 K (paramagnetic phase). Table 1 shows the fractional atomic coordinates and the isotropic atomic displacement parameters of the crystal structure of BCGO determined in $P-42,m$ SG at 10.4 K.

Magnetic structure refinement

As shown in reference [5], the AFM ordering in this material breaks the paramagnetic space group $P-42,m1'$ into different magnetic space groups (MSG) depending on the orientation of the sublattice magnetizations. For the AFM component of the sublattice magnetizations lying along the direction [100], the resulting MSG is $P2_12_12_1'$. For the AFM spin configuration along [110], the resulting MSG is $Cm'm2'$. For a more general direction of the spins in the (a,b) plane, the symmetry reduces to $P112_1'$. In zero magnetic field, it is impossible to distinguish between $P2_12_12_1'$, $Cm'm2'$ and $P112_1'$ by conventional neutron diffraction due to the presence of the magnetic domains in each case. Measurements of macroscopic quantities such as the bulk magnetization and ferroelectric polarization, combined with information from the present neutron scattering data, can help to clarify this point. The magnetic space group $P2_12_12_1'$ in the zero-field ground state can be ruled out as it does not allow spontaneous polarization along z, which is observed

Ion	Wyckoff position	X	Y	Z	U_{iso}/U_{eqv}
Ba	4e	0.33465(14)	0.16537(14)	0.49239(28)	0.0010(3)
Co	2b	0	0	0	0.0023(9)
Ge	4e	0.14085(11)	0.35915(11)	0.04031(19)	0.0027(2)
O1	2c	0	0.5	0.15996(39)	0.0044(4)
O2	4e	0.13802(16)	0.36200(16)	0.72960(27)	0.0044(3)
O3	8f	0.07906(15)	0.18452(14)	0.18825(20)	0.0043(2)

Table 1: Nuclear structure parameters of BCGO at 10.4 K in $P-42,m$

experimentally in BCGO [1]. Moreover, as was shown in Ref. [4], the phase which corresponds to $P112_1'$ cannot be reached directly from the paramagnetic state if the phase transition at T_N is of second order. Therefore, the phase with magnetic symmetry $Cm'm2'$ which displays four magnetic domains can be identified as the magnetic phase of BCGO below T_N . We performed a refinement of the magnetic structure in the orthorhombic MSG $Cm'm2'$. In the first step of the refinement, the nuclear structure parameters were fixed at the experimental values obtained at 10.4 K, while in the final step both nuclear and magnetic structures were refined simultaneously. In addition to the nuclear parameters, the magnitude of the Co magnetic moment and the canting angle φ' between its direction and [110] in the (a,b) plane was refined. The magnetic structure of BCGO ($Cm'm2'$ domain) is illustrated in figure 1. Along the c axis the moments are ordered ferromagnetically. Taking into account the melilite-like layered structure, the main magnetic interactions are expected to occur in the (a,b) plane. The strong 2D character of the magnetism in BCGO was also confirmed by the magnetization measurement [8]. As an important result of the present neutron scattering study, the magnitude of the ordered magnetic moment of Co ions could be refined with high accuracy to be $2.9 \pm 0.1 \mu_B$.

- [1] H.T. Yi et al., Appl. Phys. Lett., 92, 212904 (2008).
- [2] H. Murakawa et al., Phys. Rev. Lett., 105, 137202 (2010).
- [3] I. Kézsmárki et al., Phys. Rev. Lett., 106, 57403 (2011).
- [4] P. Toledano et al., Phys. Rev. Lett., 84, 094421 (2011).
- [5] J.M. Perez-Mato et al., Acta Cryst., 67, 264 (2011).
- [6] V. Hutana et al., Phys. Rev. Lett., 86, 104401 (2012).
- [7] V. Hutana et al., Phys. Rev. Lett., 84, 212101 (2011).
- [8] T. Sato et al., Phys. Rev. Lett., 880, 329–333 (2003).

A single-crystal neutron diffraction study of pezzottaite, $\text{Cs}(\text{Be}_2\text{Li})\text{Al}_2\text{Si}_6\text{O}_{18}$

G. D. Gatta¹, I. Adamo¹, M. Meven^{2,3}, E. Lambruschi⁴

¹Università degli Studi di Milano, Mailand, Italy

²RWTH Aachen, Institut für Kristallographie, Aachen, Germany

³Forschungszentrum Jülich GmbH, Jülich Centre for Neutron Science at MLZ, Garching, Germany

⁴Università degli Studi di Parma, Parma, Italy

The crystal chemistry and crystal structure of pezzottaite (ideally $\text{Cs}(\text{Be}_2\text{Li})\text{Al}_2\text{Si}_6\text{O}_{18}$; $a = 15.9615(6)$ Å, $c = 27.8568(9)$ Å; space group: $R\text{-}3c$) from Madagascar were investigated using Electron Microprobe Analysis - Wave Length Dispersive (EMPA-WDS), Thermogravimetry (TG) and single-crystal neutron diffraction (at 2.3 K). The structure refinement showed a non-significant presence of aluminum, beryllium or lithium at the tetrahedral $\text{Si}1$, $\text{Si}2$ and $\text{Si}3$ sites, the absence of lithium at the octahedral $\text{Al}1$, $\text{Al}2$ and $\text{Al}3$ sites, and a partial lithium/beryllium disordering between the tetrahedral Be and Li sites.

Pezzottaite, which belongs to the “beryl group”, is a Cs-bearing gemstone with the ideal composition $\text{Cs}(\text{Be}_2\text{Li})\text{Al}_2\text{Si}_6\text{O}_{18}$ [2]. Its structure (space group $R\text{-}3c$) consists of six-membered rings of

SiO_4 tetrahedra $\perp [0001]$, linked by AlO_6 octahedra and $(\text{Li},\text{Be})\text{O}_4$ tetrahedra [3]. Alkali cations and H_2O molecules lie within the six-membered ring channels along $[0001]$ and compensate for the positive charge deficit due to $\text{Li}^{+}\leftrightarrow\text{Be}^{2+}$ substitution.

Some open questions remain concerning the crystal chemistry of Cs-rich beryl/pezzottaite. For example, the level of Cs (and, therefore, the Li/Be content) at which the structure transforms from $P6/mcc$ to $R\text{-}3c$ is still unknown. In pezzottaite, the Li/Be distribution in the tetrahedral sites was modelled as completely ordered, although the similar X-ray scattering factors of Li and Be do not allow an unambiguous description of the ordering. Moreover, the configuration of water molecules, if present, is still unknown.

Due to the different neutron scattering lengths of Li and Be, single-crystal neutron diffraction represents the more appropriate experimental technique that allows us to answer the open questions regarding the crystal structure/chemistry of this mineral.

Determination of the chemical composition

A gem-quality crystal of pezzottaite originating from the type locality in Ambatovita (Madagascar) was used for this study. The chemical composition of the sample was determined using Electron Microprobe Analysis - Wave Length Dispersive (EMPA-WDS) and Thermogravimetry (TG) analyses performed up to 1,370 K.

A single-crystal (about $2.8 \times 2.4 \times 2.0$ mm³) was selected for the neutron diffraction experiment. Data collection was carried out on the hot single-crystal neutron diffractometer HEiDi at the MLZ.

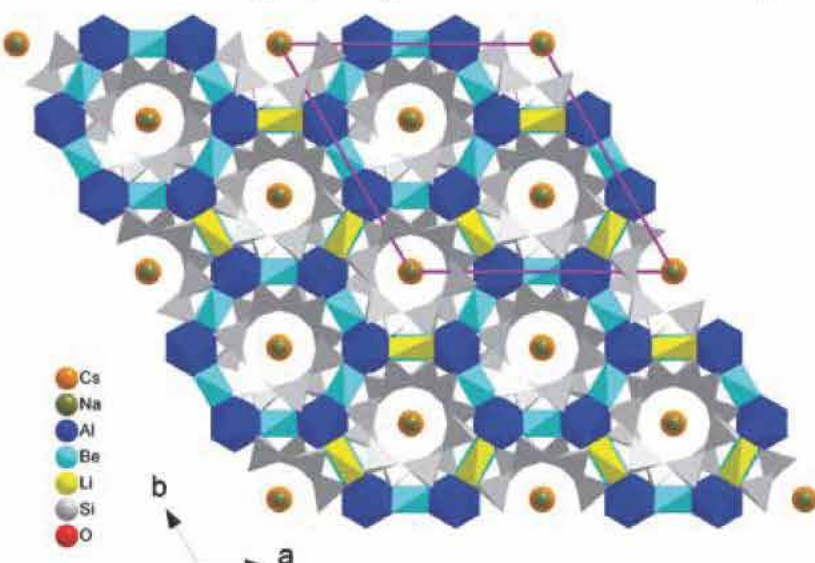


Figure 1: The crystal structure of pezzottaite viewed down $[0001]$.

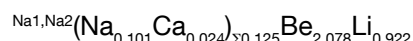
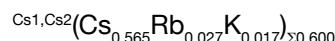
The sample was wrapped in aluminum foil and mounted onto a closed cycle cryostat to reach a minimum temperature of 2.3 K (± 0.1 K accuracy), choosing a wavelength of 0.794 Å, and a pure ω -scans mode. A total number of 7,115 reflections up to $\sin(\theta)/\lambda = 0.91$ Å⁻¹ was measured, out of which 3,657 were unique for symmetry. The integrated intensities were corrected for the Lorentz effect. The discrepancy factor for the symmetry related reflections was $R_{\text{int.}} = 0.0523$.

Structure refinement

The structural refinement was performed using Jana2006 [4] software, starting from the X-ray structural model previously reported [3]. The secondary isotropic extinction effect was corrected. The refinement was conducted using isotropic displacement parameters for all atomic sites, except for the channel Cs1 and Cs2 sites, which were refined anisotropically. With a fully ordered distribution of lithium and beryllium at the tetrahedral *Li* and *Be* sites, respectively, the refinement did not achieve the convergence. A disordered distribution of lithium and beryllium at both *Li* and *Be* sites allowed the convergence to be rapidly achieved. No evidence of lithium/aluminium disordering at the octahedral sites, nor of the oxygen or hydrogen sites, ascribable to H₂O molecules as channel content, was found. At the end of the refinement, no peak larger than $\sim 2.0/\pm 2.5$ fm/Å³ was present in the difference-Fourier map. The final agreement index (R_1) was 0.0595 for 70 refined parameter and 1,818 unique reflections with $I > 3\sigma(I)$.

No significant evidence for H₂O sites

The average chemical formula of the pezzottaite sample, obtained by EMPA-WDS, TG and neutron structure refinements is the follow:



The different neutron scattering lengths of lithium, beryllium, silicon and aluminum offered a clear picture of the site population at the tetrahedral (i.e. *Li*, *Be*, *Si1*, *Si1*, *Si2* and *Si3*) and octahedral (i.e. *Al1*, *Al2* and *Al3*) sites. In particular, *a*) Al, Be, Li are not present at the *Si1*, *Si2* and *Si3* sites, *b*) Li is absent at the octahedral *Al1*, *Al2* and *Al3* sites, *c*) a partial lithium/beryllium disordering between the tetrahedral *Be* and *Li* sites occurs.

Typical disordered distribution

The neutron structure refinement converges with a population of the *Be* site and the *Li* site represented by (96.5 % *Be* + 3.5(6) % *Li*) and (14.8(6) % *Be* + 85.2(6) % *Li*), respectively, with a little deficit of lithium (the total amount of beryllium and lithium is 2.078(18) and 0.922(18) *a.p.f.u.*, respectively). The disordered *Be/Li* distribution we found in pezzottaite is also typical for Cs/Li-rich beryl, and it appears that the change in symmetry between beryl (i.e. *P6/mcc*) and pezzottaite (i.e. *R-3c*) cannot be ascribed to the *Li/Be* ordering only, but is more likely due to the nature and bonding configuration of the channel content.

Although no significant evidence for H₂O sites was observed during the neutron refinement, due to the low amount of water molecules, we cannot exclude a disordered distribution of cations and H₂O molecules between the Cs1, Cs2, Na1 and Na2 sites. (More details of the experimental results in [1].)

[1] G.D. Gatta et al., Phys. Chem. Miner., 39, 829 (2012).

[2] F.C. Hawthorne et al., Mineral Rec., 35, 369 (2004).

[3] O.V. Yakubovich et al., Crystallogr. Rep., 54, 399 (2009).

[4] V. Petricek et al., Jana2006 (2006).

Investigation of oxygen mobility in $\text{Ca}_{12}\text{Al}_{14}\text{O}_{33+\delta}$

H. Krause¹, H. Boysen², B. Pedersen³, S.G. Ebbinghaus¹

¹Martin-Luther-Universität Halle-Wittenberg, Institut für Chemie, Halle, Germany

²Ludwig-Maximilians-Universität München, Sektion Kristallographie, München, Germany

³Technische Universität München, Forschungs-Neutronenquelle Heinz Maier-Leibnitz (FRM II), Garching, Germany

C $\text{a}_{12}\text{Al}_{14}\text{O}_{33+\delta}$ (C12A7, mayenite) shows both a variable oxygen content and high oxygen mobility at elevated temperatures. Using single crystal neutron diffraction, we investigated the structure of crystals grown by the floating zone technique between room temperature and 950 °C. We found a complex disordered arrangement of both the Ca- and cage O-atoms, which changes significantly with increasing temperature. These results provide a deeper insight into the mechanism of the oxygen transport.

At high temperatures, $\text{Ca}_{12}\text{Al}_{14}\text{O}_{33+\delta}$ (C12A7) shows unusually high oxygen mobility, which is only one order of magnitude lower than that of Y-stabilized zirconia (YSZ). This makes C12A7 an interesting material for solid oxide fuel cells, sensors and catalytic applications. The high oxygen mobility can be explained by the complex structure of mayenite, in which the $[\text{Ca}_{12}\text{Al}_{14}\text{O}_{32}]$ -units form positively charged cages. 1/6 of these

cages are occupied by (mobile) oxide ions. The transport mechanism of these ions is not yet completely understood. We used single crystal neutron diffraction at three temperatures to gain a deeper insight into the migration paths of the cage oxygen. This knowledge may lead to strategies for enhancing the oxygen conductivity.

Measurements at the diffractometer RESI

Crystals of C12A7 were grown in an optical floating zone furnace with a growth speed of 0.2 mm/h. The resulting ingots were cut into clear, bubble and crack free single crystals having a dimension of 3 x 3 x 5 mm (fig. 1). Neutron diffraction measurements up to $2\theta = 100^\circ$ were performed on the four circle diffractometer RESI using thermal neutrons with a wavelength of 1.0408 Å. A mirror furnace was used to heat the sample to 750°C and 950°C in a vacuum.

Fourfold split positions

The idealized crystal structure of C12A7 is shown in figure 2. Earlier X-ray diffraction experiments had already indicated that the real structure is more complicated by far. For example, a three-fold split Ca position was observed. In addition, the cage oxygen ions were found to be localized on a fourfold split position shifted from the center of the cages and being part of disordered AlO_4 -tetrahedra [1].

The refinement of the room-temperature single crystal neutron diffraction data basically confirmed this model but gave indication of an even more complex disordering of the Ca ions. More interestingly, the cage oxygens are also apparently distributed on additional positions. A close inspection of the Difference Fourier map revealed significant remaining scattering densities within

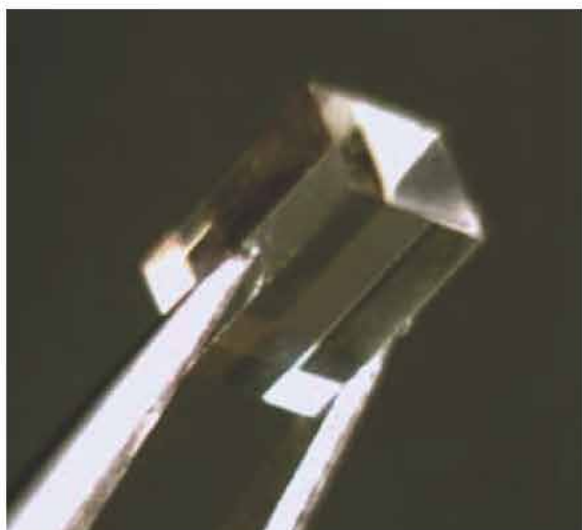


Figure 1: Photograph of the $\text{Ca}_{12}\text{Al}_{14}\text{O}_{33}$ crystal investigated.

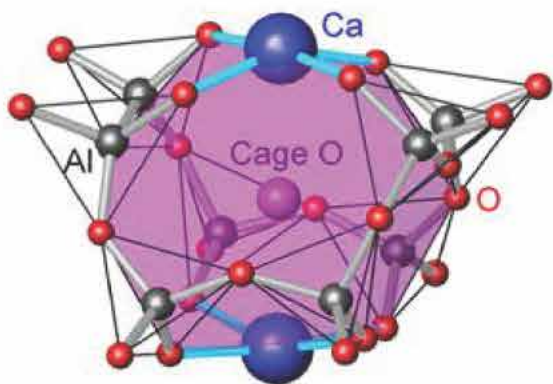


Figure 2: Idealized structure of C12A7.

the $[Ca_{12}Al_{14}O_{32}]$ framework. In figure 3 the most intense difference Fourier peaks are marked by open circles.

At high temperatures, the positions of the cage oxygens become more diffuse, reflecting the increasing thermal motion of these ions, in accordance with earlier powder neutron measurements [2].

Oxygen transport mechanism

In the most simple transport model, the mobility of the cage oxygens is explained by a direct jump from an occupied cage to a vacant one. We did not observe significant scattering intensities pointing in this direction. Therefore, a direct jump mechanism seems unlikely. On the contrary, our high temperature data indicate that an exchange between cage and framework oxygen is more likely.

Further experiments to enhance oxygen mobility
Although data evaluation is still in progress and some structural aspects need to be examined in more detail, the preliminary results enhance our knowledge of the complex structure of C12A7. In particular, it was verified that the cage oxygen atoms belong to partially occupied distorted AlO_4 -tetrahedra. In addition, no indications of a direct jump of the mobile oxygen ions from one cage to another were detected. These findings strongly support a conductivity mechanism in-

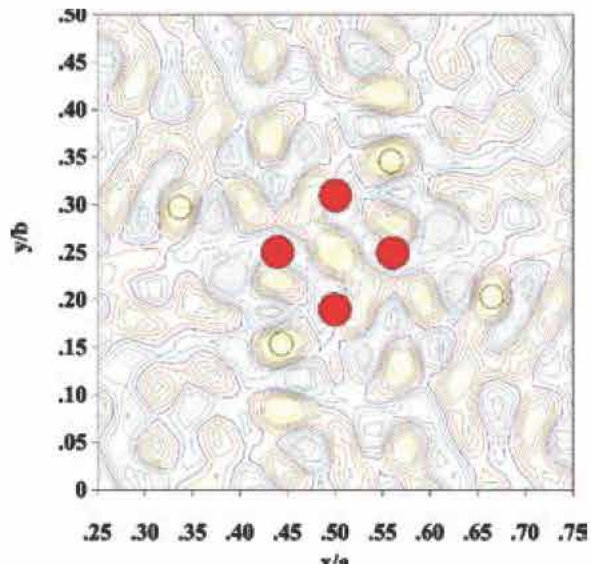


Figure 3: Difference Fourier plot around the cage center.

volving an exchange between cage and framework oxygen ions.

This result provides a new starting point for further experiments to enhance the oxygen mobility by e.g. doping to influence the cell parameter or the cage occupancy with the final aim of substituting YSZ as high temperature oxygen conductor.

[1] M. Lerch et al., Prog. Solid State Chem., 37, 81 (2009).

[2] H. Boysen et al., Acta Crystallogr., Sect. B, 63, 675, (2007).

The fundamental biomolecule guanidine through the eyes of single-crystal neutron diffraction

P. K. Sawinski¹, M. Meven^{2,3}, U. Englert¹, R. Dronskowski¹

¹RWTH Aachen, Institut für anorganische Chemie, Aachen, Germany

²RWTH Aachen, Institut für Kristallographie, Aachen, Germany

³Forschungszentrum Jülich GmbH, Jülich Centre for Neutron Science at MLZ, Garching, Germany

The fundamental biomolecule guanidine crystallizes in the orthorhombic space group *Pbca* with two symmetry-independent Y-shaped molecules in the asymmetric unit. As crystallization of guanidine is quite difficult – probably due to its sensitivity to moisture – the crystal-structure analysis has only now become possible although the molecule was first synthesized in 1861. A single-crystal neutron-diffraction study carried out at temperatures of 100 and 273 K using the HEiDi diffractometer eventually gives access to precious vibrational and bond-length data needed for a proper understanding of the molecule on the basis of anisotropic displacement parameters.

Studying hydrogen-bonding phenomena

The fundamental biomolecule guanidine, CN_3H_5 , may be looked upon as the imino-derivative of the similarly fundamental biomolecule urea, OCN_2H_4 . Although Strecker synthesized guanidine for the first time as far back as 1861, the crystal structure was, amazingly enough, unknown until 2009 [1]. We note that molecular guanidine which appears as a fragment in a plethora of various biomolecules (for example in the DNA base guanine), offers a fascinating opportunity to study hydrogen-bonding phenomena in detail. In fact, the compound features a complicated hydrogen-bond network. On the basis of an earlier single-crystal X-ray diffraction study, a set of eight hydrogen bonds had already been identified using donor–acceptor distance criteria [1]. In addition, the hydrogen-bonding energies had been calculated using density-functional theory, revealing bond strengths of up to 33.8 kJ mol^{-1} , and one of the eight hydrogen “bonds” turned out to be repulsive in nature [2]. In the following, we present the results of a single-crystal neutron-diffraction study of guanidine carried out using the HEiDi instrument. By this means, highly accurate spatial and anisotropic displacement parameters for all the atoms were derived, an experimental benchmark for further theoretical studies.

3000 Bragg reflections collected

A single crystal (72 mm^3) of guanidine suitable for neutron diffraction experiments was grown in a Schlenk tube over half a year and then subjected to structural analysis using the hot-neutron four-circle diffractometer HEiDi at the MLZ. Selected rocking scans on the very first reflections confirmed the good quality of the crystal from Gaussian-like profiles, and there were no

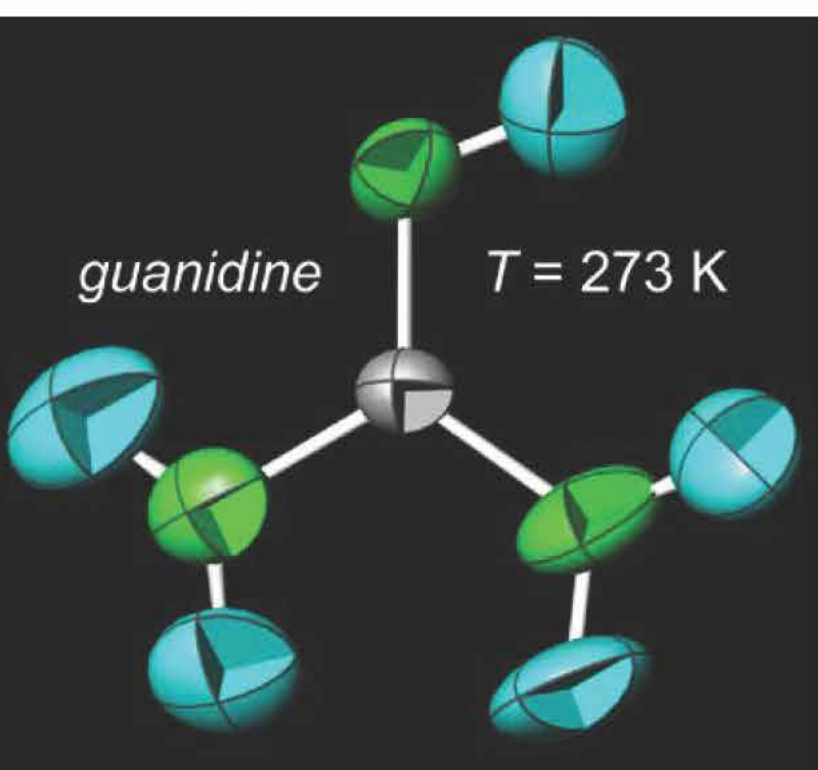


Figure 1: ORTEP representation of one of the two symmetry-independent guanidine molecules at 273 K.

signs of more than one grain. To collect all Bragg data, a full half shell ($\pm h + k \pm l$) was recorded between 7 and 30° in 2θ . There were no violations of systematic extinctions, thereby corroborating the previously known space group *Pbca*. Then, another quarter shell ($+h + k \pm l$) was recorded between 30 and 70°. In order to further optimize the data quality and stabilize its subsequent refinement, a symmetry-equivalent set of the strongest 500 reflections ($|l| > 2\sigma$) in this 2θ range with ($-h + k + l$) was also measured. In total, about 3000 reflections were collected. A second data set was obtained at 273 K. In order to measure these high-temperature data more quickly, only those reflections with significant intensities ($|l| > 3\sigma$) of the measurement at 100 K were collected, culminating in some 2000 reflections [3].

Suspicious strong bond-length shrinkage

As already known from the earlier X-ray study, the guanidine molecule is composed of a central carbon and three nitrogen atoms, forming a Y-shaped carbon–nitrogen backbone which is planar within three standard deviations. The molecule incorporates two different functional groups, namely one imino and two amino functions. Without knowing anything about the spatial parameters of the hydrogen atoms contained in these functional groups, both amino and imino functions are easy to spot by comparing their bond lengths. The short C–N distance (about 1.30 Å) is assigned to the imino function (double bond) and the longer C–N distances (about 1.37 Å) belong to the amino functions (single bonds) [3].

Puzzlingly enough, the earlier X-ray study revealed that one C–N bond exhibited an unusually strong bond-length shrinkage when the temperature was raised, together with a relatively large thermal displacement parameter of one of the involved N atoms [1]. This rather unphysical phenomenon served as a useful hint to check for a rigid-body movement of the entire molecule. Indeed, by applying a rigid-body correction based on the carefully refined anisotropic displacement parameters, the aforementioned C–N

bond arrives at a typical value of 1.37 Å at 273 K instead of the previously refined 1.34 Å. In conclusion and as already speculated by Yamada et al. the guanidine molecules move as rigid entities, and molecule #1 exhibits a larger thermal motion than molecule #2.

We also note that the previously predicted N–H bond lengths derived from density-functional theory [2] were impressively verified by this neutron study, the residual errors between theory and experiment being smaller than 0.03 Å. This comparison underlines the ability of modern quantum-chemical calculations to correctly model the hydrogen-atom positions without prior information, even in those systems which hold a large number of hydrogen bonds.

Finally, the large data set of anisotropic displacement parameters for all the hydrogen atoms was employed to search for a simple correlation between these parameters and the strengths of the corresponding hydrogen bonds, but no such correlation was detected.

Correction of the molecular movement

A self-consistent set of spatial and anisotropic displacement parameters for crystalline guanidine was derived at two different temperatures using single-crystal neutron diffraction performed using the HEiDi instrument at MLZ. The excellent data quality allowed for a rigid-body correction of the molecular movement, eventually revealing that the molecules indeed undergo libration. The unphysical thermal behavior of a C–N bond seen in an earlier single-crystal X-ray study was scrutinized and found to go back to that librational movement. We trust that the new data set will be used as a benchmark for further quantum-theoretical studies and contributes to a deeper understanding of hydrogen bonds in general.

[1] T. Yamada et al., Chem. Eur. J., 15, 5651 (2009).

[2] V. Hoepfner et al., J. Phys. Chem. A, 116, 4551 (2012).

[3] P. K. Sawinski et al., Cryst. Growth Des., 13, 1730 (2013).

Antiferromagnetic domains in $\text{YBa}_2\text{Cu}_3\text{O}_{6.0}$ detected by neutron Larmor diffraction

B. Náfrádi¹, T. Keller¹, A. Erb², B. Keimer¹

¹Max-Planck-Institut für Festkörperforschung, Stuttgart, Germany

²Walther-Meißner-Institut für Tieftemperaturforschung, Garching, Germany

High resolution Neutron Larmor diffraction measurements at TRISP helped to resolve a long standing problem related to an anomalous magneto-resistance observed in $\text{YBa}_2\text{Cu}_3\text{O}_{6.0}$ [1]. This compound is a two-dimensional antiferromagnet and becomes superconducting at higher oxygen doping levels. In this work we observed a small broadening of the Bragg peaks arising from an orthorhombic distortion of the crystal lattice in the order of $(b-a)/b = 2.6 \cdot 10^{-6}$. This distortion appears reversibly in the antiferromagnetic state and results from magnetostriction induced by antiferromagnetic domains. From the anisotropic broadening of the Bragg peaks we found that in the a-b plane the domains are larger than 10^4 unit cells.

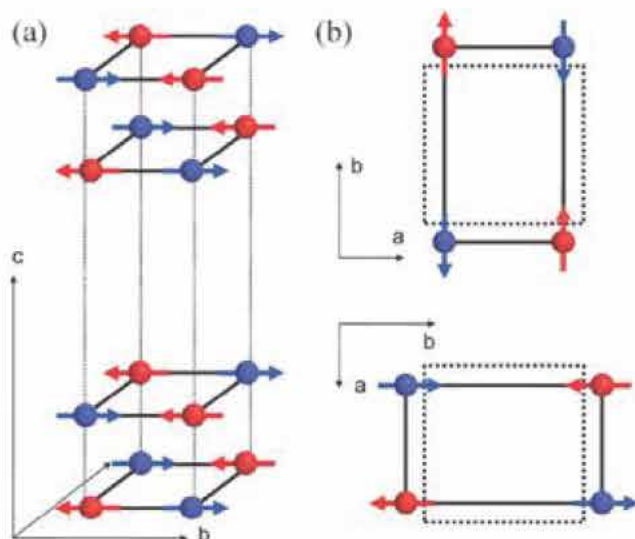


Figure 1 (a) Schematic view of the average tetragonal antiferromagnetic structure of $\text{YBa}_2\text{Cu}_3\text{O}_8$ below the Néel temperature $T_N = 420$ K. For clarity only the magnetic Cu²⁺ ions are shown. (b) The two types of orthogonal domains resolved at TRISP. Dashed rectangles represent the tetragonal paramagnetic unit cell. The solid rectangle represents the orthorhombic antiferromagnetic cell. The direction of both the orthorhombic distortion and the easy magnetization rotates 90° between domains.

Antiferromagnetic domains

The high-Tc cuprate superconductors are based on insulating antiferromagnetic parent compounds, such as the $\text{YBa}_2\text{Cu}_3\text{O}_{6.0}$ studied in this work. Superconductors are obtained by doping the parent compounds with charge carriers. A detailed description of the magnetism of the parent compounds is assumed to be a key for understanding the superconductivity [1-4].

An open question is related to the observation of an anomalous magnetoresistance within the CuO planes. One of the scenarios discussed as an explanation for this effect assumes an orthorhombic distortion of the crystal lattice resulting from orthogonal antiferromagnetic domains. The formation of antiferromagnetic domain walls costs energy and should, therefore, be forbidden. However, if strong magneto-elastic coupling is present, the long range magneto-elastic forces lead to an energetically favorable lattice distortion and spontaneous domain formation can occur [4] (fig. 1).

Precise diffraction

Using high resolution neutron Larmor diffraction (LD), we were able to confirm the existence of a small orthorhombic distortion of $(b-a)/b = 2.6 \cdot 10^{-6}$ and twinning below the Néel temperature [8]. The sample consisted of small co-aligned crystals with a total crystal mass of 10mg. Larmor diffraction [6,7] is a diffraction technique implemented at the TRISP spectrometer at the MLZ (fig. 2), a spin-echo technique providing a relative resolution for the lattice spacing or the spread of the lattice spacing in the order of 10^{-6} , that is, about 1–2 orders of magnitude better than the resolution obtained with conventional neutron or X-ray diffraction techniques. In

addition to making it possible to detect a small splitting of Bragg peaks, Larmor diffraction is an unrivalled method for measuring thermal expansion under extreme conditions not accessible by classical dilatometry, including high pressure and low temperature. We found that the orthorhombic distortion and domain structure is caused by magnetostriction, and the structural domains presented in this work are identical with magnetic domains reported earlier. [2,4] From the anisotropic broadening of the Bragg peaks, we found that, in the a-b plane, the domains are larger than 10^4 unit cells.

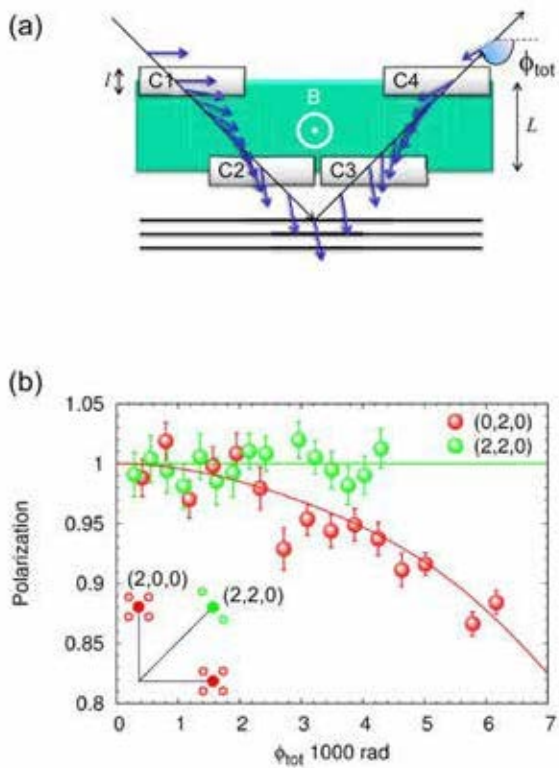


Figure 3 (a) Principle of the Larmor diffraction technique. The radio-frequency spin flip coils C1 to C4 generate an effective (virtual) static magnetic field B, leading to Larmor precession of the neutron spins. The total precession phase only depends on the lattice spacing and is independent of beam collimation and monochromaticity. (b) Normalized neutron beam polarization as a function of the total Larmor precession phase measured at $T = 300 \text{ K}$ ($T_N = 420 \text{ K}$) for both $(2,2,0)$ and $(2,0,0)$ nuclear Bragg peaks. The fast decay of the $(0,2,0)$ polarization results from the orthorhombic twinning shown in the inset. Full circles mark the reciprocal lattice points of the paramagnetic tetragonal phase.

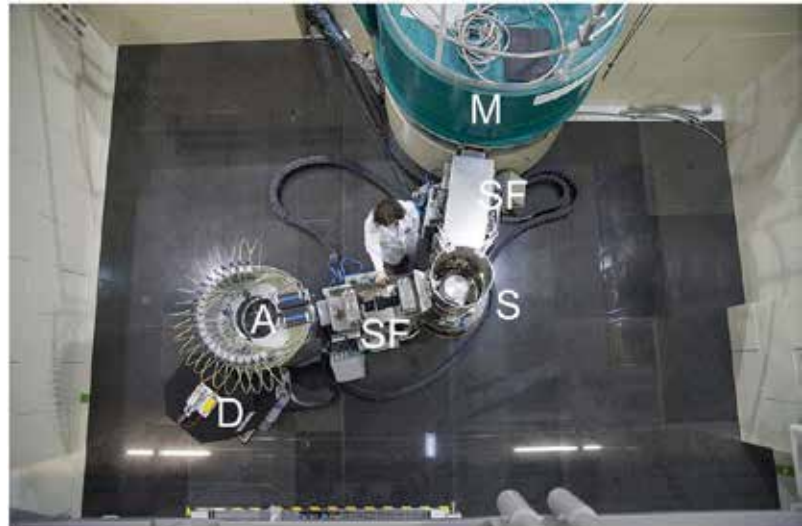


Figure 2: The TRISP (TRIple axis SPin echo) spectrometer at the MLZ is optimized for high resolution spectroscopy of elementary excitations by means of resonance neutron spin echo. It incorporates the Larmor diffraction technique. The lattice spacing and the spread of the lattice spacing arising, for example, from defects, internal strain or small splitting of Bragg peaks is measured with a relative resolution in the order of 10^{-6} , i.e. 1–2 orders of magnitude better than other diffraction techniques. The method works both for single-crystals and powders. (M: monochromator; SF: radio frequency spin flippers housed in a μ -metal shield; S: sample; A: analyzer; D: detector)..

Acknowledgements

We are grateful to A. Jánossy (Budapest University of Technology and Economics) for stimulating discussions. We thank K. Buchner for technical assistance and the German DFG for financial support under grant No. SFB/TRR 80. B.N. acknowledges support from the Prospective Research program No. PBELP2-125427 of the Swiss NSF.

- [1] S. Shamoto et al., Phys. Rev. B, 48, 13817 (1993).
- [2] M. Sato et al., Phys. Rev. Lett., 61, 1317 (1988).
- [3] A. Jánossy et al., Phys. Rev. B, 59, 1176 (1999).
- [4] H. V. Gomonay and V. M. Loktev, Phys. Rev. B, 75, 174439 (2007).
- [5] Y. Ando et al., Phys. Rev. Lett., 83, 2813 (1999).
- [6] M. T. Rekveldt et al., Europhys. Lett., 54, 342 (2001).
- [7] C. Pfleiderer et al., Science, 316, 1871 (2007).
- [8] B. Nafradi et al., unpublished (2012).

Growth and characterization of large high quality brownmillerite $\text{CaFeO}_{2.5}$ single crystals

M. Ceretti¹, A. Piovano^{2,3}, A. Cousson⁴, M. Meven⁵, G. Agostini², J. Schefer⁶, C. Lamberti² and W. Paulus¹

¹University of Montpellier 2, Institute Charles Gerhardt, Montpellier, France

²University of Turin, Department of Chemistry, Turin, Italy

³Institute Laue-Langevin, Grenoble, France

⁴Laboratoire Léon Brillouin, Gif-sur-Yvette, France

⁵Technische Universität München, Forschungs-Neutronenquelle Heinz Maier-Leibnitz (FRM II), Garching, Germany

⁶Paul Scherrer Institute, Laboratory for Neutron Scattering, Villigen, Switzerland

Large and high quality single-crystals of $\text{CaFeO}_{2.5}$ with Brownmillerite type structure were grown in an image furnace using a floating-zone technique. Structural characterization of the single crystals grown was carried out using neutron and X-ray diffraction as well as High Resolution Transmission Electron Microscopy (HRTEM) and revealed their excellence both in terms of composition homogeneity and crystalline quality. Magnetic measurements were performed on oriented crystals by Superconducting Quantum Interference Device (SQUID) and neutron diffraction in the range of 5 – 700 K in order to clear up controversial discussions on possible magnetic phase transitions. The same crystals are used for lattice dynamical investigations by Raman and inelastic neutron scattering, in order to support a new phonon assisted diffusion model for low temperature oxygen mobility in solid oxides.

Our motivation in synthesizing large and high quality single crystals of $\text{CaFeO}_{2.5}$ (fig. 1) is two-fold. On the one hand, we are interested in gain-

ing a better understanding of its lattice dynamical properties, as we were recently able to show the importance of low energy phonon modes for low temperature oxygen mobility in Brownmillerite type frameworks. We also showed that the concept of realizing oxygen diffusion via lattice instabilities and dynamically triggered internal interfaces holds for oxides of the K_2NiF_4 type family [1], bringing not only a new dimension to designing and tuning of fast oxygen ion conductors in solid oxides but also, more generally, to the understanding of low temperature solid state reactivity.

Controversially discussed magnetic properties
On the other hand, we are interested in clearing up the controversially discussed magnetic properties of $\text{CaFeO}_{2.5}$, which has been reported to show G-type antiferromagnetic ordering with a Néel temperature of 725 K [2]. However, [3] found weak ferromagnetism resulting from the formation of Dzyaloshinskiy-Moriya domains and/or phases related to intergrowths or impurities. [4] argued that the weak ferromagnetism present in their $\text{CaFeO}_{2.5}$ crystals is not related to the presence of impurities. The authors reported surprisingly on two new magnetic phase transitions at 140 K and 60 K which have not been observed so far and which remain of unknown origin. They claimed that both magnetic phase transitions should be intrinsically related to $\text{CaFeO}_{2.5}$.

Investigation of temperature dependence

In order to follow the reported magnetic phase transitions, we investigated the temperature dependence of $\text{CaFeO}_{2.5}$ for two pure and strong magnetic reflections ($1\ 2\ 0$) and ($0\ 2\ 1$) as well as one nuclear reflection ($0\ 2\ 0$), which were measured from 5 K up to 725 K on the 4-circles diffrac-

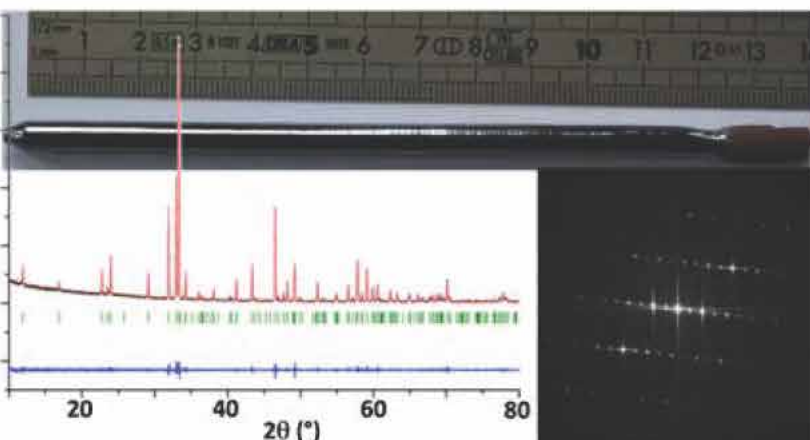


Figure 1: Top: high quality $\text{CaFeO}_{2.5}$ single crystal grown by floating zone technique using an image furnace. Bottom: XRPD pattern and TEM diffraction obtained upon grinding a portion of the single crystals.

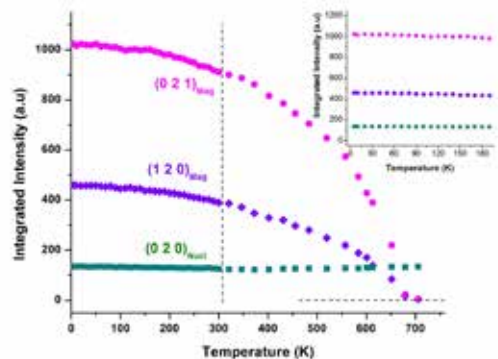


Figure 2: Evolution of the integrated intensity as a function of the temperature of the purely magnetic reflections $(0\ 2\ 1)_{\text{Mag}}$ and $(1\ 2\ 0)_{\text{Mag}}$, as well as of the purely nuclear $(0\ 2\ 0)_{\text{Nuc}}$ one. The inset shows a magnification of the low temperature region.

tometer HEiDi. As can be seen from figure 2, the intensities of the magnetic reflections increase in a monotonous continuous way below T_N , which has been fitted to 700 K, and reaches saturation at low temperature, while the nuclear intensity is constant over the whole temperature range. The $(0\ 2\ 0)$ reflection was chosen as a standard reflection, as it is the least affected reflection for the Debye–Waller factor and is thus supposed to vary only slightly with T, since it appears at a low momentum transfer of $0.068 \sin\Theta/\lambda$ (\AA^{-1}). From the changes in the intensities, we deduce only one magnetic phase transition from the paramagnetic to antiferromagnetic state occurring at $T_N = 700$ K while no further anomalies could be found around 140 K and 60 K as described by Maljuk.

Magnetic measurements of the susceptibility

We also performed magnetic measurements of the susceptibility on the similarly grown CFO single crystal already used for neutron diffraction. Susceptibility measurements were performed as a function of temperature, but also varying an applied magnetic field ($-5 \text{ T} < H < 5 \text{ T}$) along the a- and c- axes. Figure 3 shows the isothermal magnetization curves with the magnetic field applied along the c-axis at different temperatures (2 K, 5 K, 20 K and 300 K). For temperatures above 5 K, the magnetization becomes zero if no field is applied, while the 2 K data show a non-zero value. This magnetic phase transition has not been reported so far and is currently under

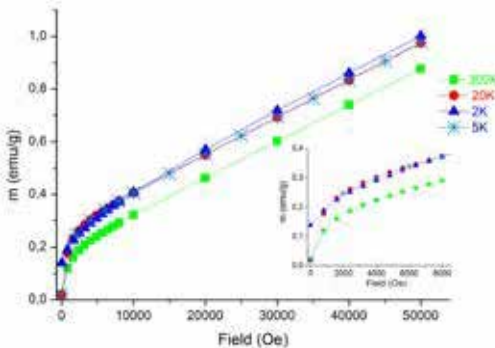


Figure 3: Magnetisation isotherms for the similarly grown CFO crystal (H/c) measured up to a field of 55 kOe at selected temperatures of 2 K, 5 K, 20 K and 300 K. The inset shows the details of the low field magnetization process.

investigation. The absence of a ferromagnetic component at 20 K has been proven by magnetization measurements with the crystal orientation along the c-axis. No hysteresis has been detected, suggesting no changes in the antiferromagnetic orientation of the magnetic moments down to this temperature.

Antiferromagnetic ordering

The magnetic structure of $\text{CaFeO}_{2.5}$ with Brown–millerite type structure was investigated using neutron diffraction on a non-twinned and highly stoichiometric single crystal. A G-type antiferromagnetic ordering was found in the temperature range $5 \text{ K} < T < 725 \text{ K}$. These studies clear up a widely discussed difference of opinion, as a series of magnetic transitions have been reported to occur towards low temperatures for the title compound. Our neutron single structure investigations confirm the oxygen stoichiometry to correspond to $\text{CaFeO}_{2.5 \pm 0.01}$ and suggest that previous findings could possibly be interpreted as relying on variations in the oxygen stoichiometry. The neutron investigations were completed using high resolution TEM studies, confirming a defect and domain free structure.

- [1] M. V. Patrakeev et al., Solid State Sci., 6, 907 (2004).
- [2] A. Nemudry et al., Solid State Sci., 4, 677 (2002).
- [3] R. Le Toquin et al., J. Am. Chem. Soc., 128, 13161 (2006).
- [4] A. Piovano, et al., J. Phys. Chem. C, 115, 1311 (2011).
- [5] M. Ceretti et al., CrystEngComm, 14, 5771 (2012).

Spatial resolved phase analysis in sodium-metal chloride batteries

M. Hofmann¹, R. Gilles¹, Y. Gao², J.T. Rijssenbeek²

¹Technische Universität München, Forschungs-Neutronenquelle Heinz Maier-Leibnitz (FRM II), Garching, Germany

²GE Global Research, One Research Circle, Niskayuna, USA

Neutron methods are powerful tools for non-destructive investigation of batteries. Taking as an example the case study of a sodium-iron chloride based battery cell, we were able to show that spatial resolved information on the cell chemistry can be obtained using neutron tomography and powder diffraction.

High temperature batteries

Sodium-metal chloride batteries [1] were first introduced in the late 1980's as they combine several advantages for battery applications, such as a high energy density, long cycle life, insensitivity to external temperature, and tolerance to short circuits. This comes in addition to low cost, easy recyclability and zero maintenance. The components of this type of battery are plain salt and metal ($M = Ni, Fe$) for the electrode material, the electrolyte and the separator is β'' -alumina which

is conductive for Na^+ ions but an insulator for electrons. The operating temperature is between 270-350 °C. The performance of such a battery is intimately tied to the distribution and morphology of the metal(s) and metal chloride(s) within the cathode. During charging and discharging a reaction front propagates from the inner surface of the β'' -alumina separator towards the cathode current collector in the centre of the cell. At the reaction front the NaCl is consumed to form MCl_2 and Na^+ ions (charge) or MCl_2 react with Na^+ ions to form M and NaCl particles (discharge).

Today, such batteries are used in heavy-duty transportation (e.g. buses, vans and hybrid locomotives) and stationary back-up power. A key barrier to further improving the battery performance is lack of understanding of what actually takes place, both chemically and morphologically, inside the battery during operation, not only at the macroscopic level but also at the microstructural level. At present, this type of battery has to be cut open for characterization. This is not only destructive and time-consuming, but such a post mortem analysis may also alter the materials and their morphology during cutting or due to their exposure to air and moisture.

Spatial resolved neutron scattering

Neutron scattering, with its unique penetrating power, as well as the good contrast even for light elements, makes it possible to study the electrochemistry within such a battery non-destructively. We used the tomography station ANTARES and the diffractometer STRESS-SPEC (fig. 1) to map out the reaction front in two sodium-metal chloride batteries. One was discharged while the other one was charged to half of its nominal capacity. In this case study the metal in the



Figure 1: Alignment of a sodium-iron chloride battery cell on the sample table of STRESS-SPEC..

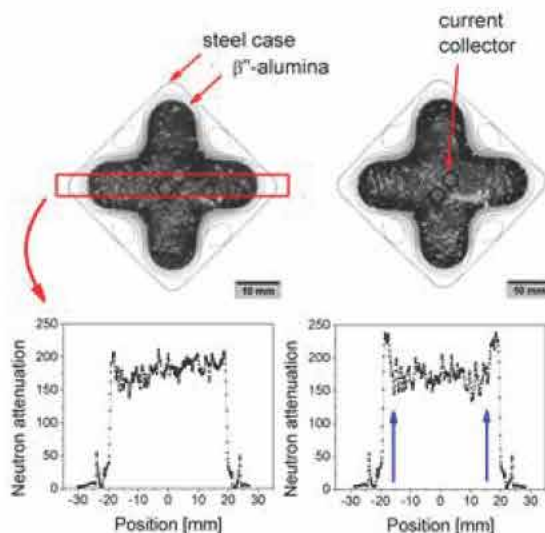


Figure 2: Horizontal reconstructed slices of the discharged (left) and the half-charged battery cell (right) from the tomography measurements at ANTARES. The red rectangle identifies the section of the slices from which the line profiles (below) were extracted.

batteries was iron. The experiments had two immediate objectives: 1) to demonstrate that the reaction front can be observed and characterized, and 2) to determine the phase composition, and morphology of the reacting components.

From the tomography data, information about the inner structure, porosity and the charge state of the respective batteries could be obtained (for more details see [2]). The charge state can be inferred due to the rise of the sodium level, as Na^+ ions travel through the ceramic electrolyte into the outer compartment of the cell when the battery is charged. Furthermore, a comparison of horizontal slices of both batteries based on the tomographic data shows that the reaction front (blue arrows in figure 2, right side) can be clearly identified, extending about 4–5 mm inwards of the β'' -alumina separator. The enhanced attenuation contrast visible in the line profile from the reconstructed slice of the half-charged cell is probably due to a higher concentration of elements with high attenuation (e.g. chlorine) close to the separator, as expected from the reaction mechanism during charging/discharging.

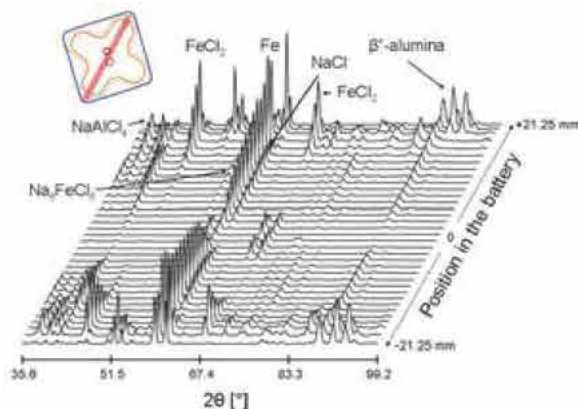


Figure 3: Diffraction patterns of the diagonal scan through the battery cell. Several key reflections of the main phases are highlighted. The measurement path is shown schematically in the sketch of the battery cell as red line.

For the diffraction experiment we took advantage of the setup at the diffractometer STRESS-SPEC to investigate small volumes within bulky samples usually used for strain measurements. A gauge volume of $2 \times 2 \times 20 \text{ mm}^3$ (with the long axis vertical) was adjusted by slits and a radial collimator and placed within the battery. Powder diffraction patterns were recorded for different positions along the diagonal of the battery (fig. 3). Using standard powder diffraction analysis methods, all crystalline phases in the battery could be identified and their phase fraction within the gauge volume determined. In addition, it was found unambiguously that sodium chloride is present only in the form of Na_6FeCl_8 [2], a phase postulated by ex-situ experiments and theoretical models. Since its position was consistent with the tomography results, the reaction front was identified as the border between the FeCl_2 and the $\text{NaCl}/\text{Na}_6\text{FeCl}_8$ phase, respectively.

Conclusions

The experiments show that reliable and quantitative information can be extracted from spatial resolved neutron methods and we are confident that this case study can be transferred to other battery types.

[1] C.H. Dustmann, J. Pow. Sources, 127, 85 (2004).

[2] M. Hofmann et al., J. Electrochem. Soc., 159, A1827 (2012).

Channel ion distribution in $A_2Ti_6O_{13}$ determines effectiveness as anode for Li-ion batteries

J. C. Pérez-Flores¹, F. García-Alvarado¹, M. Hoelzel², I. Sobrados³, J. Sanz³, A. Kuhn¹

¹Universidad CEU San Pablo, Departamento de Química, Madrid, Spain

²Technische Universität München, Forschungs-Neutronenquelle Heinz Maier-Leibnitz (FRM II), Garching, Germany

³Instituto de Ciencia de Materiales de Madrid (ICMM), Departamento Energía & Tecnologías Sostenibles, Madrid, Spain

Crystal structures of $A_2Ti_6O_{13}$ ($A = Na, Li, H$) hexatitanates, considered as innovative negative electrodes for Li ion batteries, have been investigated using neutron powder diffraction. Further details of local distortions of A channel ion coordinates have been obtained via solid state NMR experiments of the respective ^{23}Na , 7Li and 1H nuclei. Our studies show that A⁺ channel cation distribution in the mainly unaltered $[Ti_6O_{13}]^{2-}$ skeleton strongly influences lithium insertion properties and, hence, the effectiveness of these titanates as electrode material for energy storage.

Ti-based materials are important anodes for Li-ion batteries

Several Ti-based compounds are investigated as alternative anodes for Li-ion batteries due to their high safety and excellent cycling stability. Among them, $A_2Ti_6O_{13}$ hexatitanates have drawn researchers' attention due to their low redox potential (1–1.5 V vs. Li⁺/Li) and competitive capacity (175–200 mAh/g), which compare well with state-of-art spinel $Li_4Ti_5O_{12}$ [1–3]. However, A⁺ channel ions prove decisive for their electrochemical performances.

Experiments at SPODI

Neutron powder diffraction (NPD) patterns were collected on the high resolution diffractometer SPODI at the neutron source FRM II. A Ge(551) monochromator was used to select a wavelength of $\lambda = 1.5481 \text{ \AA}$. All diffraction patterns were analysed and crystal structures determined by the Rietveld method [4] with the FullProf software [5]. Na, Li and H atoms were located by Fourier synthesis maps starting from the basic $Ti_6O_{13}^{2-}$ skeleton framework, using the GFourier software.

Picking up the trail of channel ions

Difference Fourier synthesis maps (fig. 1) performed after Rietveld refinement, in which only the basic $[Ti_6O_{13}]^{2-}$ skeleton structure was considered, unambiguously revealed the location of the missing A channel atoms at 4*i* (*x*,0,*z*) positions. This is nicely illustrated in 2-D (top) and 3-D (middle) Fourier maps corresponding to the *y* = 0 section (Na) and *y* = 0.5 section (Li, H). Significant neutron scattering density is no longer detectable after introducing A atoms in their respective structural models (bottom).

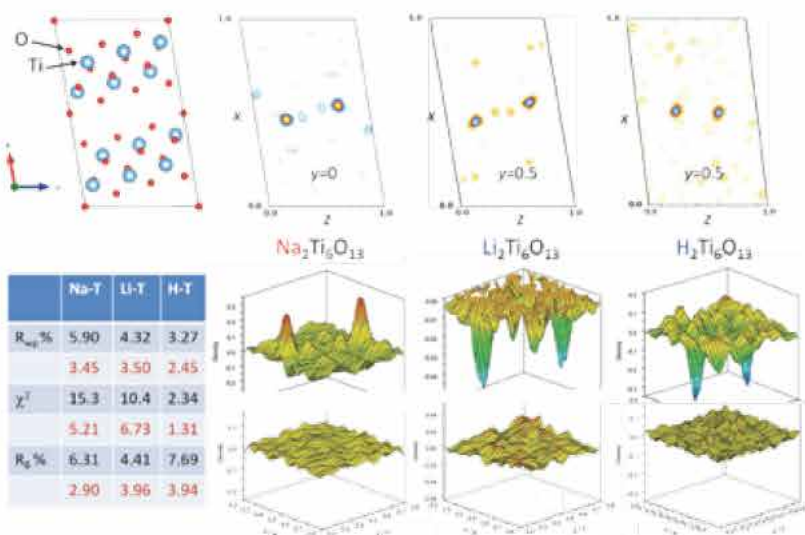


Figure 1: 2-D (top) and 3-D (middle) difference Fourier maps after Rietveld refinement of $A_2Ti_6O_{13}$ ($A = Na, Li, H$) phases considering only the $[Ti_6O_{13}]^{2-}$ skeleton structure. Successive 3-D difference Fourier maps after introducing A channel atoms in the structural model (bottom). Conventional Rietveld agreement factors before (black) and after (red) introducing A atoms in the structural model are given for clarity.

$A_2\text{Ti}_6\text{O}_{13}$ phases display monoclinic symmetry, space group C2/m, with similar unit cell parameters (table 1), proving that the $[\text{Ti}_6\text{O}_{13}]^{2-}$ network of pristine $\text{Na}_2\text{Ti}_6\text{O}_{13}$ [6] is preserved. The singular connection of octahedra sharing edges with neighbouring octahedra favours the formation of structural channels along the b -axis (fig. 2). However, Na, Li and H channel ions occupy different sites in the three titanates [7].

	$\text{Na}_2\text{Ti}_6\text{O}_{13}$	$\text{Li}_2\text{Ti}_6\text{O}_{13}$	$\text{H}_2\text{Ti}_6\text{O}_{13}$
a (Å)	15.1032(2)	15.3486(5)	14.6699(3)
b (Å)	3.74373(4)	3.7518(1)	3.74467(8)
c (Å)	9.1713(12)	9.1449(2)	9.2593(1)
β (°)	99.056(1)	99.475(2)	96.941(1)
V (Å ³)	512.10(1)	519.43(2)	504.92(1)

Table 1: Crystallographic data for $A_2\text{Ti}_6\text{O}_{13}$ ($A=\text{Na}, \text{Li}, \text{H}$), space group C2/m as obtained from neutron powder diffraction.

Na atoms in $\text{Na}_2\text{Ti}_6\text{O}_{13}$ are 8-fold coordinated by O atoms (fig. 2a). For an ideal cubic 8-fold coordination, the quadrupolar constant $C_Q = 0$ and the asymmetric parameter $\eta = 0$. However, the ²³Na MAS-NMR spectrum displays important quadrupolar interactions ($C_Q \neq 0$ and $\eta \neq 0$) that prove the displacement of Na cations from the centre of its eightfold polyhedron. In $\text{Li}_2\text{Ti}_6\text{O}_{13}$, Li cations are located out of the centre of distorted square windows (fig. 2b). For an ideal planar 4-fold coordination, $C_Q \neq 0$ and $\eta = 0$. However, the ⁷Li AS-NMR spectrum displays important quadrupolar interactions ($C_Q \neq 0$ and $\eta \neq 0$) that justify the adopted 3 + 1 coordination of Li^+ cations. In $\text{H}_2\text{Ti}_6\text{O}_{13}$ protons are covalently bound to the O3 atom (O3-H bond length: 0.961 Å). Hydrogen bonding with O5 atoms (O5-H bond distance: 1.984 Å) exists across the tunnel space (fig. 2c). The high isotropic chemical shift value of protons observed in ¹H NMR experiments of $\text{H}_2\text{Ti}_6\text{O}_{13}$, 10.2 ppm, indicates that OH groups display an important acidic character. Our structural considerations, especially regarding the channel ion site position, are in complete agreement with the Li insertion properties. Accordingly, only $\text{Na}_2\text{Ti}_6\text{O}_{13}$ allows for a true topotactic

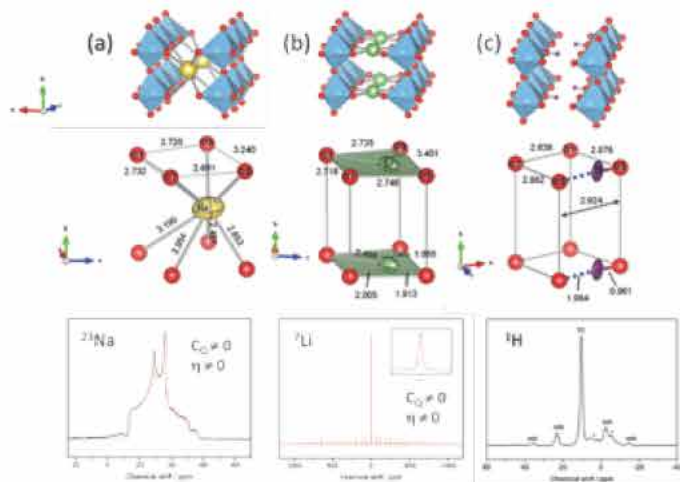


Figure 2: Crystal structures of $\text{Na}_2\text{Ti}_6\text{O}_{13}$ (a), $\text{Li}_2\text{Ti}_6\text{O}_{13}$ (b) and $\text{H}_2\text{Ti}_6\text{O}_{13}$ (c) viewed approx. down the [001] direction (top), [A-O]_n coordination in the hexatitanates (middle) and their respective MAS NMR spectra (bottom). A-O bond lengths and O-O distances are given in Å.

insertion of lithium, while topotactic Li insertion is limited in $\text{Li}_2\text{Ti}_6\text{O}_{13}$. In this case, extended lithiation produced a highly lithiated compound with nominal composition $\text{Li}_7\text{Ti}_6\text{O}_{13}$ through an irreversible reaction.

Neutron diffraction and solid state NMR are essential tools for investigating Li-ion batteries
Our results prove the stability of the $A_2\text{Ti}_6\text{O}_{13}$ hexatitanate structure for ion exchange reactions. Neutron powder diffraction revealed significant differences in the site and oxygen coordination of the A^+ tunnel cations. Results from NMR measurements showed that ²³Na ⁷Li nuclear quadrupolar constants are correlated with the distortion of nearest-neighbour oxygen coordinations of the ideal Na and Li centred polyhedra. The A^+ cation site in the hexatitanate channel structure strongly influences the lithium insertion properties of these compounds.

- [1] R. Dominko et al., *Electrochim. Commun.*, 8, 673 (2006).
- [2] J.C. Pérez-Flores et al., *J. Power Sources*, 196, 1378 (2011).
- [3] J.C. Pérez-Flores et al., *RSC Adv.*, 2, 3530 (2012).
- [4] H. Rietveld, *Acta Cryst.*, 20, 508 (1966).
- [5] J. Rodríguez-Carvajal, *J. Phys.: Condens. Matter*, 192, 55 (1993).
- [6] S. Andersson and A. D. Wadsley, *Acta Cryst.*, 14, 1245 (1961).
- [7] J.C. Pérez-Flores et al., *Dalton Trans.*, 41, 14633 (2012).

Residual stresses in steel specimens induced by laser cladding and their effect on fatigue strength

H. Köhler¹, J. R. Kornmeier², T. Seefeld¹, F. Vollertsen¹

¹Bremer Institut für angewandte Strahltechnik, Bremen, Germany

²Technische Universität München, Forschungs-Neutronenquelle Heinz Maier-Leibnitz (FRM II), Garching, Germany

Residual stresses resulting from the laser cladding of fatigue test specimens of austenitic steel and heat treatable steel with Stellite 21 are evaluated using neutron diffraction. Below the interface of cladding and base material, the former shows compressive, the latter tensile residual stresses. The locations of crack initiation during fatigue testing correspond to the findings: austenitic steel specimens crack at the surface whereas heat treatable steel specimens crack close to the interface. The fatigue strength of both combinations drops after laser cladding. The drop in heat treatable steel is significant. It can be concluded that the residual stress distribution needs to be optimized to conserve maximal fatigue strength.

Laser cladding is widely applied. However, its application is not endorsed for dynamically loaded parts as it is not possible to predict how fatigue properties are affected. Previous results have shown that the fatigue strength of round [1] and flat specimens, as well as those of complete crankshaft segments [2] seriously decreased after cladding with the cobalt-based alloy Stellite 21. The locations of crack initiation in cladded low-alloy steel 42CrMo4 specimens could be evaluated as close to the interface of the cladding and base material. The fatigue strength of the round specimen under bending load dropped by up to 70 % and under tensile-compressive load by 60 %. In contrast, cladded high-alloy steel X5CrNi18-10 specimens cracked at the surface. The fatigue strength dropped by up to only 10 %. The investigation presented here was performed to evaluate the role of residual stresses in the drop in fatigue strength using neutron diffraction, as this has proved to be

highly suitable for determining residual stresses in steels [3].

Residual stress measurement

Cylindrical fatigue test specimens of steel 42CrMo4 tempered to 350 HV0.3 and steel X5CrNi18-10 were laser cladded with Stellite 21. Details of the experimental procedure, as well as of the results of the laser processing, have been published in [2]. The following material combinations were investigated: 1.) ground 42CrMo4 base material, 2.) 42CrMo4 base material laser cladded with Stellite 21 and ground, 3.) ground X5CrNi18-10 base material and 4.) X5CrNi18-10 base material laser cladded with Stellite 21 and ground. The diameter of the uncladded and ground specimens was (10.0 ± 0.02) mm. The diameter of the cladded and ground specimens was (12.0 ± 0.02) mm. In order to measure the residual stresses using the STRESS-SPEC instrument, a neutron wavelength of 1.67 Å and a gauge volume of $1 \times 1 \times 1 \text{ mm}^3$ was applied. In every specimen, line scans in center position along the radius (radial, from center to surface) were performed. The measurements were made in a radial, tangential and axial direction. For the steel 42CrMo4 the diffraction peak of the plane $\alpha\text{Fe}\{211\}$ and for the steel X5CrNi18-10 the diffraction peak of the plane $\gamma\text{Fe}\{311\}$ was analyzed. The Young's moduli and Poisson ratios of these planes are 220 MPa and 0.31 for the former and 175 MPa and 0.28 for the latter [4]. Stress-free reference samples were cut out of the centre position of each specimen type. The gauge volume position closest to the work piece surface was partly placed outside the base material. To quantitatively determine residual stress in these locations, additional X-ray diffraction measurements were performed.

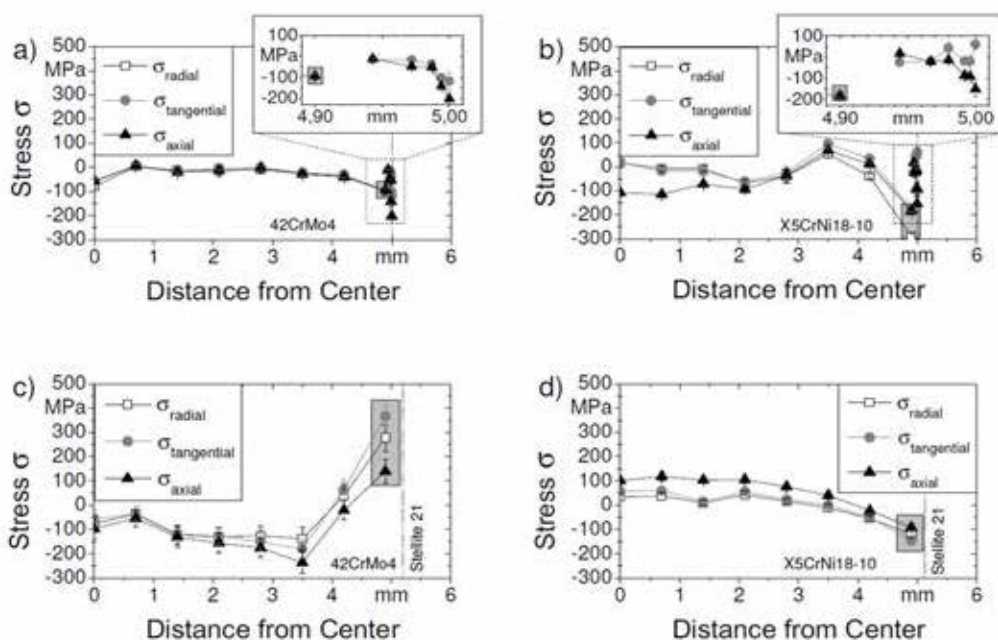


Figure 1: Residual stresses in center position; (a) and (b) in uncladded base materials; (c) and (d) in cladded base materials; gray box indicates qualitative results; in the upper right of a) and b) residual stresses evaluated by X-ray diffraction at the surfaces are given, results kindly provided by IWT – Stiftung Institut für Werkstofftechnik, Bremen.

Effect of laser cladding on residual stresses

The residual stresses evaluated are shown in figure 1. The outer position measured using neutron diffraction is marked by a gray box. Residual stresses determined using X-ray diffraction are given in the inserts in the upper right of figure 1a and figure 1b. By comparing the resulting stresses determined using X-ray as opposed to neutron diffraction, it can be evaluated that the measurement at the outer position is more accurate for 42CrMo4 than for X5CrNi18-10. Taking into account that the neutron diffraction measurement gives a mean value for a gauge volume of 1 mm³, both results can be interpreted as qualitatively similar.

The uncladded specimen of steel 42CrMo4 shows high compressive residual stresses at the surface. Below the surface, low compressive residual stress can be determined. Despite martensitic hardening in the HAZ of the steel 42CrMo4, which is generally expected to create compressive residual stresses, high tensile residual stresses could be measured near the interface of the base material and cladding. In the case of X5CrNi18-10 cladded with Stellite 21, initial compressive residual stress at the surface

was conserved after cladding and tensile residual stress was measured near the core.

Effect of residual stress on fatigue strength

The residual stresses evaluated correlate well with findings from fatigue tests: The locations of crack initiation coincide with the areas of high tensile residual stresses. The measurements confirm that the applied laser cladding process induced a residual stress situation which influences the fatigue properties negatively in the case of the substrate material 42CrMo4. To make laser cladding available for highly loaded components of such materials, further investigations are necessary to determine strategies to conserve a maximum of fatigue strength.

High-alloy steel, on the other hand, proved not to have tensile residual stresses in the interface between cladding and substrate. Considering the slight drop of 10 % in fatigue strength, this material combination can be assumed to be processable for dynamically highly loaded components.

[1] H. Koehler et al., Lasers in Manufacturing, 512 (2011).

[2] H. Koehler et al., Prod. Eng. Res. Dev., 6, 137 (2012).

[3] P. J. Withers, C. R. Physique, 8, 806 (2007).

[4] B. Eigenmann and E. Macherauch, Mat-wiss. Werkstofftech., 27, 426 (1996).

Inducing compressive residual stresses in multi-pass welds using transformation plasticity

T. Ramjaun¹, H. J. Stone¹, J. Kelleher², L. Karlsson³, J. Rebelo Kornmeier⁴,
H. K. D. H. Bhadeshia¹

¹University of Cambridge, Department of Materials Science and Metallurgy, Cambridge, UK

²Rutherford Appleton Laboratory, ISIS Facility, Didcot, UK

³University West, Department of Engineering Science, Trollhättan, Sweden

⁴Technische Universität München, Forschungs-Neutronenquelle Heinz Maier-Leibnitz (FRM II), Garching, Germany

Residual stresses in welded structures feature in safe design and can be manipulated to optimise service life. The STRESS-SPEC instrument was used to characterise such stresses across a steel welded using an alloy which transforms into ductile martensite at a temperature low enough for transformation plasticity to compensate for strains which develop through the thermal contraction of constrained joints.

Phase Transformation

As a weld cools, it contracts. Large components are not free to accommodate local thermal contraction effects associated with the deposition of a weld. This leaves critical areas of the final assembly with tensile residual stresses, which not only limit the design loads but reduce the ability to resist fatigue. Techniques including post-weld heat treatment and surface peening can mitigate the stresses but are not always practical. Here, an alternative approach is exploited, by designing an alloy which transforms at a low tempera-

ture by a displacive mechanism. The shape deformation accompanying transformation tends to cancel stresses due to thermal contraction, leaving the weld in a calm state.

Low Transformation Temperature

Weld metals usually have low carbon concentrations so that the transformation of austenite is exhausted at a temperature well above ambient, thus allowing the unabated accumulation of stresses due to thermal contraction during continued cooling. Through judicious alloying additions to create a ductile martensite [1-2], the transformation temperature can be sufficiently suppressed (~ 200 °C) so that the associated plasticity is available to compensate for contraction strains down to ambient temperatures [3]. The alloy design, based partly on mathematical modelling, not only maintains the required toughness and strength, but avoids hot-cracking and is consistent with the smooth deposition of the molten metal [4]. Residual stress measurements conducted on single pass welds have demonstrated the self-stress-relief effect [5]. The major purpose of the present work was, therefore, to establish the concept for welds which must be fabricated by depositing many layers of metal.

Atomic Strain-Gauge

Neutron diffraction is an effective method for the determination of the state of stress in welded components. Large penetration depths can be achieved, making it feasible to map the strain through at least 10 mm thick sections. By comparing the diffraction angles at the same position for two identical welded specimens, one of which has been stress relieved, it is possible to estimate the strain from which the stress may be calculated (see fig. 1).

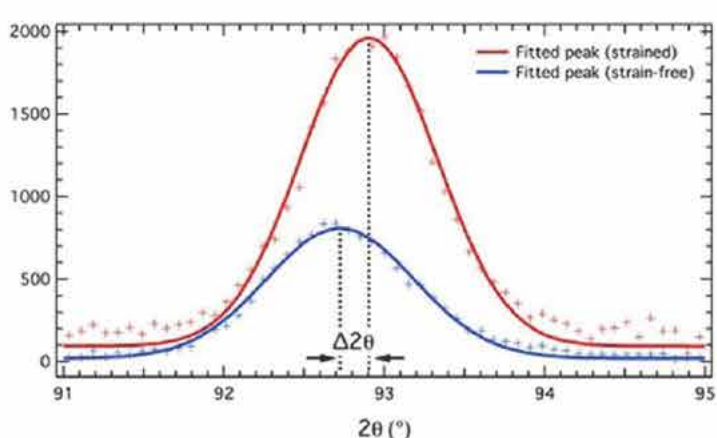


Figure 1: Diffraction angles for strained and strain-free welded specimens. The shift in 2θ value corresponds to the compressive stress at 0 mm from the weld centerline and 2.5 mm below the top surface (fig. 2).

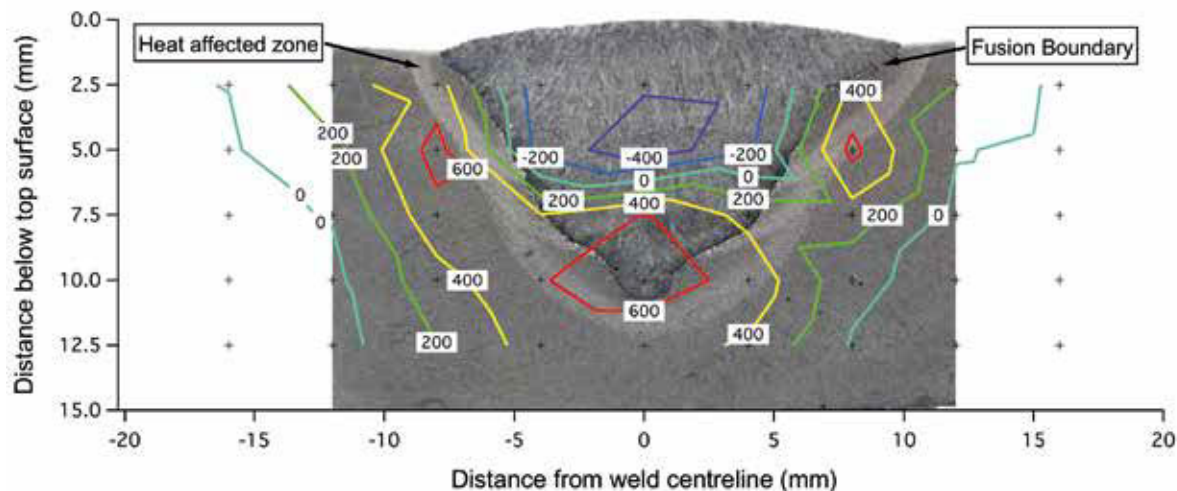


Figure 2: Stress contours superimposed on the corresponding weld macrograph. The stresses are in the longitudinal direction (out of plane of paper). The neutron diffraction measurement positions are marked by crosses.

The STRESS-SPEC instrument is customised for strain analysis and was used to create a stress map for a welded plate $350 \times 150 \times 15$ mm along the longitudinal, transverse and normal directions, respectively. The weld had three deposited layers and the inter-pass temperature was < 50 °C, to ensure each layer transformed fully to martensite before the next deposition.

Figure 2 shows the stress map estimated using neutron diffraction. Consistent with the weld geometry, the stress contours show remarkable symmetry reflected along the weld centreline. The contours, as expected, follow the fusion surface, as has been seen in similar experiments.

There is a large region of compression in the top half of the weld bead, with a maximum value of -400 MPa along the weld centreline at a depth of 2.5–5.0 mm below the top surface. Moving away from the centre at this depth, the compressive stresses gradually reduce and change sign at the fusion boundary. They then peak at 600 MPa around the heat affected zone on either side. This is not evident moving down the sample along the weld centreline. The stress change from compressive to tensile is much sharper and begins in the weld bead itself, culminating in a large tensile region in the bottom half of the specimen.

The development of tensile stresses in parts of the weld deposit is of significant interest. The results would suggest that the first-deposited layer, which is expected to have been in compression when deposited and cooled, has had its state of stress changed to tensile due to the effect of subsequent layers. This information will prove vital when designing thick welded sections with this type of alloy and highlights the contribution of neutron diffraction techniques towards industrial progress.

- [1] A. Ohta et al., Weld. World, 43, 38 (1999).
- [2] W. Wang et al., J. Mater. Sci. Technol., 18, 527 (2002).
- [3] A. Ohta et al., Int. J. Fatigue, 21, 113 (1999).
- [4] R. J. Moat et al., Sci. Technol. Weld. Join., 16, 279 (2011).
- [5] J.A. Francis et al., J. Press. Vess. Tech., 131, 0414011 (2009).

In-situ investigation of the phase transformation kinetics of Austempered Ductile Iron (ADI)

L. Meier¹, M. Hofmann²

¹Technische Universität München, utg, Garching, Germany

²Technische Universität München, Forschungs-Neutronenquelle Heinz Maier-Leibnitz (FRM II), Garching, Germany

Austempered ductile iron (ADI) is a very attractive material for applications where high strength, good ductility, wear resistance and fatigue strength are required. It is essentially a cast ductile iron that undergoes a special heat treatment to achieve these improved material properties. Neutron diffraction measurements were used to follow the phase transformation kinetics and changes in the microstructure during this heat treatment in-situ.

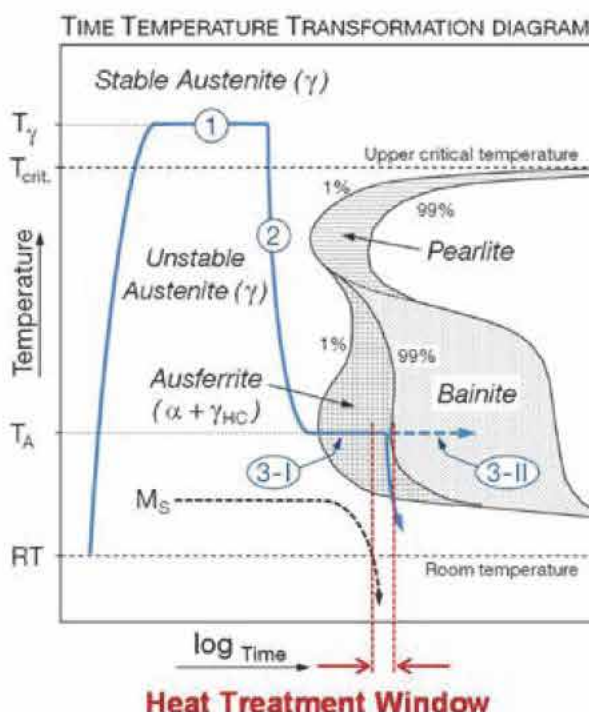


Figure 1: Schematic time-temperature-transformation diagram of cast ductile iron. The ADI heat treatment is shown as a blue line and the numbers indicate the three principal steps: austenitisation (1), quenching (2) and austempering (3).

What is ADI?

As depicted in figure 1, the heat treatment consists of austenitisation in the range of 850-950 °C (T_γ) (1), quenching (2) to a temperature range of 250-450 °C (T_A) for a 1 h to 4 h isothermal austempering (3) and subsequent cooling to room temperature. During austenitisation the as-cast matrix structure transforms into austenite and gets enriched with carbon. After quenching to the austempering temperature T_A , a two-stage phase transformation reaction takes place in ADI. In Stage I, ferrite platelets grow into the metastable austenite. As ferrite can take up only a very small amount of carbon, it is rejected into the surrounding residual austenite. The high carbon content stabilises the austenite, brings the reaction to an end and the ADI can be cooled to room temperature without the formation of martensite. The high carbon austenite (γ_{HC}) eventually decomposes into ferrite and iron carbides after long times of austempering (Stage II reaction).

The formation of both of martensite and carbides is detrimental to the mechanical properties of

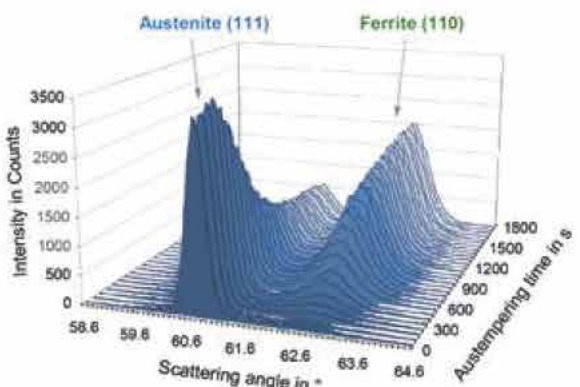


Figure 2: Neutron diffraction patterns showing the austenite (111) and ferrite (110) Bragg reflections vs. time at $T_A = 300$ °C.

ADI, so that the best heat treatment results are achieved after the end of Stage I and the beginning of Stage II (onset of carbide precipitation). The time interval between these two stages is called the heat treatment window (HTW) of the ADI reaction. The final ADI microstructure consists of graphite nodules in an “ausferritic” matrix of high carbon austenite and sheaves of ferrite plates. The proportion and morphology of these phases, which determine the balance between ductility and strength, and the HTW depend on the phase transformation kinetics which is strongly affected by composition, as-cast microstructure and heat treatment parameters (T_γ , T_A).

In-situ neutron diffraction at STRESS-SPEC

Following the typical ADI heat treatment procedures (fig. 1), cast ductile iron samples were heated to 900 °C for 30 min to fully austenitise them, quenched to austempering temperatures between 300 °C and 400 °C and aged for several hours using a mirror furnace developed for this project. Neutron diffraction data were collected on the diffractometer STRESS-SPEC during the complete heat treatment cycle with measurement times varying between 20 s and 3 min adapted to the respective heat treatment step (fig. 2). The austenite content decreases rapidly within the first 10 min and reaches a stable plateau after approximately 30-90 min, indicating the end of the Stage I reaction. The residual austenite content decreases as the austempering temperature is lowered. In the case of the sample kept at $T_A = 400$ °C, the onset of the decomposition reaction (Stage II) is observable after 110 min. In addition to the determination of phase fractions, the carbon uptake of the austenite could be monitored and characterised by the increase in the lattice constant from the in-situ neutron diffraction data (not shown here).

Among other things, information on the microstructure of the alloy can be extracted from the reflection peak shapes. For example, the evolution of the peak width of the austenite (111) and ferrite (110) Bragg reflections is depicted in figure 3a for $T_A = 300$ °C. The increase in peak

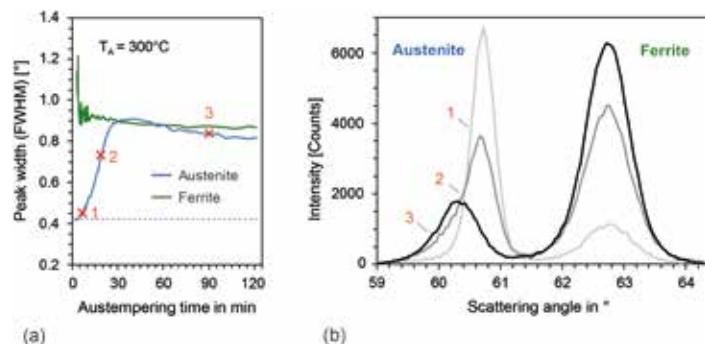


Figure 3: (a) FWHM of austenite (111) and ferrite (110) Bragg reflections at $T_A = 300$ °C. The dotted line indicates the instrumental resolution at the scattering angle $2\theta \sim 60^\circ$; (b) Bragg reflection profiles of austenite (111) and ferrite (110) at different austempering times (marked with crosses in (a)).

width in the austenite Bragg reflections is consistent with a decrease of the size of the austenite grains. Furthermore, closer inspection of the neutron data reveals an asymmetry in the peak shape of the austenite peak (e.g. profile (2) in fig. 3b). This suggests that, during the austempering reaction, a fine grained austenite phase is formed in addition to the original austenite modification. This phase is characterised by a larger lattice constant, indicating a higher carbon content of the austenite. Similar transformation behaviour (“austenite splitting” or partitioning) in steels with high silicon contents has been observed using data from recent synchrotron measurements [1].

Conclusions

Neutron diffraction was used to investigate the heat treatment behaviour of ADI and to extract time dependent phase fractions with different carbon contents. This information, together with results from optical micrographs, hardness and dilatometer measurements will be used to characterise and optimise the kinetics of the “ausferritic” phase transformation. Furthermore, analysis of the reflection profiles provided evidence for two modifications of austenite during the start of the austempering reaction.

[1] H.J. Stone et al., Proc. Royal Soc. A, 464, 1009 (2008).

BH_4^- -hindered rotations in $\beta\text{-Mg}(\text{BH}_4)_2$

D. Blanchard¹, J. Maronsson^{1,2}, M. Riktor³, J. Kehres¹, D. Sveinbjörnsson¹, E. Gil Bardaji⁴, A. Léon⁴, F. Juranyi⁵, J. Wuttke⁶, K. Lefmann^{7,8}, B. Hauback³, M. Fichtner⁴ and T. Vegge¹

¹Technical University of Denmark, Department of Energy Conversion and Storage, Roskilde, Denmark

²Technical University of Denmark, Center for Atomic Scale Materials Design, Lyngby, Denmark

³Institute for Energy Technology, Physics Department, Kjeller, Norway

⁴Karlsruhe Institute of Technology, Institute of Nanotechnology, Karlsruhe, Germany

⁵ETH Zürich and Paul Scherrer Institute, Laboratory for Neutron Scattering, Villigen, Switzerland

⁶Forschungszentrum Jülich GmbH, Jülich Centre for Neutron Science at MLZ, Garching, Germany

⁷University of Copenhagen, Niels Bohr Institute, Copenhagen, Norway

⁸European Spallation Source, Lund, Sweden

Borohydrides, with high H_2 content, are of interest for solid state hydrogen storage but have slow ab/desorption kinetics and poor reversibility. To modify these properties, further knowledge of their basic physical/chemical properties is required. Quasi-Elastic Neutron Scattering is an optimal method for studying hydrogen dynamics, thanks to the large incoherent scattering cross section of hydrogen. With measurements performed at SPHERES on $\text{Mg}(\text{BH}_4)_2$, combined with Density Functional Theory calculations, two thermally activated reorientations of the BH_4^- units were revealed, the ones about the two-fold axes being energetically more favorable than those about the three-fold axes [1].

Metal borohydrides are of interest as solid state hydrogen storage materials due to their high volumetric and gravimetric hydrogen content. However, in common with many of the complex

hydrides, they are generally thermodynamically too stable, the temperatures required to release the hydrogen are too high and they suffer from slow absorption and desorption kinetics as well as having poor reversibility.

Investigation of hydrogen dynamics

Among the borohydrides, $\text{Mg}(\text{BH}_4)_2$ has more favorable thermodynamics than, for example, LiBH_4 and attractive hydrogen capacity (14.9 mass% of H_2). Furthermore, it has been proved to be, at least partially, reversible. If one seeks to improve its storage performances and tailor its properties, in-depth knowledge of the basic physical and chemical properties is required. Therefore, we have investigated the hindered rotation of the BH_4^- units in magnesium borohydride in an effort to understand the hydrogen motions in such compounds. We used quasielastic neutron scattering (QENS), an optimal method for studying hydrogen dynamics, thanks to the large incoherent scattering cross section of hydrogen compared to all other scattering atoms.

To facilitate the analysis of the QENS measurements, Density Functional Theory (DFT) calculations were performed and valuable results, in connection with the structural features of the borohydride, were obtained.

High resolution neutron backscattering

Natural B contains 20 % of ^{10}B with a high absorption cross section of 3837 barns, therefore $\text{Mg}(\text{BH}_4)_2$ was synthesized using a ^{11}B enriched precursor (5.5×10^{-3} barns).

QENS measurements were performed with SPHERES, the high resolution neutron backscattering spectrometer, with ~ 0.08 g of $\text{Mg}(\text{BH}_4)_2$

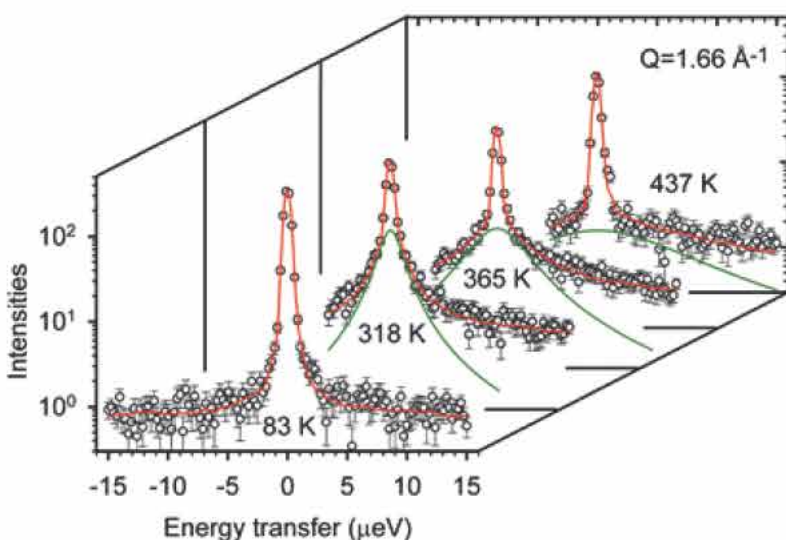


Figure 1: The QENS spectra of $\beta\text{-Mg}(\text{BH}_4)_2$ measured with SPHERES at different temperatures for $Q = 1.66 \text{ \AA}^{-1}$. The dots are the experimental data. The solid lines display the fits of the data, each consisting of a resolution broadened delta function, a Lorentzian (dashed line) and a flat background (not shown on the plots).

loaded in an Al wire sealed flat $30 \times 40 \times 0.5 \text{ mm}^3$ Al container oriented at 135° with respect to the direct beam. Si(111) monochromator and analyzer crystals were used in a backscattering geometry giving a final neutron wavelength of 6.271 \AA and an energy resolution of 0.65 \mu eV with an energy transfer range selected between $\pm 15.8 \text{ \mu eV}$. The spectra were recorded by nine detectors corresponding to a scattering vector ranging from 0.59 to 1.66 \AA^{-1} . After an inelastic scan in the temperature range from 10 to 540 K , QENS measurements were performed at 83 , 190 , 318 , 365 , 437 K . See figure 1 for an example of the QENS spectra.

The C_2 and C_3 hindered rotations

The analysis of the QENS data obtained for $\beta\text{-Mg}(\text{BH}_4)_2$ shows that, within the time scale accessible by SPHERES, two thermally activated hindered rotations of the BH_4^- unit were observed. From a comparison of the experimental results with the DFT calculations, it was found that these rotations occur around the $C_{2//}$ and C_3 axes (fig. 2). The experimental and DFT calculated energy barriers were in good agreement, with $E_{\text{ac}C_{2//}} = 39 \pm 0.5$ and $76 \pm 5 \text{ meV}$ determined experimentally as compared to DFT values ranging from 28 to 82 meV and $E_{\text{ac}C_3} = 214 \pm 4 \text{ meV}$ with values ranging from 177 to 298 meV .

Five non equivalent boron positions

DFT calculations show that, even if all the Mg-B-Mg are close to being linear and the BH_4^- have bidentate orientations, which correspond to the $C_{2//}$ -axis, small variations of the distance L (distance of the boron to the middle point of Mg-Mg), lead to noticeable differences in the energy barriers. In the crystal structure of $\beta\text{-Mg}(\text{BH}_4)_2$, five non equivalent boron positions do indeed exist! Thus, it could be stated that, in $\beta\text{-Mg}(\text{BH}_4)_2$, when the atoms are subject to thermal vibration, a distribution of L and, therefore, of the energy barriers, must exist. QENS measurements can't resolve dynamic events that are energetically too close, thus the experimental energy barriers extracted were averaged values of closely distributed values.

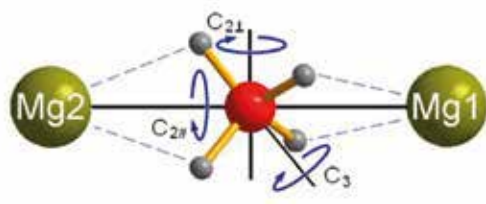


Figure 2: BH_4^- coordination environment in $\beta\text{-Mg}(\text{BH}_4)_2$ (space group Fdd)

More generally, the rotations about the $C_{2//}$ -axis were found to be energetically more favorable than those around the C_3 -axis. This could easily be explained by looking at the schematic representation of the local environment of the BH_4^- tetrahedra (fig 2). With the bidentate orientation, no Mg-H bond is broken during rotation around the $C_{2//}$ -axis while the rotation around the C_3 -axes induces two bonds braking and the one around the $C_{2\perp}$, four.

Fundamental knowledge

In order to tailor the physical properties of the borohydrides and, more generally, the complex hydrides for use as solid state hydrogen storage, comprehensive knowledge has to be gathered about their decomposition mechanisms, including microscopic information on the hydrogen dynamics.

The combined DFT-QENS approach used here is very useful and powerful when it comes to determining crucial quantities such as characteristic times and energy barriers for the hydrogen dynamics, information needed to develop new experiments and target the instruments and techniques to be used to pursue the investigations.

In-situ studies of mass transport in liquid alloys by means of neutron radiography

F. Kargl¹, M. Engelhardt¹, F. Yang¹, H. Weis¹, P. Schmakat^{2,3}, B. Schillinger³, A. Griesche⁴ and A. Meyer¹

¹Deutsches Zentrum für Luft- und Raumfahrt (DLR), Institut für Materialphysik im Weltraum, Köln, Germany

²Technische Universität München, Physik-Department E21, Garching, Germany

³Technische Universität München, Forschungs-Neutronenquelle Heinz Maier-Leibnitz (FRM II), Garching, Germany

⁴Bundesanstalt für Materialforschung und -prüfung, Berlin, Germany

Neutron radiography is a powerful tool for measuring the chemical diffusion coefficients of liquid binary and ternary alloys *in-situ*. Chemical diffusion coefficients complement self-diffusion coefficients mainly obtained by quasielastic neutron scattering. Due to different interactions, neutron radiography may, for some materials, overcome the poor contrast experienced with X-ray radiography. To this end, a novel Al_2O_3 -based furnace has also been developed. The chemical diffusion coefficient of Ag against Al for the ternary eutectic composition $\text{Al}_{68.6}\text{Cu}_{13.8}\text{Ag}_{17.6}$ is reported.

In-situ studies of chemical diffusion

Diffusion coefficients in liquid metals are one of the key parameters for a successful computer-

assisted design of solidification processes. The propagation, dimension and type of the emerging phases during solidification strongly depend on these transport coefficients. To obtain accurate measurements with minimum error, *in-situ* techniques, which allow to monitor and analyze experiments in real-time, have emerged in recent years that offer a significant improvement compared with the wellknown *ex-situ* methods. Direct measurement of the diffusion process makes it possible to identify sources of errors (segregation, formation of bubbles, etc.) and, furthermore, reduces statistical errors by evaluating many concentration profiles instead of a single one. Initially X-ray radiography (XRR) was used for measuring interdiffusion in liquid Al-Cu samples [1]. Here, we describe neutron radiography (NR) experiments. NR is a well known method, complementary to XRR in the sense that it enables one to investigate systems that lack sufficient X-ray contrast. As a result, the restrictions on materials containing a combination of high Z-elements such as e.g. Ag and Cu in the same sample, which means high X-ray absorption, may be overcome by the Z-uncorrelated behaviour of the element specific cross-sections for neutrons.

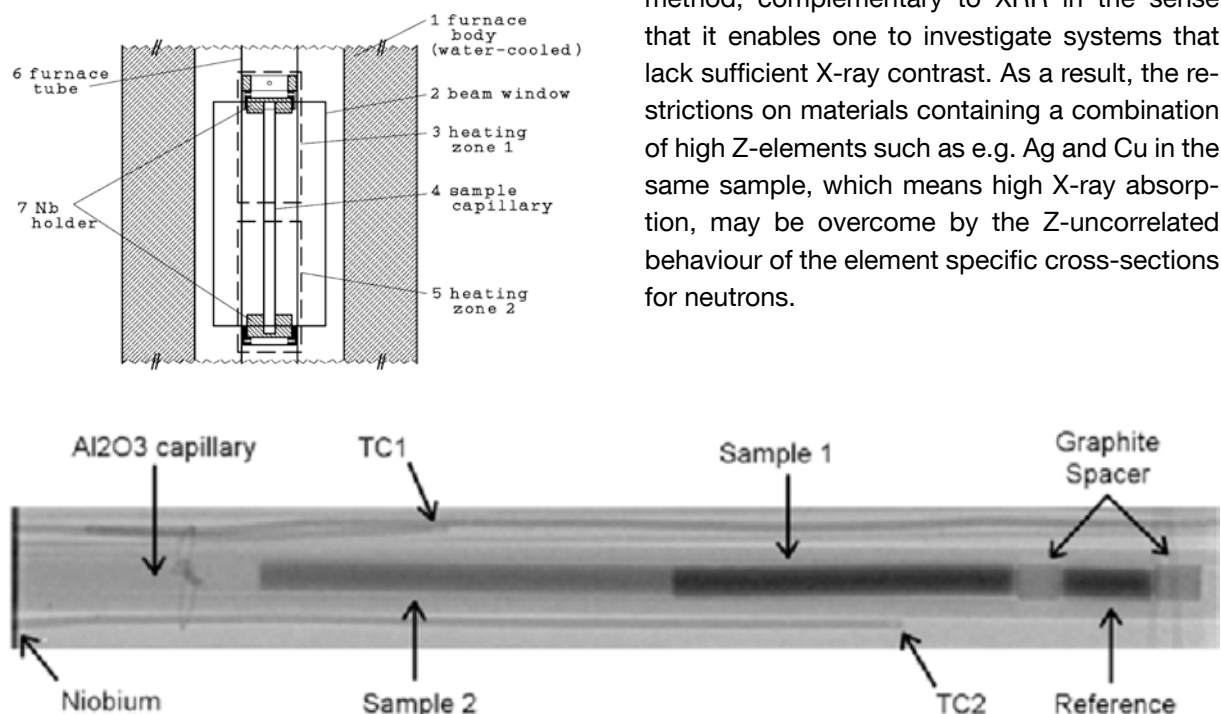


Figure 1: Top: Schematic diagram of Al_2O_3 tube furnace. Bottom: Radiographic image of furnace including the Ag-Al-Cu diffusion couple. The darker vertical wires close to the diffusion couple represent the thermocouples.

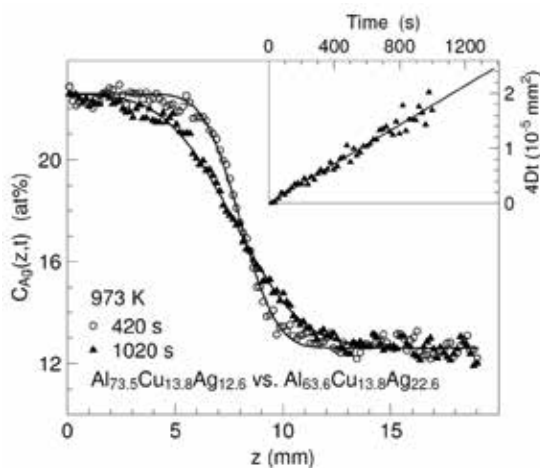


Figure 2: Ag concentration for a $\text{Al}_{73.5}\text{Cu}_{13.8}\text{Ag}_{12.6}$ vs. $\text{Al}_{63.5}\text{Cu}_{13.8}\text{Ag}_{22.6}$ diffusion couple at 973 K for two different times of diffusion (triangles). Inset: Squared diffusion length $4Dt$ shown as a function of time, with the slope of the linear fit (solid line) proportional to the chemical diffusion coefficient of Ag.

Al_2O_3 -tube furnace for neutron radiography on diffusion couples

For neutron radiography experiments carried out at the ANTARES instrument at the MLZ in Munich, a novel Al_2O_3 -based tube furnace (see fig. 1) was developed [2]. This furnace minimizes neutron scattering contributions that disturb the resolution, as previously experienced when using the standard graphite furnace used in XRR. The inner parts of the furnace subjected to neutron radiography are made entirely of Al_2O_3 . The inner parts are heat insulated with Al_2O_3 felt and housed in a water-cooled and vacuum-tight aluminum outer structure. The furnace is heated by two independently controlled heating-zones made of niobium-wire. The diffusion couples are accommodated in a Al_2O_3 capillary-tube with an inner diameter of 1.6 mm. To provide for a clear view of the diffusion couple, an axial gap of 5 mm is maintained between both independent heaters. A spring mechanism pushes onto an Al_2O_3 -rod of 1.5 mm diameter, which is inserted into the diffusion capillary and applies the necessary pressure on the sample to avoid free surfaces by compensating for volume changes during melting. The sample capillary is centered and held in between two end pieces made of

niobium in order to fix the samples, the spacers, and the reference volumes. The temperature is controlled by two thermocouples, which are located inside the furnace near the center of each diffusion. For the neutron radiography experiments, an L/D ratio of 400, a 100 μm thin scintillator, and a 2:1 macro lens were used. The resolution achieved with this setup was 31 μm per square pixel, measured with a test pattern on a silicon wafer. Individual images were recorded every 20 s, resulting in an exposure time of 13 s per image.

Chemical diffusion of Ag in the ternary eutectic of Ag-Al-Cu

Chemical diffusion in $\text{Al}_{73.5}\text{Cu}_{13.8}\text{Ag}_{12.6}$ vs. $\text{Al}_{63.5}\text{Cu}_{13.8}\text{Ag}_{22.6}$ diffusion couple was measured. The two alloys differ in their Al and Ag concentrations. However, the Cu concentration is the same. The mean composition corresponds to the ternary eutectic E1 in the ternary Ag-Al-Cu phase diagram. Ag concentration profiles recorded at a temperature of 973 K are shown in figure 2. For data evaluation, it was assumed that no significant uphill diffusion of Cu occurs in the diffusion couple with the initially constant Cu content. Changes in the recorded greyvalues were therefore attributed solely to a change in Ag concentration and, as a result, a chemical diffusion coefficient for Ag is obtained. The squared diffusion length $4Dt$ shown in the inset of figure 2 depends linearly on time. A chemical diffusion coefficient of Ag against Al of $4.4 \pm 0.4 \cdot 10^{-9} \text{ m}^2\text{s}^{-1}$ is obtained for the eutectic composition E1 in the ternary Ag-Al-Cu phase diagram at a temperature of 973 K.

[1] B. Zhang et al., Phys. Rev. Lett., 104, 035902 (2010).

[2] F. Kargl et al., J. Phys.: Condens. Matter., 23, 254201 (2011).

PGAA analysis of the younger dryas impact event

R. B. Firestone¹, Zs. Révay²

¹Lawrence Berkeley National Laboratory, Berkeley, USA

²Technische Universität München, Forschungs-Neutronenquelle Heinz Maier-Leibnitz (FRM II), Garching, Germany

According to a new hypothesis, a cosmic impact was directly responsible for extinctions and climate changes that occurred in North America 12,900 years ago. A set of archaeological samples, soils and meteoritic particles, originating from different excavation sites in the USA, were analyzed using the Prompt Gamma Activation Analysis (PGAA) instrument of MLZ. PGAA proved to be an important tool for determining the meteorite's composition and samples from the impact zone.

12,900 years ago, mammoths and megafauna became extinct and Clovis Paleo-Indian culture disappeared from the Americas. At the same time, the Laurentide Ice Sheet in Canada suddenly failed, leading to a 1300 year return of ice age conditions known as the Younger Dryas. Simultaneously, a thin sediment layer containing magnetic grains and microspherules enriched in

iridium, carbon spherules and containing nanodiamonds and a host of other markers consistent with a massive extraterrestrial impact was deposited across the Americas and into Europe. According to a new hypothesis, this impact was directly responsible for extinctions and climate changes that occurred then.

A large set of different samples, originating from different excavation sites in the US, have been analyzed using many different methods, including prompt gamma activation analysis (PGAA).

Improved PGAA

After its reconstruction last year, the improved PGAA facility is now capable of performing irradiations at high neutron flux ($6 \cdot 10^{10} \text{ cm}^{-2}\text{s}^{-1}$) using a focused beam and at medium flux ($2 \cdot 10^9 \text{ cm}^{-2}\text{s}^{-1}$) with a homogeneous beam profile. While the latter is still used for bulk samples, the high-flux method is used for the analysis of samples with masses below 1 mg. The stones were put in the beam directly, while the spherules of micro-meteorites with a total mass of 300–1000 µg were placed in 0.5 µm thick Mylar foils and irradiated in the high-flux beam for 10–20 hours (see fig. 1).

Elemental analysis of metorites

The elemental compositions were determined, the samples were classified based on the results, and these were then compared to results obtained by other analytical methods. The major components were Al, Si, S, Ca, Ti, Fe in the amounts of 1–100 µg. B, Cl, Nd, Sm, and Gd contents were 10–1000 ng. The lowest detection limits were in the order of 100 pg for boron and the rare-earths.

Analysis of the YD impact layer shows (fig. 2) remarkable similarity to the Procellarum Lunar KREEP Terrane visited by the Apollo astronauts.

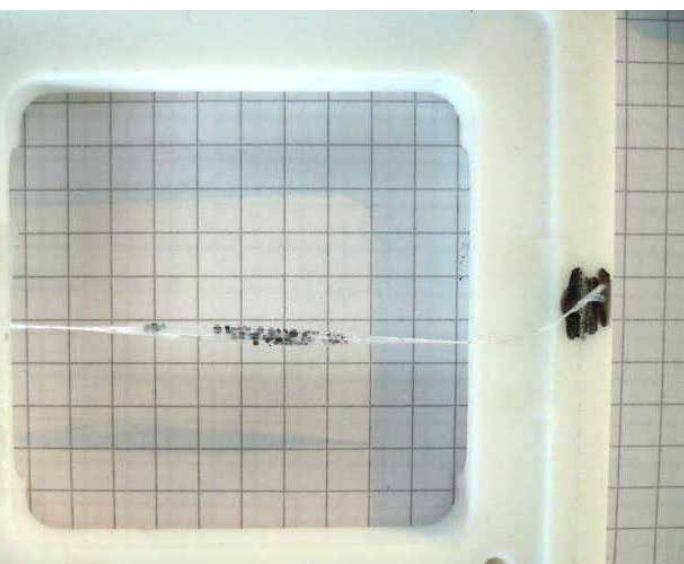


Figure 1: Spherules of micro-meteorites in Mylar foil in the sample holder frame.

Region	Number of Spherules	% with Ti/Fe > 0.3	Average with Ti/Fe > 0.3	Average Ti/Fe all spherules	PGAA Ti/FE
SW-North America	129	10.9	1.0	0.12	0.5
SE-North America	148	16.9	1.1	0.22	1.5
NE-North America	192	24.0	1.0	0.30	1.3
Great Lakes - Gainey	5	60.0	1.3	0.6	0.1
Central America	14	7.1	1.6	0.11	---
Europe	14	0	---	0	1.1
Asia	129	5.1	0.5	0.12	---

Table 1: Regional variation in the ratio of titanium to iron oxide abundances in the magnetic spherules and grains recovered from the Younger Dryas impact layer.

High water content in the magnetic grains determined by PGAA suggests they were formed in wet conditions consistent with an impact into the Laurentide Ice Sheet. The Ti/Fe ratios in magnetic grains from impact sites in the Eastern US and Europe, measured by PGAA, are much higher than known terrestrial sources where $\text{Ti}/\text{Fe} \approx 0.1$, which suggests an impact by a Ti-rich object near the Great Lakes (table 1). This is also seen in our analysis of impact spherules which are enriched in Ti in Eastern North America. Near the Great Lakes impact site, the magnetic grains are dominated by local sediments ejected by the impact. US searches for more YD impact evi-

dence have led to the discovery of other impact events (fig. 3). [1]

Future plans

PGAA proved to be an important tool for determining the meteorite's composition and samples from where it impacted Earth. The high-flux method could successfully be used for the determination of the composition of samples with masses less than 1 mg.

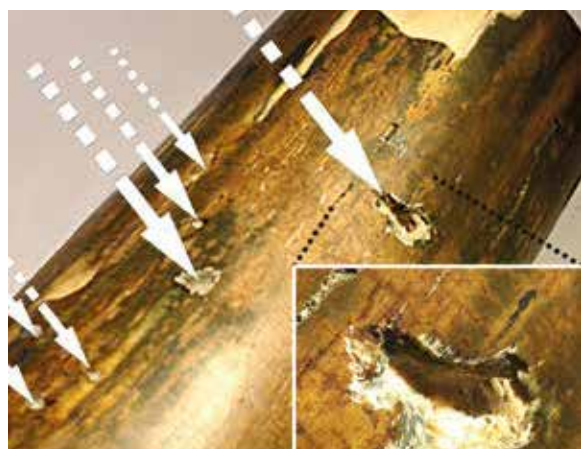


Figure 3: Searches of fossil mammoth tusks and bison skulls for evidence of damage from the YD impact led to the discovery of fossils with high velocity impact pits, only on one side of the object. PGAA analysis of particles embedded in these fossils indicated that they were mainly Fe/Ni enriched to as much as 20% nickel, consistent with normal iron meteorites. This is very different from the Ti-rich, Ni-poor composition of the YD magnetic grains. Subsequent radiocarbon dating indicated that these fossils were about 37,000 years old and from a different impact, possibly associated with the Sikhote-Alin Crater in Alaska.

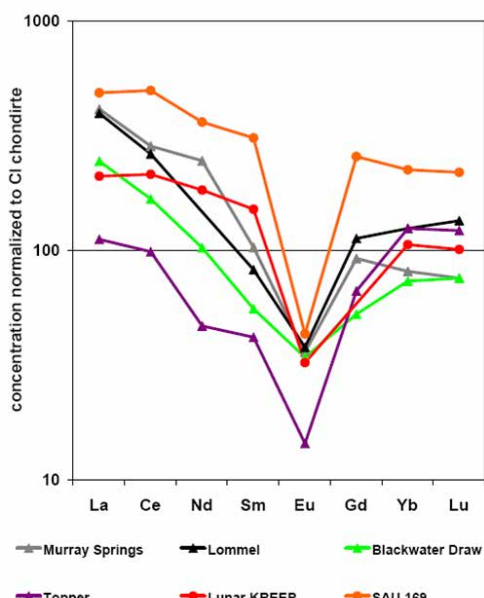


Figure 2: PGAA/NAA analysis of the YD layer at many sites shows negative Eu anomalies observed only in lunar KREEP and in SAU 169, a meteor from Oman, believed to have originated from the Procellarum Lunar KREEP Terrane region of the moon.

[1] T.E. Bunch et al., Proc. Nat. Acad. Sci., 109, E1903 (2012).

Non-destructive elemental determination of kidney stones using PGAA

E. Spyropoulou¹, P. Nasos², I. M. Siouris¹, S. Katsavounis¹, P. Kudejova³, L. Canella³

¹Democritus University of Thrace, Department of Production Engineering & Management, Xanthi , Greece

²General Hospital of Xanthi, Department Of Urology, Xanthi, Greece

³Technische Universität München, Forschungsneutronenquelle Heinz Maier-Leibnitz (FRM II), Garching, Germany

Non-destructive elemental analysis of ten kidney stones has been performed using Prompt Gamma Activation Analysis (PGAA) in order to determine their elemental composition and draw conclusions regarding their formation.

Kidney stones are produced as a result of the precipitation of saturated oxalate, urate, phosphate, and carbonate salt solutions in the kidney. Several processes have been recommended to explain their formation [1-3]. The most important are the precipitation-crystallization theory, the matrix-nucleation theory and the inhibitor-absence theory. The stone precipitation process is not properly understood yet. A supersaturation of urine with stone forming salts is of fundamental importance and a prerequisite for the necessary precipitation. The matrix nuclear theory suggests that some matrix substance forms an initial nucleus upon which further stone growth occurs. According to the inhibitor-absence theory, stone

formation could occur even in patients with normal concentration of urinary crystalloids [4]. Generally, kidney stones can be classified into four types based on their chemical composition. They are calcium oxalate stones, calcium oxalate mixed with apatite, magnesium ammonium phosphate, and uric acid and xanthine.

Prompt Gamma Activation Analysis (PGAA) is ideal for the determination of the elemental composition of materials. The results of the chemical analysis provides information on the elemental correlations and the synergistic effects on the stone formation.

Classification and chemical analysis

Ten kidney stone samples were obtained from patients at the General Hospital of Xanthi, Greece (fig. 2). The patients came from the region of Xanthi and comprise both different races and ages. Classification of the stone types was based on chemical composition. Analysis

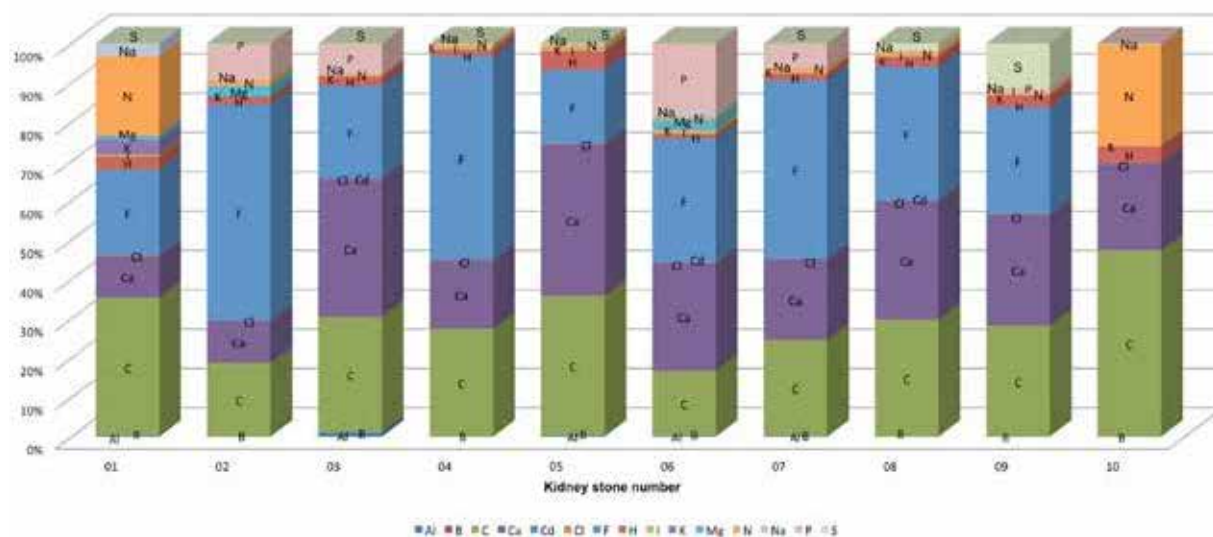


Figure 1: Quantitative analysis of the kidney stones.

of the acquired spectra was carried out using Hypermet-PC software [5] and the final chemical analysis was performed with ProSpeRo, excel macro software [6].

Seven types of stones

PGAA is a suitable technique for analysis of trace elements in complex or organic matrices, such as in kidney stones. Each kidney stone sample was sealed in a thin FEP bag and then measured. The measurement times ranged between two and four hours, depending on the size of each sample. The samples were irradiated under three different irradiation conditions. The neutron flux ranged between $2.85 \cdot 10^9 \text{ cm}^{-2}\text{s}^{-1}$ and $7.6 \cdot 10^9 \text{ cm}^{-2}\text{s}^{-2}$.

Urinal stone components may be mineral, organic or both. There are seven distinctive types of stones, but the most common groups are phosphate, oxalate, urate and struvite calculi. Most stones are of mixed composition and, among heterogeneous calculi, about 80% are made up of a mixture of calcium oxalate and calcium phosphate in various proportions.

According to the experimental results, 15 major elements were observed. The spectral analysis revealed the presence of Al, B, C, Ca, Cd, Cl, F, H, I, K, Mg, N, Na, P and S. The composition of each kidney stone can be seen in figure 1. All

Mineral Group	Major elements	Trace elements
Phosphate	Mg, P, K, Sr, Cd, Zr, Sb, I, Ba, Si, F, Zn, Rb	Pb, B
Oxalate	Ca, S, Fe, Cr, Cu	K, I, Al
Urate	Na, U, Mn, Cu, As, Se	Ca, Mg, P, Sr, Cd, Zr, Sb, Ba, Si, Cr, Zn
Struvite	Mg, P, N	Rb, Sr

Table 1: Elemental composition of kidney stones in different mineral groups.



Figure 2: Kidney stone sample.

samples contain C and Ca, confirming the existence of CaCO_3 . In addition, P and Mg were found in the samples 02 and 06, which implies that there are struvite stones (ammonium magnesium phosphate, $\text{NH}_4\text{MgPO}_4 \cdot 6\text{H}_2\text{O}$). Furthermore, for stones in the oxalate group, high sulfur content is typical. Uric acid stones contain B and Cl at higher concentrations compared to calcium oxalate stones.

To conclude, a full quantitative analysis was performed on ten kidney stones. The results showed that all samples are formed on a CaCO_3 -Nitrogen matrix. Furthermore, two stones consist of ammonium magnesium phosphate (struvite), whereas uric acid stones are also found. These results suggest that the matrix-nucleation theory most probably explains the formation of the stones, although the other theories cannot readily be discarded.

[1] O. A. Golovanova et al., J. Appl. Spectrosc., 73, 6 (2006).

[2] A. Hesse et al., Scanning Microscopy, 13, 2 (1999).

[3] A. Hodgkinson, J. Clin. Pathol., 147 (1971).

[4] S. Sarmani et al., Biological Trace Element Research, 26, 497 (1990).

[5] Hypermet-PC: http://www.iki.kfki.hu/nuclear/hypc/index_en.shtml, last downloaded 26.02.2013.

[6] Zs. Révay, Anal. Chem., 81, 6851 (2009).

An experimental determination of the relative biological effectiveness of thermal neutrons

E. Schmid¹, F. M. Wagner², L. Canella², H. Romm³, T. E. Schmid⁴

¹Ludwig-Maximilians-Universität München, Institut für Anatomie & Zellbiologie, München, Germany

²Technische Universität München, Forschungs-Neutronenquelle Heinz Maier-Leibnitz (FRM II), Garching, Germany

³Bundesamt für Strahlenschutz, Oberschleissheim, Germany

⁴Technische Universität München, Klinikum rechts der Isar, Department of Radiation Oncology, München, Germany

The induction of dicentric chromosomes in human lymphocytes (fig. 1) is the gold standard in biological dosimetry. In the wide energy range of neutrons, research on the biological effects of thermal neutrons has played a very small role and is not well documented. Blood was taken from the same donor whose blood had been used to test many other beam qualities. Whole blood was irradiated using cold neutrons at the PGAA-facility of MLZ. The absorbed energy dose was calculated from all possible interactions of the constituents of blood. For the evaluation of the biological data, the usual linear-quadratic dose-response law was applied. The maximum relative biological effectiveness with respect to ^{60}Co γ -rays, RBE_{M} , was determined as 36 ± 13 . This value is significant in radiation protection and for neutron capture therapy.



Figure 1: Microscope observation of chromosomes which are usually X-shaped. The formation of several stable centres in chromosomes is a sensitive and quantitative indicator of deteriorations due to radiation. One chromosome with two centres, a “dicentric”, is marked by the arrow.

Thermal neutrons and radiation protection

For radiological protection purposes, the maximum value of the relative biological effectiveness (RBE_{M}) for the induction of cancer in humans at low doses and the dose rates of neutrons relative to X- or γ -rays is used to compare the effects of different types of radiation. RBE_{M} values provide the primary basis for the determination of the quality or weighting factors for neutrons. As there is a lack of direct evidence for human data from epidemiological observations, one must rely on the production of dicentrics in human lymphocytes, which is the best reproducible radiological endpoint.

Sample preparation and determination of radiation dose

Blood was taken from the same donor (E. S.) whose blood had been used for irradiation experiments with widely varying neutron energies so that inter-individual variations or differences in methodology usually associated with inter-laboratory comparisons were avoided. The T-lymphocyte fraction of the blood samples represents a cell population which is quasi exclusively in the G_0 phase of the cell cycle, i.e., in a DNA pre-synthetic stage. After irradiation, the T-lymphocytes can be stimulated to blast DNA synthesis and cell division in vitro.

Whole blood was irradiated using the larger of two fields available at the PGAA facility in the neutron guide hall of FRM II, with a cold neutron flux of $6.54 \cdot 10^9 \text{ cm}^{-2}\text{s}^{-1}$ free in air. The contributions to the absorbed energy dose were calculated from all possible interactions of the constituents of blood. From the cross sections of the elemental tissue constituents and the associated deposited energies, the kerma coefficient was calculated

as $3.4 \cdot 10^{-13}$ Gy cm². About 76 % of the dose is caused by the capture reaction $^{14}\text{N}(\text{n},\text{p})^{14}\text{C}$ with the release of a highly energetic, densely ionising proton; the remainder is caused by internal and external gamma rays and electrons. Doses from 0.375 Gy to 1.875 Gy were administered.

After irradiation, chromosome preparation and staining were carried out according to standardised laboratory procedures. Only complete cells were analysed for dicentrics, centric rings and excess acentrics.

Quantification of the effect of thermal neutrons

With increasing dose D, the yield of the three above-mentioned damages increases. At all irradiation levels, the intercellular distribution of the most significant dicentrics is overdispersed. Weighted least-squares approximations are used to fit the data for the induction of dicentrics by neutrons by both a linear function $y = c + \alpha D$ and the linear-quadratic function $y = c + \alpha D + \beta D^2$, where $c = (3.2 \pm 1.4) \cdot 10^{-4}$ represents a control value of dicentrics determined earlier by the same group with blood of the same donor. According to the statistical analysis, the dose response coefficient β is not significantly different from zero, see figure 2.

The linear dose-response coefficient for the induction of dicentrics ($\alpha = 0.400 \pm 0.018$ Gy⁻¹) is used to estimate the RBE_M of thermal neutrons relative to ^{60}Co γ -rays. As a reference, a dose-response curve for estimating the RBE_M, a standard linear-quadratic reference dose-response curve for ^{60}Co γ -rays is used, which had already been applied previously to estimate the RBE_M of the fission neutron therapy facility MEDAPP at FRM II. This curve with the coefficients $\alpha = 0.011 \pm 0.004$ Gy⁻¹ and $\beta = 0.056 \pm 0.003$ Gy⁻² was determined under conditions comparable with the present investigation. The ratio of the respective α values and ^{60}Co γ -rays, delivers an RBE_M of 36.4 ± 13.3 .

No significant effect of concomitant γ -radiation

Based on the analysis of cell numbers between 800 at the lowest dose and 500 at the highest,

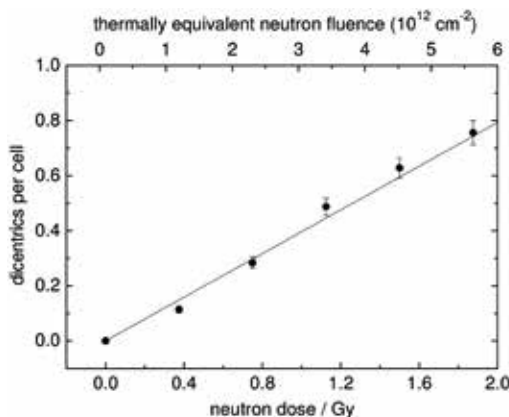


Figure 2: Dose and fluence dependence of the frequency of dicentrics in human lymphocytes obtained by irradiation with slow neutrons.

the probability of observing dicentrics attributable to concomitant γ -rays is very low. Using the linear quadratic dose-response relationship for ^{60}Co γ -rays, it can be estimated that only 1 out of 91 dicentrics at the lowest thermal neutron dose of 0.375 Gy and 8 out of 378 dicentrics at the highest thermal neutron dose of 1.875 Gy may be induced by γ -rays. In total, only 23 out of 1337 radiation-induced dicentrics (1.7 %) observed in 3200 cells analysed are attributable to the γ -ray component of the radiation field. Provided that both the neutron and the γ -ray component act independently, the remaining 1314 dicentrics can be assumed to be due to the neutron component. Thus, it seems to be justified to calculate the RBE_M of the thermal neutrons by subtracting the γ -ray contribution at any dose using the mean values of dicentric yields and their Poisson distribution from the linear-quadratic dose-response curve for ^{60}Co γ -rays. The resulting RBE_M of 47.0 ± 17.2 is not significantly different from the RBE_M of 36.4 ± 13.3 for the thermal neutrons contaminated with 24 % low-LET radiation ($z = 0.49$; p -value = 0.626). Further details regarding the methods and the full data sets are given in [1].

The antineutrino spectrum of the fission products of ^{238}U

N. Haag¹, K. Schreckenbach², L. Oberauer¹, W. Potzel¹

¹Technische Universität München, Physik-Department E15, Garching, Germany

²Technische Universität München, Forschungs-Neutronenquelle Heinz Maier-Leibnitz (FRM II), Garching, Germany

The antineutrino spectrum emitted from a nuclear reactor is generated by beta decays of the fission products of four main fuel isotopes. In the 1980s the contributions of three of them - ^{235}U , ^{239}Pu and ^{241}Pu - were individually measured by fissioning with thermal neutrons. As the last missing piece, the ^{238}U spectrum could now be determined in an experiment at the NECTAR site. A fast neutron beam induced fissions in an Uranium foil and the emitted beta spectrum was recorded and finally converted into an antineutrino spectrum.

The role of reactor antineutrinos

With an emission of $2 \cdot 10^{20}$ electron antineutrinos /s /GW nuclear reactors are valuable tools for neutrino physics. Last year, the reactor antineutrino disappearance experiments Double Chooz, Daya Bay and RENO were able to pin down the last mixing angle θ_{13} in the neutrino oscillation matrix [1,2,3]. In addition, the measurement of the antineutrino spectrum may make it possible to determine the fuel content without

any input from reactor authorities. This may lead to applications supporting the IAEA's agenda of non-proliferation [4]. As a third issue, there is an active discussion on the so-called reactor antineutrino anomaly. Recent re-calculations of the reactor-neutrino spectrum suggest that former experiments have seen too low a flux of antineutrinos. This may give a hint of the possible existence of sterile neutrinos [5].

All these points require one basic input: Knowledge of the emitted antineutrino spectrum both in shape and intensity. Measurements of the spectra emitted by U235, Pu239 and Pu241 were performed in the 1980s using a magnetic spectrometer at the ILL in Grenoble [6,7].

However, the determination of the antineutrino spectrum from the fission products of U238, which contributes about 8 % to the total power of a PWR, is more difficult, as this isotope can only be fissioned by fast neutrons. It has now become possible to determine this last missing part at the FRM as its converter facility is a unique tool for generating a high flux of fast neutrons.

The Uranium experiment at the MLZ

To this end, an experiment was installed at the NECTAR site of the SR10 beam line.

The fast neutron beam was used to induce fissions of U238 in a target foil of natural Uranium. The beta spectrum emitted in the fissions was recorded and converted into an antineutrino spectrum. The beam line has a great advantage as both thermal and fast neutrons can be used without changing the experimental setup, allowing the additional measurement of the U235 spectrum in a thermal neutron beam. The recorded U235 spectrum is then compared to that from the ILL and thus a normalisation for the fast neutron measurement is achieved. This tech-



Figure 1: The experimental setup. The Uranium target (upper left) is placed in the horizontal beam line. The beta spectrum is recorded by a module consisting of a multiwire chamber and a plastic scintillator (lower right).

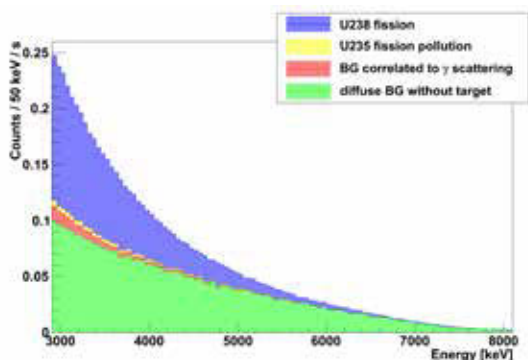


Figure 2: The beta spectrum emitted by the Uranium foil during irradiation with fast neutrons as stacked plot. The diffuse background is the main background contribution.

nique minimises all systematic errors concerning the neutron flux, beam profile, involved cross sections and detector response.

To detect the emitted electrons, a gamma-suppressing beta-telescope was designed (see fig. 1). A module providing a plastic scintillator and a photomultiplier has been developed to perform spectroscopic measurements with an energy resolution of about 8 % at 1 MeV. Since the scintillator is also sensitive to gamma radiation, a multiwire plane was included. A coincidence between the scintillator and the multiwire plane was set up, suppressing more than 99.9 % of the gamma background.

A scintillator near a reactor core

Figure 2 shows the background content and the beta spectrum. One can directly see that the main background is due to the so called diffuse events. These determine the spectrum taken with no target foil inserted – comprising all events due to diffuse neutron and gamma radiation in the vicinity of the core. This leads to a signal to background ratio equal to 1 at about 3.5 MeV, but as this event class is target independent, it can be measured accurately without introducing systematic errors. Additional background sources - determined by performing measurements on dummy targets - are subdominant and well under control.

From electrons to antineutrinos

A challenge is the conversion of the beta spectrum into an antineutrino spectrum. Here, one can make use of the fact that electrons and neu-

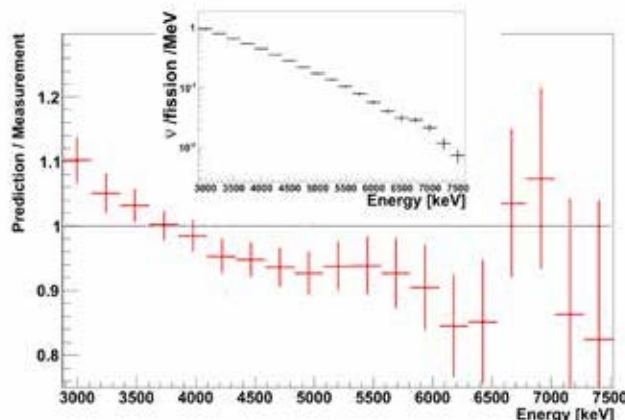


Figure 3: Inlay: The final antineutrino spectrum. As sum of thousands of beta branches, the spectrum is a featureless exponential. Main: The ratio of the measurement performed and the predictions [10]. Although there is a slight spectral deviation, the agreement is remarkable.

trinos behave in the same way as far as weak interaction is concerned. As a consequence, one effectively needs to shift the beta spectrum by the electron mass to gain the antineutrino spectrum. All remaining corrections, including the influence of the e- charge, are in the regime of 5 % [8].

In three weeks of beam time the antineutrino spectrum of the fission products of U238 in the range between 3 and 7.5 MeV was obtained. From about 3–5.5 MeV, where liquid scintillator experiments based on the inverse beta decay are most sensitive, the uncertainty achieved is in the order of only 5 %. The final results will be published in spring 2013 [9].

This measurement allows the simulations performed by various groups to be cross-checked for the first time (fig. 3.), giving valuable input to minimise the errors of reactor antineutrino experiments.

- [1] Y. Abe et al., Phys. Rev. Lett. D, 86, 052008 (2012).
- [2] F.P. An et al., Phys. Rev. Lett., 108, 171803 (2012).
- [3] J.K. Ahn et al., Phys. Rev. Lett., 108, 191802 (2012).
- [4] A. Porta et al., J. Phys.: Condens. Matter, 203, 012092 (2010).
- [5] G. Mention et al., Phys. Rev. Lett. D, 83, 073006 (2011).
- [6] K. Schreckenbach et al., Phys. Rev. Lett., 4-5, 160B (1985).
- [7] A. Hahn et al., Phys. Rev. Lett., 3, 218B (1989).
- [8] P. Vogel et al., Phys. Rev. Lett., 4, C 24 (1981).
- [9] N. Haag, PhD thesis in preparation.
- [10] Th.A. Mueller et al.: Phys. Rev. C, 83, 054615 (2011).

Using PGAA in development of the Transmutation Detector method

I. Tomandl¹, L. Viererbl², P. Kudějová³, Z. Lahodová², V. Klupák², Zs. Révay³

¹Academy of Sciences, Nuclear Physics Institute, Řež, Czech Republic

²Research Centre Řež, Řež, Czech Republic

³Technische Universität München, Forschungs-Neutronenquelle Heinz Maier-Leibnitz (FRM II), Garching, Germany

The newly proposed Transmutation Detector (TMD) method could be an alternative to, or even replace, the traditional activation detector method for neutron fluence dosimetry. To utilize all advantages of this method, one needs an isotopically highly-sensitive, nondestructive (in the sense of detector compactness as well as isotopic content), precise and standard analytical method for trace concentration determination. Prompt Gamma Activation Analysis (PGAA) seems to be a very promising method for this task. The capability of PGAA for the determination of trace concentration of transmuted stable nuclides within Ni, Au and Cu foils, which were irradiated at the LVR-15 reactor at Řež for 21 days, were tested at the PGAA facility installed at the MLZ.

Reactor dosimetry is an essential part of a nuclear safety assessment. The reactor vessel, as well as other reactor components, are continuously degraded by neutron and gamma radiation and temperature gradients. Of these factors, exposure to neutrons is the most dangerous mechanism. Thus, determination of neutron fluence in the various locations of the reactor is a very important aim of reactor dosimetry.

Neutron fluence is standardly measured using the activation detector method. To calculate neutron fluence from the activity of the irradiated activation detector, one needs to know the irradiation history. In many cases, it is difficult to reconstruct detailed information on this irradiation history. The recently suggested Transmutation Detector (TMD) method [1] can be effective without knowledge of the irradiation history. Like

the activation detector method, the TMD method uses irradiated neutron detectors. Unlike the activation method, the suggested TMD method is based on determination of the concentration of stable transmuted nuclides in the TMD dosimeters. This method does not require a knowledge of the irradiation history. On the other hand, to determine the trace concentrations of transmuted nuclides, extremely sensitive analytical methods are needed.

Prompt Gamma Activation Analysis (PGAA) is one of the prospective analytical methods for the determination of the trace concentrations of transmuted nuclides in the TMD. The sensitivity of this method varies according to the thermal neutron capture cross section of the transmuted isotope, the background signal from matrix elements, the residual activity of the transmutation detector and the general gamma-background conditions. Thus, experimental verification of the capability of PGAA to determine the trace concentration of stable nuclides within the potential materials for transmutation detectors is very important.

21 days of irradiation of detectors

Several elementary-pure materials, which might be prospective candidates for TMD detectors, were irradiated in the reactor core of LVR-15 in Řež for 21 days at a position where the total neutron fluence rate is around $2 \cdot 10^{18} \text{ m}^{-2}\text{s}^{-1}$. Taking into account thermal neutron cross sections and expected concentrations of transmuted nuclides, Ni, Cu and Au foils were selected for PGAA measurements. These measurements were performed at the PGAA facility at the MLZ. These foils were inserted into a teflon-thread target holder and irradiated by thermal neutron

TMD Element	TMD Weight (mg)	Counting time (s)	Target nuclide	Transmuted nuclide	Expected C^h (ppm)	PGAA C^{PGAA} (ppm)	γ -line energy (keV)	Counting sensitivity ¹ ($\mu\text{g}^{-1}\text{s}^{-1}$)
Ni	9.4	28 800	^{58}Ni	^{59}Ni	490	480(30)	952	0.027
			^{62}Ni	^{63}Ni	830	110(10)	1345	0.022
Cu	62	12 000	^{63}Cu	^{64}Ni	500	690(140)	1482 ²	0.00087
Au	26	25 200	^{197}Au	^{199}Hg	1.1E+04	1.1(1)E+04	368	2.3

Table 1: Comparison of theoretical and measured concentrations of transmuted nuclides. Note: Expected and PGAA concentrations, C^h and C^{PGAA} , respectively, are ratios of the number of transmuted nuclei to the total number of nuclei within target.
(¹Normalized to thermal neutron flux $1 \cdot 10^{10} \text{ cm}^{-2}\text{s}^{-1}$; ²Decay γ -line)

beam with flux $4 \cdot 10^{10} \text{ cm}^{-2}\text{s}^{-1}$ for the Ni foil and $1.5 \cdot 10^9 \text{ cm}^{-2}\text{s}^{-1}$ for the Cu and Au foils.

Comparison of PGAA results with calculation

The measured trace concentrations of transmuted nuclides were compared with calculated predictions. This comparison is presented in Table 1. The PGAA concentrations are in accordance with the calculated values. It is worth noting that the ^{199}Hg nuclid is produced from ^{197}Au by two consecutive (n,γ) processes. Unfortunately, due to interference of the most intensive secondary γ lines from the $^{198}\text{Hg}(n,\gamma)$ reaction by those from the $^{197}\text{Au}(n,\gamma)$ reaction, the concentration of ^{198}Hg in gold foil was not assigned in this experiment.

Sensitivity of PGAA method

However, by increasing the measurement time it might be possible to determine the ^{198}Hg concentration via a primary γ transition, namely 6206 keV. The simultaneous determination of the ^{198}Hg and ^{199}Hg nuclides would bring information on neutron flux at an irradiation position of TMD. The capabilities of the PGAA method to determine the trace concentration of transmuted nuclides is demonstrated by counting sensitivity in Table 1 and relative statistical errors in dependence on measurement time (fig. 1).

The counting sensitivity is related to the geometry used at MLZ and thermal neutron flux $1 \cdot 10^{10} \text{ cm}^{-2}\text{s}^{-1}$. Nevertheless, based on these numbers, a rough estimation for other facilities can be made. The error curves in fig. 1 are calculated for 21 day irradiation at the research reactor LVR-15 at Rez. With the exception of the

^{199}Hg case, these curves correspond to one- to ten-years, depending on the dosimetry position in a vessel and the type of reactor irradiation at

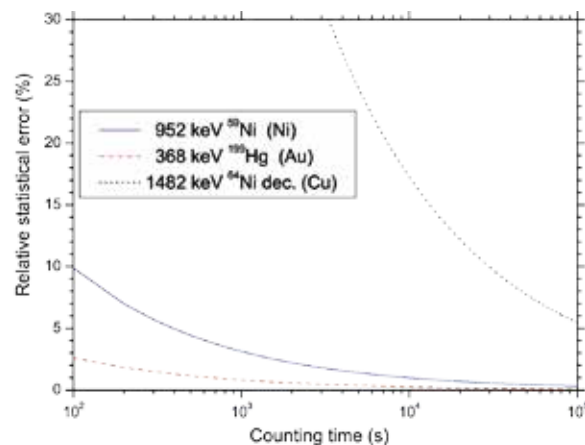


Figure 1: The dependence of statistical errors of areas on counting time for selected PGAA γ -lines originating from transmuted nuclides. The curves are normalized to 100 mg of TMD and to 21 day irradiation of TMD at LVR-15 in Rez.

nuclear power plants, where neutron fluxes are generally smaller.

It can be concluded that the PGAA method, especially for Ni-TMD, would be useable for the determination of the trace concentrations of transmuted nuclides. The transmuted nuclides in this work are mainly produced by thermal neutron capture reaction. It would be worthwhile to test other TMD materials, which would also shed some light on fast neutrons.

[1] L. Viererbl et al., Nucl. Instrum. Meth. A, 632, 209 (2011).

[2] L. Canella et al., Nucl. Instrum. Meth. A, 636, 108 (2011).

Determination of the thermal neutron capture cross section of trans-uranium actinides

M. Rossbach¹, C. Genreith¹, Zs. Revay², P. Kudejova²

¹Forschungszentrum Jülich GmbH, IEK-6: Safety Research and Reactor Technology, Jülich, Germany

²Technische Universität München, Forschungsneutronenquelle Heinz Maier-Leibnitz (FRM II), Garching, Germany

The reliability of available nuclear data for trans-uranium actinides falls far short of the requirements in many cases. Our goal is to determine the thermal neutron capture cross-sections for these nuclides with high accuracy. Actinides are radioactive, thus the neutron induced gamma radiation can be properly detected only in a high-flux neutron beam. The PGAA facility offers unique opportunities for experiments of this type. So far, Np-237 and Pu-242 nuclides have been measured in the high-flux cold neutron beam. The measurements were performed within the framework of extensive international collaboration, also supported by the BMBF.

Importance of nuclear data

Nuclear data are of great importance in nuclear research and industry. While there are many compilations and databases available world-

wide, the quality of these data falls far short of the requirements of the users. The only way to improve the reliability of these values is to re-determine them experimentally.

Trans-uranium actinides are important components of nuclear waste. The available capture cross-section data are highly unreliable (see table 1). Our main goal is to measure the thermal neutron capture cross-sections of trans-uranium actinides with high accuracy. The PGAA facility at Garching uses the strongest neutron beam in the world, which offers unique opportunities for experiments of this type.

The nuclides with long half-lives (also important components of nuclear waste) can be activated in a neutron beam with a good signal-to-background ratio, as the contribution from decay activity is relatively small. At least 1 to 10 mg per nuclide has to be irradiated depending on the respective capture cross-section. So far, a demonstration experiment has been performed in the medium-flux cold neutron beam for ²³⁷Np and ²⁴²Pu. Currently, the main emphasis is on optimization of the preparation process for reliable targets.

Determination of cross-sections

The most accurate measurement can be performed with internal standardization, when the comparator nuclide is homogeneously distributed in the sample, since this takes into account the neutron self-shielding inside the sample. This can be achieved using e.g. stoichiometric compounds such as metal chlorides or nitrates. Currently, we are using metallic gold as a very thin foil to cover the sample.



Figure 1: High-purity germanium detector with Compton-suppression system in an open lead shielding.

Nuclide	σ_n (barn) ENDF	σ_n (barn) JENDL	σ_n (barn) JEFF	Half-life (years)	Specific activi- ty (Bq/mg)
^{237}Np	180	178.1	195.8	2.144×10^6	2.61×10^4
^{239}Pu	289	271.5	272.4	2.411×10^4	2.30×10^6
^{241}Pu	360	363	363	14.290	3.84×10^9
^{242}Pu	19	19.88	18.8	3.73×10^5	1.47×10^5
^{241}Am	550	684.3	647	432.6	1.27×10^8
^{243}Am	78	79.26	76.7	7.370×10^3	7.39×10^6
^{243}Cm	130	131.4	130.2	29.1	1.87×10^9
^{244}Cm	15	15.24	10.4	18.11	3.00×10^9
^{245}Cm	360	347	359.1	8.5×10^4	6.36×10^5

Table 1: Thermal neutron capture cross-sections of a few trans-uranium actinides from different sources.

First, the detector was calibrated (see figure 1) using standard calibration sources. Secondly, the beam flux was determined using a known-mass gold foil. Then, about 10 mg of the nuclides investigated were sealed in quartz tubes. A similar set of samples was irradiated using a powder mixture of gold and the actinide oxide. All samples were irradiated in the medium- and high-flux beam of the PGAA instrument at the Forschungs-Neutronenquelle Heinz Maier-Leibnitz, FRM II in Garching.

From the detected areas of the characteristic peaks, the activities and partial cross-sections for individual gamma lines were determined after appropriate self-shielding corrections. From the decay measurement of the (n,γ) product nuclides, the total capture cross-sections were also determined.

Understanding PGAA spectra of actinides

The prompt gamma ray spectra of the $^{242}\text{PuO}_2$ and $^{237}\text{NpO}_2$ samples were evaluated using Hypermet-PC. In the gamma ray spectrum of the $^{242}\text{PuO}_2$ sample, more than 600 peaks were identified. Following subtraction of the background peaks, X-rays of Pu, the escape peaks and decay gamma rays, about 80 prompt gamma rays from ^{242}Pu were identified. The ^{241}Am isotope originates from the decay of ^{241}Pu as trace impurities in the $^{242}\text{PuO}_2$. Among the 300 peaks identified in the gamma ray spectrum of the $^{237}\text{NpO}_2$ sample, X-rays of Np and decay radiation of

^{237}Np , ^{238}Np (activation product) and ^{233}Pa (decay product of ^{237}Np), more than 100 prompt gamma ray peaks of ^{237}Np were found.

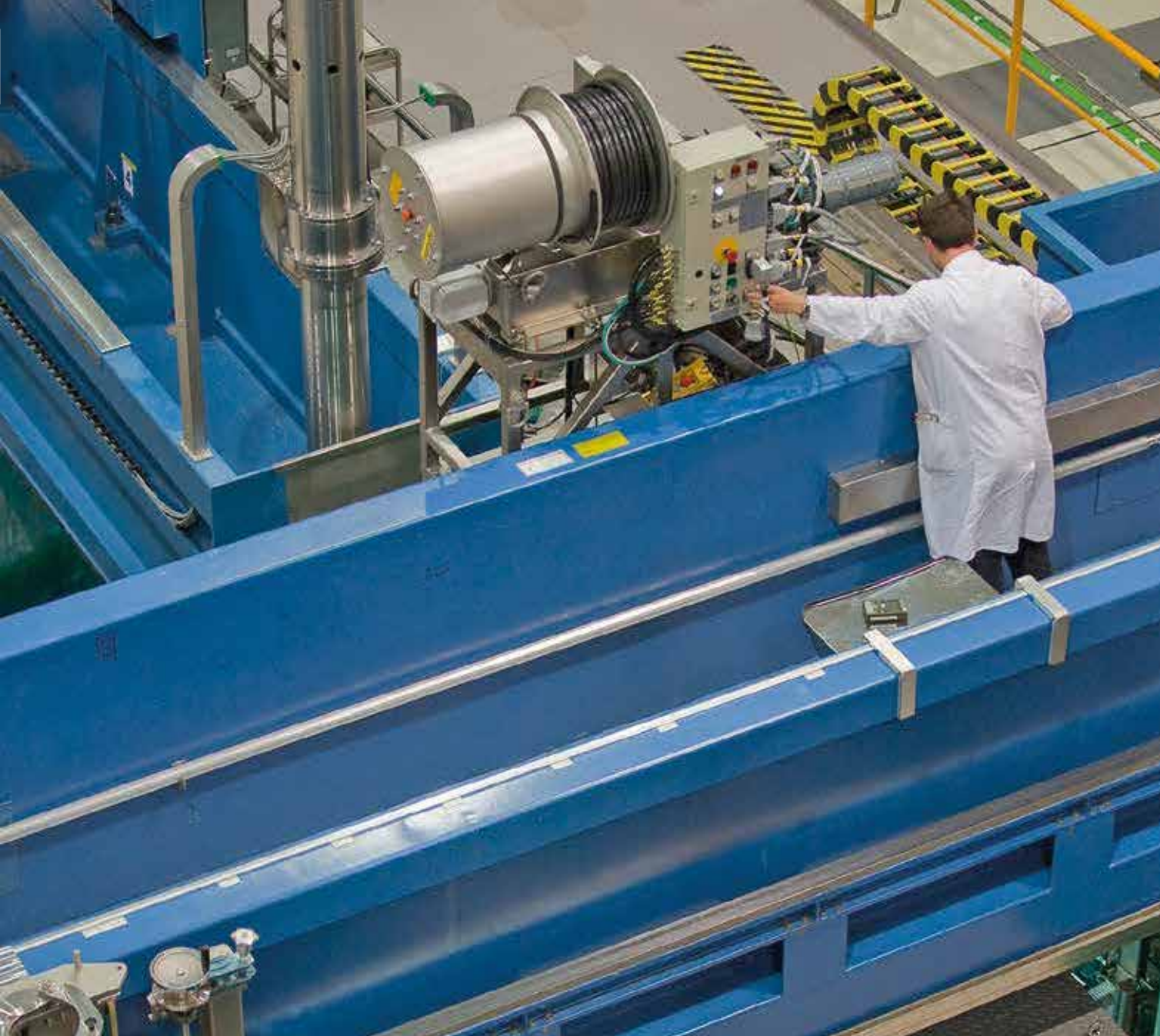
The cross-sections were determined relative to that of ^{198}Au . The thermal neutron capture cross-section value of 19.9 ± 4.0 b deduced by the 287.60 keV prompt gamma ray fits well with the existing data sets. For the ^{237}Np thermal neutron capture cross-section a value of 178.3 ± 8.0 b derived from the 1028.54 keV decay gamma ray is in agreement with existing values, with the exception of the very low value of 141.7 ± 5.4 b reported by Katoh et al. [1].

Conclusions and future plans

It can be noted that the uncertainties of the thermal capture cross-sections evaluated in this work are quite high which is basically due to uncertainties in the gamma ray emission probabilities taken from the literature. In the case of ^{237}Np , using the decay of its activation product ^{238}Np , the uncertainty of the mass determination becomes dominant and is about about 5 %. Therefore, the sample preparation procedure is under development and we hope to repeat our experiments in the near future with improved samples and deliver accurate results with uncertainties of < 5 %.

[1] T. Katoh et al., J. Nucl. Sci. Technol., 40, 559 (2003).

Reactor & Industry



4



Safe reactor operation in 2012 with 207 days of beam time for research and industrial applications

A. Kastenmüller

Technische Universität München, Forschungs-Neutronenquelle Heinz Maier-Leibnitz (FRM II), Garching, Germany

In 2012 the FRM II was safely operated in four cycles for a total of 207 days. Due to several interruptions, the planned number of 240 days of operation could not be fully achieved. The reasons for the interruptions were diverse, ranging from a scheduled short break for the exchange of a bearing at a primary pump to two automatic shutdowns due to voltage fluctuations in the external power grid of the neutron source, probably caused by thunder storms. In addition a postponement of the restart of the reactor was requested by the science division owing to essential repairs to damaged neutron guides and a gas exchange required in a beam tube due to the new installation of the positron source NEPO-MUC. The last cycle in 2012 had to be interrupted to investigate noticeable values of ^{14}C in the exhaust air during the year. Besides routine reactor operation, including various maintenance activities, numerous construction projects were started, have been completed, or are still ongoing. The connection between the reactor building and the neutron guide hall east and initial work on the latter pave the way for the exciting research that lies ahead.

Safety standards sustained and even enhanced
The FRM II delivered nuclear energy totalling 4144,76 MWd in the year 2012. In all, 207 days of beam time were available for use in research, industry and medicine. A total of 1822 periodic testing, operability checks, inspections by independent experts from the regulatory body covering different subject areas and upkeep and maintenance measures as well as 68 modifications to the facility that had to be referred to the regulatory body guaranteed that the high safety standard of the neutron source FRM II was sustained and even enhanced. There was no incident that needed to be reported during 2012.

^{14}C emission below maximum permissible value
It was possible to offset most of the interruptions and the postponed restart by curtailing the maintenance period that followed, which was achieved thanks to heightened commitment on the part of the staff of the reactor operations division. A considerable reduction in operating days, however, was the 27-day interruption of the 30th cycle from 9th November to 6th December 2012. This was not caused by a direct technical requirement, but was undertaken as a precautionary measure to allow for a detailed investigation of the reason for increased values of ^{14}C emission detected in the exhaust air in the first and third quarter of 2012. The cycle was interrupted after prior consultation with the regulatory body, the Bavarian Ministry of Environmental and Health Affairs (StMUG). On 6th December, the reactor of the Forschungs-Neutronenquelle Heinz Maier-Leibnitz (FRM II) was restarted. At that time, it was predicted after additional monitoring of ^{14}C -emission that the annual emissions of ^{14}C in the exhaust air would be below the maximum annual permissible value, as in the previous years.



Figure 1: Ion exchange filter of the heavy water system with a heating jacket for the drying of the ion exchange resins.

The partially increased emission of ^{14}C in the first and third quarter of 2012 as compared to previous years was due to more frequent drying of the ion-exchange resins that are used to clean the heavy water in the moderator system (fig. 1). In future, the ^{14}C emissions can be reduced by the simple chemical separation of CO_2 in the exhaust air.

Even though ^{14}C -emission in the range of the annual permissible value would have had no relevant radiological impact on the environment, shortly before the scheduled shutdown of the reactor on 21st December 2012 the issue resulted in it being taken up in the media in numerous press releases.

Several instruments in an implementation phase
Besides the routine operation of the neutron source, longer planned or already ongoing projects for the reconstruction and expansion of instruments reached the implementation phase and will soon be available for scientific use.. Examples include the positron source NEPOMUC, where the beam tube SR11 including the experimental tube was successfully replaced, and the neutron imaging facility ANTARES, which was reconstructed at beam tube SR4a. NEPOMUC could already start operation again at the end of 2012, ANTARES will be available to users in 2013.

Construction work in the neutron guide hall east
Even construction work to expand the experimental areas on the east side of the reactor building by a connection with the neutron guide hall east has been started with the pouring of the first concrete of the ground slab of the building struc-



Figure 2: Removal of the flywheel for the exchange of a bearing at a primary pump.



Figure 3: Construction works for the connection between the reactor building and the neutron guide hall east.

ture (fig. 3). Furthermore, two cavities in the floor of this hall for the new multi anvil press SAPHiR and the experiment nEDM were completed in 2012. This work will be continued in 2013 and includes the construction of the entrance area in the northern section of the hall and the installation of the building structure between the reactor building and the neutron guide hall east.

The project for the development and installation of an additional secondary source for the production of ultra cold neutrons in beam tube SR6, for which a license request to the regulatory body had already been made in 2009, continued with the further installation of the necessary technical infrastructure, such as laying pipes for the helium circulation system of the cryogenic installations.

Preparations for new workshop and laboratory buildings

The medium term planned construction of a workshop and a laboratory building, both of which will include additional office space, requires preparatory steps such as the clearing of the construction site by removing cables and pipes or the construction of a man-sized underground conduit for new piping and cables. Although the new buildings are not part of the reactor itself and the construction not subject to nuclear administrative procedures, the preparation as well as the future construction phase have to be carried out in close collaboration with the reactor operations division.

Progress in reactor conversion and fuel development

High-density fuel development group

Technische Universität München, Forschungs-Neutronenquelle Heinz Maier-Leibnitz (FRM II), Garching, Germany

As in past years, the working group "Hochdichte Brennstoffe" (high density fuels) continued their efforts to develop a solution for a timely conversion of FRM II to a fuel with lower enrichment. The primary candidate for this fuel is a Uranium-Molybdenum alloy, in disperse and monolithic form.

theoretical basis which strengthens the observed experimental results and interpretations [1]. The convincing results obtained serve to contribute positively to the growing international acceptance of the method. For example, samples of the Korean working group KAERI and the European LEONIDAS project were already irradiated and characterized in 2012.

Heavy ion irradiation

The working group has for quite some time used heavy ions to simulate the in-pile behaviour of nuclear fuels at the Tandem accelerator. This method has now been augmented with a solid

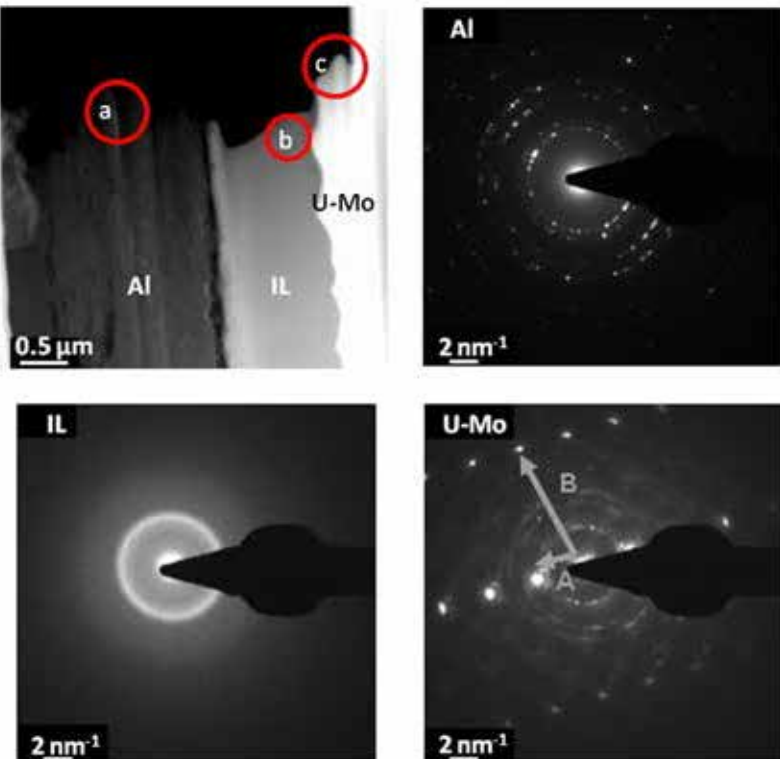


Figure 1: Left-top: Overview of layer structure. Right-top: Electron diffraction pattern of polycrystalline Al substrate. Left bottom: Amorphous IDL. Right bottom: Single grain UMo.

Amorphous interdiffusion layer

In another series of irradiation tests, it was shown for the first time that the interdiffusion layer (IDL) between UMo and Aluminium, which has been deemed responsible for a number of failures in in-pile experiments, can also be reproduced in its amorphous form with heavy ions (fig. 1) [2]. The appearance of this layer is considered a major weak point of UMo fuels and is therefore the focus of the international scientific efforts. By coating the UMo with additional materials that do not interact with the surrounding aluminium, great progress was made towards precluding the formation of this layer and retaining the fission gases in the grains or the monolithic UMo.

Full core calculations

In the field of full core calculations, a very progressive, but conservative study for the conversion of FRM II was presented to an international audience in March 2012. The fuel element design is based on disperse UMo and requires a clearly reduced enrichment of only 30 % [3]. No changes to control and safety rod systems are required. In addition, cooling circuits, pumps and other installations do not require major changes. The element would reach the same cycle length of 60 days at full reactor power of 20 MW. This is achieved by elongating the fuel plates, using a thicker fuel meat and slightly increasing the outer element

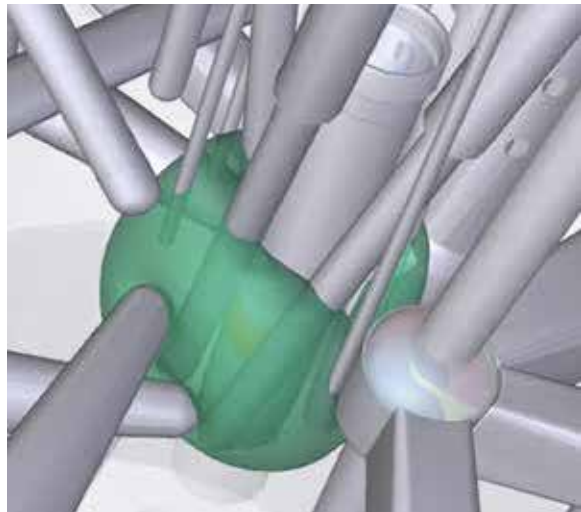


Figure 2: Reactor core in the cloud of thermal neutrons (green isosurface). The cold source is shown in blue.

diameter. The latter would become possible if the material of the central channel were changed to Zircaloy. This would allow for the necessary thinning of the tube as the outer diameter of the central channel must not be changed. Nevertheless, such a change in material remains uncertain, as well as the qualification of the necessary high density fuel of 8 g/cc in the UMo fuel meat.

Thermal hydraulic aspects

In an additional study, it was shown that there is no necessity to increase the total length of the fuel element, even if the length of the plates is changed as described above and the inlet path for the water flow at the element entrance is shortened.

A second study addresses the fact that, unlike theoretical models, fuel plates are seldom perfect in reality. To account for this, a series of simulations was carried out to quantify the impact of bonding faults between cladding and fuel on the thermal hydraulics of the fuel elements [4]. It turned out that fuels with lower thermal conductivity, e.g. UMo are generally slightly more sensitive to such non-bonds than those with higher thermal conductivity, e.g. $\text{U}_3\text{Si}_2/\text{Al}$ which is currently used at FRM II.

In order for the thermal conductivity of the fuel to be correctly incorporated into models for reactor

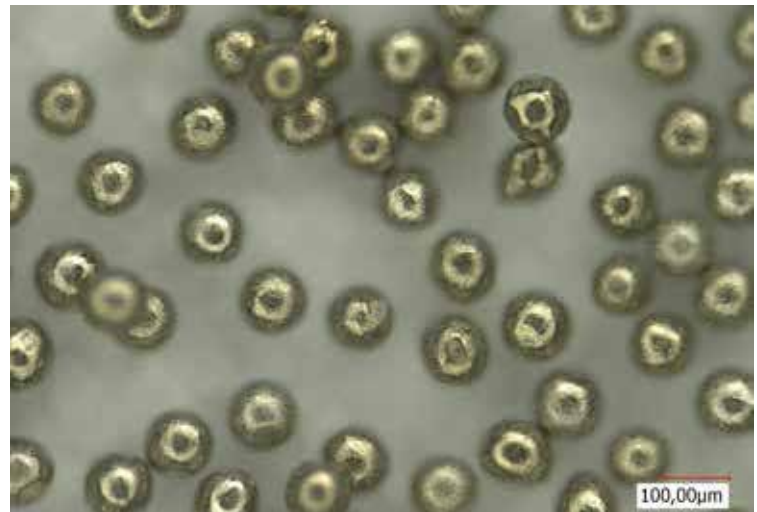


Figure 3: Atomized stainless steel.

calculations, measurements were performed on fresh and on irradiated fuel, in collaboration with the Idaho National Lab. Within the framework of the cooperation, the Scanning Thermal Diffusivity Microscope (STDM) was used, a new method with extremely high spatial resolution.

Atomized powder production at CERCA

In collaboration with CERCA, the working group has developed a device to produce atomized Uranium-Molybdenum powder. Such a powder has been used in a considerable number of test irradiations and is a promising candidate for the final fuel choice. An appropriate European production capacity is therefore considered to be one of the key steps in the necessary industrialisation of the fabrication process. The development, construction and operation of the manufacturing equipment on a trial basis are close to completion and will be finished in 2013. First experiments with a surrogate material (stainless steel) showed spherical and oxide-free powder of the desired size (fig. 3) [5].

[1] A. Heldmann, Bachelor thesis, TUM (2012).

[2] H.-Y. Chiang, T. Zweifel, J. Nuc. Mat. (2013), accepted.

[3] A. Röhrmoser, RRFM 2012, Prag (2012).

[4] H. Breitkreutz, RRFM 2012, Prag (2012).

[5] R. Schenk, RRFM 2013, St. Petersburg (2013)

Manufacturing of cylindrical LEU Mo-99 targets by sputtering

T. Hollmer, B. Baumeister, C. Steyer, W. Petry

Technische Universität München, Forschungs-Neutronenquelle Heinz Maier-Leibnitz (FRM II), Garching, Germany

Looking to the future production of molybdenum-99, the FRM II is also investigating an alternative target design, the cylindrical LEU target. Its main advantages are higher uranium density compared to current target designs and more cost-effective processing after irradiation. The FRM II is currently developing a novel manufacturing process for such a target, which is based on the direct coating of the target with uranium instead of using prefabricated foils. This leads to better thermal properties and lower manufacturing costs.

Molybdenum-99 and conversion to LEU

The decay product of molybdenum-99 (Mo-99), technetium-99m (Tc-99m), is the most widely used diagnostic medical isotope. It is used for a variety of medical investigations such as the detection of diseases or the study of organ structures and functions. Tc-99m decays to Tc-99 by emission of a 140keV photon, which can be de-

tected by scintillator devices and thereby used for medical imaging.

The main production route of Mo-99 is the nuclear fission of uranium-235 (U-235). Approximately 6 % of its fission products result in Mo-99. Currently, production involves irradiating small amounts of highly-enriched uranium (HEU) in an intense neutron flux. Due to proliferation concerns, a great deal of effort has been made in recent years to convert the production to low-enriched uranium (LEU, enrichment below 20 %).

The reduction in enrichment leads to a lower particle density of U-235 and an increased neutron capture due to U-238. One approach to compensating for this is to increase the total uranium in the irradiation targets, which can be achieved by using pure metallic uranium foils instead of a uranium dispersion in aluminum. One important advantage of metallic uranium is its mechanical separability from the cladding material after irradiation. This results in significantly less highly radioactive waste and, therefore, lower production costs.

The cylindrical target

A promising target design is the cylindrical target, which was developed by Argonne National Laboratory (ANL) together with other institutes (fig. 1). This target consists of a thin metallic LEU foil (approx. 130 µm thick) wrapped in a diffusion barrier (e.g. nickel), which is then encapsulated between two concentric aluminum cylinders. It is approx. 160 mm in length and has an outer diameter of approx. 30 mm.

The cylindrical design guarantees good structural integrity and heat transfer. The diffusion barrier



Figure 1. Sectional drawing of a cylindrical Mo-99 target.

prevents bonding of the uranium and the cladding made of aluminum during irradiation and, therefore, allows easy disassembly of the target afterwards [1].

Currently, the foils used in these targets are either produced by hot and cold rolling (Argonne National Laboratory) or by a direct casting method (Korea Atomic Energy Research Institute). Both methods have their specific assets and drawbacks. The rolling process is labor intensive, but is able to produce foils of high and homogenous quality. The direct casting method, on the other hand, is economical but the foils produced show surface irregularities and an uneven thickness [2, 3].

Direct coating technology

Based on our experience of coating uranium [4] we are currently investigating a third way of producing cylindrical LEU targets. Our approach is the physical vapor deposition (PVD) of the diffusion barrier and the uranium directly on the inside of the outer aluminum cylinder. In this way, the material is evaporated by the bombardment of argon ions from a glow plasma discharge.

This process offers several advantages over the traditional methods. Due to the sputtering geometry, the uranium sputter target will be almost fully utilized. This, together with the elimination of a preceding foil production step, will lead to lower manufacturing costs. Given an adequate sputtering reactor, it is possible to apply coatings of uniform thickness and establish good thermal contact between the layers. This meets the essential safety requirements for these targets.

Project status

The challenge here is the small geometry of the target, which is far below conventional PVD set-ups. This made it necessary to develop a completely new sputtering reactor. To this end, several concepts were developed and thermal and electromagnetic simulations were performed. The most promising concept is currently set up in a test assembly. The ongoing tests show very



Figure 2. Inside of a copper-coated target cylinder.

promising results. First targets were successfully coated with copper, as a non-radioactive surrogate (fig. 2). Currently, the process parameters are optimized to achieve the desired layer properties in a reasonable coating time.

Based on the results obtained using surrogate materials, a final sputtering reactor will be installed in our uranium laboratory within the year. The reactor will be built in an argon glove box, which allows for safe handling of uranium under condition of the highest purity.

1. National Research Council, The national academic press, Washington D.C., p. 92 (2009).
2. T.C. Wiencek, RERTR 2008, Washington, D.C.(2008).
3. A. Bakel, RERTR 2008, Washington, D.C., (2008).
4. W. Schmid, PhD thesis, urn:nbn:de:bvb:91-diss-20110816-1081597-1-6, TUM (2011).

Facts & Figures

5



Events 2012: Workshops, meetings, courses and open day

R. Bruchhaus¹, R. Georgii², R. Gilles², K. Griewatsch³, M. Hofmann², J. Krüger², I. Lommatzsch², A. Michels⁴, P. Riedel², A. Voit², R. Zorn¹

¹Forschungszentrum Jülich GmbH, Jülich Centre for Neutron Science at MLZ, Garching, Germany

²Technische Universität München, Forschungs-Neutronenquelle Heinz Maier-Leibnitz (FRM II), Garching, Germany

³Christian-Albrechts-Universität zu Kiel, Komitee Forschung mit Neutronen, Kiel, Germany

⁴University of Luxembourg, Laboratory for the Physics of Advanced Materials, Luxembourg

User Meeting 2012

Jointly organized by the FRM II and the JCNS, the 4th User Meeting was held in Garching on March 23rd (fig. 1). The last User Meeting in October 2010 marked the shut-down of the reactor and the start of the long maintenance break. Despite there having been only a few months of beamtime, the User Office received more than 100 registrations for this one-day event. Thirteen contributions were chosen for oral presentation and showed the wide range of science performed or planned at the MLZ.



Figure 1: Despite the long maintenance break, more than 100 users gathered in March for the 4th User Meeting.

Dr. Flavio Carsughi from the User Office welcomed the participants and pointed out the large number of upgrades at the instruments. Bio-Diff and MARIA became available for users and were presented in the poster session. While the second part of the day was dedicated to the instruments hosted at the MLZ as well as sample environment groups, software development and planned instruments, the first part dealt with scientific projects and show-cased the whole range of neutron scattering applications.

VDI-TUM Expert Forum

Presenting various examples of well-established as well as more recent methods of non-destructive testing in an industry related field, the 4th Expert Forum organized by VDI and TUM attracted more than 60 participants on April 17th (fig. 2 and 3). Eight highly respected experts from industry and research had been invited by the advisory board for Application Oriented Non-destructive Materials and Component Testing of the VDI, which was introduced by Achim P. Eggert.



Figure 2: Dr. Ralph Gilles (2nd f.l.) and Dr. Michael Hofmann (2nd f.r.) in discussion with a participant at the VDI-TUM Expert Forum.

During the one-day meeting chaired by Dr. habil. Ralph Gilles (FRM II), the different methods for non-destructive testing were presented. In the final panel discussion chaired by Prof. Dr. Winfried Petry, the lack of correlation between data and material properties for some of the methods was discussed. At the close, the participants were invited to visit the experimental facilities of the MLZ. The presentations can be also found at www.frm2.tum.de (see "Events").



Figure 3: The 4th VDI-TUM Expert Forum on non-destructive testing attracted more than 60 participants at the faculty of mechanical engineering.

Practical training for TUM students

Due to the reactor shutdown in the last cycle of 2012, there was only one practical training in neutron scattering for TUM students in summer 2012. A total of 17 students from the Bachelor and Master courses participated in this part of the “Fortgeschrittenenpraktikum” offered by the Physics Department. Additionally, there were eleven students from the “Werkstoff-Praktikum” of the Faculty of Engineering.

After a half-day of introduction to the FRM II and the theory of neutron scattering, each student performed two different experiments out of 13 participating instruments (HEIDI, JNSE, KWS-2, MIRA, PGAA, PANDA, PUMA, RESI, RESEDA, SPHERES, SPODI, Stress-Spec and TOFTOF). The experiments were adapted from standard user experiments typical of the physics investigated at these instruments. The experiments lasted a day each, including overnight measurements. In addition, a guided tour through the reactor was offered. Finally, the students were required to write a short report on their results for presentation in a short colloquium.

A short questionnaire showed the response of the students to be very enthusiastic. Their main highlight was the possibility of working on “real” user experiments in normal operation as opposed to standard demonstration experiments.

Workshop Micromagnetic Theory & SANS

From June 21st to 22nd, the Workshop on Micromagnetic Theory & SANS was held at the MLZ to discuss the state-of-the-art in the field with experimentalists and theorists. Dr. Andreas Michels (University of Luxembourg) gave an overview talk on magnetic SANS on nanomagnets. The basics of micromagnetism were introduced by Dr. Dmitry Berkov and Dr. Sergey Erokhin (both INNOVENT), followed by a talk by Dr. Frédéric Ott (CEA/CNRS). Prof. Ted Forgan (University of Birmingham) described the possibilities to explore new areas for the interaction of high magnetic fields with superconductors, magnetic materials and colloids in liquid suspension. Dr. Anna Sokolova (ANSTO) introduced the new time-of-flight SANS instrument BILBY, while Dr. Kathryn Krycka (NIST) reported on recent developments regarding SANS polarization analysis at NIST. The second day focused on spin structures: Dr. Sebastian Mühlbauer gave a seminar on ferromagnetic correlations of the almost anti-ferromagnetic helimagnet $\text{Ba}_2\text{CuGe}_2\text{O}_7$, Prof. Dr. Christian Pfleiderer spoke about the emergent electrodynamics of skyrmions in chiral magnets, and Jonas Kindervater explained how spherical neutron polarimetry can be used to study the transition from heli- to paramagnetism in MnSi. The day was rounded off by a talk by Dr. Artem Feoktystov (JCNS) on the SANS analysis of magnetic fluids using contrast variation.

16th JCNS LabCourse

The 16th JCNS Laboratory Course on Neutron Scattering took place from September 3rd to 14th. As in the previous years, this annual lab course was held at two locations: at the Forschungszentrum Jülich for the lecture element and at the FRM II for the experiments (fig. 4). The lab course is open to students of physics, chemistry and other natural sciences from all over the world. The first week is dedicated to lectures and exercises encompassing an introduction to neutron sources and presenting scattering theory and instrumentation. Furthermore, selected topics in condensed matter research were addressed. In the second week, eleven instruments at MLZ were made available for student training, including the neutron spin-echo spectrometer J-NSE, the backscattering spectrometer SPHERES and the small-angle scattering instruments KWS-1 and KWS-2. This year 59 students were selected from 143 applicants, 37 % being women. Since the performance of the neutron source was flawless, experiments could be carried out over all five days. The programme was completed by a welcome party in Jülich and a farewell party in Garching. The next JCNS laboratory course will take place from September 2nd to 13th, 2013; more details on www.neutronlab.de.



Figure 4: Students during the 16th JCNS Lab Course on Neutron Scattering concentrated on adjusting a sample.

26th TANGO Collaboration Meeting

The 26th TANGO Collaboration Meeting was organized by the FRM II for the first time and was held in Herrsching from September 25th to 27th. The meetings are open to everybody interested in using TANGO (a distributed network based instrument control system) including commercial companies, and they are organized alternately by one of the members of the TANGO group. Its members signed a Memorandum of Understanding which deals with the aspects of the collaboration. The European Synchrotron Radiation Facility (ESRF) and some national Synchrotron sources such as SOLEIL (France), Elettra (Italy), ALBA (Spain), DESY (Germany), MaxLab (Sweden), and SOLARIS (Poland) as well as the FRM II belong to this group.

The around 30 participants informed each other of the current state of use at their facilities and their plans for the future. The current developments in the TANGO core libraries, and of tools which could be of interest to others were also presented. After fruitful and lively discussions on the shores of lake Ammersee (fig. 5), 20 participants took the opportunity to tour the FRM II at Garching and were really impressed by the technique and scientific experiments hosted there.



Figure 5: Participants at the TANGO Collaboration Meeting during a guided tour of Andechs Monastery.



Figure 6: In the charming location of the Protestant Academy Tutzing at Lake Starnberg, 75 highly motivated attendees from Europe, USA and Japan had numerous interesting discussions during the JCNS Workshop on Soft Matter and Biophysics.

JCNS Workshop on Soft Matter and Biophysics

The JCNS and the Donostia International Physics Center (DIPC), Spain, jointly organized the 2012 workshop “Trends and Perspectives in Neutron Scattering for Soft Matter and Biophysics” held in Tutzing, Germany, from October 8th to 11th. 75 attendees took part in this event which featured 42 presentations and 16 posters. The combination of the conference’s charming location at the Protestant Academy Tutzing in conjunction with the highly motivated attendees from Europe, USA and Japan (fig. 6) created a stimulating atmosphere which resulted in numerous interesting discussions throughout the workshop (fig. 7).

Topical sessions such as Advanced Instrumentation for Soft Matter Research, Physics of Life, Soft Materials for Energy, Kinetic Processes, Sustainable Polymers, Functional Materials, Synergies between Neutrons and Simulation and Nanostructured Systems formed the basis of the workshop. Soft matter materials were described as key enablers for future renewable energy sources and biofuels.

It was clearly demonstrated that even for very complex systems, modelling is becoming more and more important to fully exploit neutron scattering experiments and deepening our basic understanding. Rapid progress in the field of soft matter research and biophysics results in an ever

increasing challenge to extend the limits of existing neutron instrumentation and to start building specially-adapted high performance instruments at both existing and future neutron sources such as the European Spallation Source (ESS). JCNS and the Institute of Complex Systems (ICS) contributed a total of eight oral presentations and eleven posters, underlining the key role of JCNS in neutron scattering-based soft matter research and advanced instrumentation. The next JCNS workshop will focus on magnetism and will be held in Tutzing from October 7th to 10th, 2013.



Figure 7: Dr. Oxana Ivanova (l.) and Dr. Noémi Székely at the JCNS Workshop in Tutzing.



Figure 8: The session on the scientific perspectives of the new European Spallation Source (ESS) was a highlight at the German Conference on Neutron Scattering held in Bonn.

German Conference on Neutron Scattering 2012

Research using neutrons was the common ground for 170 scientists from different disciplines to gather at the German Conference on Neutron Scattering in Bonn from September 24th to 26th. Scientists from particle and condensed matter physics, chemistry, biology, materials sciences, engineering sciences, right up to geology and cultural heritage used the opportunity to present their results, to exchange ideas and to gather methodological inspiration.

The meeting was organized by the JCNS at the Forschungszentrum Jülich on behalf of the German Neutron Research Committee (KFN). The session on the scientific perspectives of the European Spallation Source (ESS) to be built in Sweden was a real highlight of the conference and clearly demonstrated how powerful neutron research is and how much it will benefit from the unprecedented advances offered by the ESS (fig. 8). In recognition of this, the KFN awards the Wolfram-Prandl-Prize to young researchers using neutrons for their studies. This year, Dmytro Inosov from the Max Planck Institute (MPI) for Solid State Research in Stuttgart received the prize for his outstanding work on high-temperature superconductors.

Open Day 2012

At the traditional Open Day at the Campus Garching, held this year on October 27th, the visitors again showed great interest in a tour of the FRM II. A long queue formed at the registration desk, and by the early afternoon all tours were fully booked (fig. 9). Again, 500 participants took advantage of the opportunity. In additional presentations in the neighbouring Physics Department, the audience was able to learn more about the scientific issues researchers are dealing with at the neutron source: PD Dr. Christoph Hugenschmidt talked about materials research using



Figure 10: Dr. Anton Kastenmüller during his talk at the open day.



Figure 9: This year again, visitors to the open day were queuing at the registration desk for a tour of the FRM II. 500 participants took advantage of the opportunity.

anti-particles, Franz Michael Wagner explained tumour treatment using fission neutrons, Dr. Heiko Gerstenberg reported on the status of the Tc-99 project, Dr. habil. Ralph Gilles presented the projects related to industry at FRM II, technical director Dr. Anton Kastenmüller talked about the history, construction and exploitation of the research neutron source (fig. 10), Prof. Dr. Peter Fierlinger gave a talk on physics with ultracold neutrons and the deputy scientific director, Dr. Jürgen Neuhaus, presented new scientific findings on fatigue processes in conventional Li-ion batteries.

ExzellTUM at electronica

From November 12th to 15th, the FRM II members of the battery project ExZellTUM, together with the project coordinator Dr. habil. Ralph Gilles, presented the benefits of neutrons for battery research at the international trade fair for batteries, energy storage and innovative production ees, a special exhibition within the electronica trade show at Messe München (fig. 11). The FRM II booth was part of a joint presentation of the ExzellTUM project of the TUM organized by one of the partners, the Institute for Machine Tools and Industrial Management (iwb).



Figure 11: Visitors showed lots of interest in the ExZellTUM project presented at the electronica trade show at Messe München.

User Office: Growing together

F. Carsughi¹, I. Lommatzsch², R. Bucher², U. Kurz², M. Neuberger², B. Tonin²

¹Forschungszentrum Jülich GmbH, Jülich Centre for Neutron Science at MLZ, Garching, Germany

²Technische Universität München, Forschungs-Neutronenquelle Heinz Maier-Leibnitz (FRM II), Garching, Germany

The User Office pulls the strings behind the scenes when it comes to the organization of the scientific use of the neutron research source FRM II. It handles the proposal rounds and takes care of everything scientists visiting the neutron source in the course of their work have to deal with. For example, it informs users of the dates of their experiments, explains the necessary preparations for each visit, and issues letters of invitation for the purpose of visa applications. The visitors' service books hotel rooms if required and even bicycles can be loaned - rest assured that we are happy to give you some tips on recreational pursuits if desired!



Figure 1: Listening to one of the interesting talks at the User Meeting.

4th User Meeting

The 4th User Meeting took place at the FRM II on 23rd March. It was jointly organised by the FRM II and the JCNS and attracted more than 100 participants. This was remarkable in as much as this User Meeting was the first after the long maintenance break: The reactor restarted on October 29th, 2011 – so just five months had elapsed! The User Office was not sure if its invitation would



Figure 2: Discussions among colleagues at the User Meeting.

be taken up. The previous User Meeting had been held in October 2010, marking the reactor's shutdown and the start of the long break. Then, the main emphasis had been placed on user projects and experiments at the MLZ. This time, the instruments and their upgrades were the centre of attention. The opportunity had been seized to improve several aspects of almost all. Moreover, the sample environment groups as well as the software development groups presented their novel features. All in all the meeting was a great success once more and everybody enjoyed the talks, posters, and - last, but not least - the Bavarian beer during the lively discussions in the evening!

First joint review panels' meeting

The review panels – we have been fortunate in being able to recruit internationally renowned experts for this important task - meet twice a year to review the proposals submitted. The decision has always been made based solely on the scientific merit of the individual proposal. This guarantees the high quality of the FRM II's usage. Not only at the FRM II has this standard been a natural course of action, but this has also been



Figure 3: The referees' dinner at a typical Bavarian restaurant.

the case at the Forschungszentrum Jülich and at the Helmholtz-Zentrum Geesthacht (HZG) until their reactors were turned off in 2006 and 2010, respectively.

Many instruments made their way from Jülich to Garching and found a new home at the FRM II, operated by the outstation JCNS. Whereas the proposals submitted for experiments at the instruments operated by the HZG at the FRM II were reviewed by the FRM II panels, JCNS still kept their own panels. This came to an end with the last proposal round in 2012. It took some time to amalgamate all panels, but at the moment there are six common panels, lead by a chair person who is assisted by a secretary. Currently, the panels are divided into the following sections:

- Biology
- Imaging Analysis; Nuclear and Particle Physics
- Magnetism and Spectroscopy
- Materials Science
- Soft Matter
- Structure Research

Another innovation was the relocation of the biannual meeting from the site of the FRM II to a conference centre in Ismaning, close to Garching. Due to the heavy workload, the meeting was prolonged to two days. This offers further possibility for discussion during the dinner in a typical Bavarian restaurant in the evening.

During the final discussion, the panels' chair-

persons praised the efficiency of the new structures. In particular, the easier exchange between the individual panels and the fruitful discussions among themselves helped to improve the working environment.

Booth at the DN

This time, the German Conference on Neutron Scattering was organized by the Forschungszentrum Jülich and took place in Bonn. Besides the interesting talks and fruitful discussions during the poster sessions, there was in addition always a place to meet: The booth of FRM II, JCNS and HZG. The User Office was happy to organize this and provided all the information users and users-to-be could possibly need. Brochures and flyers as well as the latest newsletter were distributed to those visitors who were interested.

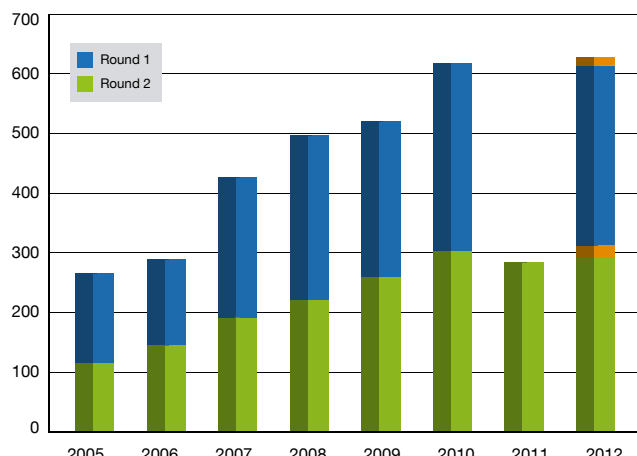


Figure 4: Proposals submitted since 2005. Orange: Proposals for instruments at SNS and ILL.

Statistics

In 2012, the reactor delivered 207 days of beam time for scientific experiments, industrial applications, and medical treatment. Due to several problems, the aim of 240 days could not be achieved.

In the first proposal round of 2012, a total of 292 proposals was submitted. The JCNS instruments at SNS and ILL attracted 20 proposals. For the second round, we received 302 proposals requesting beam time at instruments hosted in Garching and 17 proposals for the JCNS instruments abroad.

Visitors' service and public relations: Between science and safety

U. Kurz¹, P. Riedel¹, B. Tonin-Schebesta¹, A. Voit¹, A. Wenzik²

¹Technische Universität München, Forschungs-Neutronenquelle Heinz Maier-Leibnitz (FRM II), Garching, Germany

²Forschungszentrum Jülich GmbH, Jülich Centre for Neutron Science, Jülich, Germany

The primary task of the press office of the FRM II is to draw attention to the scientific and social importance of the facility. Tours of the FRM II therefore offer a unique opportunity to emphasize the scientific value of the FRM II to the public. By contrast, safety issues are far more the province of the media: Last year, these issues were brought to prominence by the nuclear incident in Fukushima. At the end of this year, the C-14 issue temporarily focused a great deal of media attention on the FRM II.

The opportunity to participate in a tour of the FRM II is one of the important pillars of public relations at the FRM II. This year, as many as 2740 people came to visit the FRM II, more than half of them pupils and students (fig. 1). It is a unique chance to demonstrate the key scientific value of the FRM II and to inspire confidence regarding the safe operation of the neutron source. Once again, the traditional Open Day held at the Garching Campus on 27th October, the tours were fully booked, with 500 people taking part. Since

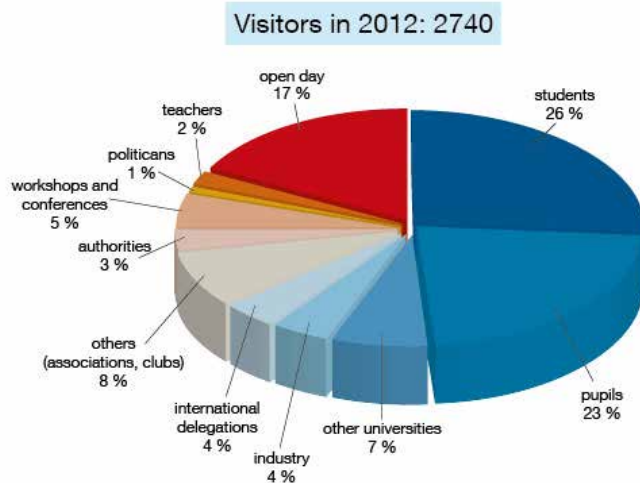


Figure 1: A total of 2740 visitors enjoyed a guided tour of the FRM II in 2012, more than half of them pupils and students.

the visitors' service has a preference for organizing tours for school and university groups, the Open Day is always a good opportunity for those who have not been able to take part in these arranged visits.

Science Café & "Garchinger Herbsttage"

In autumn, the Research Neutron Source Heinz Maier-Leibnitz (FRM II) participated for the first time in the well-established and highly successful event Cafe & Kosmos organized by the Universe Cluster, the European Southern Observatory and three Max Planck Institutes. Scientists present their research projects in a relaxed atmosphere and without technical support – for the price of a cup of coffee or a glass of wine. On September 11th, Prof. Dr. Peter Fierlinger from the Universe Cluster discussed with participants why ultra-cold neutrons can unravel the mystery of antimatter, and on October 9th, PD Dr. Christoph Hugenschmidt talked about cosmic positron sources and the benefit of positrons in materials research (fig. 2 and 3). The local pub Vereinsheim in Schwabing was fully packed with some 70 participants and each presentation was followed by a long discussion.

Every three years in mid-September, the trade show "Garchinger Herbsttage" featuring local companies and businessmen is held in Garching. Traditionally, the FRM II is also present in a very prominent booth at the entrance to the community center. In order to increase the attractiveness of the stand and make it easier to establish contact with the audience, the FRM II presented a new throwing game for children. With balls, "free neutrons", they could try to hit the target, the "nuclei" of a NaCl crystal lattice. The throwing game was a great success and we

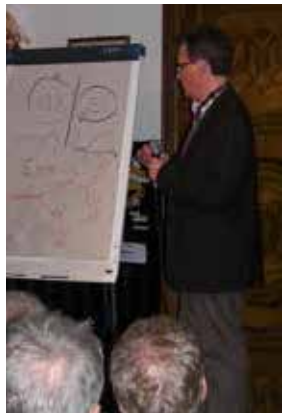


Figure 2 and 3: Café & Kosmos: Prof. Dr. Peter Fierlinger and PD Dr. Christoph Hugenschmidt during their talks at 'Vereinsheim' in Schwabing. On both evenings, the local pub was fully packed with about 70 participants.

actually ran out of 'first prizes' – FRM II T-shirts – on the second day!

Panoramic view of the reactor hall

In October, thanks to the great support of the technical operation unit, the long prepared 350 degree panoramic exposure of the reactor hall could be filmed by a specialized photographer. Earlier this year, the team already filmed the neutron guide hall – and the experimental hall is planned to be recorded in 2013. The photoshots

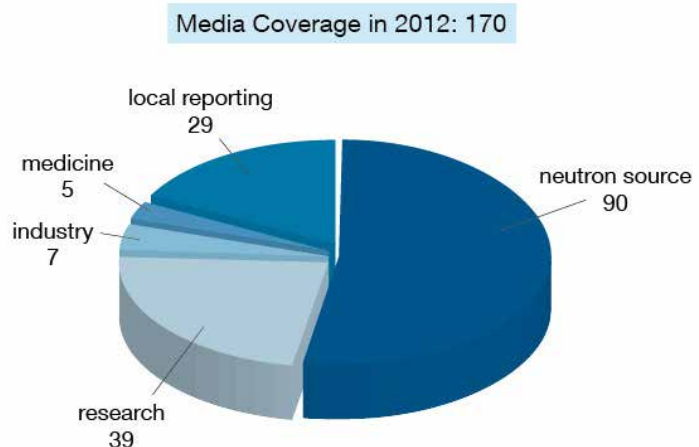


Figure 5: Most of the 170 media clippings in 2012 did concern the operation of the neutron source (90), followed by research topics (39), local reporting (29), industry (7) and medicine (5).

will be soon made available at the FRM II webpage, especially for those, who cannot visit the FRM II personally.

Cooperation with the press officers

Due to the scientific cooperation with the Helmholtz Centers, the collaboration of the press officers of the FRM II partners, especially with the JCNS of Forschungszentrum Jülich, became more intense with work on the new joint webpage www.mlz-garching.de. JCNS-press releases concerning research conducted at the FRM II were presented for the first time at the FRM II homepage as well. As one of the scientific highlights, the publication on the first evidence of the higgs mechanism in a magnet, a publication by JCNS instrument scientist Dr. Yixi Su, generated a pleasing media coverage: even Spiegel-online reported on this exciting new research result.

Media Coverage

The press releases being sent out and other issues picked up by the media such as the historic atomic egg and general safety issues as well as the C-14 issue at the end of the year, led to a total of 170 media clippings in 2012 (fig. 4). The analysis shows that most of them did concern the operation of the neutron source and safety issues (90), 39 times media reported on research topics (fig. 5).

Presserückblick 2012

Berichterstattung über die Forschungs-Neutronenquelle Heinz Maier-Leibnitz (FRM II) und ihre wissenschaftliche Kooperation im Jahr 2012

Hinweise auf Higgs-Mechanismus in einem Magneten
Garchinger Forschungsreaktor abgeschaltet

Nur für friedliche Zwecke

Wir haben den dicksten Neutronen-Strahl weltweit

WISSENSCHAFTLICH, UNTERNEHMERISCH, INTERNATIONAL

Optimiertes Hämoglobin von Mensch und Schnabeltier

2,9 Millionen Euro für Forschungsreaktor

Figure 4: Headlines in the newspaper and magazines on the FRM II in the year 2012.

Committees

Koordinierungsrat (Steering Committee)

Chairman

Prof. Dr. Sebastian Schmidt
Member of the Executive Board of
Forschungszentrum Jülich GmbH

Albert Berger
Chancellor
of the Technische Universität München

Members

Prof. Dr. Wolfgang Kaysser
Member of the Executive Board of
Helmholtz-Zentrum Geesthacht GmbH

Prof. Dr. Stephan Paul
Technische Universität München
Physik-Department E18

Thomas Frederking
Member of the Executive Board of
Helmholtz-Zentrum Berlin GmbH

Prof. Dr. Winfried Petry, Scientific Director of the
MLZ, representing TUM

MinR Stefan Kern
Federal Ministry of Education and Research

Prof. Dr. Dieter Richter, Scientific Director of the
MLZ, representing HGF institutions

MRin Dr. Ulrike Kirste
Bayerisches Staatsministerium für
Wissenschaft, Forschung und Kunst

Dr. Anton Kastenmüller
Technical Director ZWE-FRM II,
Technische Universität München

Prof. Dr. Dr. h.c. mult. Wolfgang A. Herrmann
President
Technische Universität München
represented by Prof. Dr. Thomas Hofmann,
Vice-President
of the Technische Universität München

Dr. Klaus Seebach
Administrative Director ZWE-FRM II,
Technische Universität München



The MLZ
Steering
Committee
at its meeting
in December
2012.

Wissenschaftlicher Beirat (Scientific Advisory Board)

Chairman

Prof. Dr. Peter Fratzl
Max-Planck-Institut für Kolloid- und Grenzflächenforschung, Potsdam

Members

Prof. Dr. Hartmut Abele
Atominsttitut der Österreichischen Universitäten
Technische Universität Wien, Wien

Prof. Christiane Alba-Simionescu
Laboratoire Léon Brillouin,
Centre d'Energie Atomique, Saclay

Prof. Dr. Arantxa Arbe
Unidad de Fisica de Materiales
Facultad de Quimica, San Sebastian

Prof. Dr. Andrew Harrison
Institut Laue-Langevin, Grenoble

Prof. Dr. Dirk Johrendt
Ludwig-Maximilians-Universität,
Department Chemie und Biochemie, München

Prof. Dr. Bernhard Keimer
Max-Planck-Institut für Festkörperforschung,
Stuttgart

Prof. Dr. Joël Mesot
Paul Scherrer Institut, Villigen

Prof. Dr. Joachim O. Rädler
Ludwig-Maximilians-Universität,
Department für Physik, München

Prof. Dr. Walter Reimers
Technische Universität Berlin, Institut für Werkstoffwissenschaften und -technologien, Berlin

Dr. Jens Rieger
Senior Vice President, Advanced Materials &
Systems Research
BASF SE, Ludwigshafen

Prof. Dr. Metin Tolan
Leiter Beschleuniger- & Synchrotronlabor
Technische Universität Dortmund, Dortmund

Evaluation of Beam Time Proposals: Members of the Review Panels

Prof. Ken Andersen
European Spallation Source,
Instrument Division, Lund

Dr. Tamás Belgya
Budapest Neutron Center, Budapest

Prof. Dr. Peter Böni
Technische Universität München,
Physik-Department E13, München

Prof. Dr. Jan Bonarski
Polish Academy of Sciences, Institute of Metallurgy and Materials Science, Kraków

Dr. Françoise Bourrée
Laboratoire Léon Brillouin,
Centre d'Energie Atomique, Saclay

Prof. Roberto Brusa
Università degli Studi di Trento,
Facoltà di Ingegneria, Dipartimento di Fisica,
Trento

Dr. Monica Ceretti
Université de Montpellier2,
Institut Charles Gerhardt, Montpellier

Dr. Niels Bech Christensen
Technical University of Denmark,
Institute of Physics, Roskilde

Dr. Pascale Deen
European Spallation Source (ESS AB), Lund

Prof. Dr. Stefan Egelhaaf
Heinrich-Heine-Universität Düsseldorf,
Lehrstuhl für Physik der weichen Materie, Düsseldorf

Prof. Dr. Helmut Ehrenberg
Karlsruher Institut für Technologie (KIT),
Institut für Angewandte Materialien, Karlsruhe

Dr. Marie Thérèse Fernandez-Diaz
Institut Laue-Langevin (ILL), Grenoble

Dr. Ralf Feyerherm
Helmholtz-Zentrum Berlin für Materialien und
Energie GmbH, Berlin

Dr. Peter Fouquet
Institut Laue Langevin (ILL), Grenoble

Dr. Bernhard Frick
Institut Laue Langevin (ILL), Grenoble

Dr. Victoria Garcia-Sakai
STFC Rutherford Appleton Laboratory, Didcot

Dr. Rashid Gareev
Universität Regensburg,
Fakultät für Physik, Regensburg

Prof. Giacomo Diego Gatta
Università degli Studi di Milano, Milano

Prof. Dr. Rupert Gebhard
Archäologische Staatssammlung München,
Abt. Vorgeschichte, München

Dr. Holger Gibhardt
Georg-August-Universität Göttingen,
Institut für Physikalische Chemie, Göttingen

Dr. Jens Gibmeier
Karlsruher Institut für Technologie (KIT),
Institut für Angewandte Materialien, Karlsruhe



Members of the review panels evaluating beam time at the proposal round in March 2012.

Dr. Béatrice Gillon
Laboratoire Léon Brillouin
Centre d'Energie Atomique, Saclay

Dr. Arsène Goukassov
Laboratoire Léon Brillouin
Centre d'Energie Atomique, Saclay

Dr. Christian Grünzweig
Paul Scherrer Institute, Villigen

Dr. Thomas C. Hansen
Institut Laue Langevin (ILL), Grenoble

Prof. Dr. Ian Williams Hamley
University of Reading, Reading

Dr. Thomas Hauss
Helmholtz-Zentrum Berlin für Materialien und
Energie GmbH, Berlin

Dr. Arno Hiess
European Spallation Source (ESS AB), Lund

Dr. Klaudia Hradil
Technische Universität Wien,
Röntgenzentrum, Wien

Dr. Dmytro Inosov
Max-Planck-Institut für Festkörperforschung
Stuttgart, Stuttgart

Dr. Nikolay Kardjilov
Helmholtz-Zentrum Berlin für Materialien und
Energie GmbH, Berlin

Dr. Emmanuel Kentzinger
Forschungszentrum Jülich GmbH, Jülich

Prof. Dr. Michel Kenzelmann
Paul Scherrer Institute, Laboratories for Solid
State Physics & Neutron Scattering, Villigen

Dr. Winfried Kockelmann
Rutherford Appleton Laboratory, ISIS, Didcot

Prof. Christian Krempaszky
Technische Universität München,
Fakultät für Maschinenwesen, München

Dr. Thomas Krist
Helmholtz-Zentrum Berlin für Materialien und
Energie GmbH, Berlin

Dr. Eberhard Lehmann
Paul Scherrer Institute, Villigen

Prof. Dr. Martin Lerch
Technische Universität Berlin,
Institut für Chemie, Berlin

Dr. Dieter Lott
Helmholtz-Zentrum Geesthacht GmbH,
Institut für Materialforschung, Geesthacht

Dr. Reidar Lund
University of Oslo,
Department of Chemistry, Oslo

Prof. Dr. Andreas Magerl
Universität Erlangen-Nürnberg,
Kristallographie und Strukturphysik, Erlangen

Dr. Andreas Michels
Université de Luxembourg,
Faculté des Sciences, de la Technologie et de la
Communication, Luxembourg

Prof. Dr. Martin Müller Helmholtz-Zentrum Geesthacht GmbH, Geesthacht	Dr. Simon Redfern University of Cambridge, Department of Earth Sciences, Cambridge
Dr. Bert Nickel Ludwig Maximilians-Universität München, Department für Physik, München	Prof. Dr. Günther Redhammer Universität Salzburg, Materialforschung und Physik, Salzburg
Prof. Dr. Tommy Nylander Lund University, Physical Chemistry, Lund	Dr. Walter Richtering RWTH Aachen, Institut für Physikalische Chemie, Aachen
Dr. Julian Oberdisse Université de Montpellier 2, Montpellier	Dr. Matthias Rossbach Forschungszentrum Jülich GmbH, Jülich
Prof. Dr. Luigi Paduano University of Naples “Federico II”, Chemistry Department, Naples	Dr. Margarita Russina Helmholtz-Zentrum Berlin GmbH, Institut Weiche Materie und Funktionale Materialien, Berlin
Prof. Dr. Catherine Pappas Delft University of Technology, Delft	Prof. Dr. Michael Sattler Technische Universität München, Department Chemie, München
Prof. Dr. Oskar Paris Montanuniversität Leoben, Leoben	Dr. Jürg Schefer ETH Zürich and Paul Scherrer Institut, Villigen
Prof. Dr. Wolfgang Paul Martin Luther Universität Halle-Wittenberg, Institut für Physik, Halle	Dr. Harald Schmidt Technische Universität Clausthal, Institut für Metallurgie, Clausthal
Prof. Dr. Juan-Manuel Pérez-Mato Universidad del País Vasco, Departamento de Física de la Materia Condensada y Física Aplicada II, Leioa, Bizkaia	Prof. Dr. Andreas Schönhals Bundesanstalt für Materialforschung und -prüfung, Berlin
Prof. Dr. Klaus Rätzke Christian-Albrechts Universität zu Kiel, Institut für Materialwissenschaft/Materialverbünde, Kiel	Prof. Dr. Frank Schreiber Universität Tübingen, Institut für Angewandte Physik, Tübingen



First joint review panels' meeting at Ismaning in September 2012.

Prof. Dr. Peter Schurtenberger

University of Lund,

Physical Chemistry 1, Lund

Dr. Torsten Soldner

Institut Laue-Langevin (ILL), Grenoble

Prof. Dr. Wolfgang Sprengel

Technische Universität Graz,
Institut für Materialphysik, Graz

Dr. Jochen Stahn

ETH Zürich and Paul Scherrer Institut, Villigen

Dr. Paul Steffens

Institut Laue-Langevin (ILL), Grenoble

Dr. Oliver Stockert

Max-Planck-Institut für Chemische Physik fester
Stoffe Dresden, Dresden

Dr. Susana Teixeira

Institut Laue-Langevin (ILL), Grenoble

Prof. Kristiaan Temst

Katholieke Universiteit Leuven,

Nuclear & Radiation Physics Section, Leuven

Prof. Dr. Thomas Thurn-Albrecht

Martin Luther Universität Halle-Wittenberg,

Experimentelle Polymerphysik, Halle

Prof. Dr. Tobias Unruh

Universität Erlangen-Nürnberg,

Kristallographie und Strukturphysik, Erlangen

Dr. Lambert van Eijck

Delft University of Technology,

Department of Radiation, Radionuclides and
Reactors, Delft

Prof. Dr. Regine von Klitzing

Technische Universität Berlin,

Institut für Chemie, Stranski-Laboratorium für
Physikalische und Theoretische Chemie, Berlin

Dr. Martin Weik

Institut de Biologie Structurale, Grenoble

Dr. Andrew Wildes

Institut Laue-Langevin (ILL), Grenoble

Prof. Dr. Regine Willumeit

Helmholtz Zentrum Geesthacht GmbH,
Geesthacht

Dr. Robert Wimpory

Helmholtz-Zentrum Berlin für Materialien und
Energie GmbH, Berlin

Dr. Tim Ziman

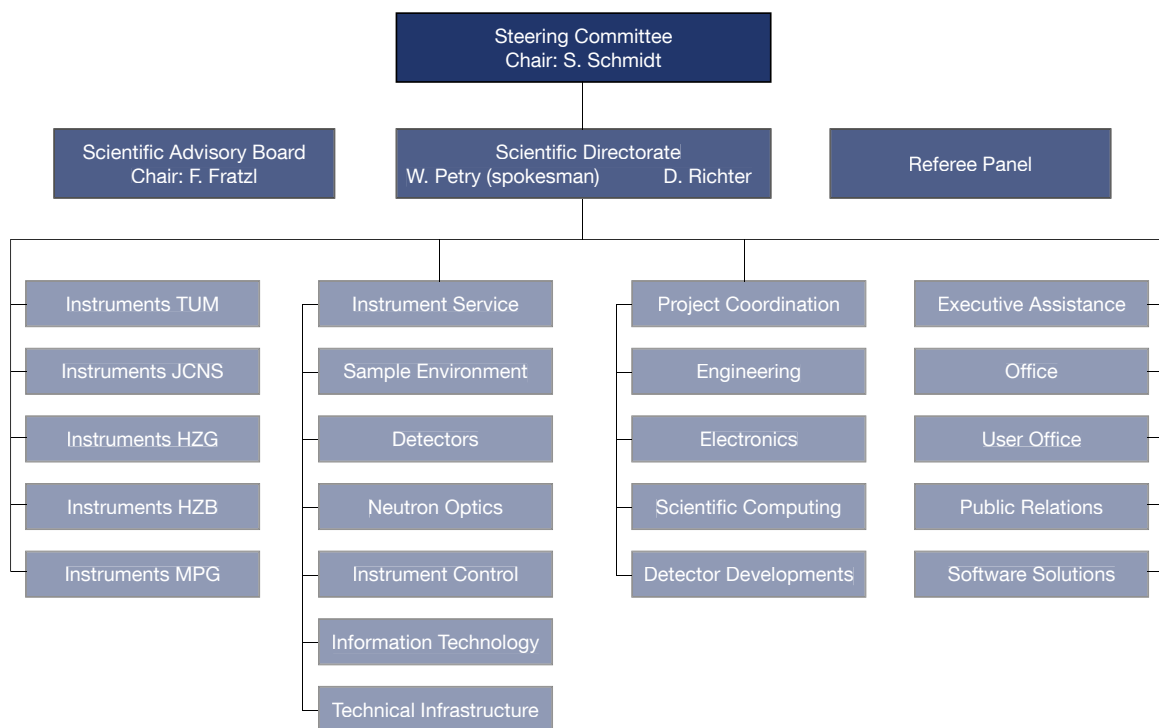
CNRS-LPMMC, Grenoble

Staff

Scientific Cooperation at the Heinz Maier-Leibnitz Zentrum (MLZ)

The Heinz Maier-Leibnitz Zentrum represents the cooperation between the Technische Universität München (TUM) and three research centres of the Helmholtz Association, namely Forschungszentrum Jülich, Helmholtz-Zentrum Geesthacht (HZG) and the Helmholtz-Zentrum Berlin (HZB), to exploit the scientific use of the Forschungs-Neutronenquelle Heinz Maier-Leibnitz. The organizational chart is shown in the figure below. MLZ is embedded in a network of strong partners including the Max Planck Society (MPG) and numerous university groups.

The Administration, Reactor and Science Division, comprising the Reactor Physics group, belong to the Integrative Research Center FRM II (ZWE-FRM II) operated by the TUM.



Scientific Director TUM

Prof. Dr. Winfried Petry, spokesman

Deputy

Dr. Jürgen Neuhaus

Office

Elisabeth Jörg-Müller

Franziska Michel

Silvia Valentin-Hantschel

Karin Kleinstück (Erasmus Mundus)

Scientific Director HGF Institutions

Prof. Dr. Dieter Richter

User Office

Dr. Flavio Carsughi

Dr. Ina Lommatsch

Ramona Bucher

Deputy

Dr. Alexander Ioffe

Executive Assistance

Dr. Rainer Bruchhaus

Dr. Connie Hesse

Public Relations

Andrea Voit

Petra Riedel

Inês Crespo (NMI3)

Silvia Valentin-Hantschel



Staff members of the FRM II at the annual summer day trip in Jetzendorf.

Instruments TUM

Dr. Jürgen Neuhaus
Dominik Bausenwein
David Behal
Christoph Berkel
Rainer Bierbaum
Georg Brandl
Karl Braun
Dr. Thomas Bücherl¹
Dr. Lea Canella
Hubert Ceeh²
Fernando Cristiano
Marcel Dickmann³
Dr. Oleksandr Dolotko⁴
Dr. Andreas Frei
Fabian Fuchs
Dr. Robert Georgii
Philipp Geselbracht
Stefan Giemsa⁵
Dr. Ralph Gilles
Dr. Alexander Grünwald⁵
Dr. Wolfgang Häußler
Dr. Michael Hofmann
Dr. Markus Hözel
Dr. Christoph Hugenschmidt
Norbert Jünke
Dr. Thomas Keller⁶
Dr. Yury Khaydukov⁶
Dr. Jens Klenke
Dr. Petra Kudejova
Dr. Thorsten Lauer
Kathrin Lehmann

Dr. Michael Leitner
Benjamin Löwe³
Dr. Wiebke Lohstroh
Andreas Mantwill²
Humphrey Morhenn⁷
Dr. Christoph Morkel
Martin Mühlbauer⁴
Nathalie Munnikes⁶
Dr. Andreas Ostermann
Dr. Jitae Park
Dr. Bjørn Pedersen
Josef Pfanzelt
Philip Pikart²
Dr. Christian Piochacz
Lucas Ravelli³
Dr. Joana Rebelo-Kornmeier
Tommy Reimann
Markus Reiner²
Dr. Zsolt Révay
Jandal Ringe
Heiko Saul
Dr. Burkhard Schillinger
Philipp Schmakat
Prof. Dr. Klaus Schreckenbach
Dr. Michael Schulz
Reinhard Schwikowski
Dr. Klaus Seemann
Dr. Anatoliy Senyshyn
Günther Seidl
Dr. Stefan Seidlmayer
Svatopluk Semecky
Luca Silvi

Dr. Giovanna Simeoni
Stefan Söllradl⁸
Dr. Oleg Sobolev⁹
Dr. Olaf Soltwedel⁶
Martin Stadlbauer
Rainer Stöpler²
Dr. Reinhard Thamm¹⁰
Dr. Anke Teichert⁹
Sebastian Vohburger
Daniela Voigt-Kiely
Franz-Michael Wagner
Dr. Nicolas Walte¹¹
Josef-Andreas Weber²
Rudolf Wildgruber
Andreas Wilhelm
Stephan Wlokka
Thorsten Zechlau
Dr. Veronika Zinth

¹Radiochemie, TUM

²Physik-Department, TUM

³Universität der Bundeswehr München

⁴Technische Universität Darmstadt

⁵Universität zu Köln

⁶Max-Planck-Institut für Festkörperforschung, Stuttgart

⁷Friedrich-Alexander-Universität Erlangen-Nürnberg

⁸Universität Bern

⁹Georg-August-Universität Göttingen

¹⁰Klinikum rechts der Isar, TUM

¹¹Universität Bayreuth



Almost the whole HZG-team at
the MLZ.

Instruments JCNS

Prof. Dr. Dieter Richter (Director JCNS)
Dr. Alexander Ioffe (Head of Outstation at FRM II)

Dr. Marie-Sousai Appavou
Dr. Nikolaus Arend
Dr. Earl Babcock
Dr. Zhenyu Di
Christian Felder
Dr. Artem Feoktystov
Dr. Henrich Frielinghaus
Zhendong Fu
Christine Gerstl
Thomas Glomann
Marco Gödel
Barbara Gold
Dennis Gurzi
Adrian Hamm
Dr. Olaf Holderer
Dr. Andreas Houben¹
Dr. Vladimir Hutanu¹
Paulo Innocente
Dr. Oxana Ivanova
Robert Klopp
Abdelillah Kobba¹
Thomas Kohnke
Dr. Denis Korolkov
Harald Kusche
Frederik Lipfert
Wolfgang Luberstetter¹
Dr. Simona Maccarrone
Dr. Stefan Mattauch
Shailesh Mishra
Dr. Martin Meven¹
Andreas Nebel
Dr. Kirill Nemkovski
Vladimir Ossovyy
Dr. Vitaliy Pipich
Stephen Price
Dr. Sabine Pütter
Dr. Aurel Radulescu
Christian Randau²
Alfred Richter

Dr. Zahir Salhi
Dr. Andrew Sazonov¹
Harald Schneider
Florian Schneider
Dr. Gerald J. Schneider
Dr. Tobias Schrader
Dr. Werner Schweika
Simon Staringer
Alexandra Steffen
Dr. Yixi Su
Dr. Noemi Szekely
Dr. Jörg Voigt
Daniel Vujevic
Dr. Jens Walter²
Baou Wu³
Dr. Michaela Zamponi

Instruments HZB
Dr. Enrico Faulhaber
Dr. Astrid Schneidewind
Florin George Stoica

Instruments HZG
Nowal Alhamdany⁴
Dr. Helmut Eckerlebe
Joergen Franke
Dr. Weimin Gan
Martin Haese-Seiller
Dr. André Heinemann
Armin Kriele
Dr. Jean-François Moulin
Matthias Pomm
Sven-Arne Siegfried

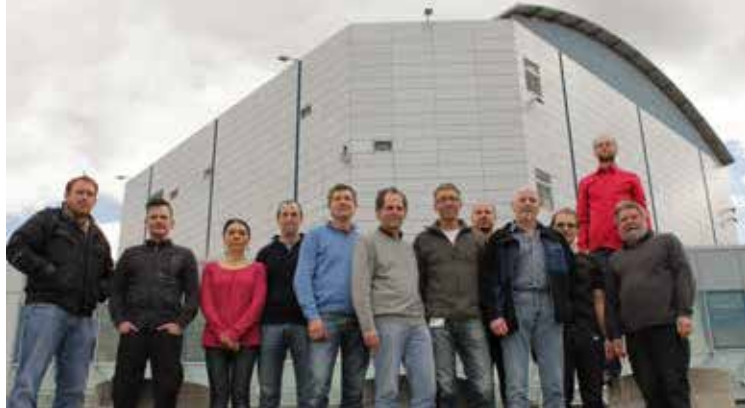
Sample Environment
Dr. Jürgen Peters
Michael Beywl
Peter Biber
Andreas Buchner
Alexander Friedrich
Markus Göhr
Heinrich Kolb

¹RWTH Aachen

²Georg-August-Universität Göttingen

³Universität Konstanz

⁴TU Clausthal



Members of the groups Sample Environment as well as Detectors and Electronics, with their heads Dr. Jürgen Peters (6th from the right) and Dr. Karl Zeitelhack (6th from the left), respectively.

Herbert Weiß
Jank Wenzlaff

Detectors and Electronics

Dr. Karl Zeitelhack
Yasin Abdullahi
Ilario Defendi
Dr. Martin Jurkovic
Max Panradl
Peter Wind
Dr. Irina Stefanescu
Machiel Zee

Neutron optics
Dr. Peter Link
Christian Breunig
Eberhard Kahle
Dr. Sergey Masalovich
Andreas Ofner
Senay Öztürk
Peter Stein
Josef Weber

IT Services
Jörg Pulz
Andreas Erb
Josef Ertl
Jörg Stoll
Hermann Westermayer

Instrument Control
Jens Krüger
Georg Kaspar
Alexander Lenz

Software Solutions
Harald Wenninger
Nataliya Ivanova
Babette Oberholz

Apprentices at the IT Services
Christina Cindric

Simon König
Pascal Neubert
Stefan Rainow
Christian Worf

Technical Infrastructure
Dr. Herbert Reithmeier
Edina Aulenbacher
Alexander Beimler
Heiner Blumenthal
Elbio Calzada
Uwe Reinecke

Scientific Computing
Dr. Joachim Wuttke
Dr. Celine Durniak
Christian Felder
Dr. Walter Van Herck
Dr. Gennady Pospelov

Integrative Research Center FRM II (ZWE-FRM II)

Board of Directors
Dr. Anton Kastenmüller, Technical Director
Prof. Dr. Winfried Petry, Scientific Director
Dr. Klaus Seebach, Administrative Director

Administration

Head
Dr. Klaus Seebach

Deputy
Reinhard Obermeier

Office
Christine Zeller

Christina Auer
Karl-Heinz Drexler
Brigitte Gallenberger



Staff members of the Department Reactor Operation, section Maintenance with its head Klaus Pfaff (in the middle of the back row).

Bernd Heck
Isabella Heinath
Karin Lüttig
Marita Neuberger
Sabine Osorio
Martina Pawlik
Kerstin Rickert
Sylvia Rubsch
Günter Wagner

Visitors' service
Ulrike Kurz
Dott. Bianca Tonin-Schebesta

Petra Müller
Bernhard Neugebauer
Klemens Otto
Thomas Ramel
Adelheid Schindler
Michael Schmidt
Johann Schreiner
David Schrulle
Daniela Strobl
Michaela Uhlmann
Hans-Jürgen Werth
Josef Wetzl
Susanne Wolff

Reactor Division

Head of Reactor Division

Dr. Anton Kastenmüller

Office

Sylvia Rubsch
Marita Neuberger
Barbara Tiepke

Security

Ralf Brosche
Johann Stephani

Department Reactor Monitoring and Radiation Protection

Dr. Helmut Zeising
Johann Aigner
Dubravka Bahmet
Rita Bertsch
Wolfgang Dollriß
Nihad Hodzic
Harry Hottmann
Florian Jeschke
Marcel Kaleve
Vanessa Kindel
Waldtraud Kluge
Daniela Lewin
Roland Maier

Department reactor enhancement

Dr. Andreas Kusterer
Holger Bamberger
Alen Begic
Wilhelm Bünten
Johann Fink
Thomas Fliegner
Bernhard Foth
Andreas Galsterer
Mira Giourges
Christian Herzog
Andreas Huber
Philipp Jüttner
Martin Kinzler
Karin Lichtenstein
Ralf Lorenz
Britta Polлом
Andreas Scharl
Robert jun. Schlecht
Uwe Stiegel
Dieter von Plata
Volker Zill

Department Reactor Operation

Dr. Axel Pichlmaier/ Attila Bancsov
Rainer Becker
Michaela Benedikt
Albin Benke
Robert Binsch



Staff members of the Department Irradiation and Sources with its head Dr. Heiko Gerstenberg (2nd from the right).

Oliver Breu
Manfred Danner
Christian Feil
Martin Flieher
Horst Gampfer
Wolfgang Glashäuser
Hubert Groß
Friedrich Gründer
György Guld
Lutz Herdam
Simone Herrmann
Florian Hofstetter
Konrad Höglauer
Thomas Kalk
Georg Kaltenegger
Frank Kewitz
Marc-Guido Krümpelmann
Johann Kund
Adolf Lochinger
Gerd Mauermann
Albert Meilinger
Markus Moser
Klaus Pfaff
Dr. Anton Röhrmoser
Ludwig Rottenkolber
Gerhard Schlittenbauer
Christiane Wickfelder
Michael Wöhner
Christian Ziller
Ismail Zöybek

Department Irradiation and Sources
Dr. Heiko Gerstenberg
Jens Birko
Alexander Draack
Jean-Marie Favoli
Heiko Fischer
Michael Fuß
Wolfgang Lange
Dr. Xiaosong Li
Volker Loder
Jens Molch
Christian Müller

Dietmar Päthe
Heike Schulz
Benjamin Schweiger
Norbert Wiegner
Andreas Wirtz

Department Electric Control Systems
Roland Schätzlein
Werner Buchner
Andreas Düring
Franz Götz
Robert Krammer
Karl-Heinz Mayr
Thomas Metzger
Johann Wildgruber

FRM (old)
Stefan Förg
Josef Waronitzka

Conventional infrastructure
Karola Frey
Andreas Heinath
André Wienholz

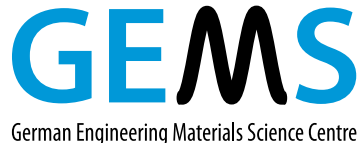
Science Division

Reactor physics
Dr. Anton Röhrmoser
Hsin-Yin Chiang
Dr. Harald Breitkreutz
Dr. Rainer Großmann
Tobias Hollmer
Tanja Huber
Dr. Rainer Jungwirth
Robert Schenk
Christian Steyer
Tobias Zweifel

Partner institutions



Bayerisches Geoinstitut
Universität Bayreuth
www.bgi.uni-bayreuth.de



German Engineering Materials Science Centre

Georg-August-Universität Göttingen

- Institut für Physikalische Chemie
www.uni-pc.gwdg.de/eckold
- Geowissenschaftliches Zentrum
www.gzg.uni-goettingen.de



German Engineering Materials Science Centre GEMS
Helmholtz-Zentrum Geesthacht GmbH

www.hzg.de



Helmholtz-Zentrum Berlin
für Materialien und Energie GmbH

www.helmholtz-berlin.de



Karlsruher Institut für Technologie

Jülich Centre for Neutron Science JCNS
Forschungszentrum Jülich GmbH

www.jcns.info



Karlsruher Institut für Technologie

- Institut für Angewandte Materialien – Energiespeichersysteme (IAM-ESS)
www.iam.kit.edu

Ludwig-Maximilians-Universität München

- Sektion Kristallographie
www.lmu.de/kristallographie
- Sektion Physik
www.softmatter.physik.uni-muenchen.de



Max-Planck-Institut für Festkörperforschung, Stuttgart
www.fkf.mpg.de



Paul Scherrer Institut

- Labor für Radio- und Umweltchemie
www.psi.ch/lch



RWTH Aachen

- Institut für Kristallographie
www.xtal.rwth-aachen.de
- Institut für Anorganische Chemie
www.ac.rwth-aachen.de



TU Clausthal

Technische Universität Clausthal

- Institut für Werkstoffkunde und Werkstofftechnik
www.iww.tu-clausthal.de



TECHNISCHE
UNIVERSITÄT
DRESDEN

Technische Universität Dresden

- Institut für Festkörperphysik
www.physik.tu-dresden.de/ifp



Technische Universität München

Technische Universität München

- E13 – Lehrstuhl für Funktionelle Materialien
www.e13.physik.tu-muenchen.de
- E18 – Lehrstuhl für Experimentalphysik I
www.e18.ph.tum.de
- E21 – Lehrstuhl für Neutronenstreuung
www.e21.ph.tum.de
- Exzellenzcluster „Origin and Structure of the Universe“
www.universe-cluster.de
- Klinikum Rechts der Isar
www.med.tum.de
- RCM - Radiochemie München
www.rcm.tum.de



Universität der Bundeswehr München

- Institut für Angewandte Physik und Messtechnik
www.unibw.de/irt2

Universität zu Köln



Universität zu Köln

- Institut für Kernphysik
www.ikp.uni-koeln.de
- II. Physikalisches Institut
www.ph2.uni-koeln.de

Imprint

Publisher:

Technische Universität München
Forschungs-Neutronenquelle
Heinz Maier-Leibnitz (FRM II)
Lichtenbergstr. 1
85747 Garching
Germany

Phone: +49.89.289.14966
Fax: +49.89.289.14995
Internet: www.mlz-garching.de
E-mail: mlz@mlz-garching.de

Editors:

Dr. Henrich Frielinghaus
Dr. Connie Hesse
Dr. Michael Hofmann
Dr. Christop Hugenschmidt
Dr. Vladimir Hutanu
Elisabeth Jörg-Müller
Dr. Peter Link
Dr. Ina Lommatsch
Dr. Stefan Mattauch
Dr. Jürgen Neuhaus
Dr. Andreas Ostermann
Dr. Bjørn Pedersen
Dr. Zsolt Révay
Petra Riedel
Dr. Yixi Su

Photographic credits:

Astrid Eckert, Andreas Heddergott, TUM:
6 (bottom, 1st and 2nd from left, right), 13, 133

Wenzel Schürmann, TUM:
6, 8 (3rd from top), 9 (3rd from top), 10 (1st and 3rd from top), 22 (bottom), 125, 134, 135, 136 (left),
140

Forschungszentrum Jülich:
6 (bottom, 2nd from right)

ESS AB:
24

Dr. Michael Schöbel, FRM II:
35

Messe München GmbH:
139 (bottom)

Editors and authors:
other images

Design and typesetting:
Ramona Bucher
Dr. Connie Hesse
Dr. Ina Lommatsch
Petra Riedel
Benjamin Sanchez
Daniel Scherzer
Adrian Weis

Publications

Scientific publications 2012

In total, the Heinz Maier-Leibnitz Zentrum (MLZ) received notice of 173 scientific publications in 2012.

For more details, please check the online version of the annual report 2012 at

<http://www.mlz-garching.de/annual-reports>

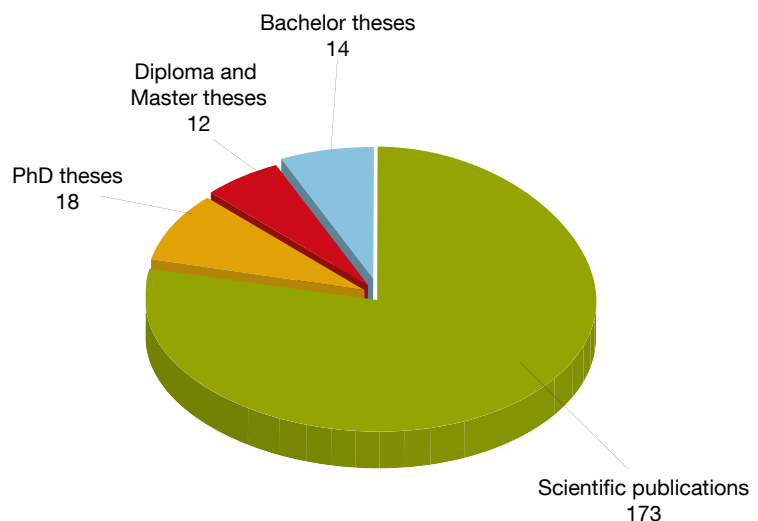
or the online publications archive at

www.frm2.tum.de/en/aktuelles/info-documents/publications-archive

Theses 2012

In total, 14 Bachelor theses, 12 Diploma and Master theses as well as 18 PhD theses supervised by staff of the scientific cooperation and based on experiments carried out at the MLZ were completed in 2012.

A detailed list can be found in the online version of the annual report 2012.



Number of scientific publications and completed theses at the Heinz Maier-Leibnitz Zentrum in 2012.

Publications

1. S.-V. Ackebauer, A. Senyshyn, H. Borrmann, U. Burkhardt, A. Ormeci, H. Rosner, W. Schnelle, M. Gamza, R. Gumeniuk, R. Ramlau, E. Bischoff, J. Schuster, F. Weitzer, A. Leithe-Jasper, L. Tjeng and Y. Grin
Structural Transformation with “Negative Volume Expansion”: Chemical Bonding and Physical Behavior of TiGePt
Chem. Eur. J. 18, 6272 (2012).
2. T. Adams, A. Chacon, M. Wagner, A. Bauer, G. Brandl, B. Pedersen, H. Berger, P. Lemmens and C. Pfleiderer
Long-Wavelength Helimagnetic Order and Skyrmion Lattice Phase in Cu₂OSeO₃
Phys. Rev. Lett. 108, 237204 (2012).
3. I. Altarev, S. Chesnevskaya, W. Feldmeier, P. Fierlinger, A. Frei, E. Gutsmiedl, F. Kuchler, P. Link, T. Lins, M. Marino, S. Paul, G. Petzoldt, A. Pichlmaier, R. Stoepler, S. Stuiber and B. Taubenheim
A next generation measurement of the electric dipole moment of the neutron at the FRM II
Il Nuovo Cimento 35C, 122 (2012).
4. M. Arzillo, G. Mangiapia, A. Pezzella, R. K. Heenan, A. Radulescu, L. Paduano and M. d'Ischia
Eumelanin Buildup on the Nanoscale: Aggregate Growth/Assembly and Visible Absorption Development in Biomimetic 5,6-Dihydroxyindole Polymerization
Biomacromolecules 13, 2379 (2012).
5. J. Bahadur, D. Sen, S. Mazumder, B. Paul, H. Bhatt and S. G. Singh
Control of Buckling in Colloidal Droplets during Evaporation-Induced Assembly of Nanoparticles
Langmuir 28, 1914 (2012).
6. R. Barth, M. G. H Vicente, O. Harling, W. Kiger, K. Riley, P. Binns, F. Wagner, M. Suzuki, T. Aihara, I. Kato and S. Kawabata
Current status of boron neutron capture therapy of high grade gliomas and recurrent head and neck cancer
Radiat. Oncol. 7, 146 (2012).
7. P. M. Benson, M. J. Heap, Y. Lavallée, A. Flaws, K.-U. Hess, A. Selvadurai, D. B. Dingwell and B. Schillinger
Laboratory simulations of tensile fracture development in a volcanic conduit via cyclic magma pressurisation
Earth Planet. Sci. Lett. 349-350, 231 (2012).
8. D. Bhowmik, N. Malikova, J. Teixeira, G. Mériguet, O. Bernard, P. Turq and W. Haussler
Study of tetrabutylammonium bromide in aqueous solution by neutron scattering
Eur. Phys. J. Special Topics 213, 303 (2012).
9. R. Biehl
Structure and dynamics of proteins
Lecture Notes of the 43rd IFF Spring School: Scattering Methods for Condensed Matter Research: Towards

- Novel Applications at Future Sources,
*Schriften des Forschungszentrum Jülich,
 Schlüsseltechnologien* 33 (2012).
10. D. Blanchard, J. B. Maronsson, M. D. Riktor, J. Kheres, D. Sveinbjörnsson, E. Gil Bardají, A. Léon, F. Jurányi, J. Wuttke, K. Lefmann, B. C. Hauback, M. Fichtner and T. Vegge
Hindered Rotational Energy Barriers of BH_4 -Tetrahedra in $\beta\text{-Mg}(\text{BH}_4)_2$ from Quasielastic Neutron Scattering and DFT Calculations
J. Phys. Chem. C 116, 2013 (2012).
11. N. Boucharat, D. Wang, E. Gil Bardaji, M. Fichtner and W. Lohstroh
Effect of a Ti-based additive on the desorption in isotope labeled $\text{LiB}(\text{H,D})_4$ - $\text{Mg}(\text{H,D})_2$ nanocomposites
J. Phys. Chem. C 116, 11877 (2012).
12. G. Brandl, J. Lal, J. Carpenter, L. Crow, L. Robertson, R. Georgii, P. Böni and M. Bleuel
Tests of modulated intensity small angle scattering in time of flight mode
Nucl. Instr. Meth. A 667, 1 (2012).
13. H. Breitkreutz and W. Petry
Simulation of the time-evolution of oxide layers surrounding cladding-meat contact faults (non-bonds) and their thermal-hydraulic implications
Transactions: RRFM-2012, April 21 – 25, St. Petersburg, Russia (2012).
14. M. Brodeck, F. Alvarez, J. Colmenero and D. Richter
Single Chain Dynamic Structure Factor of Poly(ethylene oxide) in Dynamically Asymmetric Blends with Poly(methyl methacrylate). Neutron Scattering and Molecular Dynamics Simulations
Macromolecules 45, 536 (2012).
15. T. Brückel, G. Heger, D. Richter, G. Roth and E. Zorn
Laboratory Course Neutron Scattering: Experimental Manuals
Schriften des Forschungszentrum Jülich, Schlüsseltechnologien 40 (2012).
16. T. Brückel, G. Heger, D. Richter, G. Roth and E. Zorn
Laboratory Course Neutron Scattering: Lectures
Schriften des Forschungszentrum Jülich, Schlüsseltechnologien 39 (2012).
17. T. E. Bunch, R. E. Hermes, A. M. Moore, D. J. Kennett, J. C. Weaver, J. H. Wittke, P. S. DeCarli, J. L. Bischoff, G. C. Hillman, G. A. Howard, D. R. Kimbel, G. Kletetschka, C. P. Lipo, S. Sakai, Z. Revay, A. West, R. B. Firestone and J. P. Kennett
Very high-temperature impact melt products as evidence for cosmic airbursts and impacts 12,900 years ago
Proc. Natl. Acad. Sci. U. S. A. 109, E1903 (2012).
18. S. Busch, L. C. Pardo, C. Smuda and T. Unruh
The picosecond dynamics of the phospholipid dimyristoylphosphatidylcholine in mono- and bilayers
Soft Matter 8, 3576 (2012).
19. M. Ceretti, A. Piovano, A. Cousson, T. Berthier, M. Meven, G. Agostini, J. Schefer, C. Lamberti and W. Paulus
Growth and characterization of large high quality brownmillerite $\text{CaFeO}_{2.5}$ single crystals
CrystEngComm 14, 5771 (2012).
20. L.-J. Chang, S. Onoda, Y. Su, Y.-J. Kao, K.-D. Tsuei, Y. Yasui, K. Kakurai and M. Lees
Higgs transition from magnetic Coulomb liquid to ferromagnet in $\text{Yb}_2\text{Ti}_2\text{O}_7$
Nat. Commun. 3, 992 (2012).
21. M. Daum, A. Frei, P. Geltenbort, E. Gutsmiedl, P. H. H.-C. Koch, A. Kraft, T. Lauer, A. M. S. Paul and G. Zsigmond
A low-pass velocity filter for ultracold neutrons
Nucl. Instr. Meth. A 675, 103 (2012).
22. J. Davaasambuu, F. Güthoff, M. Petri,

- K. Hradil, H. Schober, J. Ollivier and G. Eckold
Phonon-lifetimes in demixing systems
J. Phys.: Condens. Matter 24, 255401 (2012).
23. A. A. Deeg, T. E. Schrader, H. Strzalka, J. Pfizer, L. Moroder and W. Zinth
Amyloid-Like Structures Formed by Azobenzene Peptides: Light-Triggered Disassembly
Spectroscopy: An International Journal 27, 387 (2012).
24. Z. Di, D. Posselt, D.-M. Smilgies, R. Li, M. Rauscher, I. I. Potemkin and C. M. Papadakis
Stepwise Swelling of a Thin Film of Lamellae-Forming Poly(styrene-b-butadiene) in Cyclohexane Vapor
Macromolecules 45, 5185 (2012).
25. M. Dolgushev and M. Krutyeva
Coherent Dynamic Structure Factor of a Polymer Chain Confined Into a Harmonic Radial Potential
Macromol. Theory Simul. 21, 565 (2012).
26. O. Dolotko, A. Senyshyn, M. Mühlbauer, K. Nikolowski, F. Scheiba and H. Ehrenberg
Fatigue Process in Li-Ion Cells: An In Situ Combined Neutron Diffraction and Electrochemical Study
J. Electrochem. Soc. 159, A2082 (2012).
27. N. Dubrovinskaia, L. Dubrovinsky, M. Hanfland and M. Hofmann
Diamond anvils with a spherical support designed for X-ray and neutron diffraction experiments in DAC
High Pressure Res. 32, 537 (2012).
28. M. Däubler, H. Breitkreutz, W. Petry and R. Macian-Juan
New reactor safety analysis of FRM II compact core using TRACE/PARCS
Transactions: RRFM-2012, April 21 – 25, St. Petersburg, Russia (2012).
29. H. Ehrenberg, A. Senyshyn, M. Hinterstein and H. Fuess
- In Situ Diffraction Measurements: Challenges, Instrumentation, and Examples**
In: Modern Diffraction Methods, E. J. Mittermeijer and U. Welzel (ed.), Wiley-VCH Verlag GmbH & Co. KGaA, Weinheim, chapter 16, 491 (2012)
30. B. Emre, I. Dincer, M. Hoelzel, A. Senyshyn and Y. Elerman
Investigation of the nature of the unusual magnetic behavior of $\text{La}_{0.65}\text{Nd}_{0.35}\text{Mn}_2\text{Si}_2$ compound by neutron diffraction study
J. Magn. Magn. Mater. 324, 622 (2012).
31. S. Ener, J. Neuhaus, W. Petry, R. Mole, K. Hradil, M. Siewert, M. E. Gruner, P. Entel, I. Titov and M. Acet
Effect of temperature and compositional changes on the phonon properties of Ni-Mn-Ga shape memory alloys
Phys. Rev. B: Condens. Matter Mater. Phys. 86, 144305 (2012).
32. H. Frielinghaus
Small Angle Scattering and Large Scale Structures
Lecture manuscripts of the 43rd IFF Spring School: Scattering Methods for Condensed Matter Research: Towards Novel Applications at Future Sources, *Schriften des Forschungszentrum Jülich, Schlüsseltechnologien* (2012).
33. H. Frielinghaus, O. Holderer, F. Lipfert, M. Kerscher, S. Mattauch and D. Richter
Microemulsions as model fluids for enhanced oil recovery: dynamics adjacent to planar hydrophilic walls
EPJ Web of Conferences 33, 03005 (2012).
34. H. Frielinghaus, O. Holderer, F. Lipfert, M. Monkenbusch, N. Arend and D. Richter
Scattering depth correction of evanescent waves in inelastic neutron scattering using a neutron prism
Nucl. Instr. Meth. A 686, 71 (2012).
35. H. Frielinghaus, M. Kerscher, O. Holderer,

- M. Monkenbusch and D. Richter
Acceleration of membrane dynamics adjacent to a wall
Phys. Rev. E: Stat., Nonlinear, Soft Matter Phys. 85, 041408 (2012).
36. G. Friemel, W. P. Liu, E. A. Goremychkin, Y. Liu, J. T. Park, O. Sobolev, C. T. Lin, B. Keimer and D. S. Inosov
Conformity of spin fluctuations in alkali-metal iron selenide superconductors inferred from the observation of a magnetic resonant mode in $K_xFe_{2-y}Se_2$
Europhys. Lett. 99, 67004 (2012).
37. M. Frotscher, A. Senyshyn and B. Albert
Neutron Diffraction at Metal Borides, Ru_2B_3 and Os_2B_3
Z. anorg. und allg. Chem. 638, 2078 (2012).
38. B. Fåk, T. Keller, M. Zhitomirsky and A. Chernyshev
Roton-Phonon Interactions in Superfluid 4He
Phys. Rev. Lett. 109, 155305 (2012).
39. F.-X. Gallat, A. P. S. Brogan, Y. Fichou, N. McGrath, M. Moulin, M. Härtlein, J. Combet, J. Wuttke, S. Mann, G. Zaccai, C. J. Jackson, A. W. Perriman and M. Weik
A Polymer Surfactant Corona Dynamically Replaces Water in Solvent-Free Protein Liquids and Ensures Macromolecular Flexibility and Activity
J. Am. Chem. Soc. 134, 13168 (2012).
40. F.-X. Gallat, A. Laganowsky, K. Wood, F. Gabel, L. van Eijck, J. Wuttke, M. Moulin, M. Härtlein, D. Eisenberg, J.-P. Colletier, G. Zaccai and M. Weik
Dynamical Coupling of Intrinsically Disordered Proteins and Their Hydration Water: Comparison with Folded Soluble and Membrane Proteins
Biophys. J. 103, 129 (2012).
41. W. M. Gan, C. Randau, M. Hofmann, H. G. Brokmeier, M. Mueller and A. Schreyer
Peak broadening and peak shift pole figures investigations by STRESS-SPEC diffractometer at FRM II
J. Phys.: Conf. Ser. 340, 012100 (2012).
42. R. Garg, A. Senyshyn and R. Ranjan
Complex structural phase transitions in slightly Ca modified $Na_{0.5}Bi_{0.5}TiO_3$
J. Phys.: Condens. Matter 24, 455902 (2012).
43. Y. Garmay, A. Shvetsov, D. Karellov, D. Lebedev, A. Radulescu, M. Petukhov and V. Isaev-Ivanov
Correlated motion of protein subdomains and large-scale conformational flexibility of RecA protein filament
J. Phys.: Conf. Ser. 340, 012094 (2012).
44. G. D. Gatta, I. Adamo, M. Meven and E. Lambruschi
A single-crystal neutron and X-ray diffraction study of pezzottaite, $Cs(Be_2Li)Al_2Si_6O_{18}$
Phys. Chem. Miner. 39, 829 (2012).
45. G. D. Gatta, R. M. Danisi, I. Adamo, M. Meven and V. Diella
A single-crystal neutron and X-ray diffraction study of elbaite
Phys. Chem. Miner. 39, 577 (2012).
46. A.-C. Genix, A. Arbe, J. Colmenero, J. Wuttke and D. Richter
Neutron Scattering and X-ray Investigation of the Structure and Dynamics of Poly(ethyl methacrylate)
Macromolecules 45, 522 (2012).
47. H. Gerstenberg
Neutron Transmutation Doping of Silicon at Research Reactors
IAEA TECDOC 1681 (2012).
48. H. Gerstenberg and A. Kastenmüller
Die Forschungs-Neutronenquelle Heinz Maier-Leibnitz (FRM II)- Deutschlands modernster Forschungsreaktor
ATW - Internationale Zeitschrift für Kernenergie 10 (2012).

49. C. Gerstl, M. Brodeck, G. Schneider, Y. Su, J. Allgaier, A. Arbe, J. Colmenero and D. Richter
Short and Intermediate Range Order in Poly(alkylene oxide)s. A Neutron Diffraction and Molecular Dynamics Simulation Study
Macromolecules 45, 7293 (2012).
50. C. Gerstl, G. J. Schneider, A. Fuxman, M. Zamponi, B. Frick, T. Seydel, M. Koza, A.-C. Genix, J. Allgaier, D. Richter, J. Colmenero and A. Arbe
Quasielastic Neutron Scattering Study on the Dynamics of Poly(alkylene oxide)s
Macromolecules 45, 4394 (2012).
51. R. Gilles, I. M. Siouris, W. Kockelmann, D. Visser, S. Katsavounis, J. M. Walter, M. Hoelzel and M. Brunelli
Determination of phase compositions in ceramics from Gobi desert using complementary diffraction techniques
J. Radioanal. Nucl. Chem. (2012).
52. R. Gilles, P. Strunz, D. Mukherji, M. Hofmann, M. Hoelzel and J. Rösler
Stability of phases at high temperatures in CoRe based alloys being developed for ultra-high temperature applications
J. Phys.: Conf. Ser. 340, 012052 (2012).
53. C. Gold, P. Gross, L. Peyker, G. Eickerling, G. G Simeoni, O. Stockert, E. Kampert, F. Wolff-Fabris, H. Michor and E.-W. Scheidt
Interplay between crystal field splitting and Kondo effect in $\text{CeNi}_9\text{Ge}_{4-x}\text{Si}_x$
J. Phys.: Condens. Matter 24, 355601 (2012).
54. M. Granite, A. Radulescu and Y. Cohen
Small-Angle Neutron Scattering from Aqueous Dispersions of Single-Walled Carbon Nanotubes with Pluronic F127 and Poly(vinylpyrrolidone)
Langmuir 28, 11025 (2012).
55. J. de Groot, K. Marty, M. Lumsden, A. Christianson, S. Nagler, S. Adiga, W. Borghols, K. Schmalzl, Z. Yamani,
S. Bland, R. de Souza, U. Staub, W. Schweika, Y. Su and M. Angst
Competing Ferri- and Antiferromagnetic Phases in Geometrically Frustrated LuFe_2O_4
Phys. Rev. Lett. 108, 037206 (2012).
56. M. Große, M. Steinbrück, J. Stuckert, A. Kastner and B. Schillinger
Application of neutron radiography to study material processes during hypothetical severe accidents in nuclear reactors
J. Mater. Sci. 47, 6505 (2012).
57. S. Grüner, Z. Sadjadi, H. E. Hermes, A. V. Kityk, K. Knorr, S. U. Egelhaaf, H. Rieger and P. Huber
Anomalous front broadening during spontaneous imbibition in a matrix with elongated pores
Proc. Natl. Acad. Sci. U. S. A. 109, 10245 (2012).
58. S. Gupta, S. K. Kundu, J. Stellbrink, L. Willner, J. Allgaier and D. Richter
Advanced rheological characterization of soft colloidal model systems
J. Phys.: Condens. Matter 24, 464102 (2012).
59. C. Heintze, M. Hernández-Mayoral, A. Ulbricht, F. Bergner, A. Shariq, T. Weissgärber and H. Frielinghaus
Nanoscale characterization of ODS Fe–9%Cr model alloys compacted by spark plasma sintering
J. Nucl. Mater. 428, 139 (2012).
60. A. Heldmann, R. Jungwirth, H. Breitkreutz and W. Petry
Energy and lattice damage distribution at the interface UMo-Al: Comparison of fission fragments and heavy-ions
Proceedings: RERTR-2012, October 14 – 17, Warsaw, Poland (2012).
61. L. Helfen, T. F. Morgeneyer, F. Xu, M. N. Mavrogordato, I. Sinclair, B. Schillinger and T. Baumbach
Synchrotron and neutron laminography for three-dimensional imaging of

- devices and flat material specimens**
Int. J. Mater. Res. 2, 170 (2012).
62. R. Hengstler-Eger, P. Baldo, L. Beck, J. Dorner, K. Ertl, P. Hoffmann, C. Hugenschmidt, M. Kirk, W. Petry, P. Pikart and A. Rempel
Heavy ion irradiation induced dislocation loops in AREVA's M5® alloy
J. Nucl. Mater. 423, 170 (2012).
63. J. Hewett, H. Weerts, R. Brock, J. Butler, P. Fierlinger et al.
Fundamental Physics at the Intensity Frontier
The Proceedings of the 2011 workshop on Fundamental Physics at the Intensity Frontier (2012).
64. M. Hoelzel, A. Senyshyn, N. Juenke, H. Boysen, W. Schmahl and H. Fuess
High-resolution neutron powder diffractometer SPODI at research reactor FRM II
Nucl. Instr. Meth. A 667, 32 (2012).
65. I. Hoffmann, P. Heunemann, B. Farago, I. Grillo, O. Holderer, M. Päch and M. Gradzielski
Structure and dynamics of nanoemulsions: Insights from combining dynamic and static neutron scattering
Phys. Rev. E: Stat., Nonlinear, Soft Matter Phys. 86, 061407 (2012).
66. M. Hofmann, R. Gilles, J. T. Rijssenbeek, Y. Gao and M. J. Mühlbauer
Spatially Resolved Phase Analysis in Sodium Metal Halide Batteries: Neutron Diffraction and Tomography
J. Electrochem. Soc. 159, A1827 (2012).
67. A. Houben, W. Schweika, T. Brückel and R. Dronskowski
New neutron-guide concepts and simulation results for the POWTEX instrument
Nucl. Instr. Meth. A 680, 124 (2012).
68. T. Huber, R. Jungwirth, A. Röhrmoser, W. Petry, D. Staicu, M. Ernstberger, H. Thiele, A. Zappia, D. Wachs, C. Charousse, B. Stepnik, P. Lemoine and F. Charollais
Thermal Conductivity Measurement of IRIS-TUM Fuel Plates (Disperse U-8wt.%-Mo)
Transactions: RRFM-2012, April 21 – 25, St. Petersburg, Russia (2012).
69. T. Huber, W. Petry, M. Fig, R. Kennedy, A. Robinson and D. Wachs
First Results of Scanning Thermal Diffusivity Microscope (STDM) Measurements on Irradiated Monolithic and Disperse Fuel
Proceedings: RERTR-2012, October 14 – 17, Warsaw, Poland (2012).
70. C. Hugenschmidt, C. Piochacz, M. Reiner and K. Schreckenbach
The NEPOMUC upgrade and advanced positron beam experiments
New J. Phys. 14, 055027 (2012).
71. C. Hugenschmidt, K. Schreckenbach, D. Habs and P. Thirolf
High-intensity and high-brightness source of moderated positrons using a brilliant beam
Appl. Phys. B: Lasers Opt. 106, 241 (2012).
72. V. Hutana, A. Sazonov, M. Meven, H. Murakawa, Y. Tokura, S. Bordács, I. Kézsmárki and B. Nafradi
Determination of the magnetic order and the crystal symmetry in the multiferroic ground state of Ba₂CoGe₂O₇
Phys. Rev. B: Condens. Matter Mater. Phys. 86, 104401 (2012).
73. A. Ioffe, E. Babcock, S. Mattauch, V. Pipich, A. Radulescu and M. Appavou
³He Neutron Spin Filters at the JCNS: Towards Wide-Angle Polarization Analysis and the Separation of Coherent/Incoherent Scattering from Non-Deuterated Biological Objects
Chinese Journal of Physics 50, 137 (2012).
74. F. Jach, P. Höhn, A. Senyshyn, M. Ruck

- and R. Kniep
Synthesis and Crystal Structure of the Highly Reduced Metalate $\text{Ba}_3[\text{Ir}(\text{CN})_3]$
Z. anorg. und allg. Chem. 638, 1959 (2012).
75. T.-S. Jun, F. Hofmann, M. Hofmann and A. Korsunsky
Residual stress characterization in 12%-Cr steel friction stir welds by neutron diffraction
J. Strain Anal. Eng. Des. 47, 203 (2012).
76. M. Jungwirth, H. Breitkreutz, F. M. Wagner and T. Bücherl
Determination of the photon spectrum in an intense fission neutron beam
J. Instrum. 7, C03022 (2012).
77. R. Jungwirth, T. Zweifel, H. Chiang, W. Petry, F. Charollais, P. Lemoine, Y. Calzavara, H. Guyon, S. van den Berghe, A. Leenaers, E. Koonen, B. Stepnik and C. Jarousse
Ion irradiation of UMo/Al fuel samples with 7wt% and 12wt% Si inside the matrix (E-FUTURE II)
Transactions: RRFM-2012, April 21 – 25, St. Petersburg, Russia (2012).
78. M. Kayhan, E. Hildebrandt, M. Frotscher, A. Senyshyn, K. Hofmann, L. Alff and B. Albert
Neutron diffraction and observation of superconductivity for tungsten borides, WB and W_2B_4
Solid State Sci. 14, 1656 (2012).
79. J.-H. Kim, I. Vrejoiu, Y. Khaydukov, T. Keller, J. Stahn, A. Rühm, D. K. Satapathy, V. Hinkov and B. Keimer
Competing interactions at the interface between ferromagnetic oxides revealed by spin-polarized neutron reflectometry
Phys. Rev. B: Condens. Matter Mater. Phys. 86, 180402 (2012).
80. J. Kindervater, W. Häußler, A. Tischendorf and P. Böni
Neutron-spin-echo from polarizing samples
J. Phys.: Conf. Ser. 340, 012030 (2012).
81. E. J. Kintzel, M. K. Kidder, A. C. Buchanan, P. F. Britt, E. Mamontov, M. Zamponi and K. W. Herwig
Dynamics of 1,3-Diphenylpropane Tethered to the Interior Pore Surfaces of MCM-41
J. Phys. Chem. C 116, 923 (2012).
82. G. Konrad, H. Abele, M. Beck, C. Drescher, D. Dubbers, J. Erhart, H. Fillunger, C. Gösselsberger, W. Heil, M. Horvath, E. Jericha, C. Klauser, J. Klenke, B. Märkisch, R. K Maix, H. Mest, S. Nowak, N. Rebrova, C. Roick, C. Sauerzopf, U. Schmidt, T. Soldner, X. Wang, O. Zimmer and T. Perc
Neutron Decay with PERC: a Progress Report
J. Phys.: Conf. Ser. 340, 012048 (2012).
83. D. Korolkov, P. Busch, L. Willner, E. Kentzinger, U. Rücker, A. Paul, H. Frielinghaus and T. Brückel
Analysis of randomly oriented structures by grazing-incidence small-angle neutron scattering
J. Appl. Crystallogr. 45, 245 (2012).
84. S. V. Kozhevnikov, V. K. Ignatovich, Y. V. Nikitenko, F. Ott, F. Radu, A. Rühm and J. Major
Neutron magnetic resonance and non-specular reflection from a magnetic film placed in an oscillating magnetic field
J. Phys.: Conf. Ser. 340, 012084 (2012).
85. C. Krey, S. Legl, S. Dunsiger, M. Meven, J. Gardner, J. Roper and C. Pfleiderer
First Order Metamagnetic Transition in $\text{Ho}_2\text{Ti}_2\text{O}_7$ Observed by Vibrating Coil Magnetometry at Milli-Kelvin Temperatures
Phys. Rev. Lett. 108, 257204 (2012).
86. H. Köhler, K. Partes, J. Rebelo Kornmeier and F. Vollertsen
Residual Stresses in Steel Specimens Induced by Laser Cladding and their Effect on Fatigue Strength
Physics Procedia 39, 354 (2012).

87. M. Laurati, P. Sotta, D. R. Long, L.-A. Fillot, A. Arbe, A. Alegría, J. P. Embs, T. Unruh, G. J. Schneider and J. Colmenero
Dynamics of Water Absorbed in Polyamides
Macromolecules 45, 1676 (2012).
88. M. Lebsanft, A. Grüning, A. Liehr, J. Rebelo Kornmeier, W. Zinn and B. Scholtes
Residual Stresses in Flange Shafts Produced by Thermo-Mechanical Metal Forming Operations
eds. H.-P. Heim, D. Biermann, Wiss. Skripten, 19 (2012).
89. M. Leitner, H. Ceeh and J.-A. Weber
Eliminating spatial distortions in Anger-type gamma cameras
New J. Phys. 14, 123014 (2012).
90. Y. Li, G. Yu, M. Chan, V. Balédent, Y. Li, N. Barisic, X. Zhao, K. Hradil, R. Mole, Y. Sidis, P. Steffens, P. Bourges and M. Greven
Two Ising-like magnetic excitations in a single-layer cuprate superconductor
Nat. Phys. 8, 404 (2012).
91. A. Logéat, T. Köhler, U. Eisele, B. Stiaszny, A. Harzer, M. Tovar, A. Senyshyn, H. Ehrenberg and B. Kozinsky
From order to disorder: The structure of lithium-conducting garnets $\text{Li}_{7-x}\text{La}_3\text{Ta}_x\text{Zr}_{2-x}\text{O}_{12}$ ($x = 0\text{-}2$)
Solid State Ion. 206, 33 (2012).
92. G. Mangiapia, G. D'Errico, L. Simeone, C. Irace, A. Radulescu, A. Di Pascale, A. Colonna, D. Montesarchio and L. Paduano
Ruthenium-based complex nanocarriers for cancer therapy
Biomaterials 33, 3770 (2012).
93. A. Mark, J. Francis, H. Dai, M. Turski, P. Hurrell, S. Bate, J. R. Kornmeier and P. Withers
On the evolution of local material properties and residual stress in a three-pass SA508 steel weld
Acta Mater. 60, 3268 (2012).
94. A. Meier-Koll, V. Pipich, P. Busch, C. M. Papadakis and P. Müller-Buschbaum
Phase Separation in Semidilute Aqueous Poly(N-isopropylacrylamide) Solutions
Langmuir 28, 8791 (2012).
95. M. Meven
Powder and Single Crystal Diffractometry: Chemical and Magnetic Structures
Lecture Notes of the 43rd IFF Spring School: Scattering Methods for Condensed Matter Research: Towards Novel Applications at Future Sources, *Schriften des Forschungszentrum Jülich, Schlüsseltechnologien* 33 (2012).
96. A. Michels, D. Honecker, F. Döbrich, C. D. Dewhurst, K. Suzuki and A. Heinemann
Observation of cross-shaped anisotropy in spin-resolved small-angle neutron scattering
Phys. Rev. B: Condens. Matter Mater. Phys. 85, 184417 (2012).
97. D. Mikhailova, B. Schwarz, A. Senyshyn, A. M. T. Bell, Y. Skourski, H. Ehrenberg, A. A. Tsirlin, S. Agrestini, M. Rotter, P. Reichel, J. M. Chen, Z. Hu, Z. M. Li, Z. F. Li and L. H. Tjeng
Magnetic properties and crystal structure of $\text{Sr}_3\text{CoIrO}_6$ and $\text{Sr}_3\text{NiIrO}_6$
Phys. Rev. B: Condens. Matter Mater. Phys. 86, 134409 (2012).
98. M. Monkenbusch
Instruments for Neutron Scattering
Lecture Notes of the 43rd IFF Spring School: Scattering Methods for Condensed Matter Research: Towards Novel Applications at Future Sources, *Schriften des Forschungszentrum Jülich, Schlüsseltechnologien* 33 (2012).
99. H. Morhenn, S. Busch and T. Unruh
Chain dynamics in a hexadecane melt as seen by neutron scattering and identified by molecular dynamics simulations
J. Phys.: Condens. Matter 24, 375108 (2012).

100. M. Mourigal, M. Enderle, B. Fåk, R. K. Kremer, J. M. Law, A. Schneidewind, A. Hiess and A. Prokofiev
Evidence of a Bond-Nematic Phase in LiCuVO₄
Phys. Rev. Lett. 109, 027203 (2012).
101. D. Mukherji, P. Strunz, S. Piegert, R. Gilles, M. Hofmann, M. Hoelzel and J. Rösler
The Hexagonal Close-Packed (HCP) ⇌ Face-Centered Cubic (FCC) Transition in Co-Re-Based Experimental Alloys Investigated by Neutron Scattering
Metall. Mater. Trans. A 43A, 1834 (2012).
102. A. Muñoz, J. Martínez, M. Monge, B. Savoini, R. Pareja and A. Radulescu
SANS evidence for the dispersion of nanoparticles in W-1Y₂O₃ and W-1La₂O₃ processed by hot isostatic pressing
International Journal of Refractory Metals and Hard Materials 33, 6 (2012).
103. A. Neubauer, F. Jonietz, M. Meven, R. Georgii, G. Brandl, G. Behr, P. Böni and C. Pfleiderer
Optical float-zoning growth of high-quality Cu₂MnAl single crystals
Nucl. Instr. Meth. A 688, 66 (2012).
104. L. Oss-Ronen, J. Schmidt, V. Abetz, A. Radulescu, Y. Cohen and Y. Talmon
Characterization of Block Copolymer Self-Assembly: From Solution to Nanoporous Membranes
Macromolecules 45, 9631 (2012).
105. K. Osterloh, T. Bücherl, U. Zscherpel and U. Ewert
Image recovery by removing stochastic artefacts identified as local asymmetries
J. Instrum. 7, C04018 (2012).
106. G. Pabst, C. Lonez, M. Vandenbranden, J. Jestin, A. Radulescu, J.-M. Ruysschaert and T. Gutberlet
Stalk-free membrane fusion of cationic lipids via an interdigitated phase
Soft Matter 8, 7243 (2012).
107. H. Palancher, A. Bonnin, V. Honkimäki, T. Buslaps, M. Grasse, B. Stepnik and T. Zweifel
Quantitative crystallographic analysis of as-fabricated full size U-Mo/Al(Si) nuclear fuel plates
J. Alloys Compd. 527, 53 (2012).
108. H. Palancher, A. Bonnin, V. Honkimäki, P. Cloetens, H. Suhonen, T. Zweifel, R. Toucoulo, A. Rack and M. Voltolini
Coating thickness determination in highly absorbent core-shell systems
J. Appl. Crystallogr. 45, 906 (2012).
109. J. C. Perez-Flores, C. Baehtz, M. Hoelzel, A. Kuhn and F. Garcia-Alvarado
Full structural and electrochemical characterization of Li₂Ti₆O₁₃ as anode for Li-ion batteries
Phys. Chem. Chem. Phys. 14, 2892 (2012).
110. J. C. Perez-Flores, C. Baehtz, M. Hoelzel, A. Kuhn and F. Garcia-Alvarado
H₂Ti₆O₁₃, a new protonated titanate prepared by Li⁺/H⁺ ion exchange: synthesis, crystal structure and electrochemical Li insertion properties
RSC Advances 2, 3530 (2012).
111. J. C. Perez-Flores, F. Garcia-Alvarado, M. Hoelzel, I. Sobrados, J. Sanz and A. Kuhn
Insight into the channel ion distribution and influence on the lithium insertion properties of hexatitanates A₂Ti₆O₁₃ (A = Na, Li, H) as candidates for anode materials in lithium-ion batteries
Dalton Trans. 41, 14633 (2012).
112. L. Pintschovius and M. Hofmann
Stress Analysis by Neutron Diffraction
In: Modern Diffraction Methods, E. J. Mittermeier and U. Welzel (ed.), Wiley-VCH Verlag GmbH & Co. KGaA, Weinheim, chapter 6, 155 (2012)
113. M.-T. Popescu, C. Tsitsilianis, C. M. Papadakis, J. Adelsberger, S. Balog, P. Busch, N. A. Hadjiantoniou and C. S. Patrickios
Stimuli-Responsive Amphiphilic

T. Müller Charge and spin order in highly stoichiometric YFe_2O_4-delta single crystals RWTH Aachen (2012).	C. Fuchs Fertigungskonstruktion und FEM-Simulationen einer Hochfrequenzspule Hochschule München (2012).
T. Weber MIEZE in Theory, Simulation and Experiment Technische Universität München (2012).	S. Günther: Inbetriebnahme und Kalibrierung eines Probenhalters für Materialbestrahlungstests Technische Universität München (2012).
Master theses	
L. Avila Gray Effect of Magnetic Field in the Phonon Dispersion of Ni₂MnGa Magnetic Shape Memory Alloy Ludwig-Maximilians-Universität München (2012).	A. Heldmann Energie- und Gitterschädenverteilung am Übergang UMo-Al: Vergleich von Spaltprodukten und Schwerionen Technische Universität München (2012).
M. van den Berg Hydrogen Dynamics in Complex Hydrides: Hydrogen Motion in the Reaction System of Lithium Amide and Magnesium Hydride Ludwig-Maximilians-Universität München (2012).	T. Huber Messung der Wärmekapazität und Dichte verschiedener UMo Proben Technische Universität München (2012).
M. Dyakonova New polymeric systems for drug delivery Technische Universität München (2012).	K. Kahl Charakterisierung eines Cascade-Detectors am MIRA, FRM II Technische Universität München (2012).
P. Schmidt Towards smaller samples: focusing techniques at a constant wavelength neutron reflectometer Technische Universität München (2012).	M. Rutzinger Konverterabhängige Tests von GEM-Detektoren zum ortsaufgelösten Nachweis der Annihilationsstrahlung Technische Universität München (2012).
Bachelor theses	
M. Daimer Set up of a laser-pumped atomic magnetometer to characterize an extremely uniform magnetical environment Technische Universität München (2012).	A. Schneider Design and development of the data and slow control acquisition system for the TUM neutron electric dipole moment (nEDM) experiment Technische Universität München (2012).
E. Erdnüß Development of high efficient pulsing and accelerating components for the NEPOMUC positron beam Hochschule München (2012).	R. Schönberger Simulation des Transports und der Speicherung von ultrakalten Neutronen TUM School of Education (2012).
Facts and Figures	

- School: Scattering Methods for Condensed Matter Research: Towards Novel Applications at Future Sources, *Schriften des Forschungszentrum Jülich, Schlüsseltechnologien* 33 (2012).
128. D. Richter, M. Monkenbusch and D. Schwahn
Structure Characterization in Fourier Space - Neutron Scattering
In: Polymer Science: A Comprehensive Reference 2, 331 (2012).
129. W. Richtering and A. Pich
The special behaviours of responsive core-shell nanogels
Soft Matter 8, 11423 (2012).
130. K. Rolfs, M. Chiemlus, J. Guldbakke, R. Wimpory, A. Raatz, W. Petry, P. Müllner and R. Schneider
Key properties of Ni-Mn-Ga based single crystals grown with the SLARE-technique
Adv. Eng. Mater. 14, 614 (2012).
131. J. Rolph, A. Evans, A. Paradowska, M. Hofmann, M. Hardy and M. Preuss
Stress relaxation through ageing heat treatment – a comparison between in situ and ex situ neutron diffraction techniques
C. R. Phys. 13, 307 (2012).
132. J. Rolph, M. Preuss, N. Iqbal, M. Hofmann, S. Nikov, M. C. Hardy, M. G. Glavicic, R. Ramanathan and A. Evans
Residual Stress Evolution during Manufacture of Aerospace Forgings
In: Superalloys 2012, 881 (2012).
133. S. Rosenfeldt, F. Ludel, C. Schulreich, T. Hellweg, A. Radulescu, J. Schmelz, H. Schmalz and L. Harnau
Patchy worm-like micelles: solution structure studied by small-angle neutron scattering
Phys. Chem. Chem. Phys. 14, 12750 (2012).
134. M. Rovira-Esteva, N. A. Murugan, L. C. Pardo, S. Busch, J. L. Tamarit, G. J. Cuello and F. J. Bermejo
Differences in first neighbor orientation behind the anomalies in the low and high density trans-1,2-dichloroethene liquid
J. Chem. Phys. 136, 124514 (2012).
135. A. Röhrmoser, H. Breitkreutz and W. Petry
Extended studies of FRM II core conversion with UMo dispersive fuel at a prolonged fuel element
Transactions: RRFM-2012, April 21 – 25, St. Petersburg, Russia (2012).
136. S. Sabyasachi, M. Patra, S. Majumdar, S. Giri, S. Das, V. S. Amaral, O. Iglesias, W. Borghols and T. Chatterji
Glassy magnetic phase driven by short-range charge and magnetic ordering in nanocrystalline $\text{La}_{1/3}\text{Sr}_{2/3}\text{FeO}_{3-\delta}$
Magnetization, Moessbauer, and polarized neutron studies
Phys. Rev. B: Condens. Matter Mater. Phys. 86, 104416(2012).
137. S. Salzinger, S. Huber, S. Jakob, P. Busch, R. Jordan and C. Papadakis
Aggregation behavior of thermo-responsive poly(2-oxazoline)s at the cloud point investigated by FCS and SANS
Colloid Polym. Sci. 290, 385 (2012).
138. D. K. Satapathy, M. A. Uribe-Laverde, I. Marozau, V. K. Malik, S. Das, T. Wagner, C. Marcelot, J. Stahn, S. Brück, A. Rühm, S. Macke, T. Tietze, E. Goering, A. Frañó, J. H. Kim, M. Wu, E. Benckiser, B. Keimer, A. Devishvili, B. P. Toperverg, M. Merz, P. Nagel, S. Schuppler and C. Bernhard
Magnetic Proximity Effect in $\text{YBa}_2\text{Cu}_3\text{O}_7/\text{La}_{2/3}\text{Ca}_{1/3}\text{MnO}_3$ and $\text{YBa}_2\text{Cu}_3\text{O}_7/\text{LaMnO}_{3+\delta}$ Superlattices
Phys. Rev. Lett. 108, 197201 (2012).
139. C. Scherzinger, O. Holderer, D. Richter and W. Richtering
Polymer dynamics in responsive microgels: influence of cononsolvency and microgel architecture
Phys. Chem. Chem. Phys. 14, 2762 (2012).

140. E. Schmid, F. M. Wagner, L. Canella, H. Romm and T. E. Schmid
RBE of thermal neutrons for induction of chromosome aberrations in human lymphocytes
Radiat. Environ. Biophys. (2012).
141. D. Schwahn, V. Pipich and D. Richter
Composition and Long-Range Density Fluctuations in PEO/PMMA Polymer Blends: A Result of Asymmetric Component Mobility
Macromolecules 45, 2035 (2012).
142. S. Seki, J.-H. Kim, D. Inosov, R. Georgii, B. Keimer, S. Ishiwata and Y. Tokura
Formation and rotation of skyrmion crystal in a chiral-lattice insulator Cu₂OSeO₂
Phys. Rev. B: Condens. Matter Mater. Phys. 85, 220406(R) (2012).
143. D. Sen, J. Bahadur, S. Mazumder, G. Verma, P. Hassan, S. Bhattacharya, K. Vijai and P. Doshi
Nanocomposite silica surfactant microcapsules by evaporation induced self assembly: tuning the morphological buckling by modifying viscosity and surface charge
Soft Matter 8, 1955 (2012).
144. A. Senyshyn, H. Boysen, R. Niewa, J. Banys, M. Kinka, Y. Burak, V. Adamiv, F. Izumi, I. Chumak and H. Fuess
High-temperature properties of lithium tetraborate Li₂B₄O₇
J. Phys. D: Appl. Phys. 45, 175305 (2012).
145. A. Senyshyn, M. Mühlbauer, K. Nikolowski, T. Pirling and H. Ehrenberg
"In-operando" neutron scattering studies on Li-ion batteries
J. Power Sources 203, 126 (2012).
146. S. Singh, R. Rawat, S. E. Muthu, S. D'Souza, E. Suard, A. Senyshyn, S. Banik, P. Rajput, S. Bhardwaj, A. Awasthi, R. Ranjan, S. Arumugam, D. Schlagel, T. Lograsso, A. Chakrabarti and S. Barman
Spin-Valve-Like Magnetoresistance in Mn₂NiGa at Room Temperature
Phys. Rev. Lett. 109, 246601 (2012).
147. N. Smolin, R. Biehl, G. Kneller, D. Richter and J. Smith
Functional Domain Motions in Proteins on the 1-100 ns Timescale: Comparison of Neutron Spin-Echo Spectroscopy of Phosphoglycerate Kinase with Molecular-Dynamics Simulation
Biophys. J. 102, 1108 (2012).
148. R. S. Solanki, S. K. Mishra, A. Senyshyn, I. Ishii, C. Moriyoshi, T. Suzuki, Y. Kuroiwa and D. Pandey
Antiferrodistortive phase transition in pseudorhombohedral (Pb_{0.94}Sr_{0.06}) (Zr_{0.550}Ti_{0.450})O₃: A combined synchrotron x-ray and neutron powder diffraction study
Phys. Rev. B: Condens. Matter Mater. Phys. 86, 174117 (2012).
149. A. M. Stadler, C. J. Garvey, A. Bocahut, S. Sacquin-Mora, I. Digel, G. J. Schneider, F. Natali, G. M. Artmann and G. Zaccai
Thermal fluctuations of haemoglobin from different species: adaptation to temperature via conformational dynamics
J. R. Soc. Interface 9, 2845 (2012).
150. S. Stanglmaier, S. Hertrich, K. Fritz, J.-F. Moulin, M. Haese-Seiller, J. O. Rädler and B. Nickel
Asymmetric Distribution of Anionic Phospholipids in Supported Lipid Bilayers
Langmuir 28, 10818 (2012).
151. J. Stellbrink
Neutron Scattering: Lectures of the JCNS Laboratory Course held at Forschungszentrum Jülich and the research reactor FRM II of TU Munich : In cooperation with RWTH Aachen and University of Münster
Schriften des Forschungszentrum Jülich, Schlüsseltechnologien 39, 6.2 (2012).
152. P. Strunz, D. Mukherji, R. Gilles, T. Geue and J. Rösler
Investigation of metal-matrix

- composite containing liquid-phase dispersion**
J. Phys.: Conf. Ser. 340, 012098 (2012).
153. T. Sunn Pedersen, J. Danielson, C. Hugenschmidt, G. Marx, X. Sarasola, F. Schauer, L. Schweikhard, C. Surko and E. Winkler
Plans for the creation and studies of electron–positron plasmas in a stellarator
New J. Phys. 14, 035010 (2012).
154. A. Szytula, B. Penc, M. Hofmann and J. Przewoznik
Antiferromagnetism of ThCr₂Si₂
Solid State Commun. 152, 1027 (2012).
155. S. Toth, B. Lake, K. Hradil, T. Guidi, K. Rule, M. Stone and A. Islam
Magnetic soft modes in the distorted triangular antiferromagnet alpha-CaCr₂O₄
Phys. Rev. Lett. 109, 127303 (2012).
156. M. Turski, J. Francis, P. Hurrell, S. Bate, S. Hiller and P. Withers
Effects of stop–start features on residual stresses in a multipass austenitic stainless steel weld
Int. J. Pressure Vessels Pip. 89, 9 (2012).
157. M. Uchman, M. Štěpánek, S. Prévost, B. Angelov, J. Bednár, M.-S. Appavou, M. Gradzielski and K. Procházka
Coassembly of Poly(ethylene oxide)-block-poly(methacrylic acid) and N-Dodecylpyridinium Chloride in Aqueous Solutions Leading to Ordered Micellar Assemblies within Copolymer Aggregates
Macromolecules 45, 6471 (2012).
158. L. Vasylechko, U. Burkhardt, W. Schnelle, H. Borrman, F. Haarmann, A. Senyshyn, D. Trots, K. Hiebl and Y. Grin
Order/disorder in YbNi_{1±x}Ga_{2±x} ($x \leq 0.08$): Crystal structure, thermal expansion and magnetic properties
Solid State Sci. 14, 746 (2012).
159. F. M. Wagner, B. Loepert-Kabasakal and H. Breitkreutz
Neutron medical treatment of tumours - a survey of facilities
J. Instrum. 7, C03041 (2012).
160. J. L. Wang, S. J. Campbell, M. Hofmann, M. Hoelzel, R. Zeng, S. X. Dou and S. J. Kennedy
Structural properties and magnetic phase transition in HoNi₂Mn (⁵⁷Fe)
J. Appl. Phys. 111, 07E334 (2012).
161. F. Weber, L. Pintschovius, K. Hradil and D. Petitgrand
Phonon lineshapes in the vortex state of the phonon-mediated superconductor YNi₂B₂C
Phys. Rev. B: Condens. Matter Mater. Phys. B85, 224525 (2012).
162. J. Wuttke
Comment on “Elastic incoherent neutron scattering operating by varying instrumental energy resolution: Principle, simulations, and experiments of the resolution elastic neutron scattering (RENS)” [Rev. Sci. Instrum. 82, 105115 (2011)]
Rev. Sci. Instrum. 83, 107101 (2012).
163. J. Wuttke
Quasielastic Scattering
Lecture Notes of the 43rd IFF Spring School: Scattering Methods for Condensed Matter Research: Towards Novel Applications at Future Sources, *Schriften des Forschungszentrum Jülich, Schlüsseltechnologien* 33 (2012).
164. J. Wuttke
Laplace–Fourier Transform of the Stretched Exponential Function: Analytic Error Bounds, Double Exponential Transform, and Open-Source Implementation “libkww”
Algorithms 5, 604 (2012).
165. J. Wuttke, A. Budwig, M. Drochner, H. Kämmerling, F.-J. Kayser, H. Kleines, V. Ossovyi, L. C. Pardo, M. Prager, D. Richter, G. J. Schneider, H. Schneider and S. Staringer

- SPHERES, Jülich's high-flux neutron backscattering spectrometer at FRM II**
Rev. Sci. Instrum. 83, 075109 (2012).
166. R. Würschum, B. Oberdorfer, E.-M. Steyskal, W. Sprengel, W. Puff, P. Pikart, C. Hugenschmidt and R. Pippan
Free volumes in bulk nanocrystalline metals studied by the complementary techniques of positron annihilation and dilatometry
Physica B: Condensed Matter 407, 2670 (2012).
167. F. Zhang, F. Roosen-Runge, M. Skoda, R. Jacobs, M. Wolf, P. Callow, H. Frielinghaus, V. Pipich, S. Prevost and F. Schreiber
Hydration and interactions in protein solutions containing concentrated electrolytes studied by small-angle scattering
Phys. Chem. Chem. Phys. 14, 2483 (2012).
168. T. Zinn, L. Willner, R. Lund, V. Pipich and D. Richter
Equilibrium exchange kinetics in n-alkyl-PEO polymeric micelles: single exponential relaxation and chain length dependence
Soft Matter 8, 623 (2012).
169. R. Zorn
Neutron Scattering: Lectures of the JCNS Laboratory Course held at Forschungszentrum Jülich and the research reactor FRM II of TU Munich : In cooperation with RWTH Aachen and University of Münster
Schriften des Forschungszentrum Jülich, Schlüsseltechnologien 39, 11.1 (2012).
170. R. Zorn
Correlation Functions Measured by Scattering Experiments
Lecture Notes of the 43rd IFF Spring School: Scattering Methods for Condensed Matter Research: Towards Novel Applications at Future Sources,
Schriften des Forschungszentrum Jülich, Schlüsseltechnologien 33 (2012).
171. R. Zorn
Sample shape contribution to the resolution function of time-of-flight neutron scattering spectrometers
Nucl. Instr. Meth. A 674, 85 (2012).
172. T. Zweifel, H. Palancher, A. Bonnin, F. Charollais, A. Leenaers, S. van den Berghe, R. Jungwirth, W. Petry and P. Lemoine
Study of Si and ZrN coated UMo atomised particles using high energy XRD
Transactions: RRFM-2012, April 21 – 25, St. Petersburg, Russia (2012).

Theses

Doctoral theses

J. Adelsberger
Struktur und Kinetik thermoresponsiver Hydrogele

Technische Universität München (2012).

S. Busch
The Pico- to Nanosecond Dynamics of Phospholipid Molecules

Technische Universität München (2012).

S. Ener
Lattice Dynamics in Ferromagnetic Shape Memory Alloy System Ni-Mn-Ga

Technische Universität München (2012).

F. Groitl
High Resolution Spectroscopy with the Neutron Resonance Spin Echo Method

TU Berlin (2012).

J. de Groot
Charge, spin and orbital order in the candidate multiferroic material LuFe₂O₄

RWTH Aachen (2012).

R. M. Hengstler-Eger
Ion Irradiation Studies of the Origins of Pressurized Water Reactor Fuel Assembly Deformation

Technische Universität München (2012).

- E. T. Hoppe
Physikalische Eigenschaften von Polybutadienschmelzen am Polymer-Festkörper-Kontakt und im Volumen
Technische Universität München (2012).
- G. T. M. Hörnig
Untersuchungen zur Aerosolabscheidung in AGR-Wärmetauschern
Technische Universität München (2012).
- F. Jonietz
Spin Transfer Torques and Spin Fluctuations in Helimagnets
Technische Universität München (2012).
- R. Meier
Novel Structuring Routines for Organic Photovoltaics
Technische Universität München (2012).
- A. Meier-Koll
Neutronenkleinwinkelstreuung und Brillouinspektroskopie an thermoresponsiven Hydrogelen
Technische Universität München (2012).
- M. Meyer
The Microscopic Structure of Polymer Grafted Nanoparticles
WWU Münster (2012).
- B. M. Naveen Kumar
Crystal and spin structure and their relation to physical properties in some geometrical and spin spiral multiferroics
RWTH Aachen (2012).
- J. Park
Spin Dynamics in 122-Type Iron-Based Superconductors
Universität Stuttgart (2012).
- P. Pikart
Advances in Coincident Doppler Broadening Spectroscopy: Element Selective Studies on Metallic Nanolayers with Monoenergetic Positrons
Technische Universität München (2012).
- A. Sepe
Structural ordering in block copolymer thin films
Technische Universität München (2012).
- R. G. Valicu
Design and tests of an adaptive focusing neutron guide
Technische Universität München (2012).
- Q. Zhong
Structure and transition behavior of novel thermo-responsive polymer films
Technische Universität München (2012).
- Diploma theses**
- M. Fuchs
Wärmeleitmessungen an UMo
Technische Universität München (2012).
- A. Fuxmann
Seitenkettendynamik in Poly(n-hexylmethacrylat) und Poly(n-decylmethacrylat)
Technische Universität München (2012).
- T. Gigl
Temperaturfeldanalyse an einem NEPOMUC-Testaufbau und Messung der Positronenstrahlparameter
Technische Universität München (2012).
- B. Gold
Polymerdynamik in Nanokompositen mit attraktiven Wechselwirkungen
Universität Regensburg (2012).
- J. Kindervater
From Heli- to Paramagnetism in MnSi: Polarization Analysis with MiniMuPAD
Technische Universität München (2012).
- M. Kugler
Helimagnons in Single-k MnSi: Investigated with the Cold Neutron Triple-Axis Spectrometer MIRA-2
Technische Universität München (2012).

T. Müller Charge and spin order in highly stoichiometric YFe_2O_4-delta single crystals RWTH Aachen (2012).	C. Fuchs Fertigungskonstruktion und FEM-Simulationen einer Hochfrequenzspule Hochschule München (2012).
T. Weber MIEZE in Theory, Simulation and Experiment Technische Universität München (2012).	S. Günther: Inbetriebnahme und Kalibrierung eines Probenhalters für Materialbestrahlungstests Technische Universität München (2012).
Master theses	
L. Avila Gray Effect of Magnetic Field in the Phonon Dispersion of Ni₂MnGa Magnetic Shape Memory Alloy Ludwig-Maximilians-Universität München (2012).	A. Heldmann Energie- und Gitterschädenverteilung am Übergang UMo-Al: Vergleich von Spaltprodukten und Schwerionen Technische Universität München (2012).
M. van den Berg Hydrogen Dynamics in Complex Hydrides: Hydrogen Motion in the Reaction System of Lithium Amide and Magnesium Hydride Ludwig-Maximilians-Universität München (2012).	T. Huber Messung der Wärmekapazität und Dichte verschiedener UMo Proben Technische Universität München (2012).
M. Dyakonova New polymeric systems for drug delivery Technische Universität München (2012).	K. Kahl Charakterisierung eines Cascade-Detectors am MIRA, FRM II Technische Universität München (2012).
P. Schmidt Towards smaller samples: focusing techniques at a constant wavelength neutron reflectometer Technische Universität München (2012).	M. Rutzinger Konverterabhängige Tests von GEM-Detektoren zum ortsaufgelösten Nachweis der Annihilationsstrahlung Technische Universität München (2012).
Bachelor theses	
M. Daimer Set up of a laser-pumped atomic magnetometer to characterize an extremely uniform magnetical environment Technische Universität München (2012).	A. Schneider Design and development of the data and slow control acquisition system for the TUM neutron electric dipole moment (nEDM) experiment Technische Universität München (2012).
E. Erdnüß Development of high efficient pulsing and accelerating components for the NEPOMUC positron beam Hochschule München (2012).	R. Schönberger Simulation des Transports und der Speicherung von ultrakalten Neutronen TUM School of Education (2012).
Facts and Figures	

M. Steinmaßl

**Minimization of remanent magnetic fields
for the measurement of the electric dipole
moment of the neutron**

Technische Universität München (2012).

J. Weber

**Optical pumping of $^{199}\text{-Hg}$ atoms with an UV
laser**

Technische Universität München (2012).

A. Wurm

**Development of a gas-flow cooling system
for a new measurement of the electric dipole
moment of $^{129}\text{-Xe}$**

Technische Universität München (2012).

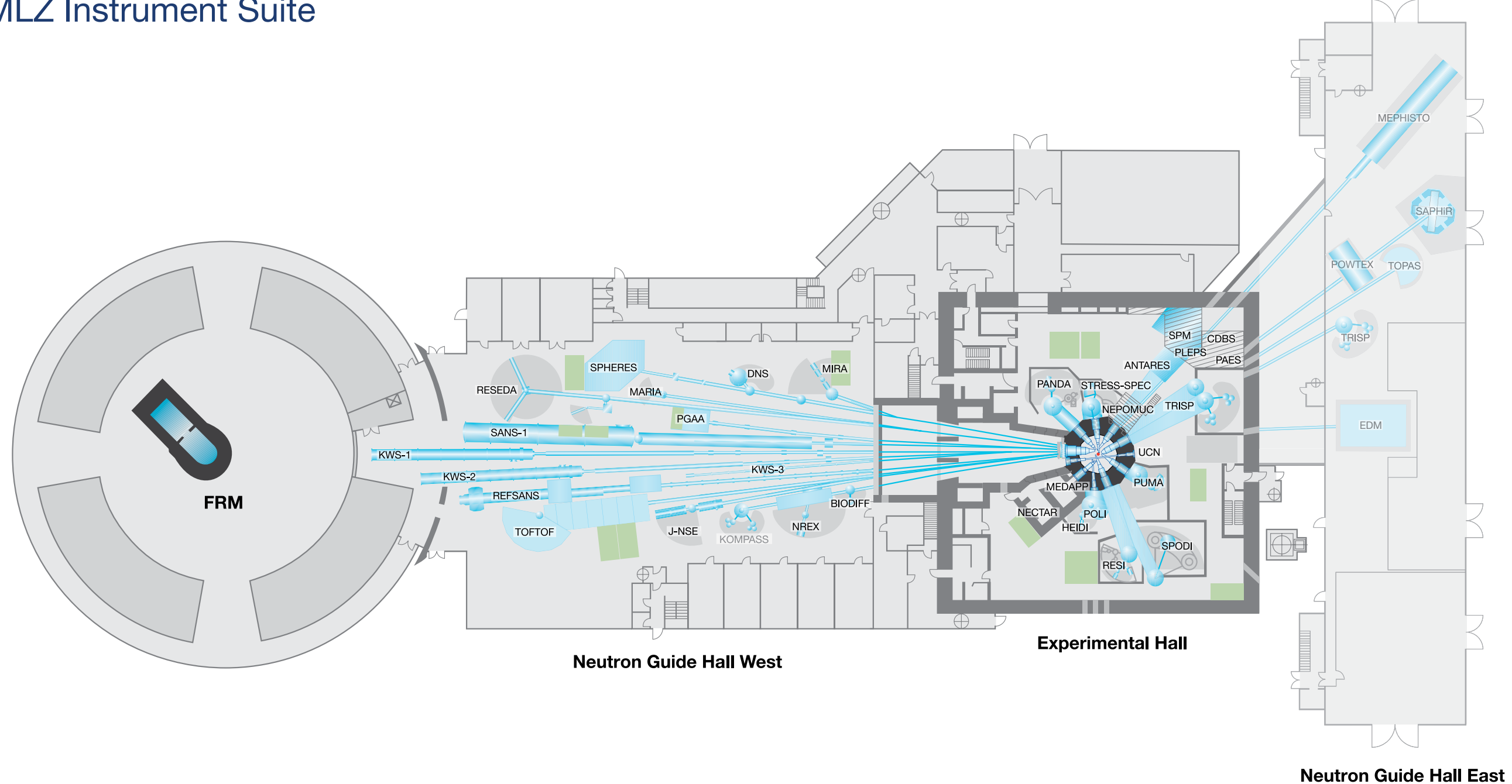
Miscellaneous

Philipp Baur

**Neutronenstrukturmessung von
Glukosekristallen**

TUM Kolleg Seminararbeit, Otto-von-Taube
Gymnasium, Gauting (2012).

MLZ Instrument Suite



Instrument	Description	Neutrons	Status	Operated by	Funding
ANTARES	Radiography and tomography	cold	operation (2013)	TUM	TUM
BIODIFF	Diffractometer for large unit cells	cold	operation	TUM, JCNS	TUM, FZJ
DNS	Diffuse scattering spectrometer	cold	operation	JCNS	FZJ
HEIDI	Single crystal diffractometer	hot	operation	RWTH Aachen	FZJ
J-NSE	Spin-echo spectrometer	cold	operation	JCNS	FZJ
KOMPASS	Three axes spectrometer	cold	construction	Uni Köln, TUM	BMBF
KWS-1	Small angle scattering	cold	operation	JCNS	FZJ
KWS-2	Small angle scattering	cold	operation	JCNS	FZJ
KWS-3	Very small angle scattering	cold	operation	JCNS	FZJ
MARIA	Magnetic reflectometer	cold	operation	JCNS	FZJ
MEPHISTO	Facility for particle physics, PERC	cold	reconstruction	TUM	TUM, DFG
MIRA	Multipurpose instrument	cold	operation	TUM	TUM
MEDAPP	Medical irradiation treatment	fast	operation	TUM	TUM
NECTAR	Radiography and tomography	fast	operation	TUM	TUM
NEPOMUC	Positron source, CDBS, PAES, PLEPS, SPM	-	operation	TUM, UniBw München	TUM, BMBF
NREX	Reflectometer with X-ray option	cold	operation	MPI Stuttgart	MPG
PANDA	Three axes spectrometer	cold	operation	TU Dresden, JCNS	FZJ

Instrument	Description	Neutrons	Status	Operated by	Funding
PGAA	Prompt gamma activation analysis	cold	operation	Uni Köln, PSI	TUM
PUMA	Three axes spectrometer	thermal	operation	Uni Göttingen, TUM	TUM
POLI	Single-crystal diffractometer polarized neutrons	hot	operation	RWTH Aachen	BMBF, FZJ
POWTEX	Time-of-flight diffractometer	thermal	construction	RWTH Aachen, Uni Göttingen, JCNS	BMBF, FZJ
REFSANS	Reflectometer	cold	operation	GEMS	HZG
RESEDA	Resonance spin-echo spectrometer	cold	operation	TUM	TUM
RESI	Single crystal diffractometer	thermal	operation	LMU	TUM
SANS-1	Small angle scattering	cold	operation	TUM, GEMS	TUM, HZG
SAPHIR	Six anvil press for radiography and diffraction	thermal	construction	BGI	BMBF
SPHERES	Backscattering spectrometer	cold	operation	JCNS	FZJ
SPODI	Powder diffractometer	thermal	operation	KIT	TUM
STRESS-SPEC	Materials science diffractometer	thermal	operation	TUM, TU Clausthal, GEMS	TUM, HZG
TOFTOF	Time-of-flight spectrometer	cold	operation	TUM	TUM
TOPAS	Time-of-flight spectrometer	thermal	construction	JCNS	FZJ
TRISP	Three axes spin-echo spectrometer	thermal	operation	MPI Stuttgart	MPG
UCN	Ultra cold neutron source, EDM	ultra-cold	construction	TUM	TUM, DFG



Heinz Maier-Leibnitz Zentrum (MLZ)

www.mlz-garching.de

Title image on the front:

The central part of SAPHiR, the Six Anvil Press for High Pressure Radiography and Diffraction.
SAPHiR is the first instrument, that was installed in the new neutron guide hall east.

Title image on the back:

Magnetic field compensation system of the EDM experiment in the neutron guide hall east. The discovery of an electric dipole moment of the neutron (nEDM) would be a step towards an explanation of the matter anti-matter asymmetry in the Universe.